

Dissertation
submitted to the
Combined Faculty of Natural Sciences and Mathematics
of Heidelberg University, Germany
for the degree of
Doctor of Natural Sciences

Put forward by
Michael, Weber
born in: Trier, Germany
Oral examination: 16.06.2021

MINSTED Fluorescence Nanoscopy

Referees:

Prof. Dr. Dr. hc. mult. Stefan Hell

Prof. Dr. Ulrich Schwarz

Für meine Frau Rachel und meine Familie

Abstract

A nanoscopy method, MINSTED, was developed. MINSTED localizes fluorescent emitters using STED to achieve single-digit nanometric localization precision with minimal amount of detected photons. Organic fluorophores to suit the demands of MINSTED microscopy were synthesized and tested. Initially, photoswitchable diarylethenes were optimized by reducing their cycloreversion quantum yield and increasing the water solubility, which enabled their use for single molecule localization microscopy. Exposed to STED light, undesired photochemical reactions through higher excited states prohibited their application in MINSTED nanoscopy. Therefore, the photoactivatable siliconrhodamine ONB-2SIR was designed for high resilience towards two-photon activation by the STED light. Additionally, a special conjugation and purification protocol was created to circumvent its hydrophobicity. A localization precision of 2 nm was achieved on immobilized single emitters by MINSTED with only 200 detected photons. Primary antibodies conjugated with ONB-2SIR were used to image cellular samples with a median fluorophore localization precision of 2.1 nm.

Eine neue Nanoskopie Methode, MINSTED, wurde entwickelt, welche fluoreszierende Emitter durch STED bis in den einstelligen Nanometerbereich genau lokalisiert und dies mit einer minimalen Anzahl an detektierten Photonen erreicht. Organische Fluorophore wurden synthetisiert und getestet, um die Anforderungen der MINSTED-Mikroskopie zu erfüllen. Zunächst wurden photoschaltbare Diarylethene durch die Verringerung ihrer Ringöffnungs-Quantenausbeute und eine Verbesserung ihrer Wasserlöslichkeit optimiert. Unerwünschte photochemische Reaktionen über höhere angeregte Zustände durch STED-Licht verhinderten aber ihren Einsatz in der MINSTED Nanoskopie. Das photoaktivierbare Siliziumrhodamin ONB-2SIR wurde auf hohe Resilienz gegenüber Zweiphotonenaktivierung durch den STED-Laser hin optimiert und ein spezielles Konjugations- und Aufreinigungsprotokoll wurde entwickelt, um seine schlechte Wasserlöslichkeit zu umgehen. Auf immobilisierten

Einzelemittlern wurde durch MINSTED eine Lokalisationsgenauigkeit von 2 nm mit nur 200 detektierten Photonen erreicht. Primäre Antikörper gekoppelt mit ONB-2SIR auf zellulären Proben führten zu einer Lokalisationspräzision der Fluorophore von 2.1 nm im Median.

Contents

1. Introduction	3
1.1. Fourier optics and the conventional resolution limit	4
1.2. Molecular bonds and Fluorescence	8
1.3. Xanthenic Fluorophores	12
1.4. Diarylethenes	14
1.5. Nanoscopy	15
1.5.1. Single molecule localization nanoscopy	15
1.5.2. Coordinate targeted nanoscopy	16
1.5.3. MINFLUX and MINSTED	18
2. Manuscripts	22
2.1. Prologue	22
2.2. Manuscript I: Photoswitchable Diarylethenes	23
2.3. Manuscript II: Photoactivatable Siliconrhodamine	34
2.4. Manuscript III: MINSTED	43
3. Discussion	53
4. Summary	59
5. Acknowledgement	61
6. Supporting Information	62
6.1. Manuscript I: Photoswitchable Diarylethenes	62
6.2. Manuscript II: Photoactivatable Siliconrhodamine	127
6.3. Manuscript III: MINSTED	164
7. Publications	180

Bibliography

181

1. Introduction

The interaction of light with matter is the basis of numerous physical phenomena. These interactions such as scattering or absorption have a specific probability expressed by the cross section, which depends on the type of matter and wavelength of the photon. Without relying on electronic transitions, which are the origin of absorption, the interaction cross sections of light with matter is generally very small. A benzene ring, for example, has a scattering cross-section of only $\sim 10^{-25} \text{ cm}^2$ with light of 400 nm wavelength [1]. By intense irradiation of 1 kWcm^{-2} , i.e. a photon flux of $2 \cdot 10^{25} \text{ cm}^{-2}$, only about two photons are scattered per second. This makes light an ideal tool to investigate processes inside cells or tissues reported without much interaction with the sample per se, as biological cells, comprising of mainly water and organic molecules, are fairly transparent. A small chemical modification, namely the addition of one nitro and one amine group in the para-position of benzene yields *p*-nitroaniline. This still small molecule has an electronic transition at 400 nm with a cross section of $4.7 \cdot 10^{-17} \text{ cm}^2$. The same light intensity, which resulted in only two scattered photons per second, yields $9.4 \cdot 10^8$ absorptions per second. Although this interaction is strong, it is difficult to measure a single absorption event, since the photon flux obeys the Poisson statistics due to the quantum nature of photons. Single interactions can be detected by using fluorescence, where the molecule absorbs photons and photons of lower energy are emitted with a certain probability, defined as the quantum yield. A fluorophore with unity quantum yield emits one lower energy photon per absorbed photon, making single-photon interactions easily detectable. By specifically labelling compartments, structures or molecules within a cell, different aspects of their function and interactions can be studied using fluorescence. However, the resolution of conventional light microscopy is limited by diffraction. Different methods have been developed to overcome this limitation and to extract diffraction-unlimited spatial information from fluorescent emitters.

Fluorescence microscopy and its advanced nanoscopy methods are based on the physical

principles of light passing through an optical system and the photo-physical properties of luminescent molecules. This chapter summarizes the principles of optical microscopy and the chemophysical fundamentals of fluorescent dyes. It focuses on xanthenic fluorophores as an example of fluorescent dyes with wide applicability and use for fluorescence microscopy. Next, the chemophysical principles underlying the photoswitchable diarylethenes are described and different nanoscopy methods are presented, which rely on specific properties of fluorophores to break the diffraction barrier. Finally, the new MINSTED concept is introduced and compared to the established MINFLUX method, both currently being the most photon efficient methods to achieve single-digit nanometric resolution.

1.1. Fourier optics and the conventional resolution limit

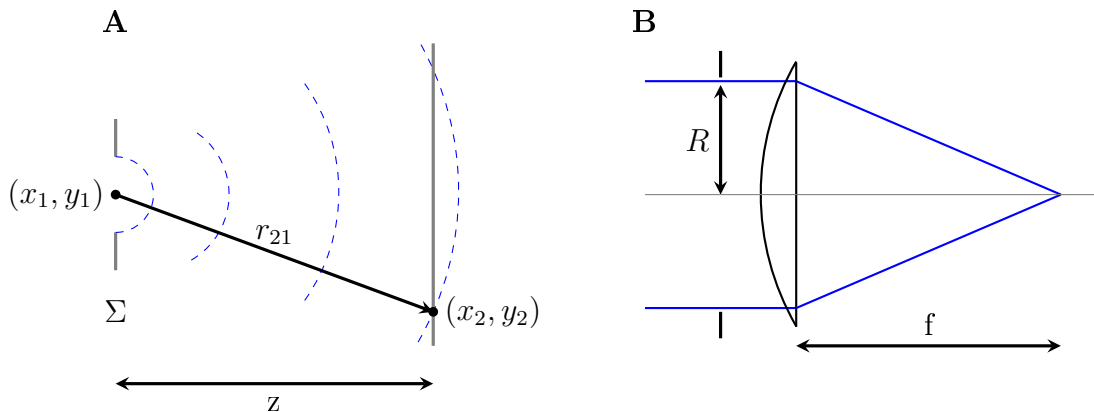


Figure 1.1.: Huygens principle (A) and paraxial lens (B).

The propagation of light through an optical system can be described using Fourier optics as presented by Goodman [2] upon which the following considerations are based. A microscope as an optical system is called diffraction-limited and achieves its maximal spatial resolution if the system transforms an incident spherical wave from a point source into a converging wave with a perfect spherical shape, which converges into a single focal point. No distortions, called aberrations, are introduced in such a diffraction-limited system and its properties can be easily calculated by Fourier optics, which relies on the wave nature of light. Each wave can be described as a superposition of other waves, which is the

fundamental idea behind the Huygens-Fresnel principle as expressed in (1.1).

$$\begin{aligned}
 U(x_2, y_2) &= \frac{z}{j\lambda} \iint_{\Sigma} U(x_1, y_1) \frac{e^{j k r_{12}}}{r_{12}^2} dx_1 dy_1 \\
 I &= |U|^2 \\
 r_{12} &= \sqrt{z^2 + (x_2 - x_1)^2 + (y_2 - y_1)^2} \\
 k &= \frac{2\pi}{\lambda}; z = z_2 - z_1
 \end{aligned} \tag{1.1}$$

The complex phasor U expresses the phase and the intensity I of the light wave at a given point. The phasor evolution is described by a superposition of spherical waves emitted at each point within the aperture Σ with the phasor present at this point. Using a second order Taylor polynomial of r_{21} in (1.1) and retaining only the terms up to the second order, the so-called Fresnel approximation is obtained. The Fresnel approximation is valid in the near-field of the aperture with only small angles of diffraction involved [2].

$$U(x_2, y_2) = \frac{e^{j k z}}{j\lambda z} \iint_{\Sigma} U(x_1, y_1) \exp \left[\frac{j k}{2z} [(x_1 - x_2)^2 + (y_1 - y_2)^2] \right] dx_1 dy_1 \tag{1.2}$$

Another approximation can be made by assuming the propagation distance z to be much larger than the aperture, yielding the so-called Fraunhofer approximation (1.3), which is valid for the far field.

$$U(x_2, y_2) = \frac{e^{j k z}}{j\lambda z} e^{j \frac{k}{2z}(x_2^2 + y_2^2)} \iint_{\Sigma} U(x_1, y_1) \exp \left[-j \frac{2\pi}{\lambda z} (x_1 x_2 + y_1 y_2) \right] dx_1 dy_1 \tag{1.3}$$

The Fraunhofer approximation as written in (1.3) can be recognized as a Fourier transform of the phasor in combination with phase manipulating terms. Assuming a circular aperture, as present in most microscopy objectives, of radius R and uniform illumination yields the phasor U_a

$$\begin{aligned}
 U_a(x, y) &= A \text{circ}(x, y) \\
 \text{circ}(x, y,) &= \begin{cases} 1, & x^2 + y^2 < R^2 \\ 0.5, & x^2 + y^2 = R^2 \\ 0, & x^2 + y^2 > R^2 \end{cases}
 \end{aligned} \tag{1.4}$$

A thin lens with negligible thickness directly placed after the aperture modifies the phasor U_a to U_l due to its focal length f .

$$U_l(x, y) = A \text{circ}(x, y) e^{-j \frac{k}{2f} (x^2 + y^2)} \quad (1.5)$$

If the radius R of the aperture is small compared to the focal length of the lens f , the Fresnel approximation (1.2) can be considered to be valid. As another effect of this restriction, the angles between the optical axis and the light rays are small and such a system is called to be paraxial. The Fresnel approximation at the focal point $z = f$ is reduced by U_l to the Fraunhofer approximation of the aperture.

$$U(x_2, y_2) = \frac{e^{j k f}}{j \lambda f} e^{j \frac{k}{2f} (x_2^2 + y_2^2)} \iint_{-\infty}^{+\infty} A \text{circ}(x_1, y_1) \exp \left[-j \frac{2\pi}{\lambda f} (x_1 x_2 + y_1 y_2) \right] dx_1 dy_1 \quad (1.6)$$

By switching from Cartesian to radial coordinates and applying the limit of the radial aperture, the expression can be further simplified to

$$U(r_2, \theta_2) = A \frac{e^{j k f}}{j \lambda f} e^{j \frac{k r_2^2}{2f}} \int_0^R dr_1 r_1 \int_0^{2\pi} d\theta_1 \exp \left[-j \frac{2\pi}{\lambda f} r_1 r_2 \cos(\theta_2 - \theta_1) \right] \quad (1.7)$$

The angular integral of this expression can be solved using the zeroth order Bessel function J_0 and by change of variables, the radial integral yields the first order Bessel function J_1 .

$$\begin{aligned} U(r_2) &= A \frac{e^{j k f}}{j \lambda f} e^{j \frac{k r_2^2}{2f}} 2\pi \int_0^R dr_1 r_1 J_0 \left(\frac{2\pi r_1 r_2}{\lambda f} \right) \\ &= A \frac{e^{j k f}}{j} e^{j \frac{k r_2^2}{2f}} \frac{R^2}{r_2} J_1 \left(\frac{2\pi r_2 R}{\lambda f} \right) \end{aligned} \quad (1.8)$$

The shape of the radial profile of the resulting phasor depends only on the first order Bessel function J_1 divided by the radial variable r_2 . In order to be able to separate two fluorophores, the space between them should be at least the distance d between the central maximum and the first minimum of the calculated phasor, which occurs at the minimum of the Bessel function $J_1(\pi a)$ at $a = 1.22$. The intensity distribution I of this particular phasor is called Airy pattern.

$$\begin{aligned}
I(r_2) &= A^2 \frac{R^4}{r_2^2} \left| J_1 \left(\frac{2\pi r_2 R}{\lambda f} \right) \right|^2 \\
d &= 0.61 \frac{\lambda f}{R}
\end{aligned}
\tag{1.9}$$

The optical resolution is often expressed using the numerical aperture NA of the objective lens, which consists of the index of refraction n of the media and the maximum half-angle α of the illuminating cone. In an optical system for undistorted lateral imaging, the angle α is linked with the aperture radius and the focal length by the sine function. The refractive index n links the speed of light inside the media c with its value in vacuum c_0 . Since the energy of a photon, which depends on its frequency ν , is always conserved, the wavelength of the photon inside the media λ is different from its value in vacuum λ_0 .

$$\begin{aligned}
\text{NA} &= n \sin(\alpha) \\
\frac{R}{f} &= \sin(\alpha) \\
n &= \frac{c_0}{c} \\
c &= \nu \lambda \Rightarrow \lambda = \frac{\lambda_0}{n} \\
d &= 0.61 \frac{\lambda_0}{\text{NA}}
\end{aligned}
\tag{1.10}$$

In conventional microscopy this diffraction barrier sets a limit for the achievable resolution, which lies at around 200 nm for visible light and a high-NA oil-immersion objective. By using special arrangements of illumination and detection, an at the best two-fold improvement can be achieved (Airy-scan [3], rescanning microscopy [4], etc.). The diffraction barrier can thus only fundamentally be overcome by exploiting the physiochemical properties of the fluorophores.

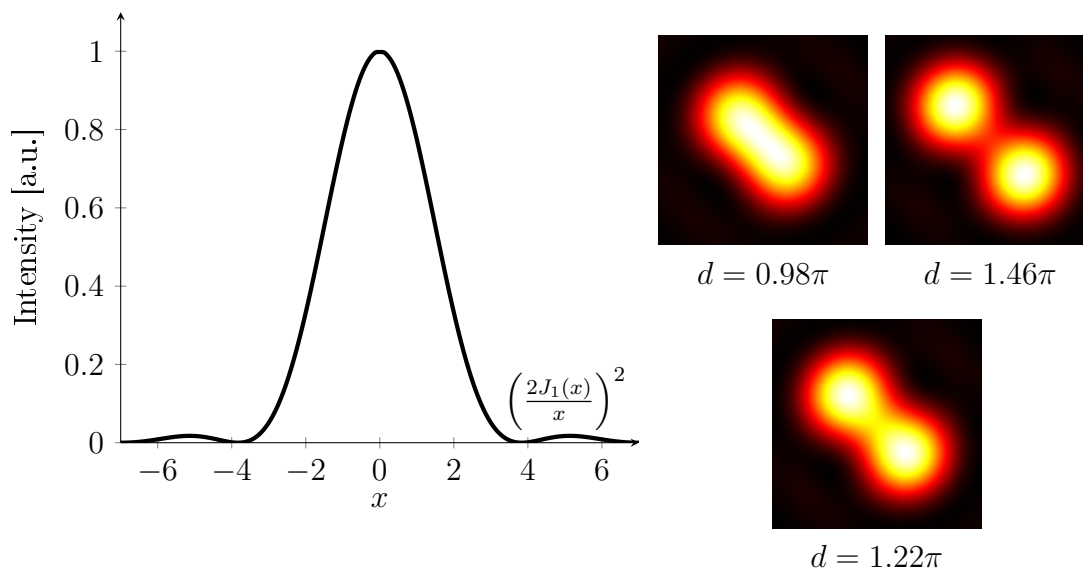


Figure 1.2.: Intensity profile of the Airy pattern and 2D intensity of two emitters separated by d .

1.2. Molecular bonds and Fluorescence

The absorption and fluorescence of light by molecules is based on the interactions of photons with the molecular orbitals of the molecule. In particular, the frontier orbitals (HOMO: highest occupied molecular orbital; LUMO: lowest unoccupied molecular orbital) are often accountable for the characteristic interaction of molecules with light. These molecular orbitals are also responsible for the formation of chemical bonds and their energy difference defines the wavelength of the interacting photon. To be able to form molecular bonds, the atomic orbitals of the binding atoms must overlap. Therefore, the shape of the atomic orbitals are important for the formation of molecular orbitals. The shape of an atomic orbital depends on the position of the electron in the electron shells and can either be of type s, p, d or f. The two most important atomic orbitals for organic chemistry are the s and p orbitals, since d orbitals only exist in electron shells which are first occupied in the 4th period of the Periodic Table, whereas the mostly used elements in organic chemistry are within the first three periods. S orbitals have a circular shape, whereas p orbitals have the shape of a “dumbbell”.

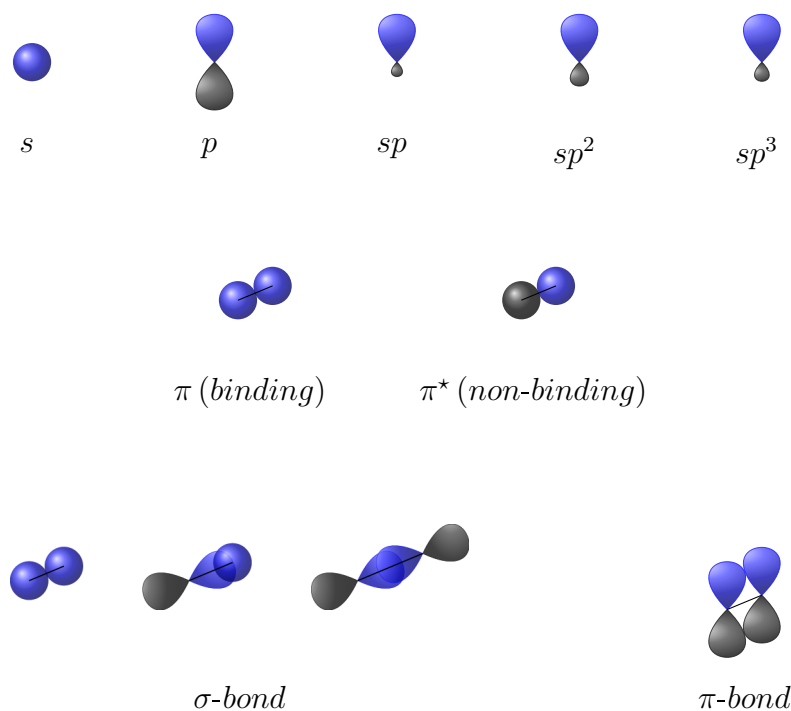


Figure 1.3.: Atomic orbitals and molecular bonds

Besides these basic atomic orbitals, so-called hybrid orbitals can be formed. The most important element for organic chemistry, carbon, is capable of forming up to four bonds. Its first electron shell is fully filled and is not participating in formation of molecular orbitals. The second shell consists of a filled 2s orbital and three 2p orbitals, where only two of them are occupied with only one electron. Since three p orbitals would occupy the whole space around the atom (p orbitals are larger than s orbitals), in order to be able to form four bonds, s and p orbitals must form hybrid orbitals (sp , sp^2 , sp^3). Depending on the phase of their wavefunction, the overlapping atomic orbitals form either binding or non-binding molecular orbitals. Binding orbitals have energy levels lower than the atomic orbitals, whereas non-binding orbitals, which are marked with a star, have higher energy levels than the atomic orbitals. Depending on the orientation of the participating atomic orbitals being either collinear or parallel, the molecular orbitals are called σ or π bonds. The absorption of a photon can excite an electron inside a binding orbital to a non-occupied non-binding orbital. Due to the formation of multiple bonds within an average-sized molecule, a large set of binding and non-binding molecular orbitals are formed, which are creating a whole absorption spectra for each molecule. The energy diagram of the simple hydrocarbon ethene is shown in Figure 1.2.

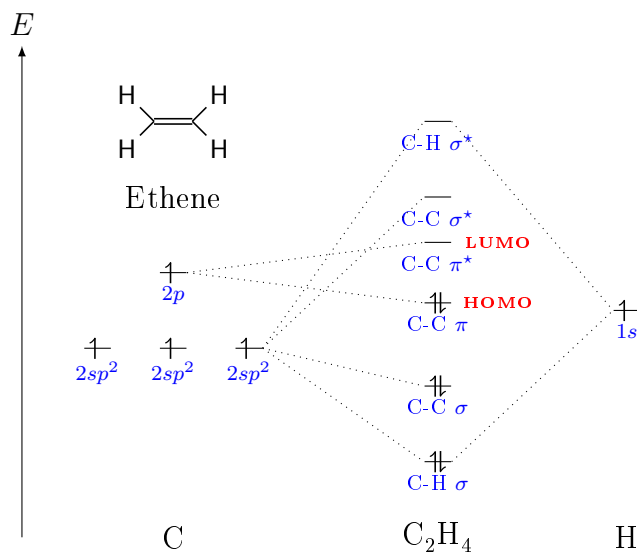


Figure 1.4.: Chemical structure and simplified energy diagram of the molecular orbitals in ethene.

The HOMO and LUMO levels of this molecule are the π and π^* molecular orbits formed by the interactions of the p atomic orbitals of the carbon atoms. These p orbitals form one of the bonds within the double bond. In the case of ethene, the energy difference between the HOMO and LUMO level is equal to the energy of a photon with a wavelength of 185nm [5]. Such a highly energetic UV photon would be unfavorable for fluorescence microscopy due to its harmful effects to other organic molecules and the opacity of most materials at this wavelength. In order to obtain fluorophores with a smaller separation between HOMO and LUMO level and therefore with an absorption in the visible or near-infrared region of the light, two different approaches can be followed. The first one uses the fact that a chain of carbon atoms bound through alternating single and double bonds form a so-called conjugated system. The atomic p orbitals, which are forming the double bonds, are not only overlapping at the position of the double bonds, but also at the single bonds. The four atomic p orbitals in two neighboring double bonds are therefore creating a new set of four molecular orbitals and the single and double bonds are transformed into conjugated bonds with a uniform bond length. This results in an increase in the HOMO and a decrease in the LUMO energy. The larger the conjugated system, the lower the energy difference between HOMO and LUMO becomes. The second option for achieving a smaller separation between HOMO and LUMO level is the introduction of electron donating groups into the structure. These auxochromes shift the absorption towards lower photon energy (red or bathochromic shift). Electron withdrawing groups (antiauxochromes) lead to

larger separation between the HOMO and LUMO levels and induce a blue or hypsochromic shift. The combination of an auxochrome and an antiauxochrome on a conjugated system does not cancel out the effects, but increases the electron donation by the auxochrome and therefore its bathochromic shift. These push-pull systems are a very effective way to shift the absorption and fluorescence of relatively small conjugated systems into the visible spectra of light. This strategy is often preferred over extending the conjugated system, since large molecules offer more vibrational pathways to convert the energy into heat rather than emitting a photon, which results in a lower quantum yield of the fluorophore. The HOMO and LUMO level of a fluorophore with an extended conjugated and push-pull system is depicted in Figure 1.5.

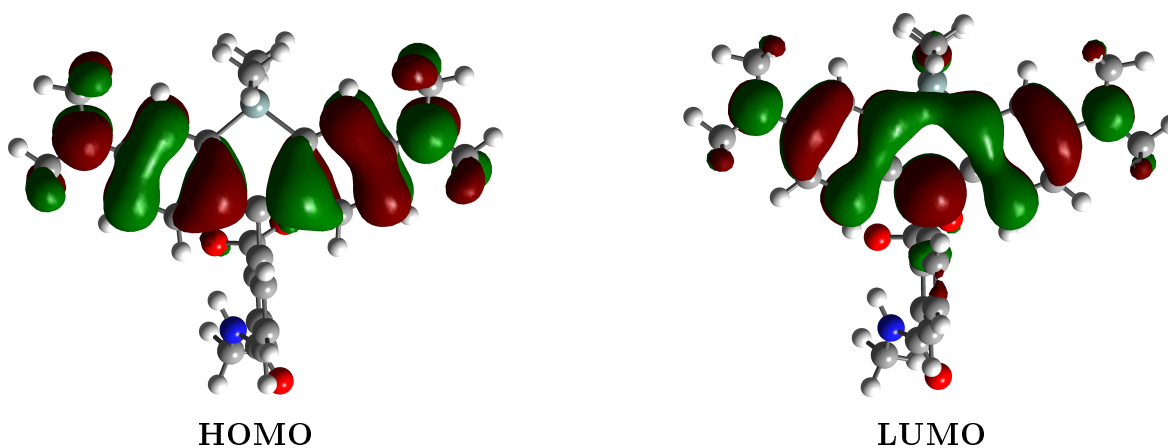


Figure 1.5.: Isodensity surface plot of HOMO and LUMO level of 4-methylamide siliconrhodamine with different phases of the wavefunction in green and red (courtesy of Jonas Bucevicius).

Whereas the energies of the transitions are defined by the molecular orbitals, their shape and strength in the absorption and fluorescence spectra are set by the vibrational modes of the molecule. The absorption of a photon leads to a near-instantaneous rearrangement of the electron density on the molecule, which results in a subsequent repositioning of the nuclei. This relaxation process lowers the energy of the now occupied level and implies a red-shift of the emitted fluorescence photon. Since the absorption and emission processes are on the time scale of femtoseconds, whereas the relaxation after absorption or fluorescence takes picoseconds, the relaxed HOMO and LUMO levels are not accessible for the photonic processes. Instead, absorption and fluorescence are favoring final states with similar nuclear coordinates like their initial state (Franck-Condon principle). These are higher

vibrational states of the relaxed HOMO and LUMO, which are often similar in both. For most fluorophores, the absorption and fluorescence spectra are therefore mirror images of each other, like in rhodamine B shown in Figure 1.2.

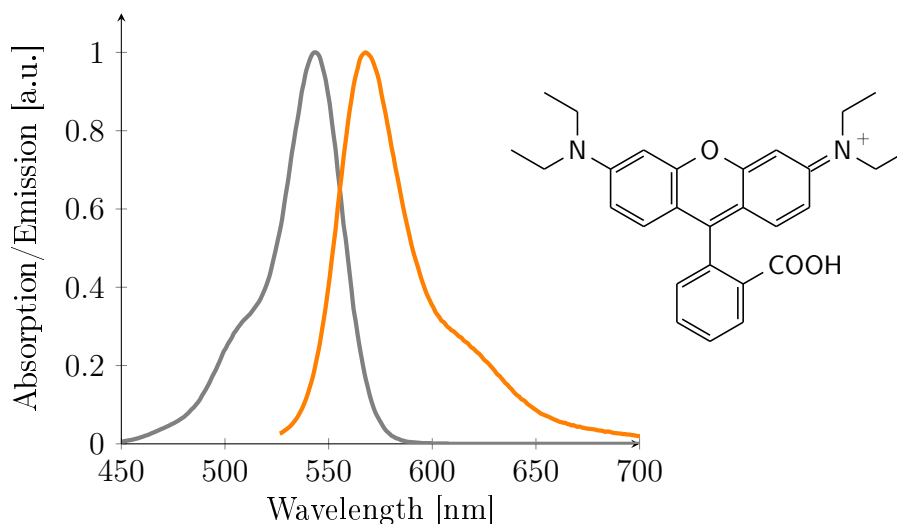


Figure 1.6.: Chemical structure, Absorption (gray) and fluorescence (orange) spectra of rhodamine B in ethanol.

1.3. Xanthenic Fluorophores

Rhodamine B is a xanthenic fluorophore, one of the most commonly used class of fluorescent dyes. Due to their great structural variability, their absorption wavelength can be tuned from the blue visible range to the near-infrared. The chromophore consists of a relatively small conjugated system with two heteroatoms at opposite sides of the molecule, which function as an auxochrome (hydroxyl or amine) and an antiauxochrome (aldehyde or quaternary ammonium) dependent on the mesomeric structure. The conjugated system can be extended at these heteroatoms or electron-donating groups can be attached to shift the absorption to lower photon energies. At the center of the chromophore, electron-withdrawing groups result in the same effect, due to their antiauxochromic behavior.

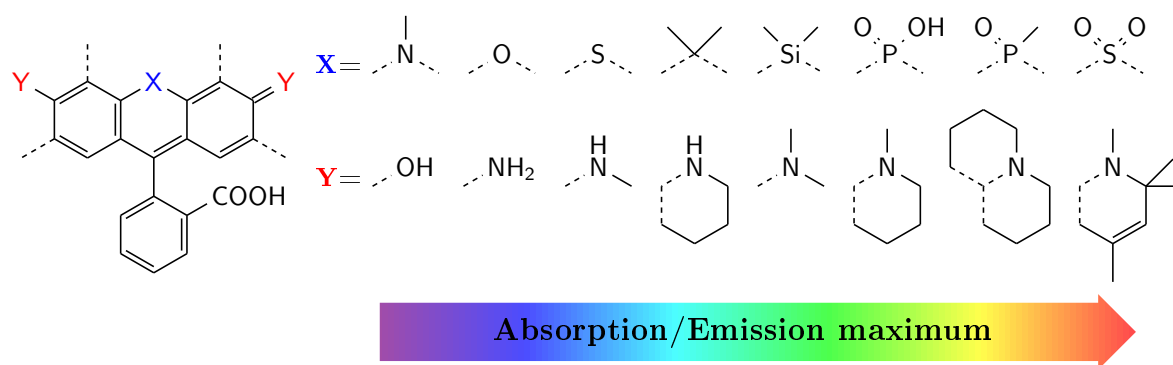


Figure 1.7.: Chemical structure of xanthenic fluorophores and spectral shift due to chemical modifications.

Apart from the spectral flexibility, xanthenic fluorophores feature a switching mechanism based on a nucleophilic attack on their electron-poor conjugated system, which facilitates the synthesis of photoactivatable, photoswitchable and analyte-sensitive chromophores. The nucleophilic attack on the central carbon atom by an intra- or extra-molecular nucleophile splits the conjugated system, inducing a strong bathochromic shift into the UV. Xanthenic chromophores bearing a 3-carboxyl group as internal nucleophile are in an equilibrium between the fluorescent zwitterion and the closed non-fluorescent lactone form. This equilibrium can be shifted by the solvent or by chemical modifications of the molecule. Attaching electron-withdrawing groups to the conjugated system favors the lactone form, whereas electron-donating groups shift the equilibrium towards the zwitterion form. By using photocleavable electron-withdrawing groups, xanthenic dyes can be converted into photoactivatable fluorophores with a thermodynamically stable off- and on-state. Such photoactivatable fluorophores can be activated only once. Any implementation of photoswitchability with multiple switching cycles on xanthenic dyes themselves yields thermodynamically instable on-states.

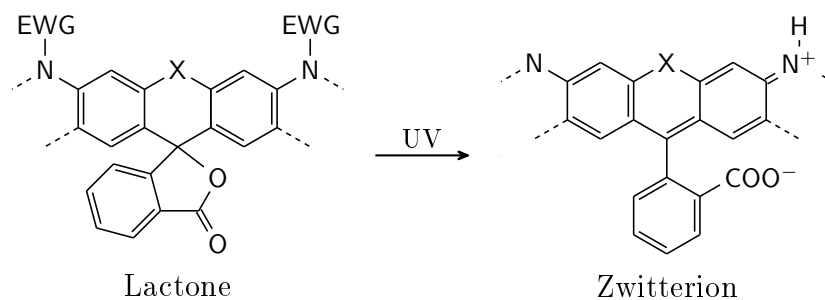


Figure 1.8.: Electron-withdrawing groups (EWG) force xanthenic fluorophores into the non-fluorescent lactone form. Photocleavage of the EWG by UV light shifts the equilibrium towards the fluorescent zwitterion form.

1.4. Diarylethenes

Thermodynamically stable off- and on-states and multiple switching cycles are key features of diarylethenes. Designed and mainly used in organic solvents and polymers, these photoswitchers have been adapted in the last years for fluorescence microscopy [6]. The switching mechanism stems from the formation and breaking of a single bond, which results in a rearrangement of the other bonds connecting or disconnecting the two conjugated systems on both ends of the molecule. Depending on the structure of the diarylethene, either none, or only one or both states show fluorescence induced by the same light that switched them between the two states.

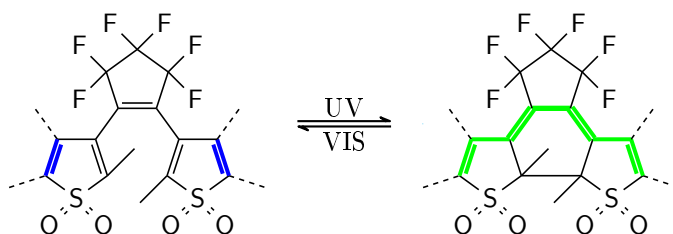


Figure 1.9.: Photoswitching of diarylethene by UV and visible light connects (green) and disconnects (blue) the conjugated systems.

1.5. Nanoscopy

Although the information transported by a single photon is limited, theoretically unlimited spatial resolution can still be achieved by exploiting the different characteristics of the fluorescence. The key to retrieve subdiffractional information is to make the fluorophores discernable by switching these between an on- and off-state. Long-lasting off-states like in photoactivatable xanthenic fluorophores or photoswitchable diarylethenes enables the localization of single fluorescent emitters based on their diffraction-limited images by stochastic switching to the on-state. The coordinate of the active fluorophore is then encoded in the image. If the switching to the off-state can be driven by light, saturating this process with a beam owning a position of zero-intensity results in an inhibition of the fluorescence except near this point. The fluorescence photons then only report the number of molecules in this subdiffractional region. The position of zero intensity is then the reference coordinate for the fluorescence. Since this coordinate is injected into the sample, this type of nanoscopy is called coordinate-targeted. Each method features different strengths and downsides and requires fluorophores with special properties, as outlined below.

1.5.1. Single molecule localization nanoscopy

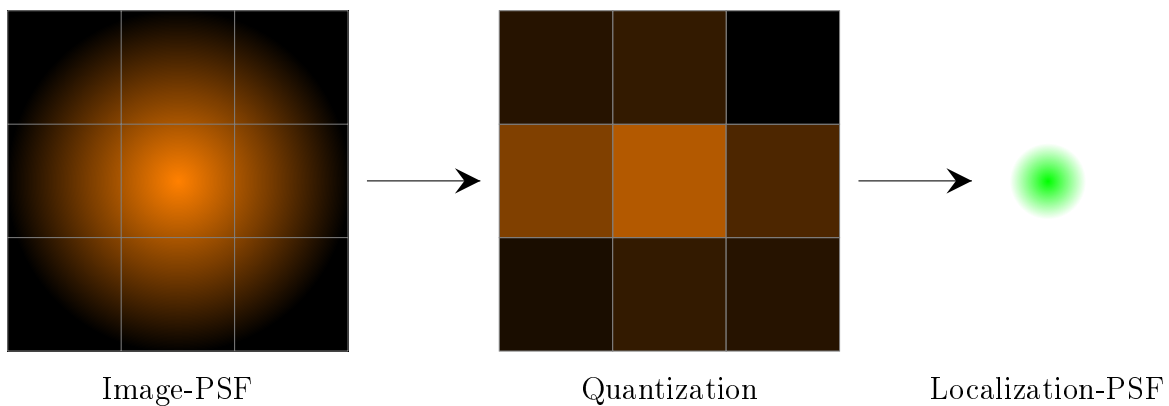


Figure 1.10.: Single molecule localization.

Single fluorescent molecules appear at best as a diffraction-limited spot in the image. By sampling this image and finding the center of mass of its intensity distribution, the position of the emitter can be localized with subdiffractional precision. This localization breaks the

diffraction barrier only if a known number of emitters, preferentially one, is active in each diffractive PSF and all other fluorophores are in an off-state. This condition of sparse distribution of emitters can be obtained with switchable or activatable probes. Depending on the switching mechanism used, the name of this method varies (e.g. PALM [7], STORM [8], GSDIM [9]). Due to the quantization of the emission in photons, the signal at each sampling point in the image obeys the Poisson distribution, i.e. shows the so-called shot-noise. The standard deviation of the expected number of photons N_i at each sampling point is given by $\sqrt{N_i}$. The localization precision σ of these methods therefore not only depends on the standard deviation σ_{PSF} of the point spread function (PSF) of the optical system, which in turn depends on the wavelength λ of the emitted photons, but also by the total number of detected photons N .

$$\sigma \propto \frac{\sigma_{\text{PSF}}}{\sqrt{N}} \propto \frac{\lambda}{\sqrt{N}} \quad (1.11)$$

In background-free samples with bright fluorophores, a localization precision below 10nm is commonly demonstrated and very high resolution can be achieved in the reconstructed image. In practice, the number of emitted photons limits the localization precision. For each twofold improvement in the resolution, the number of photons must be quadrupled. Although a first improvement in the resolution can be easily achieved, each further improvement becomes more costly. Moreover, the background within the relatively large image of the PSF worsens the achievable resolution. As these methods cannot reliably distinguish between several active emitters within a PSF, mis-localization artifacts occur if the emitters are recognized as a single one.

1.5.2. Coordinate targeted nanoscopy

The limitation of the resolution to the PSF not only applies to the emitted photons, but also to the excitation beam. Its wavelength and the numerical aperture of the optical system limit the minimal size of an illumination spot in the sample. Fortunately, illumination patterns with one or multiple points of zero-intensity minima can be created, which allows driving photo-physical processes everywhere except at these intensity zeros. If these processes are used to switch the molecules from an emissive to a dark state, the region with active fluorophores is no longer limited by diffraction. Different methods have been developed using this principle and differ in the used active and inactive form of the molecule

(e.g. GSD [10], RESOLFT [11], STED [12]).

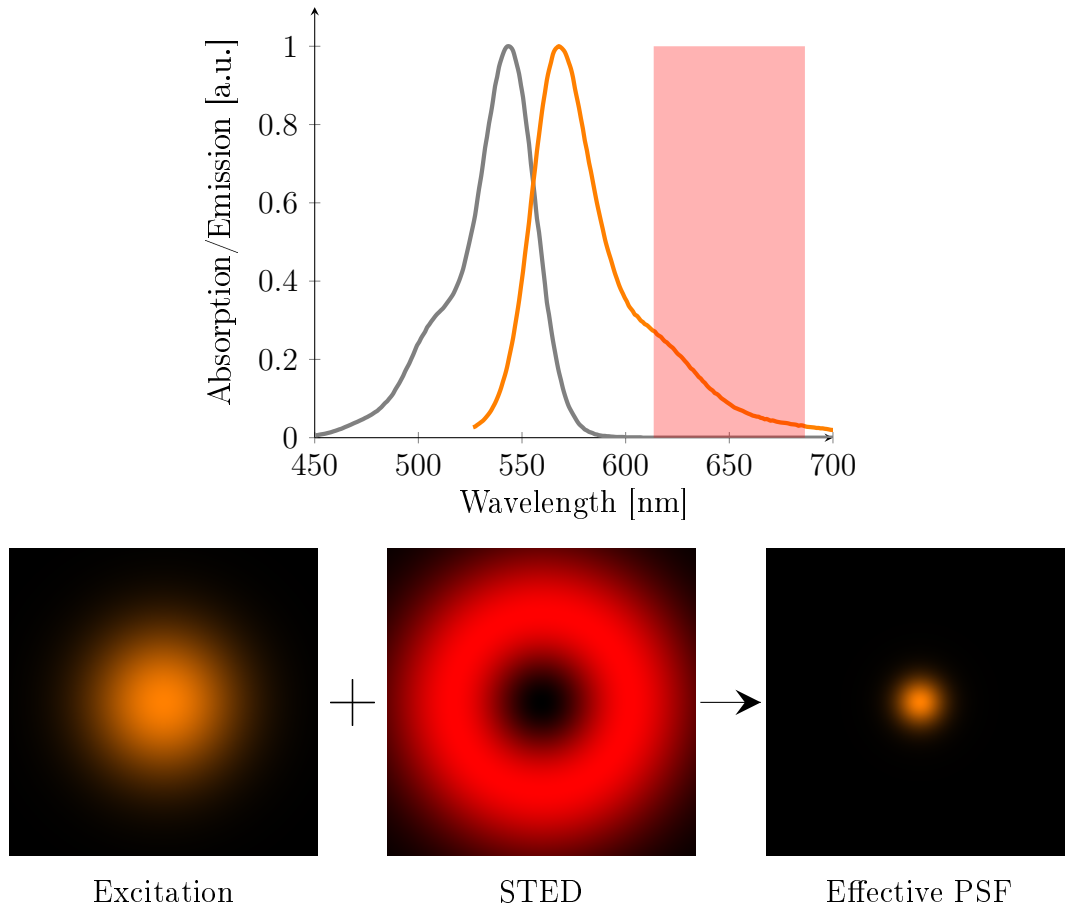


Figure 1.11.: Typical STED wavelength region with respect to the absorption (gray) and emission (orange) spectra of the (exemplary) fluorophore rhodamine B and STED principle.

By driving excited fluorophores back into their ground states by stimulated emission, STED can be applied in principle to every fluorophore. Two electronic states with a low coherence time are equally populated by shining in light with a wavelength corresponding to the energy difference between the states. If the lower level is a higher vibrational level of the ground state of a fluorescent molecule, which itself relaxes quickly to the ground state, stimulated emission can efficiently prevent the population of the excited state of fluorescent molecules. Since the vibrational relaxation is on the timescale of picoseconds, the excited-state electron is overwhelmingly pumped towards the lower level with laser pulses of the order of one nanosecond duration. The process of depopulation can be described in this

case as a linear process dependent on the light intensity. By using a TEM_{01}^* , “donut” mode as the de-excitation laser beam, a Gaussian shaped effective PSF is achieved at sufficiently high de-excitation intensities. The standard deviation σ of the effective PSF depends on the intensity I of the STED beam and a fluorophore- and wavelength-specific saturation intensity I_{sat} , which describes the intensity needed to halve the excited state occupancy.

$$\sigma \propto \frac{\sigma_{\text{PSF}}}{\sqrt{1 + \frac{I}{I_{\text{sat}}}}} \quad (1.12)$$

STED is not only able to discriminate fluorophores with a separation smaller than the diffraction limit σ_{PSF} , but it also creates a subdiffraction effective PSF for each emitter. In practice, the resolution of STED microscopy is limited by the photostability of the fluorophore, by a non-zero intensity minimum of the STED donut and by the light-tolerance of the sample. Therefore, STED nanoscopy rarely achieves a full width at half maximum of 20nm [13] [14]. In particular, the de-excitation beam can also excite the molecule into higher excited states and thereby promote bleaching.

1.5.3. MINFLUX and MINSTED

Both implementations of the nanoscopy on/off concept, single molecule localization and coordinate targeted nanoscopy, can yield moderate improvements in the resolution with only a low number of detected photons or a low de-excitation intensity. In order to achieve a single-digit nanometer resolution, extremely high photon numbers or laser intensities are needed, which is difficult to achieve in experiments. Therefore more photon or laser power efficient methods are needed to achieve this goal on a regular basis and with good fidelity. When looking at the strengths and weaknesses of single molecule localization and coordinate targeted nanoscopy, it becomes obvious that both methods complement each other perfectly and their combination would be very attractive. The precision of single molecule localization is strongly defined by the size of the PSF, which STED can further reduce by confining the coordinates of possible emission. The separation of active fluorophores can be performed in single molecule switching on length scales which are not accessible by STED. Furthermore, STED can suppress the emission of active emitters nearby, which reduces the background and lowers the probability of mis-localizations. The localization of a fluorophore in a raster-scanned STED image would expose the fluorophore

to high STED light intensities which would promote bleaching before a sufficient signal is collected. Furthermore, bleaching before the complete effective PSF is imaged would result in a skewed localization. Another approach to localize a fluorophore is to detect the modulations in the fluorescence relative to the positioning of the excitation beam. The excitation PSF can be fitted to the fluorescence signal collected at few positions to retrieve the fluorophore position. A different approach is to scan the excitation in a circular pattern and to readjust the center position of the scan pattern based on the detections. The position estimation can then be calculated by averaging these center positions. The localization precision of the first approach can be analytically calculated by the Cramér-Rao bound and the second method approaches these predicted values for sufficiently high number of recenter steps to average out the contribution of the starting center position. The Cramér-Rao bound (1.13) sets a lower limit to the standard deviation $\sigma(\theta)$ of an unbiased estimator by using the Fisher-Information $I(\theta)$.

$$\sigma_{\text{CR}}(\theta) \geq \frac{1}{\sqrt{I(\theta)}} \quad (1.13)$$

The Fisher-Information $I(\theta)$ can be expressed as the expectation value of the square of the logarithm of the likelihood function $f(X, \theta)$ in the single dimensional case by (1.14).

$$I(\theta) = E \left[\left(\frac{\partial \log(f(X, \theta))}{\partial \theta} \right)^2 \right] = -E \left[\frac{\partial^2 \log(f(X, \theta))}{\partial \theta \partial \theta} \right] \quad (1.14)$$

Since the number of detected photons follows a Poisson statistics, the likelihood function for X_i detected photons can be expressed by their mean value m_i .

$$\begin{aligned} \log(f(X, \theta)) &= \sum_i (X_i \log(m_i) - m_i - \log(X_i!)) \\ \frac{\partial \log(f(X, \theta))}{\partial \theta} &= \sum_i \frac{\partial m_i}{\partial \theta} \left(\frac{X_i}{m_i} - 1 \right) \\ \frac{\partial^2 \log(f(X, \theta))}{\partial \theta \partial \theta} &= \sum_i \frac{\partial^2 m_i}{\partial \theta \partial \theta} \left(\frac{X_i}{m_i} - 1 \right) - \left(\frac{\partial m_i}{\partial \theta} \right)^2 \frac{X_i}{m_i^2} \end{aligned} \quad (1.15)$$

The Cramér-Rao bound can therefore be calculated by

$$\sigma_{\text{CR}}(\theta) \geq \frac{1}{\sqrt{\sum_i \left(\frac{\partial m_i}{\partial \theta} \right)^2 \frac{1}{m_i}}} \quad (1.16)$$

For the further considerations, two different PSF shapes are used. The first one is a Gaussian shaped one, as an approximation for the confocal Airy disc and an accurate representation of the effective STED PSF, and the second one is the “donut” shaped TEM₀₁^{*} mode.

$$\begin{aligned} f_{\text{Gauss}}(r) &= e^{\frac{-r^2}{2\sigma_{\text{PSF}}^2}} \\ f_{\text{Donut}}(r) &= \frac{e r^2}{2\sigma_{\text{PSF}}^2} e^{\frac{-r^2}{2\sigma_{\text{PSF}}^2}} \end{aligned} \quad (1.17)$$

Assuming a molecule to be at the center of two excitation beam positions, which are separated by L , a total number of N photons are collected and constant background β is included in these detected photons. In the case of a Gaussian shaped beam, the localization precision can be calculated as shown in equation (1.18).

$$\begin{aligned} m_i &= \alpha (f_{\text{Gauss}}(r_i) + \beta) \\ N &= \sum_i m_i \\ \theta = r; \quad r_1 &= \frac{L}{2}; \quad r_2 = -\frac{L}{2} \\ SBR_{\text{eff}} &= \frac{f_{\text{Gauss}}(\frac{L}{2})}{\beta} = \frac{f_{\text{Gauss}}(-\frac{L}{2})}{\beta} \\ \frac{\partial m_i}{\partial r} &= -\frac{\alpha r_i}{\sigma_{\text{PSF}}^2} f_{\text{Gauss}}(r_i) \\ &= -\frac{m_i r_i}{\sigma_{\text{PSF}}^2 (f_{\text{Gauss}}(r_i) + \beta)} f_{\text{Gauss}}(r_i) \\ \sum_i \left(\frac{\partial m_i}{\partial \theta} \right)^2 \frac{1}{m_i} &= N \frac{\left(\frac{L}{2}\right)^2}{\sigma_{\text{PSF}}^4 \left(1 + \frac{\beta}{f_{\text{Gauss}}(\frac{L}{2})}\right)^2} \\ \sigma_{\text{CR}}^{\text{Gauss}}(0) &\geq \frac{2\sigma_{\text{PSF}}^2 (1 + SBR_{\text{eff}}^{-1})}{\sqrt{NL}} \end{aligned} \quad (1.18)$$

In order to be able to detect the direction of a small displacement Δr correctly, the ratio κ between the exposure with the higher signal and the one with the lower signal must be maximized.

$$\kappa = \frac{e^{\frac{(\frac{L}{2}-\Delta r)^2}{2\sigma_{PSF}^2}} + \beta}{e^{\frac{(\frac{L}{2}+\Delta r)^2}{2\sigma_{PSF}^2}} + \beta} \quad (1.19)$$

$$\lim_{\beta \rightarrow 0} : \kappa = e^{\frac{L\Delta r}{\sigma_{PSF}^2}}$$

Both expressions (1.18) and (1.19) yield a strong correlation of the achievable resolution and correct assignment of the displacement direction with the diameter of the scan pattern L . If the background can be neglected, the best resolution is achieved with large L because the signal of the exposure in the direction of the displacement Δr approaches zero slower than the exposure in the opposite direction with increasing L . This concept of localizing a fluorophore by probing the molecule position with an excitation beam whose profile is approaching a local zero is called MINFLUX [15], which is often implemented using a TEM_{01}^* mode excitation beam. In this case the central zero of the TEM_{01}^* mode is used and a smaller L leads to a higher precision as shown in equation (1.20).

$$SBR_{\text{eff}} = \frac{f_{\text{Donut}}(\frac{L}{2})}{\beta} \quad (1.20)$$

$$\sigma_{\text{CR}}^{\text{Donut}} \geq \frac{L(1 + SBR_{\text{eff}}^{-1})}{\sqrt{N}4(1 - \frac{L^2}{8\sigma^2})}$$

If the background is excitation dependent, the improvement by bringing the excitation zero closer to the fluorophore is limited and an optimal L can be calculated [15]. This can be explained by the decreasing signal to background ratio (SBR) near the excitation zero, where the signal from the emitter decreases. The formulae for the localization precision (1.18) and (1.19) contain a second option for improving the precision by decreasing the size of the PSF σ_{PSF} . This can be achieved by the use of STED. Although large L values would in this case still improve the localization precision, they would subject the fluorophore to high STED intensities, which would enhance bleaching [13]. Therefore, the emitter should only be probed by the edge of the effective PSF close to the FWHM as a compromise between bleaching and localization precision. If the diameter or the scan pattern L are directly linked to the size of the effective PSF, both the signal and the STED laser intensity applied to the fluorophore remain constant irrespective of the used effective PSF size. This results in being able to probe the emitter with a relatively small σ_{PSF} and achieve a high localization precision without pronounced bleaching.

2. Manuscripts

2.1. Prologue

The implementation of the new microscopy technique called MINSTED was the main goal of this thesis. The lack of suitable dyes for this type of microscopy was addressed by optimizing two different fluorophore classes to meet the demands of MINSTED. The stability of the active fluorophores under STED light and the sparse activation of single molecules with little influence by the STED light were the main optimization parameters. The photoswitchable diarylethenes were identified as an interesting fluorophore class for single molecule localization microscopy because of their thermally stable on- and off-states. Diarylethenes have been extensively used in organic solvents or polymers in the past, but their applicability to fluorescence microscopy of fixed cells was only recently shown by introducing solubilizing carboxyl groups [6]. These variants were designed for RESOLFT imaging with a focus on fast off-switching. This results in a low number of photons emitted before switching off, since the off-switching is driven by the excitation wavelength. The main objective was to increase the number of emitted photons per cycle to use these fluorophores for single molecule microscopy like STORM or possibly MINSTED. As an alternative to photoswitchable diarylethenes, photoactivatable xanthenic fluorophores were also considered. Although these fluorophores are only activated once, xanthenic dyes can be used for STED microscopy with only a few exceptions. To make these caged fluorophores suitable for MINSTED, they should be reasonably stable against activation by the STED light. Otherwise, while localizing one emitter, other dyes could be activated and impede the measurement or be bleached by the high STED intensity. By using photoconvertible fluorophores, MINSTED should not only be able to localize single emitters with a single-digit nanometric localization precision, but also to image cellular samples with a comparable precision.

2.2. Manuscript I: Photoswitchable Diarylethenes

Published on May 4, 2017 in the Journal of the American Chemical Society.

Reprinted with permission from "**Fluorescent Photoswitchable Diarylethenes for Biolabeling and Single-Molecule Localization Microscopies with Optical Super-resolution**". Benoît Roubinet, Michael Weber, Heydar Shojaei, Mark Bates, Mariano L. Bossi, Vladimir N. Belov, Masahiro Irie, and Stefan W. Hell, *Journal of the American Chemical Society* 2017 139 (19), 6611-6620, DOI: 10.1021/jacs.7b00274" Copyright 2017 American Chemical Society.

Contribution

I performed and optimized the STORM nanoscopy measurements to evaluate the synthesized diarylethenes; analyzed the measurements; and participated in writing the manuscript.

Fluorescent Photoswitchable Diarylethenes for Biolabeling and Single-Molecule Localization Microscopies with Optical Superresolution

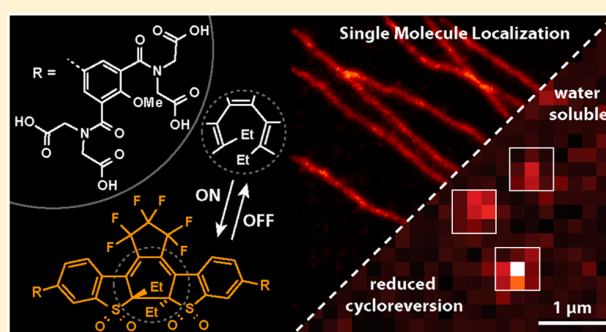
Benoit Roubinet,[†] Michael Weber,[†] Heydar Shojaei,[†] Mark Bates,[†] Mariano L. Bossi,[†] Vladimir N. Belov,^{*,†} Masahiro Irie,^{*,†} and Stefan W. Hell^{*,†}

[†]Department of Nanobiophotonics, Max Planck Institute for Biophysical Chemistry, Am Fassberg 11, 37077 Göttingen, Germany

^{*}Research Center for Smart Molecules, Department of Chemistry, Rikkyo University, Nishi-Ikebukuro 3-34-1, Toshimaku, Tokyo 171-8501, Japan

Supporting Information

ABSTRACT: A modular assembly of water-soluble diarylethenes (DAEs), applicable as biomarkers for optical nanoscopy, is reported. Reversibly photoswitchable 1,2-bis(2-alkyl-6-phenyl-1-benzothiophene-1,1-dioxide-3-yl)perfluorocyclopentenes possessing a fluorescent “closed” form were decorated with one or two methoxy group(s) attached to the *para*-position(s) of phenyl ring(s) and two, four, or eight carboxylic acid groups. Antibody conjugates of these DAEs feature low aggregation, efficient photoswitching in aqueous buffers, specific staining of cellular structures, and photophysical properties (high emission efficiencies and low cycloreversion quantum yields) enabling their application in superresolution microscopy. Images of tubulin, vimentin, and nuclear pore complexes are presented. The superresolution images can also be acquired by using solely 488 nm light without additional photoactivation with UV light. These DAEs exhibit reversible photoswitching without requiring any additives to the imaging media and open new paths toward the modular design of fluorescent dyes for bioimaging with optical superresolution.



INTRODUCTION

Superresolution fluorescence microscopies of the past two decades have revolutionized optical imaging in the life and materials sciences.^{1,2} Object features at distances on the (bio)molecular scale, i.e., far below the diffraction limit, can be resolved as a result.^{3,4} All concepts with such spatial resolution ultimately distinguish adjacent molecules by transiently rendering them in a dark state (*off*) and a fluorescent one (*on*) for registration.⁵ In this way, fluorescent molecules at sub-diffraction distances can be distinguished by sequential detection.⁵ The different techniques are usually grouped in two classes, according to the way the superresolution is achieved. In coordinate-targeted methods [e.g., stimulated emission depletion (STED),^{6–8} reversible saturable (switchable) optically linear fluorescence transitions (RESOLFT),^{9,10} ground state depletion (GSD),^{11,12} and (saturated) structured illumination ((S)SIM),^{13,14}], the position of the *on* and *off* states is determined by a pattern of light eliciting an *on*→*off* or *off*→*on* transition in the sample, except at predetermined positions of the pattern with vanishing intensity. In coordinate–stochastic superresolution modalities [e.g., stochastic optical reconstruction microscopy (STORM),^{15,16} photoactivated localization microscopy (PALM),^{17,18} GSD with intramolecular return (GSDIM),^{19,20} and direct stochastic

optical reconstruction microscopy (dSTORM)²¹], molecular *off*→*on* events take place molecule by molecule, with the molecules located at random positions. The unique features and advantages of the two superresolution families have been extensively reviewed.^{2,22–26} Importantly, the coordinate–stochastic approaches, such as STORM, require the detection of fluorophores at the single-molecule (SM) level.^{15,17}

Superresolution microscopes are built with conventional state-of-the-art optics, and the crucial factor responsible for surpassing the diffraction barrier is the state transition of the fluorophores. Thus, the fluorophore states as well as their photophysical and -chemical properties are important. Not surprisingly, superresolution techniques have elicited a renewed interest in photoswitchable fluorescent probes.^{27–31} In this line, new molecular photoswitches with improved and outstanding properties matching the demanding conditions of modern optical nanoscopy determine, to a large extent, the progress of the research field. The general requirements for the markers include high brightness and photostability, large spectral separation and signal contrast between states (i.e., large difference in the fluorescence efficiency), and high ensemble

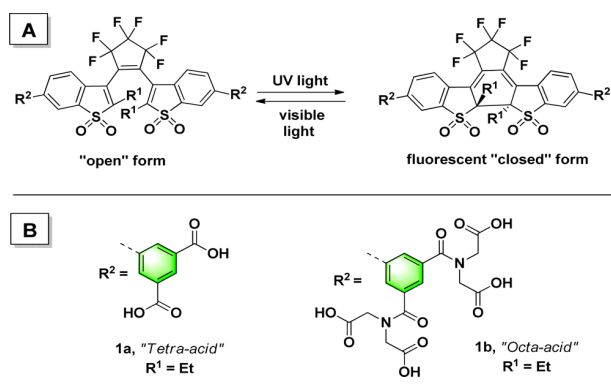
Received: January 9, 2017

Published: April 24, 2017

modulation (i.e., high probability of conversion to at least one of the states; in general, to the *off* state), as well as fast and controllable switching rates (preferably optically addressable).

Diarylethenes (DAEs) represent one of the most fatigue-resistant classes of photochromic compounds fulfilling most of these requirements,³² but their application for bioimaging and in fluorescence nanoscopies was always challenged by poor solubility in aqueous media and by the fact that they were rarely fluorescent [neither in the “open” form (OF) nor in the “closed” form (CF)].³³ Recently, new photochromic sulfones with fluorescent closed-ring isomers based on “oxidized” 1,2-bis(2-alkyl-6-aryl-1-benzothiophen-3-yl)perfluorocyclopentenes (Scheme 1) were shown to have emission efficiencies of up to

Scheme 1. (A) Sulfone Derivatives of Diarylethenes (DAEs), with a Colored and Highly Fluorescent Closed-Ring Isomer Emitting in the Visible Range,^{34,35} and (B) Carboxylated Water-Soluble Photochromic and Fluorescent DAEs Previously Used for Superresolution RESOLFT Imaging³⁶



~90%.³⁷ The switching photochromic unit is intrinsically not water-soluble, but the new DAE derivatives allowed a viable and promising approach to be realized. For example, we have recently reported reversibly photoswitchable dyes decorated with four and eight carboxylic acid groups (compounds 1a and 1b, Scheme 1B). They exhibited fluorescence modulation in aqueous buffers at biologically relevant pH values (as free markers and conjugates with secondary antibodies).³⁶ Images of immunolabeled cells, with a spatial resolution beyond the

diffraction barrier, were obtained using conjugates of compounds 1a,b in RESOLFT microscopy, a coordinate-targeted imaging technique. However, our attempts to use dyes 1a,b in coordinate-stochastic approaches yielded poor images, because their switching properties in aqueous media were inadequate for detection as SMs (see Discussion below).^{38,39} Recently, Wöll and co-workers⁴⁰ reported a hydrophobic sulfone-DAE with naphthyl substituents (R^2 in Scheme 1) and applied it for the first time in STORM of soft-matter (cylindrical micelles of amphiphilic block copolymers). Such structures are highly apolar. These lipophilic markers are far from optimal for bioimaging, unless they are encapsulated into bipolar carriers or decorated with hydrophilic groups.^{41,42}

Taking into consideration these results, we embarked on the development of new DAEs that can be used with stochastic SM-based fluorescence nanoscopies, for imaging under biologically relevant conditions. With compounds 1a,b as leads, we present here a rational approach to the design of water-soluble DAEs, applicable as biomarkers and detectable at the SM level. Furthermore, their performance in SM localization based superresolution techniques (e.g., PALM/STORM) is demonstrated in the present report.

RESULTS AND DISCUSSION

In stochastic nanoscopy, the large majority of markers must be brought to (or already reside in) the *off* state, except for a very sparse population that is in the *on* state. After localization and *off*-switching, this sparse group of “active” emitters is constantly renewed (from the ensemble of “dark” markers) and recorded in a sequence of image frames. After the positions of the markers are extracted from such frames, using a localization algorithm,⁴³ the superresolution image is rendered as a two- or three-dimensional plot of the emitter positions. Thus, two important requirements for markers in stochastic techniques are (1) a high number of photons emitted per excursion into the *on* state, to ensure a high localization accuracy,⁴⁴ and (2) the possibility to achieve a high [*off*]/[*on*] ratio (generally $>10^3$) to allow for a high labeling density.^{23,30,45} The second condition depends on the efficient conversion to the non-emitting form in the photostationary state, under irradiation with *off*-switching light (sufficient absorption at $\lambda_{on \rightarrow off}$ is required). Importantly, this feature is inherent to DAE-sulfones, because the *off* state is the stable open-ring isomer.

Scheme 2. Symmetric Dimethoxy DAEs and Their Carboxylated Analogues

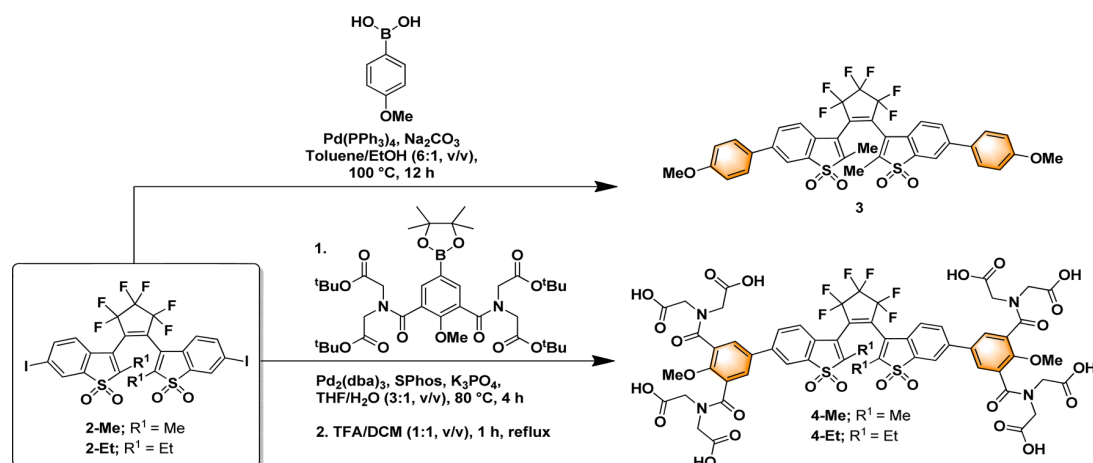
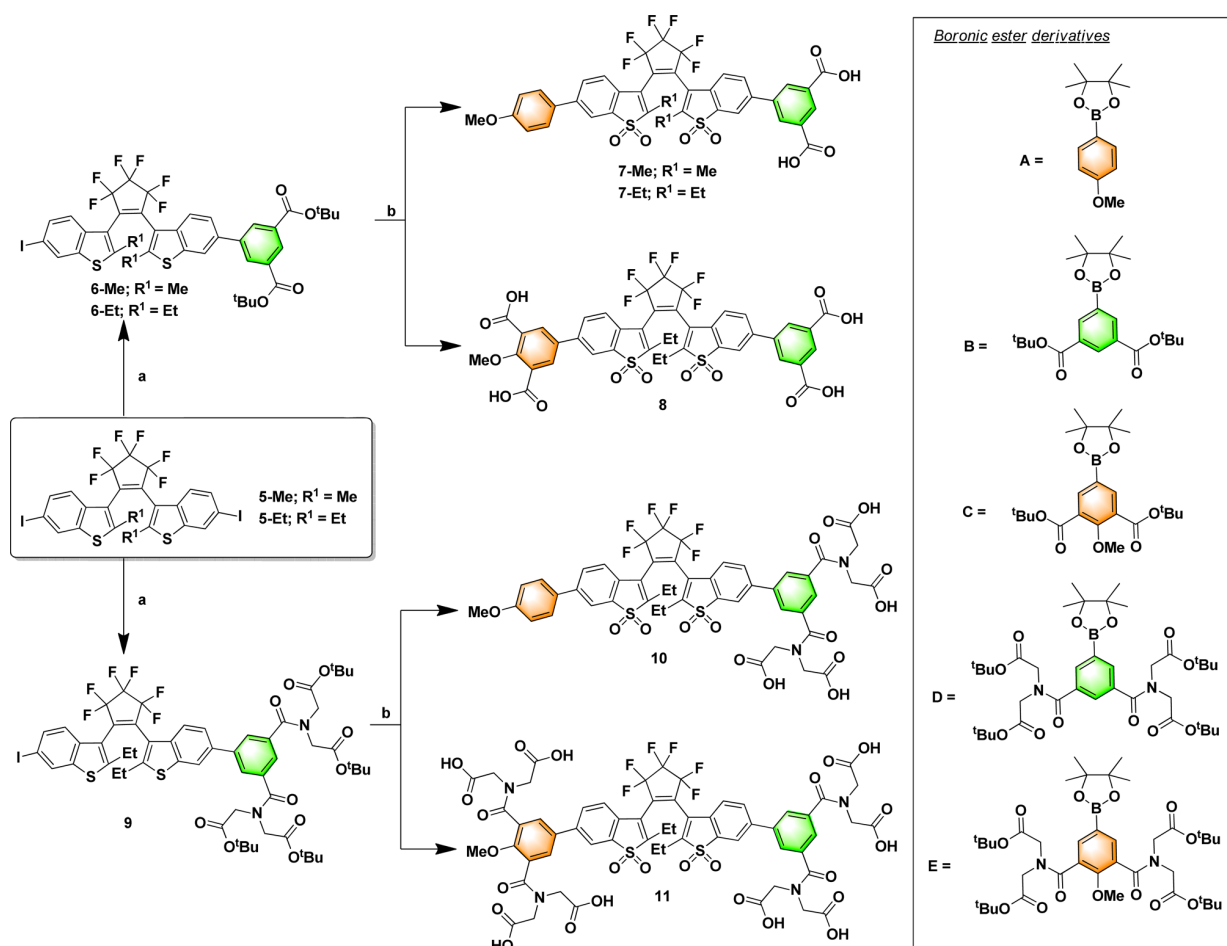


Table 1. Photophysical Properties of Carboxylated DAEs in Methanol

dye	substitution pattern			$\lambda_{\text{abs}}^{\text{max}}$ [nm]/ ϵ [$\text{M}^{-1} \text{cm}^{-1}$] ^a		$\lambda_{\text{em}}^{\text{max}}$ [nm]	Φ_{fluo}^b	Φ_{isom}		$\Phi_{\text{fluo}}/\Phi_{\text{on} \rightarrow \text{off}}$
	p/p' ^e	CO_2H^f	$N_{\text{CO}_2\text{H}}^g$	OF	CF	CF	CF	OF \rightarrow CF ^c	CF \rightarrow OF ^d	
1b ^h	H/H	4:4	8	331/16000	448/44500	523/552	0.70	2.4×10^{-1}	2.6×10^{-3}	270
3	M/M	0:0	0	354/18000	480/48700	608	0.61	1.6×10^{-3}	6.6×10^{-6}	92000
4-Et	M/M	4:4	8	338/16900	460/42800	578	0.70	1.6×10^{-2}	1.3×10^{-4}	5400
4-Me	M/M	4:4	8	340/14600	449/49100	575	0.46	1.4×10^{-2}	1.5×10^{-4}	3100
7-Me	M/H	0:2	2	340/18100	463/45300	623	0.36	1.2×10^{-3}	1.0×10^{-5}	36000
7-Et	M/H	0:2	2	340/17300	471/48300	617	0.41	1.3×10^{-3}	1.4×10^{-5}	29000
10	M/H	0:4	4	337/17700	471/46600	617	0.44	6.1×10^{-2}	1.7×10^{-5}	26000
8	M/H	2:2	4	333/18100	451/49500	564	0.59	2.0×10^{-2}	4.7×10^{-4}	1300
11	M/H	4:4	8	334/20100	454/52600	575	0.64	1.8×10^{-2}	1.9×10^{-4}	3400

^aLowest energy absorption peak. ^bFluorescence quantum yield. ^cMeasured at 365 nm. ^dMeasured at 470 nm (see Supporting Information for details). ^eNature of substituent at the p -position/ p' -position of the phenyl rings: H = hydrogen, M = methoxy. ^fNumber of carboxylic acid substituents for the "left": "right" sides of the molecule. ^gTotal number of the carboxylic acid residues in the molecule; ^hProperties of the parent DAE.³⁶

Scheme 3. Synthesis of Asymmetric DAEs^a

^aConditions: (a) B or D (1 equiv), $\text{Pd}_2(\text{dba})_3$, SPhos, K_3PO_4 , THF/ H_2O (3:1, v/v), 80 °C, 24 h; (b) 1. A, C, or E (3 equiv), $\text{Pd}_2(\text{dba})_3$, SPhos, K_3PO_4 , THF/ H_2O (3:1, v/v), 80 °C, 24 h; 2. *m*-CPBA, DCM, r.t., 24 h; 3. $\text{CF}_3\text{CO}_2\text{H}$ /DCM (1:1, v/v), 1 h, reflux.

Therefore, a complete conversion to this isomer (i.e., $[\text{off}]/[\text{on}] \rightarrow \infty$) should be achieved by irradiation with visible light, where only the closed-ring isomer absorbs. The first requirement, i.e., the photons per burst, is directly proportional to the ratio of emission efficiency (Φ_{fluo}) and the $\text{on} \rightarrow \text{off}$ quantum yield ($\Phi_{\text{on} \rightarrow \text{off}}$), because fluorescence emission and off -switching

are the two key processes competing for the depopulation of the same excited state (S_1 of the emitting isomer). Compound 1b presents $\Phi_{\text{fluo}}/\Phi_{\text{on} \rightarrow \text{off}} < 300$; with a photon collection efficiency (CEF) of $\sim 10\%$, and around 30 photons per burst (i.e., $N_{\text{ph}} = \text{CEF} \times \Phi_{\text{fluo}}/\Phi_{\text{on} \rightarrow \text{off}}$) are expected to be detected in average. For this reason, this compound is not suitable for

STORM, and slowing the *off*-switching rate by at least 1 order of magnitude lower $\Phi_{\text{on} \rightarrow \text{off}}$ is necessary. A straightforward way to achieve such an improvement is to increase electronic “push-pull” effects in the chromophore by adding donor substituents to the *para*-positions in one or two terminal phenyl groups.^{37,46,47} In this case, the *p*-methoxyphenyl group has a “push” effect (donor), and the sulfonic residues, as well as the perfluorocyclopentene ring, “pull” the π -electron density and act as acceptors. To test this idea and study the spectra and properties of the simple model DAE, we prepared compound **3** with two *p*-methoxy groups (Scheme 2) and measured its photophysical properties in methanol (Table 1). Indeed, in this solvent we achieved a 35-fold increase in the number of photons per burst (with respect to **1b**). In addition, a bathochromic shift (+20 nm in the OF) and a surprisingly large bathofluoric shift (+60 nm) were also observed. To provide solubility in aqueous solutions at physiological pH, anti-aggregation properties, and the reactive group required for conjugation, eight carboxylates were additionally introduced (compounds **4-Me** and **4-Et**, Scheme 2). Suzuki–Miyaura cross-coupling reactions between 1,2-bis(1-benzothiophene-1,1-dioxide-3-yl)perfluorocyclopentenes (**2-Me**⁴⁶ or **2-Et**³⁷) and a new pinacol ester of 2-methoxy-3,5-di(*N*-imino-diacetate)boronic acid were used for the preparation of symmetric DAEs (with carboxylate residues protected by *tert*-butyl groups). The acidic treatment with $\text{CF}_3\text{CO}_2\text{H}$ in CH_2Cl_2 cleaved the *tert*-butyl esters, and the dimethoxy “octa-acids” **4-Me** and **4-Et** were isolated (with 12% yield for **4-Me** and 55% for **4-Et**). Ethyl groups in positions 2 and 2' may provide better fluorescence quantum yields in highly polar solvents than methyl groups.⁴⁸

Additional asymmetric DAEs were designed and prepared in order to influence the switching properties (compounds **7-Me**, **7-Et**, **8**, **10**, and **11** in Scheme 3), and all of them were decorated with several carboxylic acid groups (two, four, or eight) fully ionizable at $\text{pH} > 6$. These syntheses were more challenging because it was necessary to prevent the formation of large amounts of symmetric byproducts. The preliminary attempts to produce asymmetric DAEs from C-6(6')-diiodide disulfone (**2-Me** or **2-Et** in Scheme 2) failed or gave low yields (less than 20% for the first cross-coupling reaction involving only one iodine substituent from two).⁴⁹ The low selectivity can be explained by the faster second step affording the product of disubstitution. Indeed, only one synthesis leading to an asymmetric and non-oxidized DAE possessing one aryl group (at C-6) and one halogen (at C-6') has been reported to provide a good yield (over 50%, starting from the corresponding diiodide).⁵⁰ To overcome the problem of selectivity, we decided to start with an unoxidized and obviously less reactive C-6(6')-diiodide “disulfide” (**5-Me** or **5-Et** in Scheme 3), build the dissymmetric cores, and oxidize both benzothiophene units at the final step. After optimization, the Suzuki–Miyaura cross coupling indeed afforded the monosubstitution product, but only in moderate yields of 25–42%, when 1 equiv of the “first” boronate ester was applied in a mixture of THF/ H_2O (3:1, v/v), in the presence of K_3PO_4 and SPhos/ $\text{Pd}(\text{dba})_2$. The second cross-coupling step proceeded under the same conditions with 3 equiv of another boronate ester and afforded the asymmetric non-oxidized DAEs in good yields (>50%).

Oxidation under mild conditions with 3-chloroperbenzoic acid (*m*-CPBA) followed by cleavage of the *tert*-butyl protecting group ($\text{CF}_3\text{CO}_2\text{H}$ in CH_2Cl_2) afforded five new dissymmetric

DAEs (Scheme 3) possessing two (**7-Me**, **7-Et**), four (**8**, **10**), or eight (**11**) carboxylic acid groups. The properties of symmetric and asymmetric polycarboxylated switches in methanol are presented in Table 1; normalized absorption and emission spectra in methanol and aqueous phosphate-buffered saline (PBS) are shown in Figure 1. In general, all of them presented good properties in polar solvents, with reversible photoswitching with 365 nm/470 nm light and emission efficiencies of 0.36–0.70.

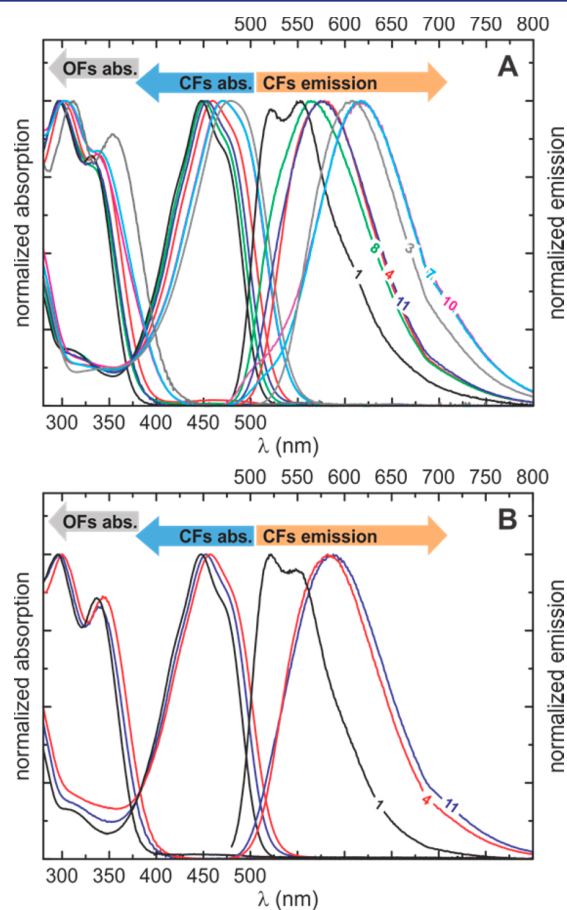


Figure 1. Normalized absorption and emission spectra of DAEs (Table 1) in methanol (A) and aqueous PBS (B). Compound **1** refers to **1b**, “octa-acid” DAE without methoxy substituents in the *para*-position of the phenyl ring, and compound **4** refers to **4-Et**.

Complete conversion to the closed-ring isomer was observed upon irradiation with UV light. This is a result of the high ratio between the cyclization and cycloreversion quantum yields ($\Phi_{\text{OF} \rightarrow \text{CF}}/\Phi_{\text{CF} \rightarrow \text{OF}}$) and has been observed for sulfone derivatives of DAE with benzothiophene units.^{37,46} The absence of competing thermal reactions is explained by extremely high thermal barriers (over 188 kJ/mol) between the isomers,⁵¹ in the potential energy surface of the ground state of DAEs.⁵² The closed forms of key compounds **4-Et** and **11** were isolated by HPLC and were shown to be stable at room temperature in the dark at least for several weeks (in methanol).

Upon introduction of one or two methoxy substituents, the emission became less structured (accompanied by a loss of the shoulder observed for compounds **1a** and **1b**) and the emission

Table 2. Photophysical Properties of Hydrophilic and Water-Soluble DAEs in PBS at pH 7.4

dye	substitution pattern			$\lambda_{\text{abs}}^{\text{max}}$ [nm]/ ϵ [$\text{M}^{-1}\text{cm}^{-1}$] ^a	$\lambda_{\text{em}}^{\text{max}}$ [nm]	Φ_{fluo}^b	Φ_{isom}			$\Phi_{\text{fluo}}/\Phi_{\text{on}\rightarrow\text{off}}$	$B_{488\text{ nm}}^i$
	p/p' ^c	CO_2H^f	$\text{N}_{\text{CO}_2\text{H}}^g$				OF	CF	CF		
1b ^h	H/H	4:4	8	337/16500	447/45600	522	0.57	2.3×10^{-1}	2.0×10^{-3}	290	1.4×10^4
4-Et	M/M	4:4	8	345/17100	457/37300	582	0.45	1.5×10^{-3}	1.8×10^{-4}	2500	1.3×10^4
11	M/H	4:4	8	338/21600	453/53800	588	0.34	6.5×10^{-3}	1.6×10^{-4}	2100	1.3×10^4

^aLowest energy absorption peak. ^bFluorescence quantum yield. ^cMeasured at 365 nm. ^dMeasured at 470 nm (see Supporting Information for details). ^eNature of substituent at the p -position/ p' -position of the phenyl rings: H = hydrogen, M = methoxy. ^fNumber of carboxylic acid substituents for the “left”/“right” side of the molecule. ^gTotal number of the carboxylic acid residues in the molecule. ^hProperties of the parent DAE. ⁱBrightness $B = \epsilon \times \Phi_{\text{fluo}}$.

band wider. Only small red shifts (<10 nm) in the absorption band of the open-ring isomer (except for compound 3), with respect to compound **1b**, were observed. The presence of amide groups nearby the methoxy residues counteracts the electron-donating effect of methoxyls. Nevertheless, the shift of the red-edge of these bands is noticeable (Figure 1), and it enables the use of activation laser with longer wavelengths (e.g., 375 nm). The absorption bands of the closed-ring isomers present a moderate red-shift (of up to 30 nm), with a larger emission red-shift of up to \sim 100 nm. Importantly, upon introduction of methoxy groups, the isomerization quantum yields $\Phi_{\text{CF}\rightarrow\text{OF}}$ decreased \sim 1–2 orders of magnitude, with nearly no effects in the emission efficiencies. Note that the free carboxylic acid groups are indispensable for providing the crucial features (fluorescence and photoswitching) in aqueous buffers. The properties of compounds **4-Me** and **7-Me** possessing 2(2')-methyl groups are very similar to the properties of the analogues with 2(2')-ethyl groups, but the former have somewhat lower emission efficiencies.

Due to high emission efficiencies and low cycloreversion quantum yields (i.e., high $\Phi_{\text{fluo}}/\Phi_{\text{on}\rightarrow\text{off}}$), all mono- or dimethoxylated DAEs in Table 1 are excellent candidates for markers applicable in PALM/STORM techniques. However, only those that retain their solubility and photoswitching properties in aqueous buffers are suitable for imaging under biological conditions. Compounds **8** and **10** with four carboxylic acid groups are fairly soluble in aqueous PBS (in the OF) but emit only poorly in this solvent (fluorescence quantum yields 0.04 and <0.01, respectively). In water, the CF of compound **10** showed indication of aggregation (i.e., after photoinduced cyclization). In contrast, compounds **4-Et** and **11**, with eight carboxylates, presented only mild reduction in the isomerization efficiency (in aqueous PBS vs methanol), and no signs of aggregation in aqueous media (at concentrations 10–20 μM). The properties of these “octa” carboxylated analogues were then studied in more detail in aqueous PBS (pH 7.4) (Figure 1B and Table 2).

The most remarkable and valuable change introduced by one or two methoxy substituents is an order of magnitude increase in the ratio $\Phi_{\text{fluo}}/\Phi_{\text{on}\rightarrow\text{off}}$ also in aqueous environments. The relatively high values of $\Phi_{\text{fluo}}/\Phi_{\text{on}\rightarrow\text{off}}$ (2000–2500) make these compounds promising candidates for SM-based stochastic nanoscopy. As in methanol, this increase is due to the low quantum yields of the ring-opening reaction, since the emission quantum yields are on the same order. In addition, the brightness with 488 nm excitation ($B = \epsilon_{488\text{ nm}} \times \Phi_{\text{fluo}}$; an appropriate laser for all compounds) is very similar for all dyes.

In view of these results, the most promising DAEs **4-Et** and **11** were used for labeling of the secondary antibodies and STORM experiments. The two-step labeling protocol (see Experimental Section) provided a reproducible control of the

degree of labeling (DOL). The obtained bioconjugates were stable and showed no precipitation or aggregation after several months, stored in a refrigerator at 4 $^{\circ}\text{C}$, in PBS at pH 6.5 and without addition of stabilizing agents (e.g., BSA). Both compounds (**4-Et** and **11**) retained their photoswitching abilities after bioconjugation with secondary antibodies (Figure S1), and presented no reduction in emission efficiency of the closed-ring isomer with respect to the free dye (e.g., a **4-Et**-anti-rabbit with DOL = 3.5 has a $\Phi_{\text{fluo}} \approx 0.46$, and **11**-anti-rabbit with DOL = 4.7 has a $\Phi_{\text{fluo}} \approx 0.38$). Moreover, the specificity of the antibodies was also retained, as it was verified by confocal imaging (Figures S2 and S3), on samples pre-irradiated with UV light (wide-field illumination). To this end, Vero cells were stained with the prepared bioconjugates using a standard protocol (described in Supporting Information). In such experiments, switching off of the fluorescence emission was immediately evident; the signal faded in the imaged areas as a result of the illumination, and it was recovered after exposure to UV light for a few seconds.

After the successful preparation of photoswitchable and highly fluorescent bioconjugates of compounds **4-Et** and **11**, we attempted imaging of immunolabeled intracellular structures in a wide-field STORM microscope (Figure S4). We first confirmed that the detection of the closed-ring isomer at the SM level was possible using total internal reflection (TIRF) excitation at 488 nm and detection with a 582/75 bandpass filter (see the Supporting Information for a description of the microscope).

Images were recorded on an electron multiplying charge-coupled device (EMCCD) camera running at a frame-rate of 100 Hz. The average number of photons per detected SM switching event was on the order of $N_{\text{ph}} \approx 100$ –300 (slightly varying with excitation intensity, sample conditions, and calculation method; see Figure S5), in accordance with the predicted value (taking $\Phi_{\text{fluo}}/\Phi_{\text{on}\rightarrow\text{off}}$ from Table 2, and CEF \approx 0.1 estimated from the microscope’s optical components’ specifications), from ensemble measurements with the free marker or the bioconjugates. Photoactivation was attempted with 405 and 375 nm lasers, with the latter being more efficient and providing more reliable control of the on-switching process, as expected from the absorption spectra of the open isomers (Figure 1B). Remarkably, after optimization of the immunolabeling protocol, it was possible to acquire up to \sim 200 000 frames before any additional photoactivation by UV light was necessary (Figure 2); i.e., the image frames contained sufficient switching events to render meaningful STORM images using only 488 nm excitation light. The activation in the absence of UV light is ascribed to the optical transition induced by the absorption at the so-called “Urbach tail” (in our case at 488 nm), or by anti-Stokes Raman scattering. The molecule in the vibrationally excited state can undergo an optical transition into

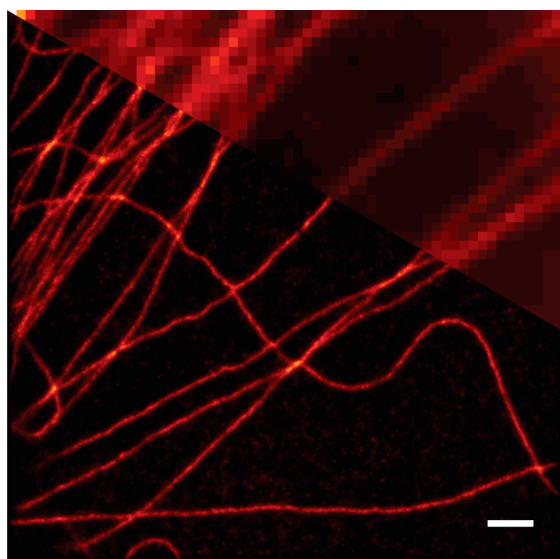


Figure 2. Superresolution image (STORM) *without activation light* of Vero cells immunostained with a primary antibody against tubulin and a secondary antibody labeled with compound **4-Et** (DOL = 3.5). Mounting medium used was PBS (pH 7.4). A wide-field image, generated as the sum of all frames, is overlaid on the upper part of the image. Scale bar, 1 μm ; image frames, 200 000; localizations, $\sim 1 \times 10^6$.

an electronically excited state by irradiation with light, the wavelength of which is longer than that of 0–0 transition.^{53–56} Whenever the activation rate is too low, resulting in few localizations per frame (imparting excessive recording times), the activation laser can be enabled (Figure S6) and its power increased to maintain a reasonable number of localizations per frame. Images acquired without and with the photoactivation laser (375 nm) were identical within experimental error (Figures 3 and S5A,B).

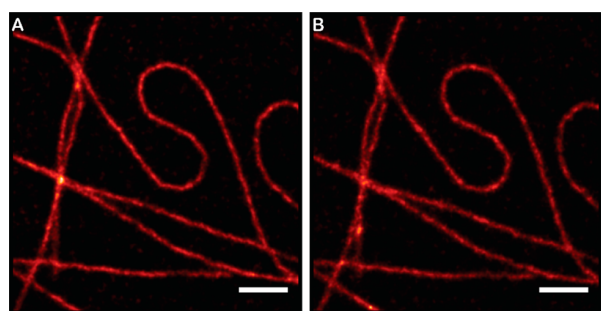


Figure 3. Superresolution images (STORM) of Vero cells immunostained with primary antibody against tubulin and secondary antibodies with compound **4-Et** without (A) and with (B) UV activation. The colormaps are drawn to the same scale. Mounting medium used was PBS (pH 7.4). Scale bar, 1 μm ; image frames (raw), 50 000 each case; localizations, $\sim 90\,000$ each.

The photoisomerization quantum yields (OF \rightarrow CF) of compounds **4-Et** and **11** are 2 orders of magnitude lower than that of compound **1b** (in aqueous PBS; Table 2). Half of the initial fluorescence of cells immunolabeled with compound **1b** was bleached after performing ~ 20 cycles by using pulses of 375 and 491 nm light.³⁶ Therefore, compounds **4-Et** and **11** were not expected to be more photostable than compound **1b**.

A rough estimation of the average number of switching cycles may be based on the observation that SMs of fluorescent dyes (including photochromic fluorescent DAEs) generally decompose after 10^6 – 10^7 excitation cycles.^{57–59} If we consider the values of the isomerization quantum yields for one complete cycle (OF–CF–OF) of compounds **4-Et** and **11** (Table 2), we may estimate that the average number of switching cycles is expected to be on the order of ~ 10 . Evaluation of the fatigue resistance of compounds **4-Et** and **11** in diluted methanolic and aqueous solutions showed that they can endure several tens of cycles (Figure S7).

Further subcellular structures were also immunolabeled to test the utility of the prepared bioconjugates. In Figure 4,

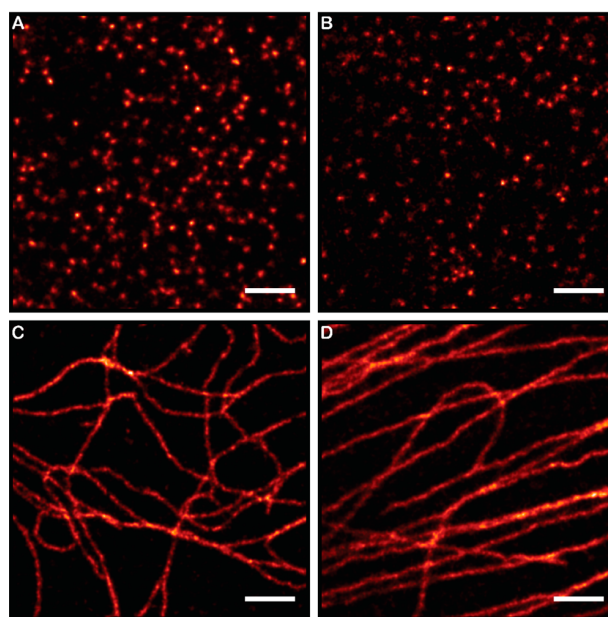


Figure 4. Superresolution images (STORM) of bioconjugates of compound **4-Et** (A,C) and compound **11** (B,D) on different intracellular structures. Mounting medium was PBS (pH 7.4). Vero cells were immunolabeled with primary antibodies against NUP153 (A,B), vimentin (C), and tubulin (D). Anti-mouse (A,B) and anti-rabbit (C,D) secondary antibodies were used. Scale bar, 1 μm ; localizations, 86 000 (A), 17 000 (B), 50 000 (C), and 155 000 (D).

images of tubulin, vimentin, and nuclear pore complexes with bioconjugates of compounds **4-Et** and **11** are presented. Anti-mouse and anti-rabbit secondary antibodies with DOLs values in the range 3.5–6 yielded similar imaging performance. Imaging of thicker samples was found to be more challenging, due to the high amount of out-of-plane photoactivated markers (when using the 375 nm activation laser), produced by the relatively high cyclization efficiency ($\propto \epsilon_{\text{OF}}^{375\text{ nm}} \times \Phi_{\text{OF}\rightarrow\text{CF}}$). In this case, switched-on markers accumulate in those planes, where the excitation light (488 nm), also responsible for the *off*-switching process, has low intensity (due to TIR illumination conditions). Therefore, thicker sample areas exhibit higher background fluorescence which makes localization less precise. For that reason, the localization accuracy, and thus the resolution of the final images, is lower in densely labeled and thick areas.

To determine the spatial resolution of the images obtained through the switching and localization of the new DAEs at the SM level, a Fourier ring correlation (FRC) analysis was

applied.^{60,61} The FRC curve and the 2σ threshold line were plotted for the localizations presented in Figure 2 and are shown in Figure S8. According to this method, a resolution of $\sim 90 \pm 10$ nm was estimated.

CONCLUSIONS

We prepared new DAEs intended for superresolution microscopy of biological samples in aqueous solutions. The properties of a photoswitchable and fluorescent core were optimized through chemical modifications. We achieved a sufficient number of photons per incursion into the *on* state—a necessary property for detection at the SM level—and at the same time retained the switching performance in buffered aqueous solutions. Another key property is a high conversion ratio to the *off* state, which enabled high density labeling. A complete back-conversion to this isomer is in principle possible by irradiation with visible light with $\lambda > 450$ nm, providing a nearly unlimited $[off]/[on]$ ratio. In practice, however, it was found that 488 nm light can also induce the cyclization reactions producing the fluorescent closed-ring isomers, in addition to the ring-opening reactions. These features provided the opportunity to acquire high quality superresolution images using a single laser, without the need for additional photo-activation via UV excitation.

The spectral properties of compounds **4-Et** and **11** (and their bioconjugates) make these DAEs reliable blue-excitable probes (i.e., 440–488 nm); in a spectral region where high quality synthetic markers are not abundant.³⁰ Moreover, a large Stokes-shift of ~ 100 nm makes them almost unique, as in general long Stokes-shift markers for fluorescence microscopy are rare; in particular, in all superresolution techniques, including those based on STORM. Thus, the presented probes may be also very valuable for multicolor (superresolution) imaging with a single excitation laser,⁶² for instance in combination with standard (short Stokes shift) fluorescent dyes used in STORM. Importantly, the photoswitching of DAEs involves singlet-excited states,⁵² and thus the presence of blinking buffers is expected to strongly affect their photoswitching behavior. In particular, the presence of thiols and other strong nucleophiles is prohibitive, as they can add to the very electron-deficient “central” double bond of the perfluorocyclopentene residue. Indeed, attempts to apply compound **4-Et** in a common blinking buffer (Glox/catalase + MEA)⁴³ resulted in poor images (Figure S9). Therefore, DAEs are expected to work in combination with markers that do not require the presence of oxygen removal media, and/or thiols.²⁷ This is in fact one of the most important and distinct aspects of the new DAE-biomarkers: superresolution images can be recorded without addition of oxygen scavengers (such as the Glox/catalase system), thiols, methyl viologen, ascorbic acid, or any other specific chemical additives commonly used to control the switching of the markers (“blinking buffers”). As a mounting medium (Figures 2–4, S2, S3, and S5), we used aqueous PBS, adjusted to pH 7.4. The obvious and most relevant advantage of this approach is the possibility to extend it to live-cell imaging. Examples of markers for PALM/STORM microscopy that can function without additives have been shown.^{30,63,64} However, in most cases much better images were obtained with the aid of the additives mentioned above, or in the presence of complex mounting media compromising or even excluding the possibility of the observation of living specimens.^{26,65–67}

Unlike the case of many dyes used in superresolution microscopy, the processes for *on*- and *off*-switching of DAEs are

well defined, understood, and controlled: it is the cyclization and cycloreversion of the photochromic core (Scheme 1A). Thus, all the rich evidence available for the rational design of DAEs may be applied for optimization of their properties.^{37,48,68–71} As a result, important chemical modifications can be envisaged, aimed at optimizing $\Phi_{OF \rightarrow CF}$ and $\Phi_{CF \rightarrow OF}$ values and thus providing more switching cycles. Further structural changes will tune the emission color and target specific groups/functionalities, with no need to change or re-optimize the mounting medium. In particular, we are presently working on increasing the $\Phi_{fluor}/\Phi_{CF \rightarrow OF}$ ratio to improve the attainable spatial resolution in conventional SM stochastic nanoscopies (e.g., STORM). Alternatively, the fluorophores described here could be applied in the recently reported SM localization nanoscopy based on a patterned excitation profile with a local minimum (MINFLUX).⁷² In combination with the drastic reduction of the required photons for SM localization provided by MINFLUX, the photons per cycle emitted by fluorophores **4-Et** and **11** in aqueous media should be sufficient to achieve nanometer-scale spatial resolution.

EXPERIMENTAL SECTION

General Remarks. Chemicals and Reagents. Flash column chromatography was performed using cartridges from Interchim (PF-SIHC, 15 μ M, 25 or 40 g SiO₂) or Teledyne Isco (RediSepRf, 35 μ M, 24 or 40 g SiO₂). Analytical TLC was performed on Merck Millipore ready-to-use plates with silica gel 60 (F₂₅₄). The spots were visualized by illumination with a UV lamp ($\lambda = 254$ and 365 nm) and/or staining with aqueous KMnO₄ solution. Anhydrous DMF were purchased from Sigma-Aldrich and stored over 4 Å molecular sieves. HPLC gradient-grade acetonitrile (CH₃CN) was obtained from Sigma-Aldrich. Aqueous buffers (PBS, pH 6.5) and NaHCO₃ (pH 8.3) used for the preparation of bioconjugates and in the fluorescence assay, as well as mobile phases for HPLC, were prepared with water purified by means of an ELGA system. Unless stated otherwise, all chemicals were used as received from commercial sources without further purification. The following starting material were synthesized according to literature procedures: 5-bromo-2-methoxyisophthalic acid,⁷³ 1,2-bis(2-ethyl-6-iodobenz[*a*]thiophen-1,1-dioxide-3-yl)-perfluorocyclopentene,³⁷ 1,2-bis(2-methyl-6-iodobenz[*a*]thiophen-1,1-dioxide-3-yl)perfluorocyclopentene,⁴⁶ *tert*-butyl iminodiacetate,⁷⁴ and boronic esters **B** and **D**.³⁶ Secondary antibodies (AffiniPure sheep anti-mouse IgG (H+L)) were obtained from Jackson ImmunoResearch Laboratories, Inc. PD-10 desalting columns used for the isolation of the conjugates with antibodies were purchased from GE Healthcare Europe GmbH.

Instruments and Methods. ¹H, ¹⁹F, and ¹³C NMR spectra were recorded at 25 °C on an Agilent 400-MR and Varian Inova 500 spectrometers. Chemical shifts are given in parts per million (ppm) using the residual solvent peak(s) as a reference.⁷⁵ Multiplicities of the signals are described as follows: s = singlet, d = doublet, t = triplet, q = quartet, m = multiplet or overlap of nonequivalent resonances. *J* values are expressed in Hz. The NMR spectra of hydrophilic diarylethenes (DAEs) were recorded in DMF-*d*₇ according to our previous work.³⁶ Each DAE derivative presented in this article was obtained as a mixture of two open forms (OF)—antiparallel (*ap*) and parallel (*p*)—and the closed-ring isomer (CF). These isomers could be detected separately by NMR spectroscopy. Due to asymmetry, it was often impossible to assign the signals to each form of DAEs. In this case, we write *p/ap*; the *ap* and *p* forms of the “open” isomers gave one peak in HPLC (and could not be isolated separately due to rapid interconversion). Analytical RP-HPLC was carried out with a Knauer Azura HPLC system equipped with a DAD detector. Automated flash purifications on regular silica gel and reversed phase (RP-C₁₈) cartridges were performed with a Biotage Isolera One device. Mass spectra with electro-spray ionization (ESI-MS) were recorded on a Varian 500-MS spectrometer (Agilent). High-resolution ESI-MS (ESI-HRMS) were

recorded on a MICROTOF spectrometer (Bruker) equipped with an Apollo ion source and a direct injector with an LC-autosampler Agilent RR 1200. Absorption spectra were recorded on a Varian Cary 4000 UV-vis spectrophotometer, and emission spectra were recorded on a Varian Cary Eclipse fluorescence spectrophotometer. Fluorescence quantum yields were measured at 25 °C using fluorescein in NaOH (0.1 M) as a reference. Determination of the quantum efficiencies of the isomerization reactions were performed in a homemade setup. Irradiation was performed in 1 cm path quartz cuvettes under continuous stirring, using LEDs at 365 ± 4 nm and 470 ± 12 nm (Thorlabs) as irradiation sources. The intensities of the irradiation light were determined using azobenzene in methanol (365 nm) and Aberchrome 670 in toluene (470 nm), as chemical actinometers. Absorption and emission of the solutions were monitored after each short irradiation step until the photostationary state was reached. Data analysis was performed as described previously.⁷⁶

High-Performance Liquid Chromatography. System A: RP-HPLC (Eurosphere II, 100–5 C₁₈ column, 5 μ m, 4.0 \times 150 mm) with CH₃CN and 0.05% aqueous trifluoroacetic acid (0.05% aqueous TFA, pH ~2.0) as eluents [linear gradient from 30% to 70% of CH₃CN in 20 min] at a flow rate of 1.2 mL/min; UV-vis detection with diode array and at 254 nm (OF) and 460 nm (CF). System B: automated flash purification on Biotage Isolera One (ISO-1EW) device (cartridge PF-C₁₈-HC, 30 μ M, with 20 g of RP silica gel) with the following eluent: 0.1% aqueous TFA/CH₃CN, 7:3, at a flow rate of 20 mL/min for 15 min; UV detection at 254 nm.

Syntheses. Detailed synthetic procedures for the preparation of boronic esters (B and E), DAEs derivatives (3, 7-Me, 7-Et, 8, and 10), and all intermediates used for their preparations (S3–S13) are given in the Supporting Information. Structures of all new DAEs were fully characterized and confirmed by NMR spectra (¹H, ¹³C, and ¹⁹F), HRMS, and HPLC (for the free carboxylates); see data in the Supporting Information.

Compound 4-Me. To a solution of 1,2-bis(2-methyl-6-iodo-1-benzothiophen-1,1-dioxide-3-yl)perfluorocyclopentene⁴⁶ (63 mg, 0.081 mmol) in a mixture of THF/H₂O (4 mL, 3:1, v/v) were added arylboronic ester E (131 mg, 0.17 mmol, 2.1 equiv), K₃PO₄ (51.5 mg, 0.24 mmol, 3 equiv), SPhos (2.0 mg, 4.8 μ mol, 6 mol %), and Pd(dba)₂ (1.4 mg, 2.4 μ mol, 3 mol %); the suspension was purged for 5 min with Ar (Ar “bubbling”) and stirred for 4 h at reflux. The reaction mixture was diluted with EtOAc, washed with brine (3 \times 25 mL), dried over Na₂SO₄, and concentrated. The residue was purified by flash chromatography on silica gel (*n*-hexane/EtOAc, with a gradient from 95:5 to 50:50) to afford *tert*-butyl ester of compound 4-Me as a yellow solid (28 mg, 20% yield). This ester (28 mg, 15.3 μ mol) was dissolved in a mixture of TFA/DCM (6 mL, 1:1, v/v) and heated with stirring for 1 h at reflux. The reaction mixture was concentrated in vacuum and subjected to flash chromatography using a RP-C₁₈ cartridge (system B). The product-containing fractions were pooled and lyophilized to give compound 4-Me as an amorphous yellow solid (12 mg, 57% yield). *ap:p* = 60:40. ¹H NMR (400 MHz, DMF-*d*₇): δ = 8.34 (s, 1.2 H, *ap*), 8.26 (s, 0.8 H, *p*), 8.12 (d, *J* = 8.2 Hz, 1.2 H, *ap*), 8.03 (m, 0.8 H, *p*, masked by NMR solvent), 7.90 (d, *J* = 7.3 Hz, 0.8 H, *p*), 7.81 (d, *J* = 8.0 Hz, 1.2 H, *ap*), 7.77 (s, 2.4 H, *ap*), 7.68 (s, 1.6 H, *p*), 4.58 (m, 4.0 H, *p/ap*), 4.23 (m, 12.0 H, *p/ap*), 3.92 (m, 6.0 H, *p/ap*, masked partially by NMR solvent), 2.38 (s, 2.3 H, *p*), 2.27 (s, 3.7 H, *ap*). ¹³C NMR (126 MHz, DMF-*d*₇): δ = 171.9, 171.3, 169.5, 154.3, 145.9, 145.5, 142.7, 141.0, 137.0, 136.9, 133.8, 130.9, 129.3, 129.1, 129.1, 125.5, 125.4, 124.2, 124.1, 121.6, 121.5, 118.7, 116.6, 114.6, 52.0, 48.5, 9.4, 9.3. ¹⁹F NMR (376 MHz, DMF-*d*₇): δ = -110.23 (m, 4.0 F, *p/ap*), -130.30 (m, 2.0 F, *p/ap*). HR-MS (ESI, negative mode): 1379.1646 [M-H]⁻ (found), 1379.1673 (calculated for C₅₇H₄₅F₆N₄O₂₆S₂, [M-H]⁻). HPLC (system A): *t*_R = 4.4 min (2% HPC area, CF); 6.0 min (96% HPLC area, OF).

Compound 4-Et. To a solution of 1,2-bis(2-ethyl-6-iodo-1-benzothiophen-1,1-dioxide-3-yl)perfluorocyclopentene³⁴ (50 mg, 0.062 mmol) in a mixture of THF/H₂O (4 mL, 3:1, v/v) were added arylboronic ester E (100 mg, 0.13 mmol, 2.1 equiv), K₃PO₄ (40 mg, 0.19 mmol, 3 equiv), SPhos (1.6 mg, 4 μ mol, 6 mol %), and

Pd(dba)₂ (1.1 mg, 2 μ mol, 3 mol %); the suspension was purged for 5 min with Ar (Ar “bubbling”) and stirred for 4 h at reflux. The reaction mixture was diluted with EtOAc, washed with brine (3 \times 25 mL), dried over Na₂SO₄, and concentrated. The residue was purified by flash chromatography on silica gel (*n*-hexane/EtOAc, with a gradient from 95:5 to 50:50) to afford the *tert*-butyl ester of compound 4-Et as a yellow solid (87 mg, 76% yield). This *tert*-butyl ester (87 mg, 46.8 μ mol) was dissolved in a mixture of TFA/DCM (6 mL, 1:1, v/v) and heated with stirring for 1 h at reflux. The reaction mixture was concentrated in vacuum and subjected to flash chromatography using a RP-C₁₈ cartridge (system B). The product-containing fractions were pooled and lyophilized to give compound 4-Et as an amorphous yellow solid (47.8 mg, 72% yield). *ap:p* = 75:25. ¹H NMR (400 MHz, DMF-*d*₇): δ = 8.33 (s, 1.5 H, *ap*), 8.21 (s, 0.5 H, *p*), 8.12 (d, *J* = 8.1 Hz, 1.5 H, *ap*), 8.03 (m, 0.5 H, *p*, masked by NMR solvent), 7.88 (d, *J* = 7.9 Hz, 0.5 H, *p*), 7.82 (d, *J* = 8.1 Hz, 1.5 H, *ap*), 7.77 (m, 3.0 H, *ap*), 7.68 (m, 1.0 H, *p*), 4.60 (m, 4.0 H, *p/ap*), 4.26 (m, 12.0 H, *p/ap*), 3.92 (m, 6.0 H, *p/ap*, masked partially by NMR solvent), 2.79 (m, 1.5 H, *p/ap*, masked partially by NMR solvent), 2.60 (m, 2.5 H, *p/ap*), 1.41 (t, *J* = 7.4 Hz, 1.5 H, *p*), 1.00 (t, *J* = 7.6 Hz, 4.5 H, *ap*). ¹³C NMR (126 MHz, DMF-*d*₇): δ = 171.9, 171.3, 169.6, 154.5, 150.2, 150.0, 143.1, 141.1, 137.6, 137.4, 134.0, 133.8, 131.0, 129.3, 129.1, 128.8, 125.6, 124.0, 121.4, 121.3, 116.5, 52.0, 48.5, 20.1, 19.9, 12.7, 12.5. ¹⁹F NMR (376 MHz, DMF-*d*₇): δ = -109.50 (m, 4.0 F, *p/ap*), -130.73 (m, 2.0 F, *p/ap*). HR-MS (ESI, positive mode): 1431.1927 [M+Na]⁺ (found), 1431.1951 (calculated for C₅₉H₅₀F₆N₄NaO₂₆S₂, [M+Na]⁺). HPLC (system A): *t*_R = 5.1 min (1% HPLC area, CF); 7.3 min (97% HPLC area, OF).

Compound 11. A solution of *tert*-butyl ester of compound 11 (36 mg, 0.0211 mmol) in a mixture of TFA/DCM (6 mL, 1:1, v/v) was heated with stirring for 1 h at reflux. The reaction mixture was concentrated in vacuum and subjected to flash chromatography using a RP-C₁₈ cartridge (system B). The product-containing fractions were pooled and lyophilized to give compound 11 as an amorphous yellow solid (16 mg, 55% yield). *ap:p* = 70:30. ¹H NMR (500 MHz, DMF-*d*₇): δ = 13.40 (s, 8.0 H, CO₂H), 8.49 (d, *J* = 1.7 Hz, 0.7 H, *ap*), 8.39 (d, *J* = 1.7 Hz, 0.3 H, *p*), 8.33 (s, 0.7 H, *ap*), 8.22 (dd, *J* = 8.1 and 1.8 Hz, 0.7 H, *ap*), 8.12 (m, 0.6 H, *p*), 8.00–7.91 (m, 3.0 H, *p/ap*), 7.89–7.82 (m, 2.0 H, *p/ap*), 7.78–7.73 (m, 1.4 H, *p/ap*), 7.55 (t, *J* = 1.5 Hz, 0.7 H, *ap*), 7.50 (t, *J* = 1.5 Hz, 0.3 H, *p*), 4.65–4.53 (m, 1.8 H, *p/ap*), 4.36 (s, 3.0 H, *p/ap*), 4.33 (s, 1.3 H, *p/ap*), 4.30 (s, 3.1 H, *p/ap*), 4.26–4.18 (m, 6.0 H, *p/ap*), 3.95 (s, 2.4 H, *p/ap*), 3.89 (s, 1.4 H, *p/ap*), 2.84–2.75 (m, 2.3 H, *p/ap*, masked partially by NMR solvent), 2.66–2.56 (m, 1.7 H, *p/ap*), 1.43–1.38 (m, 1.9 H, *p*), 1.01 (t, *J* = 7.5 Hz, 4.2 H, *ap*). ¹³C NMR (126 MHz, DMF-*d*₇): δ = 172.2, 171.9, 171.6, 171.5, 171.3, 171.3, 169.5, 167.3, 154.4, 150.3, 150.0, 143.4, 143.2, 139.7, 138.5, 138.3, 137.6, 137.6, 137.4, 134.9, 134.6, 134.4, 133.8, 131.7, 130.1, 129.6, 129.6, 129.1, 129.1, 127.6, 127.6, 126.5, 125.8, 123.9, 123.9, 122.1, 121.9, 121.4, 121.2, 52.9, 52.1, 49.1, 48.6, 20.1, 19.9, 12.7, 12.5. ¹⁹F NMR (471 MHz, DMF-*d*₇): δ = -109.45 (m, 4.0 F, *p/ap*), -130.60 (m, 2.0 F, *p/ap*). ESI-MS (negative mode): *m/z* (rel. int., %) = 688.5 (100) [M-2H]²⁻, 1377.5 (50) [M-H]⁻ (found), 1378.1 (calculated for C₅₈H₄₇F₆N₄O₂₅S₂, [M-H]⁻). HPLC (system A): *t*_R = 5.0 min (3% HPLC area, CF); 7.2 min (96% HPLC area, OF).

Bioconjugates of Compounds 4-Et and 11. Secondary antibodies were labeled using a two-step protocol consisting of (1) *in situ* activation of the corresponding dye, and (2) addition of the secondary antibody. First, 1 mg of the dye was dissolved in 250 μ L of DMF followed by addition of *N*-hydroxysuccinimide (NHS) (1.4 equiv) and 1-ethyl-3-(3-(dimethylamino)propyl)carbodiimide (EDC) (10 equiv). The mixture was stirred at room temperature for 1 h. Then, 25–50 μ L of the mixture (0.1–0.2 mg of dye) was added to a solution of 1 mg of the protein in 1 mL of a buffered solution (pH ~8.3) and stirred for 1 h at room temperature. The conjugates were then purified by gel filtration (Sephadex G-25 prepacked columns) with PBS, pH 6.5, followed by a fast dialysis in a protein concentrator with a molecular weight cutoff (MWCO) of 10 kDa (Vivaspin500, GE-Healthcare). Protein-containing fractions (0.5 mL each) were centrifuged at 5000 rpm until the volume was reduced to 250 μ L (~5 min), and then the

same buffer was added to recover the starting volume. The process was repeated until no free dye was measured in the filtrate and the DOL remained constant, assessed by UV-vis spectrometry (Nanodrop ND-1000, Thermo Fisher Scientific).

Microscopy. The imaging of cellular structures was performed using a custom-built wide-field microscope with a TIRF illumination system, similar to systems previously reported.⁴³ Further descriptions are provided in the [Supporting Information](#) (Figure S4). Data processing and image rendering were also reported previously.⁴³ The histograms of the localized SM events (i.e., STORM images) were rendered as two-dimensional Gaussians with standard deviation $\sigma = 20$ nm.

■ ASSOCIATED CONTENT

Supporting Information

The Supporting Information is available free of charge on the ACS Publications website at DOI: [10.1021/jacs.7b00274](https://doi.org/10.1021/jacs.7b00274).

Details of the analytical and preparative liquid chromatography separations; full description of the syntheses of boronic esters (S1, C, and S2) and DAEs (S3–S13, 7-Me, 7-Et, 8, 10); immunolabeling and fluorescence imaging conditions (confocal and super-resolution); photoswitching fatigue resistance of compounds 4-Et and 11 in methanolic and aqueous solutions (in cuvettes); FRC analysis of the images; comparison of STORM images in the presence and absence of “blinking buffer”; NMR spectra; and HPLC traces of the new DAEs, including Schemes S1–S4 and Figures S1–S9 (PDF)

■ AUTHOR INFORMATION

Corresponding Authors

*vbelov@gwdg.de

*iriam@rikkyo.ac.jp

*shell@gwdg.de

ORCID

Mark Bates: 0000-0003-0668-5277

Vladimir N. Belov: 0000-0002-7741-4653

Stefan W. Hell: 0000-0002-9638-5077

Notes

The authors declare no competing financial interest.

■ ACKNOWLEDGMENTS

M.B. was supported by an EMBO long-term fellowship. We are indebted to the Bundesministerium für Bildung und Forschung (BMBF, Germany) for funding in the program KMU-innovativ: Photonik/Optische Technologien (FKZ 13N12995; to SWH). We thank J. Bienert (MPIBPC), Dr. H. Frauendorf, Dr. M. John and co-workers (Institut für Organische und Biomolekulare Chemie, Georg-August-Universität, Göttingen, Germany) for recording spectra. We thank Marcel Leutenegger for fruitful discussions and technical support. We are indebted to Jens Schimpfhauser and Jan Seikowski (MPIBPC) for the synthesis of 1,2-bis(2-ethyl-6-iodo-1-benzothiophen-1,1-dioxide-3-yl)perfluorocyclopentene and 3,5-di(*tert*-butylcarboxyphenyl)boronic acid, pinacol ester. We thank E. Rothermel and T. Gilat for assistance with cell preparation and biolabeling experiments.

■ REFERENCES

- (1) Hell, S. W. *Science* **2007**, *316*, 1153–1158.
- (2) Hell, S. W. *Nat. Methods* **2009**, *6*, 24–32.
- (3) Donnert, G.; Keller, J.; Medda, R.; Andrei, M. A.; Rizzoli, S. O.; Luhrmann, R.; Jahn, R.; Eggeling, C.; Hell, S. W. *Proc. Natl. Acad. Sci. U. S. A.* **2006**, *103*, 11440–11445.
- (4) Willig, K. I.; Rizzoli, S. O.; Westphal, V.; Jahn, R.; Hell, S. W. *Nature* **2006**, *440*, 935–939.
- (5) Hell, S. W. *Nat. Biotechnol.* **2003**, *21*, 1347–1355.
- (6) Hell, S. W.; Wichmann, J. *Opt. Lett.* **1994**, *19*, 780–782.
- (7) Westphal, V.; Rizzoli, S. O.; Lauterbach, M. A.; Kamin, D.; Jahn, R.; Hell, S. W. *Science* **2008**, *320*, 246–249.
- (8) Berning, S.; Willig, K. I.; Steffens, H.; Dibaj, P.; Hell, S. W. *Science* **2012**, *335*, 551–551.
- (9) Hofmann, M.; Eggeling, C.; Jakobs, S.; Hell, S. W. *Proc. Natl. Acad. Sci. U. S. A.* **2005**, *102*, 17565–17569.
- (10) Grotjohann, T.; Testa, I.; Leutenegger, M.; Bock, H.; Urban, N. T.; Lavoie-Cardinal, F.; Willig, K. I.; Eggeling, C.; Jakobs, S.; Hell, S. W. *Nature* **2011**, *478*, 204–208.
- (11) Hell, S. W.; Kroug, M. *Appl. Phys. B: Lasers Opt.* **1995**, *60*, 495–497.
- (12) Bretschneider, S.; Eggeling, C.; Hell, S. W. *Phys. Rev. Lett.* **2007**, *98*, 218103.
- (13) Gustafsson, M. G. L. *Proc. Natl. Acad. Sci. U. S. A.* **2005**, *102*, 13081–13086.
- (14) Heintzmann, R.; Jovin, T. M.; Cremer, C. J. *Opt. Soc. Am. A* **2002**, *19*, 1599–1609.
- (15) Rust, M. J.; Bates, M.; Zhuang, X. W. *Nat. Methods* **2006**, *3*, 793–795.
- (16) Bates, M.; Huang, B.; Dempsey, G. T.; Zhuang, X. W. *Science* **2007**, *317*, 1749–1753.
- (17) Betzig, E.; Patterson, G. H.; Sougrat, R.; Lindwasser, O. W.; Olenych, S.; Bonifacino, J. S.; Davidson, M. W.; Lippincott-Schwartz, J.; Hess, H. F. *Science* **2006**, *313*, 1642–1645.
- (18) Hess, S. T.; Girirajan, T. P. K.; Mason, M. D. *Biophys. J.* **2006**, *91*, 4258–4272.
- (19) Fölling, J.; Bossi, M.; Bock, H.; Medda, R.; Wurm, C. A.; Hein, B.; Jakobs, S.; Eggeling, C.; Hell, S. W. *Nat. Methods* **2008**, *5*, 943–945.
- (20) Testa, I.; Wurm, C. A.; Medda, R.; Rothermel, E.; von Middendorf, C.; Fölling, J.; Jakobs, S.; Schonle, A.; Hell, S. W.; Eggeling, C. *Biophys. J.* **2010**, *99*, 2686–2694.
- (21) Heilemann, M.; van de Linde, S.; Schüttelz, M.; Kasper, R.; Seefeldt, B.; Mukherjee, A.; Tinnefeld, P.; Sauer, M. *Angew. Chem., Int. Ed.* **2008**, *47*, 6172–6176.
- (22) Hell, S. W.; Sahl, S. J.; Bates, M.; Zhuang, X. W.; Heintzmann, R.; Booth, M. J.; Bewersdorf, J.; Shtengel, G.; Hess, H.; Tinnefeld, P.; Honigsmann, A.; Jakobs, S.; Testa, I.; Cognet, L.; Lounis, B.; Ewers, H.; Davis, S. J.; Eggeling, C.; Klenerman, D.; Willig, K. I.; Vicidomini, G.; Castello, M.; Diaspro, A.; Cordes, T. *J. Phys. D: Appl. Phys.* **2015**, *48*, 443001–443036.
- (23) Bates, M.; Huang, B.; Zhuang, X. *Curr. Opin. Chem. Biol.* **2008**, *12* (5), 505–514.
- (24) Huang, B.; Bates, M.; Zhuang, X. W. *Annu. Rev. Biochem.* **2009**, *78*, 993–1016.
- (25) Wegel, E.; Gohler, A.; Lagerholm, B. C.; Wainman, A.; Uphoff, S.; Kaufmann, R.; Dobbie, I. M. *Sci. Rep.* **2016**, *6*, 27290.
- (26) Turkowyd, B.; Virant, D.; Endesfelder, U. *Anal. Bioanal. Chem.* **2016**, *408*, 6885–6911.
- (27) Lehmann, M.; Lichtner, G.; Klentz, H.; Schmoranzler, J. *J. Biophotonics* **2016**, *9*, 161–170.
- (28) Irie, M.; Fukaminato, T.; Matsuda, K.; Kobatake, S. *Chem. Rev.* **2014**, *114*, 12174–277.
- (29) Shoji, Y.; Yagi, A.; Horiuchi, M.; Morimoto, M.; Irie, M. *Isr. J. Chem.* **2013**, *53*, 303–311.
- (30) Jeong, Y. C.; Yang, S. I.; Ahn, K. H.; Kim, E. *Chem. Commun.* **2005**, 2503–2505.
- (31) Jeong, Y.-C.; Yang, S. I.; Kim, E.; Ahn, K.-H. *Tetrahedron* **2006**, *62*, 5855–5861.
- (32) Roubinet, B.; Bossi, M. L.; Alt, P.; Leutenegger, M.; Shojaei, H.; Schnorrenberg, S.; Nizamov, S.; Irie, M.; Belov, V. N.; Hell, S. W.

Angew. Chem., Int. Ed. **2016**, *55*, 15429–15433; *Angew. Chem.* **2016**, *128*, 15655–15659.

(33) Heilemann, M.; Dedecker, P.; Hofkens, J.; Sauer, M. *Laser Photonics Rev.* **2009**, *3*, 180–202.

(34) Vogelsang, J.; Steinhauer, C.; Forthmann, C.; Stein, I. H.; Person-Skegros, B.; Cordes, T.; Tinnefeld, P. *ChemPhysChem* **2010**, *11*, 2475–2490.

(35) Chozinski, T. J.; Gagnon, L. A.; Vaughan, J. C. *FEBS Lett.* **2014**, *588*, 3603–3612.

(36) Dempsey, G. T.; Vaughan, J. C.; Chen, K. H.; Bates, M.; Zhuang, X. W. *Nat. Methods* **2011**, *8*, 1027–1036.

(37) Uno, K.; Niikura, H.; Morimoto, M.; Ishibashi, Y.; Miyasaka, H.; Irie, M. *J. Am. Chem. Soc.* **2011**, *133*, 13558–13564.

(38) Fukaminato, T.; Sasaki, T.; Kawai, T.; Tamai, N.; Irie, M. *J. Am. Chem. Soc.* **2004**, *126*, 14843–14849.

(39) Irie, M.; Fukaminato, T.; Sasaki, T.; Tamai, N.; Kawai, T. *Nature* **2002**, *420*, 759–760.

(40) Nevskiy, O.; Sysoiev, D.; Oppermann, A.; Huhn, T.; Wöll, D. *Angew. Chem., Int. Ed.* **2016**, *55*, 12698–12702. Nevskiy, O.; Sysoiev, D.; Oppermann, A.; Huhn, T.; Wöll, D. *Angew. Chem.* **2016**, *128*, 12890–12894.

(41) Wu, T.; Johnsen, B.; Qin, Z.; Morimoto, M.; Baillie, D.; Irie, M.; Branda, N. R. *Nanoscale* **2015**, *7*, 11263–11266.

(42) Bälter, M.; Li, S.; Morimoto, M.; Tang, S.; Hernando, J.; Guirado, G.; Irie, M.; Raymo, F. M.; Andréasson, J. *Chem. Sci.* **2016**, *7*, 5867–5871.

(43) Bates, M.; Dempsey, G. T.; Chen, K. H.; Zhuang, X. W. *ChemPhysChem* **2012**, *13*, 99–107.

(44) Thompson, R. E.; Larson, D. R.; Webb, W. W. *Biophys. J.* **2002**, *82*, 2775–2783.

(45) Shroff, H.; Galbraith, C. G.; Galbraith, J. A.; Betzig, E. *Nat. Methods* **2008**, *5*, 417–423.

(46) Gillanders, F.; Giordano, L.; Diaz, S. A.; Jovin, T. M.; Jares-Erijman, E. A. *Photochem. Photobiol. Sci.* **2014**, *13*, 603–612.

(47) Irie, M.; Sakemura, K.; Okinaka, M.; Uchida, K. *J. Org. Chem.* **1995**, *60*, 8305–8309.

(48) Takagi, Y.; Kunishi, T.; Katayama, T.; Ishibashi, Y.; Miyasaka, H.; Morimoto, M.; Irie, M. *Photochem. Photobiol. Sci.* **2012**, *11*, 1661–1665.

(49) Díaz, S. A.; Gillanders, F.; Susumu, K.; Oh, E.; Medintz, I. L.; Jovin, T. M. *Chem. - Eur. J.* **2017**, *23*, 263–267.

(50) Krayushkin, M. M.; Bogacheva, A. M.; Levchenko, K. S.; Kobleva, O. I.; Valova, T. M.; Barachevskii, V. A.; Pozzo, J.-L.; Struchkova, M. I.; Shmelin, P. S.; Kalik, M. A.; Baryshnikova, T. K.; Charushin, V. N. *Mendeleev Commun.* **2013**, *23*, 78–80.

(51) Isegawa, M.; Morokuma, K. *J. Phys. Chem. A* **2015**, *119*, 4191–4199.

(52) Ishibashi, Y.; Umesato, T.; Kobatake, S.; Irie, M.; Miyasaka, H. *J. Phys. Chem. C* **2012**, *116*, 4862–4869.

(53) Urbach, F. *Phys. Rev.* **1953**, *92*, 1324–1324.

(54) Kinoshita, S.; Nishi, N.; Saitoh, A.; Kushida, T. *J. Phys. Soc. Jpn.* **1987**, *56*, 4162–4175.

(55) Arai, Y.; Ito, S.; Fujita, H.; Yoneda, Y.; Kaji, T.; Takei, S.; Kashihara, R.; Morimoto, M.; Irie, M.; Miyasaka, H. *Chem. Commun.* **2017**, *53*, 4066–4069.

(56) Mizuno, K.; Matsui, A.; Sloan, G. J. *J. Phys. Soc. Jpn.* **1984**, *53*, 2799–2806.

(57) Hofkens, J.; Maus, M.; Gensch, T.; Vosch, T.; Cotlet, M.; Köhn, F.; Herrmann, A.; Müllen, K.; De Schryver, F. J. *J. Am. Chem. Soc.* **2000**, *122*, 9278–9288.

(58) Fukaminato, T.; Umemoto, T.; Iwata, Y.; Irie, M. *Chem. Lett.* **2005**, *34*, 676–677.

(59) Eggeling, C.; Widengren, J.; Rigler, R.; Seidel, C. A. M. *Anal. Chem.* **1998**, *70*, 2651–2659.

(60) Nieuwenhuizen, R. P. J.; Lidke, K. A.; Bates, M.; Puig, D. L.; Grunwald, D.; Stallinga, S.; Rieger, B. *Nat. Methods* **2013**, *10*, 557–562.

(61) Banterle, N.; Bui, K. H.; Lemke, E. A.; Beck, M. *J. Struct. Biol.* **2013**, *183*, 363–367.

(62) Bossi, M.; Fölling, J.; Belov, V. N.; Boyarskiy, V. P.; Medda, R.; Egner, A.; Eggeling, C.; Schonle, A.; Hell, S. W. *Nano Lett.* **2008**, *8*, 2463–2468.

(63) Gu, X. G.; Zhao, E. G.; Zhao, T.; Kang, M. M.; Gui, C.; Lam, J. W. Y.; Du, S. W.; Loy, M. M. T.; Tang, B. Z. *Adv. Mater.* **2016**, *28*, 5064–5071.

(64) Uno, S. N.; Kamiya, M.; Yoshihara, T.; Sugawara, K.; Okabe, K.; Tarhan, M. C.; Fujita, H.; Funatsu, T.; Okada, Y.; Tobita, S.; Urano, Y. *Nat. Chem.* **2014**, *6*, 681–689.

(65) Nahidiazar, L.; Agronskaia, A. V.; Broertjes, J.; van den Broek, B.; Jalink, K. *PLoS One* **2016**, *11*, e0158884.

(66) Olivier, N.; Keller, D.; Rajan, V. S.; Gonczyk, P.; Manley, S. *Biomed. Opt. Express* **2013**, *4*, 885–899.

(67) Sauer, M.; Heilemann, M. *Chem. Rev.* **2017**, DOI: 10.1021/acs.chemrev.6b00667.

(68) Taguchi, M.; Nakagawa, T.; Nakashima, T.; Kawai, T. *J. Mater. Chem.* **2011**, *21*, 17425–17432.

(69) Pang, S. C.; Hyun, H.; Lee, S.; Jang, D.; Lee, M. J.; Kang, S. H.; Ahn, K. H. *Chem. Commun.* **2012**, *48*, 3745–3747.

(70) Ai, Q.; Pang, S. C.; Ahn, K.-H. *Chem. - Eur. J.* **2016**, *22*, 656–662.

(71) Takagi, Y.; Morimoto, M.; Kashihara, R.; Fujinami, S.; Ito, S.; Miyasaka, H.; Irie, M. *Tetrahedron* **2017**, DOI: 10.1016/j.tet.2017.03.040.

(72) Balzarotti, F.; Eilers, Y.; Gwosch, K. C.; Gynnå, A. H.; Westphal, V.; Stefani, F. D.; Elf, J.; Hell, S. W. *Science* **2017**, *355*, 606–612.

(73) Li, F.; Basile, V. M.; Pekarek, R. T.; Rose, M. J. *ACS Appl. Mater. Interfaces* **2014**, *6*, 20557–20568.

(74) Paramelle, D.; Cantel, S.; Enjalbal, C.; Amblard, M.; Forest, E.; Heymann, M.; Geourjon, C.; Martinez, J.; Subra, G. *Proteomics* **2009**, *9*, 5384–5388.

(75) Gottlieb, H. E.; Kotlyar, V.; Nudelman, A. *J. Org. Chem.* **1997**, *62*, 7512–7515.

(76) Deniel, M. H.; Lavabre, D.; Micheau, J. C., Photokinetics under Continuous Irradiation. In *Organic Photochromic and Thermochromic Compounds: Vol. 2: Physicochemical Studies, Biological Applications, and Thermochromism*; Crano, J. C., Guglielmetti, R. J., Eds.; Springer US: Boston, MA, 2002; pp 167–209.

NOTE ADDED AFTER ASAP PUBLICATION

This paper published without the final changes on May 4, 2017; the correct version reposted on May 5, 2017.

2.3. Manuscript II: Photoactivatable Siliconrhodamine

Published on October 23, 2020 in Chemistry A European Journal.

"Photoactivatable Fluorophore for Stimulated Emission Depletion (STED) Microscopy and Bioconjugation Technique for Hydrophobic Labels. Michael Weber, Taukeer A. Khan, Lukas J. Patalag, Mariano Bossi, Marcel Leutenegger, Vladimir N. Belov, and Stefan W. Hell, *Chem. Eur. J.* **2021** *27*, 421, DOI: 10.1002/chem.202004645" is published under the terms of the Creative Commons CC BY licence Copyright 2020 Chemistry - A European Journal published by Wiley-VCH GmbH.

Contribution

Together with Vladimir L. Belov and Stefan W. Hell, I designed the study and was primarily responsible for writing the manuscript. Furthermore, I characterized the fluorophores on the microscope, captured images and established the labelling and purification strategy.

■ Photoactivation

Photoactivatable Fluorophore for Stimulated Emission Depletion (STED) Microscopy and Bioconjugation Technique for Hydrophobic Labels

Michael Weber,^[a] Taukeer A. Khan,^[a] Lukas J. Patalag,^[a, c] Mariano Bossi,^[b]
Marcel Leutenegger,^[a] Vladimir N. Belov,^[a] and Stefan W. Hell*^[a, b]

Abstract: The use of photoactivatable dyes in STED microscopy has so far been limited by two-photon activation through the STED beam and by the fact that photoactivatable dyes are poorly solvable in water. Herein, we report ONB-2SiR, a fluorophore that can be both photoactivated in the UV and specifically de-excited by STED at 775 nm. Like-

wise, we introduce a conjugation and purification protocol to effectively label primary and secondary antibodies with moderately water-soluble dyes. Greatly reducing dye aggregation, our technique provides a defined and tunable degree of labeling, and improves the imaging performance of dye conjugates in general.

Introduction

The conversion of a non-fluorescent compound into a fluorescent form and back is at the heart of fluorescence microscopy (nanoscopy) with diffraction-unlimited spatial resolution. While the earliest methods (STED,^[1] GSD,^[2] (S)SIM,^[3] RESOLFT^[4]) utilized structured light patterns to modulate the emission capability of fluorophores in order to make adjacent details distinguishable, the methods called STORM,^[5] PALM,^[6] GSDIM^[7] or dSTORM^[8] made nearby features distinguishable by individually switching the marker molecules to an emissive state for a brief period of detection and localization. The combined use of single molecule switching (activation and de-activation) for separation and patterned illumination for localization (MIN-

FLUX^[9]) allows achieving even molecule-scale resolution in lens-based fluorescence microscopy. In any case, all superresolution microscopy approaches require fluorophores with properties tailored to the particular imaging technique.

Multiple pathways can be taken in order to convert non-fluorescent molecules to fluorophores and vice versa. Besides reversibly photo-switchable fluorescent dyes, which rarely provide sufficient contrast between the non-fluorescent and fluorescent states, irreversibly 'photoactivatable' dyes are the most common and abundant. Photoactivation (i.e. conversion into a state in which the dye can be excited to fluorescence) of organic dyes is often based on a Wolff rearrangement^[10] or Norrish Type II reactions.^[11] The most important features of a good photoactivatable fluorophore are a high photoconversion degree, bright fluorescence, good water-solubility, and insensitivity to light other than the specific activation wavelength. Among the most useful types of fluorophores suitable for superresolution microscopy are rhodamines, carbopyronines, silicon rhodamines and related xanthene structures with extended conjugated systems. The switching capacity for these structures is often achieved by transfer to a poorly conjugated system; in particular, cyclic and uncharged derivatives (esters, amides) formed upon an intramolecular nucleophilic attack. While such transformations significantly decrease water-solubility, thus making bioconjugation quite challenging, the hydrophilic properties can be restored by the use of polar groups and linkers.^[12] Such „masked“ fluorophores have been extensively used for single-molecule localization microscopy.^[13] Nonetheless, the combination of a photoactivation and STED imaging offers unique possibilities in superresolution, such as counting the number of fluorophores participating in STED imaging.^[14] The spatial control of the active fluorophores can be used to protect the fluorophores from bleaching by the STED laser and to increase the spatial resolution. On the other

[a] M. Weber, Dr. T. A. Khan, Dr. L. J. Patalag, Dr. M. Leutenegger,
Dr. V. N. Belov, Prof. Dr. Dr. h.c. mult. S. W. Hell
Department of NanoBiophotonics
Max Planck Institute for Biophysical Chemistry
Am Faßberg 11, 37077 Göttingen (Germany)
E-mail: stefan.hell@mpiibpc.mpg.de

[b] Dr. M. Bossi, Prof. Dr. Dr. h.c. mult. S. W. Hell
Department of Optical Nanoscopy
Max Planck Institute for Medical Research
Jahnstraße 29, 69120 Heidelberg (Germany)

[c] Dr. L. J. Patalag
present address: Stratingh Institute for Chemistry
Zernike Institute for Advanced Materials
University of Groningen
Nijenborgh 4, 9747 AG Groningen (The Netherlands)

 Supporting information and the ORCID identification number(s) for the author(s) of this article can be found under:
<https://doi.org/10.1002/chem.202004645>.

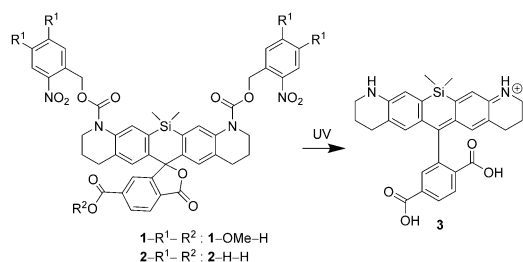
 © 2020 The Authors. Chemistry - A European Journal published by Wiley-VCH GmbH. This is an open access article under the terms of the Creative Commons Attribution License, which permits use, distribution and reproduction in any medium, provided the original work is properly cited.

hand, realizing this combination brings about additional complexity, since high resolution STED microscopy entails relatively high photon fluxes eliciting uncontrolled activation by two-photon absorption from the typically pulsed STED laser beam.^[13b] Silicon rhodamines (SiR) are widely used in fluorescence microscopy and STED nanoscopy, especially for live-cell imaging. A photoactivatable SiR with photocleavable 4,5-dimethoxy-2-nitrobenzyl (*DiMeO-ONB*) groups was reported and applied in photoactivation localization microscopy (PALM) of actin.^[13d] However, this caging group is cleaved by the STED light, which precludes its use in STED nanoscopy. We found that the activation by the STED beam may be as high as 10% after one scan, thus making any prior sequential (time-lapse) measurements of other fluorophores impossible due to progressively increasing activation of *DiMeO-ONB*. We introduce a photoactivatable SiR (ONB-2SiR, see Scheme 1), which has been designed to overcome this drawback. In STED nanoscopy, ONB-2SiR produces images with excellent quality and without two-photon activation. Without the use of complex solubilizing modifications of the structure, we introduce a general conjugation and purification technique, which overcomes the limitations associated with low water-solubility and dye aggregation that would lead to low degrees of labelling (DOL) and unspecific antibody staining. We expect this protocol to be applica-

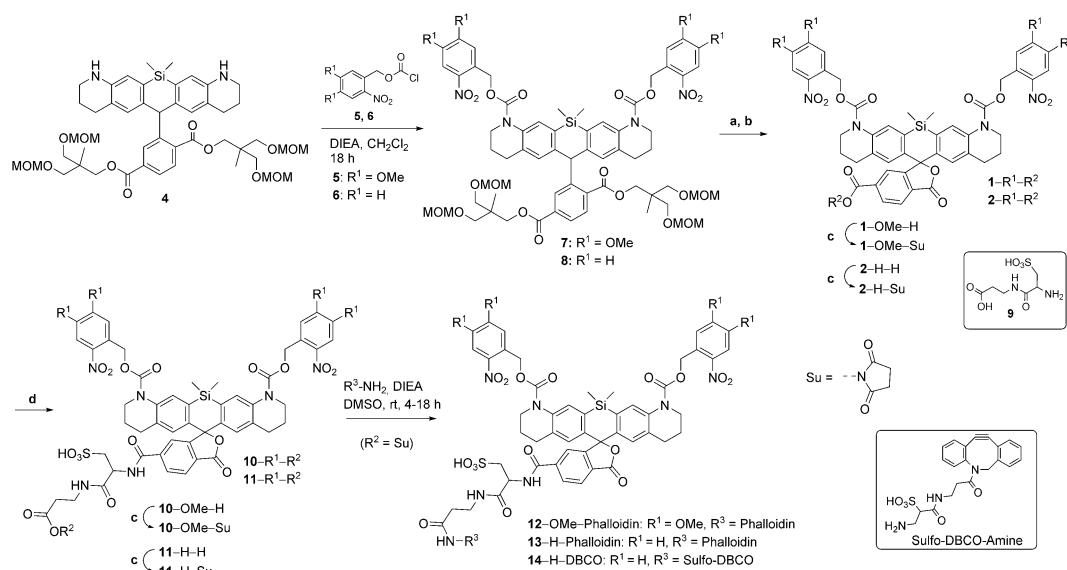
ble and efficient for bioconjugation of any hydrophobic dye or molecule, far beyond caged xanthene fluorophores.

Results and Discussion

A key process in STED microscopy is the rapid transfer of the excited fluorophores from the first excited singlet state S_1 back to a high vibrational level of the ground state S_0 by stimulated emission. To avoid the undesired excitation by the stimulating beam, its wavelength is typically chosen at the red edge of the fluorophore emission band. The most popular laser wavelengths for STED are 590 nm, 660 nm, and particularly 775 nm which is readily available and widely used due to its low photo-toxicity and high tissue penetration. To achieve a high resolution, the cross section of stimulated emission, which is proportional to the emission probability at that wavelength, should be maximized. As a compromise between STED efficiency and spurious excitation by the STED beam, fluorophores emitting between 610–680 nm (emission maximum) are depleted at 775 nm. To date, the best performing dyes in STED microscopy are mostly xanthenes featuring high photostability, large fluorescence quantum yields and extinction coefficients of about $10^5 \text{ cm}^{-1} \text{ M}^{-1}$. An emission maximum at about 660 nm can be achieved with rhodamines, carbopyronines, SiRs and germano-rhodamines. We chose a photoactivatable SiR^[13d] as a scaffold because of the excellent STED performance of SiRs with a 775 nm STED beam^[15] and the compatibility of these dyes with live-cell experiments.^[15–16] The *ortho*-nitrobenzyl photocaging groups, which can be chemically introduced into the SiR structure are shown in Scheme 1. Importantly, this caging strategy leads to a fluorophore without an electric charge and with poor solubility in water. In order to compensate for these undesirable properties, we used a „universal solubilizer“^[12] (see Scheme 2), as had been previously applied on a diazoketone to improve its poor solubility. The relatively



Scheme 1. Photoactivation of SiR by photocleavage of *ortho*-nitrobenzyl carbamates.



Scheme 2. Synthesis of leuco-dyes, photoactivatable dyes and their conjugates decorated with a hydrophilizer linker, phalloidin and strained alkyne. Reagents and conditions: (a) LiOH, THF, H₂O, 55 °C, 48 h; (b) DDQ, CH₂Cl₂, H₂O, rt, 18 h; (c) TSTU, DIEA, DMSO, rt, 1–18 h; (d) 9, DIEA, DMSO, rt, 1–18 h.

high STED beam intensities applied in STED nanoscopy can lead to adverse two-photon induced photoreactions in the UV region.^[13b] The *DiMeO-ONB* photocleavable group has substantial absorption around 400 nm, a region where two-photon interactions with the 775 nm STED beam can take place (Figure 1). To prevent or reduce this effect, we decided to shift the absorption of the photocleavable group to shorter wavelengths by using the *ortho*-nitrobenzyl (*ONB*) group without additional substituents. However, this choice may lead to complications because the light transmission of the optical components of the microscope is low in the UV region, and aberrations are difficult to compensate at the wavelength of 350–370 nm required for the one-photon activation (1PA) of *oNB*, compared to the 405 nm wavelength often used for cleaving *DiMeO-ONB*. Nevertheless, many microscopes are equipped with an excitation light source <400 nm (e.g. for DAPI imaging), which turned out to be sufficient for uncaging of *ONB* through a 1PA process.

In Scheme 2, we show the synthesis of caged SiR bearing the 6-carboxyl group for bioconjugation. The complete synthetic procedures are given in the Supporting Information. Compound **4** reacted with commercially available chloroformate (**5**) and freshly prepared *o*-nitrobenzyl chloroformate^[17] (**6**) to give caged *leuco*-SiR **7** and **8**. Saponification of esters **7** and **8** using aq. LiOH in THF yielded the desired dicarboxylic acids with 35% and 37% yield, respectively. These intermediates were oxidized with DDQ to obtain the target caged SiR **1-OMe-H** and **2-H-H** in 90% yield (Scheme 2). The free carboxyl group at C-6 of the pendant phenyl ring was used as a bioconjugation handle. To overcome the poor water-solubility of the caged dye, we attached a short sulfonate linker **9** (the „universal solublizer“^[12]) to the dye before bioconjugation. Compounds **1-OMe-H** and **2-H-H** were converted to *N*-hydroxysuccinimide esters and reacted with hydrophilizer **9** to give the more water-soluble compounds **10-OMe-H** and **11-H-H** with 57% and 96% yields, respectively (Scheme 2). The hydrophi-

lized caged dyes were converted to NHS esters **10-OMe-Su** and **11-H-Su**, and these active esters were then used to produce conjugates with antibodies and ligands. The NHS esters **10-OMe-Su** and **11-H-Su** reacted with aminophalloidin in DMSO to provide the phalloidin conjugates **12-OMe-Phalloidin** and **13-H-Phalloidin**. Similarly, the dibenzocyclooctyne containing dye **14-H-DBCO** was prepared by reacting the sulfo-DBCO-amine with NHS ester **11-H-Su**. The compound **14-H-DBCO** was used to obtain antibody conjugates of **ONB-2SiR** by means of click chemistry.

Since the photo-physical properties are only weakly influenced by additional linkers,^[12] the spectroscopic analysis was performed on the compounds without a hydrophilizer linker. The absorption spectra of compounds **1-OMe-H**, **2-H-H** and the reference compound **3** (uncaged dye) are given in Figure 1. Due to the limited solubility of the caged compounds, studies were performed in mixtures of buffered aqueous solutions (phosphate 100 mM, pH 7) and acetonitrile (1:1). The replacement of the *DiMeO-ONB* groups with *ONB* resulted in a hypsochromic shift of the absorption maximum of almost 100 nm. At 355 nm, the ratio of the absorption coefficients (compound **1-OMe-H**/ compound **2-H-H**) is 12.6. Nevertheless, compound **2-H-H** has a residual absorption „foot“ in the range 350–405 nm, which is sufficient for activation with a commercially available laser or wide-field illumination source. Both compounds show no detectable absorption and fluorescence in the red before activation. The activation of both compounds was performed in bulk experiments with a 365 nm LED source. To evaluate the quantum yields of the uncaging reactions, 1–2 μM solutions of caged compounds were irradiated in a custom setup with UV light until the starting material was consumed (Figure 2 and **S13–4**). The growth of the absorption maximum of the photoproduct **3** (insets in Figure 2) shows a bi-exponential behavior suggesting a consecutive two-step reaction (Figure 2C). The temporal evolution at the wavelength where all the products (including the byproducts produced by the caging groups) are expected to absorb (i.e. 316 nm or 390 nm), shows a mono-exponential growth in agreement with this hypothesis.

To confirm this reaction sequence, LC-MS experiments (Figures S1, S2) were performed in the course of irradiation (at the same irradiation conditions as shown in Figure 2A, B). The presence of the mono-caged fluorophores as intermediates was confirmed by MS analysis (Figures S1, S2). In addition, we observed these intermediates predominantly in the closed (lactone) forms, even under acidic conditions used in HPLC runs (0.1% TFA in aqueous MeCN). Thus, we assume that these compounds are also in the closed form at pH 7, and the only products absorbing at 640 nm are the final, completely uncaged substances.

Remarkably, a clean photoreaction is observed throughout the whole irradiation period, with three compounds in each case (**1-OMe-H** and **2-H-H**) present in the proposed sequence (the nitroso benzaldehydes were not detected). Only traces of byproducts absorbing at 250–700 nm were observed. The emission quantum yield and fluorescence lifetime of the fluorescent product (in the reaction mixtures at the end of the

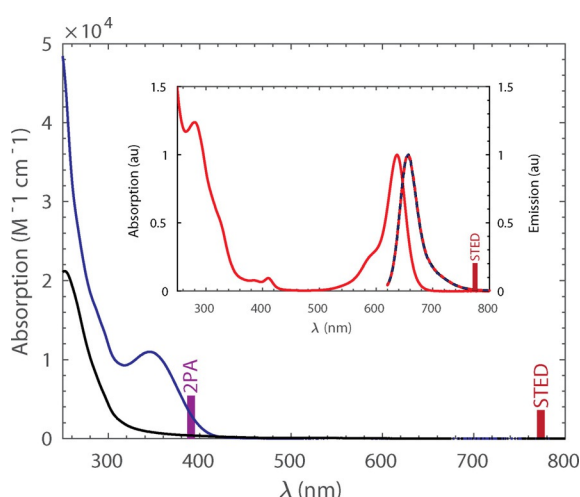


Figure 1. Absorption of compounds **1-OMe-H** (blue) and **2-H-H** (black) in a 1:1 mixture of acetonitrile and aq. phosphate buffer (100 mM, pH 7). The inset shows the normalized absorption and fluorescence of **3** (red) together with the fluorescence of **1-OMe-H** and **2-H-H** after UV activation.

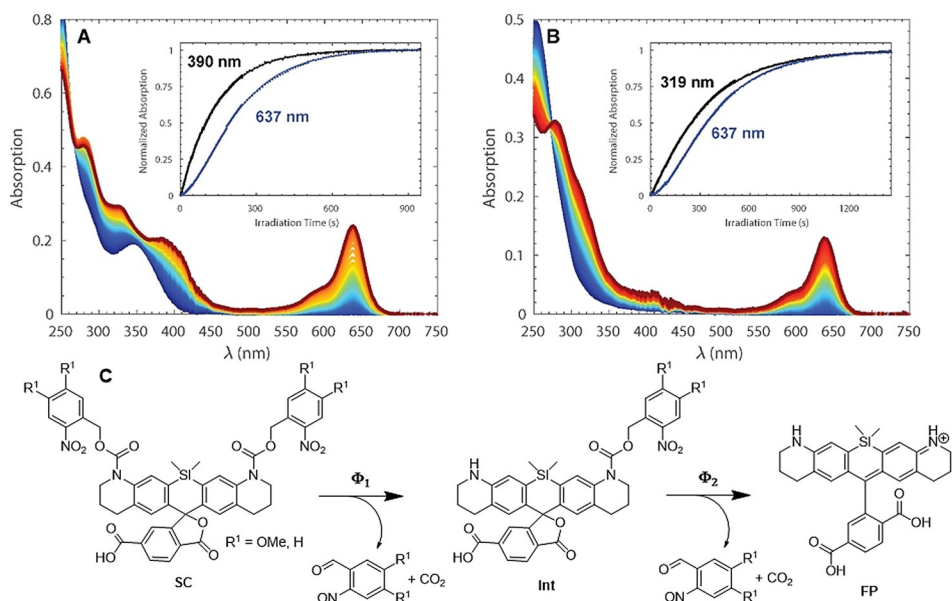


Figure 2. Uncaging experiments with compounds 1-Ome-H (A) and 2-H-H (B) in a 1:1 mixture of acetonitrile and aq. phosphate buffer (100 mM, pH 7). The time is color-coded from blue to red. Solutions were stirred and irradiated with 365 nm light, and the absorption was monitored at constant intervals (at 20 °C). The insets show the temporal evolutions at 637 nm (blue symbols), where only the final product absorbs, and at a wavelength where the intermediate and the final product absorb (A: 316 nm or B: 390 nm, black symbols), along with a global fit (black/blue lines) fitting a scheme with two consecutive reactions. (C) Proposed uncaging process, consisting of two consecutive photochemical reactions.

photolysis) were identical in both cases to the reference compound **3** (Figures S3), excluding the presence of any observable fluorescent byproducts.

By integrating the areas under the HPLC peaks, the concentration changes of the three reactants were calculated. A global fit to consecutive reaction schemes yielded the values for $(\epsilon_{SC,Int}^{\lambda_{irr}} \times \phi_{1,2})$ listed in Table 1. The absorption coefficients of the starting compounds (double-caged 1-Ome-H and 2-H-H) are known, but the ones of the intermediates (single-caged) are difficult to measure (only reaction constants were extracted from the fits). However, assuming that the absorption coefficient of the intermediate at the irradiation wavelength (365 nm) is half of the starting compound, the quantum yield of the second reaction was evaluated and listed in the table. The conversion quantum yield for the second step is slightly larger than for the first step. The uncaging efficiencies under irradiation with 365 nm wavelength for each step are 8–10 times higher for the ONB cage than for the DiMeO-ONB cage.

The phalloidin conjugates 12-Ome-Phalloidin and 13-H-Phalloidin were applied in fixed HeLa cells and imaged with a commercial STED microscope (Abberior Instruments) featuring a

STED laser emitting pulses of ≈ 1.2 ns duration at 775 nm wavelength. The oil-immersion objective lens had a numerical aperture of 1.4. The results are shown in Figure 3. The images before activation and the full-size images are shown in Figure S5. ONB-2SiR exhibits a negligible signal before UV activation, whereas the DiMeO-ONB analogue shows a significantly higher (but for most applications still acceptable) signal under the same conditions. Both conjugates were activated with a broadband 400 nm LED to saturation and imaged by STED microscopy. Since both dyes share the same activated chromophore, the images exhibit the same resolution. The two-photon activation (2PA) of the dyes by the STED light was tested by scanning a fresh region several times in the following sequence: (i) first confocal image scan directly after preparation; (ii) scan with STED light only (image not shown); (iii) second confocal image scan; (iv) UV activation (image not shown); (v) third confocal image scan. In step (ii) the STED beam had the same power as used for the STED images in Figure 3A–B, namely approx. 90 mW time-averaged power, amounting to ≈ 430 MW cm⁻² of pulse peak intensity.

Table 1. Reaction parameters of the photochemical reactions. Extinction coefficients and quantum yields are measured at irradiation wavelength of 365 nm.^[a]

Compd.	Extinction coefficient of starting compound: $\epsilon_{SC}^{\lambda_{irr}} \left[\frac{1}{M \cdot cm} \right]$	Extinction coefficient of intermediate: $\epsilon_{Int}^{\lambda_{irr}} = \frac{1}{2} \epsilon_{SC}^{\lambda_{irr}} \left[\frac{1}{M \cdot cm} \right]$	$\epsilon_{SC}^{\lambda_{irr}} \times \phi_1$	$\epsilon_{Int}^{\lambda_{irr}} \times \phi_2$	Quantum yield of first reaction: ϕ_1	Quantum yield of second reaction: ϕ_2
1-Ome-H	8800	4400	44	32	0.005	0.007
2-H-H	575	287	28	16	0.049	0.056

[a] The DiMeO-ONB analog shows a high signal (9.5% relative to the signal after UV activation) after scanning once with only the STED beam, whereas the ONB-2SiR analog shows only a very minor, negligible signal increase.

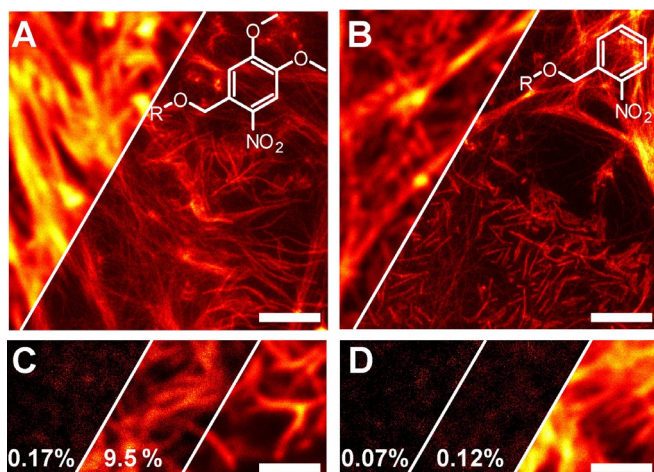


Figure 3. Images of actin filaments in fixed HeLa cells labelled with compounds 12-OMe-Phalloidin (A, C) and 13-H-Phalloidin (B, D). A, B: Confocal (left) and STED (right) images after activation with UV light below 400 nm wavelength. C, D: Confocal image sequence of the same sample region, (from left to right): after preparation; after one scan with exposure to STED light only; and after UV activation. The numbers in C and D show the signals relative to the signal after UV activation. Scale bar: 2 μm .

The blue shift in the absorption of the *ONB* (with respect to *DiMeO-ONB*) resulted in a remarkable absence of 2PA with the nanosecond-pulsed 775 nm STED beam. The undesired residual activation of the *ONB* analogue, as well as the fluorescence

before UV activation, remained negligible compared to the signal after UV activation. The activation of the *ONB* analogue was also tested at 405 nm wavelength, which has been reported to be an efficient activation light for the *DiMeO-ONB* cage.^[13d] Only sparse activation was observed (Figure S6A, B).

To allow the labelling of different cellular structures, the NHS-ester of the *ONB* analogue 11-H-Su was used to produce antibody conjugates with primary/secondary antibodies. First attempts using a standard labeling protocol (< 3% DMSO or DMF in aqueous buffer) were unsuccessful, probably due to the poor solubility of the dyes. The solubilizing linker seems to be insufficient on its own to provide good conjugation of the caged dye. The same results were obtained with the *DiMeO-ONB* variant 10-OMe-Su. Since further solubilizing chemical modifications would require a new synthesis route, we opted for adapting the conjugation and purification routines.

We increased the amount of organic solvent (DMSO or DMF) in the coupling reaction to 30% to facilitate the dissolution and reaction of the lipophilic dye. After conjugation, the antibodies aggregated, and the unreacted dye could not be completely separated from the protein using size-exclusion chromatography, dialysis or MWCO spin filters. Cells stained with these antibodies were used for fluorescence microscopy as shown in Figure 4A. The labelled microtubules are weakly visible in the wide-field image with a high intra- and extracellular background, which can be attributed to the unreacted dye. For obtaining better performing antibodies, we first optimized

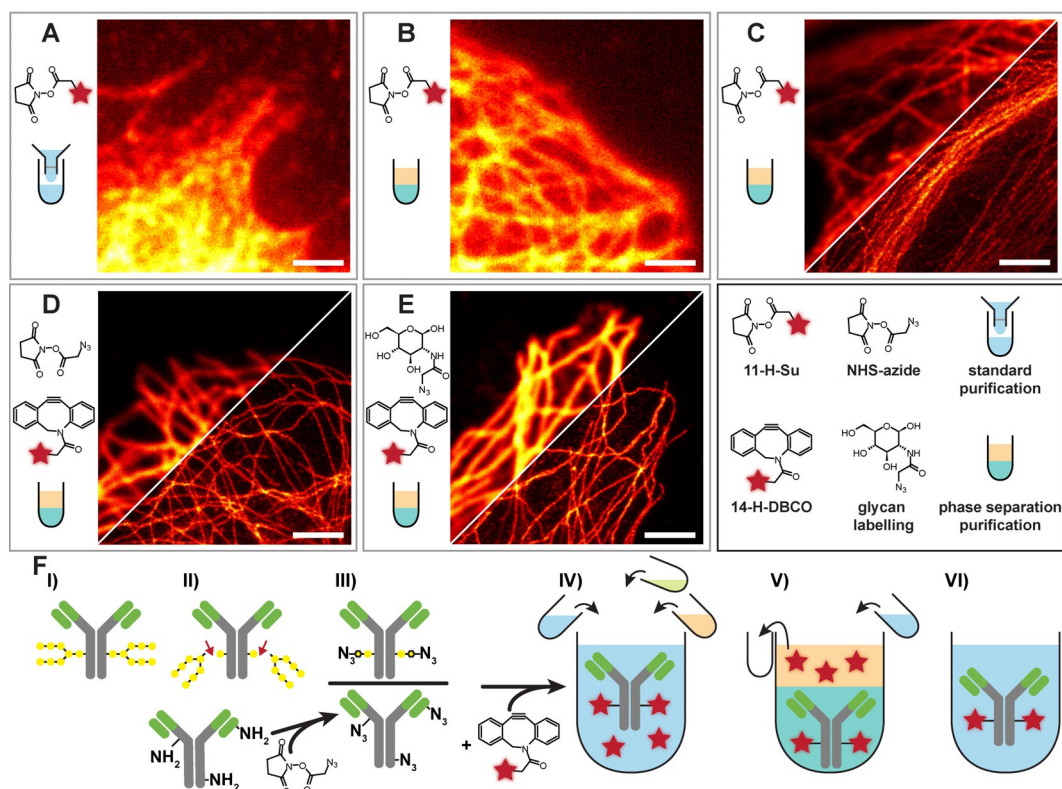


Figure 4. Fixed U2OS cells labeled with primary antibody against tubulin and secondary antibody conjugated with 11-H-Su (A–C) or 14-H-DBCO (D, E) using standard (A) or phase-separation purification (B–E) with NHS (A–C), NHS-azide (D) or glycan-azide (E). F shows the antibody modification and purification protocol: I–III) cleavage of glycans, attachment of azide modified sugars or azide introduction through NHS-azide, IV) reaction with 14, addition of water, saturated ammonium sulfate solution and *tert*-butanol, V) removal of organic phase, VI) final antibody solution. Scale bar: 2 μm .

the purification of the conjugates, to remove the unreacted dye from the antibody solution.

In order to separate the lipophilic dye from the labelled antibodies, we developed a new separation technique based on the three phase partitioning (TPP) method.^[18] We used *tert*-butanol as an organic co-solvent and saturated ammonium sulfate solution to induce a phase separation in the *tert*-butanol/DMF/water system. The lipophilic dye accumulates in the organic (*tert*-butanol) phase and can be removed (together with most of the DMF), whereas the antibody remains in the aqueous phase. Before saturated $(\text{NH}_4)_2\text{SO}_4$ and *tert*-butanol were added to the antibody dye solution, the mixture was diluted with distilled water to compensate the loss by the water content of the organic phase. The amounts of distilled water, saturated $(\text{NH}_4)_2\text{SO}_4$ and *tert*-butanol can be adjusted to obtain the desired volume of the aqueous phase (to concentrate or dilute the protein), salt concentration (salts partition mainly into the aqueous phase) and volume of the organic phase. The salt concentration was kept low and the purified antibodies were diluted with buffer, in order to prevent the antibody from precipitating. Wide-field, confocal and STED images using labelled secondary antibodies purified by this method are shown in Figure 4B–C. The wide-field image shows dense labelling of the microtubules without intra- or extracellular background. The STED images are punctuated, whereas the confocal images show homogenous labelling. Variations in the ratio between antibody and NHS-ester 11-H-Su did not significantly improve the image quality. The aggregation of the antibodies was still observed, even with the new purification method. The punctuated STED images also indicated a low DOL.

With the new purification technique at hand, we started optimizing the conjugation procedure to improve the DOL and reduce the aggregation of the antibodies upon labelling. Since the desired aminolysis of NHS-esters is compromised by hydrolysis, and the concentration of the dye in water is an important parameter, we exchanged the reactive groups to a hydrolytically stable azide alkyne pair in a strain-promoted „click chemistry“. First, azide groups were introduced into antibodies by converting free amines to azides with *N*-hydroxysuccinimidyl azidoacetate. The azide-containing antibodies were purified by size exclusion chromatography. Then, the modified antibodies reacted with a dye bearing a dibenzocyclooctene (DBCO) residue 14-H-DBCO and were purified using the new method. The confocal and STED images obtained with these antibodies are shown in Figure 4D. The structures appear densely labelled even in the STED images. However, partial precipitation of the protein after purification was still observed (which often happens in the course of labelling with hydrophobic dyes). The low water solubility of the dye putatively limits the maximal amount of dye attachable to the antibody before precipitation occurs. Thus, the DOL needs to be precisely controlled between the minimum, defined by the fluorescence needed for obtaining informative images, and the maximum levels, limited by aggregation. In order to control the DOL and target the conjugation to a specific site of the antibodies, we enzymatically modified the glycans on the heavy chain of the antibody.^[19] The number of glycan chains attached to the IgG anti-

bodies, which is two for most species, then defines the DOL. Different types of antibodies (secondary and primary) were tested with this conjugation and purification technique, and no aggregation was observed, even after storage for months in solution. The confocal and STED images of tubulin labelled with primary and secondary antibodies are presented in Figure 4E. Notice that no background is observed despite dense labelling of the structure.

The photoactivatable dye ONB-2SiR conjugated to primary or secondary antibodies was further tested for different imaging applications. Although it was primarily designed for STED imaging, the dye can also be used in PALM. Figure S6C shows a PALM image obtained using 405 nm light for uncaging, which we show to induce sparse activation of the ONB caged fluorophore.

The resilience against 2PA protects the dye from bleaching and allows using ONB-2SiR to extend the number of channels of a STED microscope equipped with a nanosecond-pulsed 775 nm STED beam. First, an image is acquired with the signal from a normal fluorescent dye (i.e. uncaged). This dye is then bleached using intense excitation. Subsequently, a second caged dye is activated by UV light and imaged. The activated second dye may feature similar spectral properties as the first dye, such that it can be imaged under similar conditions as the first dye. Thereby, a second detection window can be added to any spectral channel of a fluorescence microscope. This method is particularly useful for STED microscopy with 775 nm STED wavelength as it neither requires attribution by the excitation and/or detection wavelengths of the fluorophores, nor by their fluorescence lifetimes, nor by the linear un-mixing of their signals.

To test the concept for visualizing different cellular structures, one of the primary antibodies was conjugated with compound 14-H-DBCO, and two others were labelled with primary and secondary antibodies decorated with Alexa 594 and Abberior STAR 635P fluorophores. The combinations of primary and secondary antibodies amplify the signals, whereas the primary antibodies decorated only with 14-H-DBCO have two fluorophores per antibody via the glycan labeling, and produce darker images.

The three-color images with these fluorophores are presented in Figure 5. The full images are shown in Figure S7. Although the ONB-2SiR-decorated primary antibodies are unamplified by secondary antibodies, the signal of ONB-2SiR greatly exceeds any residual unbleached STAR 635P, which can be seen by the low signal after activation in the nucleus at the bottom of the image compared to the bright signal in the mitochondria (see Figure 5C). The structure, labelled with primary antibody conjugated to ONB-2SiR, shows a comparable image quality to the STAR 635P primary/secondary antibody-labelled structure, even though the latter is with amplification.

Conclusions

We synthesized a new photoactivatable SiR fluorophore (ONB-2SiR) for STED microscopy, which is stable against two-photon activation with the routinely applied STED pulses at 775 nm

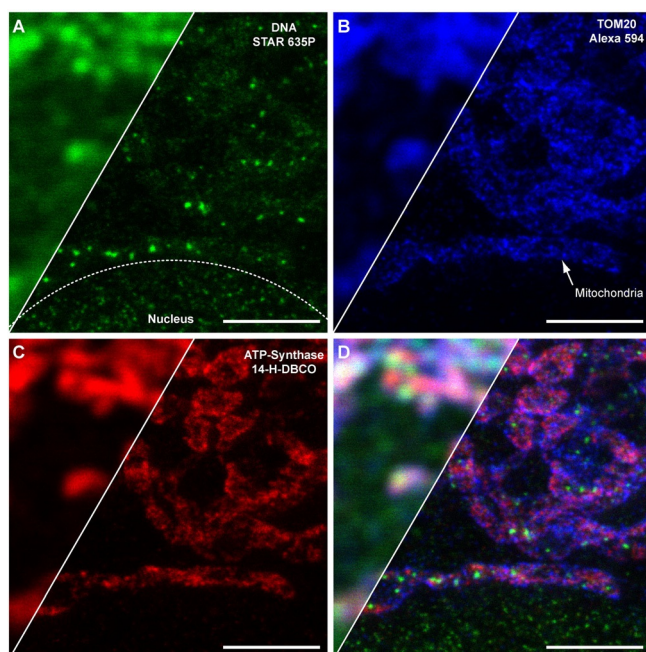


Figure 5. Confocal (left) and STED (right) images of fixed U2OS cells labelled with primary antibody against DNA (A: green), TOM20 (B: blue) and ATP-Synthase B (C: red) labelled with 14-H-DBCO (activated by UV light below 400 nm wavelength) and secondary antibodies labelled with STAR 635P (green) and Alexa 594 (blue). The images show mitochondria and a part of the nucleus (bottom of the images). An overlay of all colors is shown in D. Scale bar: 2 μm .

wavelength. The fluorophore is also suitable for single-molecule localization microscopy, such as PALM, or the more recent nanoscopy called MINIFLUX. The versatility of ONB-2SIR should enable the same sample preparation for different microscopy techniques to realize spatial resolutions ranging from diffraction- to label-limited. The ability to optimize sample preparation and access the labelled structure also with STED microscopy is very helpful for single-molecule localization techniques as well. To compensate the intrinsic hydrophobicity of caged dyes like ONB-2SIR, we introduced a new coupling and purification protocol that can be used to conjugate aggregating and poorly water-soluble dyes to antibodies. The protocol provides definite and constant values of DOL and reduces the antibody aggregation while preserving their affinity.

Acknowledgements

The authors acknowledge the financial support provided by the German Bundesministerium für Bildung und Forschung (grant FKZ 13N14122). We thank Dr. Alexey N. Butkevich for fruitful discussions and starting compounds, and Dr. Mark Bates for providing the microscope and support for the PALM measurements. We thank Jens Schimpfhauser and Jan Seikowski (Chemistry Facility, MPI BPC) for the synthesis of intermediates. We are indebted to Jürgen Bienert (Chemistry Facility, MPI BPC), Dr. H. Frauendorf, Dr. M. John and co-workers (Institut für organische und biomolekulare Chemie, University of

Göttingen, Germany) for recording spectra. We thank Dr. Stefan Stoldt for help with the antibody selection and Dr. Stefan J. Sahl for advice on the manuscript. We thank Dr. Ellen Rothermel and Tanja Gilat for assistance with cell culture and the preparation of labeled cells. Open access funding enabled and organized by Projekt DEAL.

Conflict of interest

The authors declare no conflict of interest.

Keywords: fluorescence · optical superresolution · photoactivation · protein labelling · stimulated emission depletion (STED)

- [1] a) S. W. Hell, J. Wichmann, *Opt. Lett.* **1994**, *19*, 780–782; b) V. Westphal, S. O. Rizzoli, M. A. Lauterbach, D. Kamin, R. Jahn, S. W. Hell, *Science* **2008**, *320*, 246–249; c) S. Berning, K. I. Willig, H. Steffens, P. Dibaj, S. W. Hell, *Science* **2012**, *335*, 551.
- [2] a) S. W. Hell, M. Kroug, *Appl. Phys. B: Lasers and Opt.* **1995**, *60*, 495–497; b) S. Bretschneider, C. Eggeling, S. W. Hell, *Phys. Rev. Lett.* **2007**, *98*, 218103.
- [3] a) M. G. Gustafsson, *Proc. Natl. Acad. Sci. USA* **2005**, *102*, 13081–13086; b) R. Heintzmann, T. M. Jovin, C. Cremer, *J. Opt. Soc. Am. A* **2002**, *19*, 1599–1609.
- [4] S. W. Hell, S. Jakobs, L. Kastrop, *Appl. Phys. A* **2003**, *77*, 859–860.
- [5] a) M. J. Rust, M. Bates, X. Zhuang, *Nat. Methods* **2006**, *3*, 793–796; b) M. Bates, B. Huang, G. T. Dempsey, X. Zhuang, *Science* **2007**, *317*, 1749–1753.
- [6] a) E. Betzig, G. H. Patterson, R. Sougrat, O. W. Lindwasser, S. Olenych, J. S. Bonifacio, M. W. Davidson, J. Lippincott-Schwartz, H. F. Hess, *Science* **2006**, *313*, 1642–1645; b) S. T. Hess, T. P. K. Girirajan, M. D. Mason, *Biophys. J.* **2006**, *91*, 4258–4272.
- [7] a) J. Fölling, M. Bossi, H. Bock, R. Medda, C. A. Wurm, B. Hein, S. Jakobs, C. Eggeling, S. W. Hell, *Nat. Methods* **2008**, *5*, 943–945; b) I. Testa, C. A. Wurm, R. Medda, E. Rothermel, C. von Middendorf, J. Fölling, S. Jakobs, A. Schönle, S. W. Hell, C. Eggeling, *Biophys. J.* **2010**, *99*, 2686–2694.
- [8] M. Heilemann, S. van de Linde, M. Schuttelpelz, R. Kasper, B. Seefeldt, A. Mukherjee, P. Tinnefeld, M. Sauer, *Angew. Chem. Int. Ed.* **2008**, *47*, 6172–6176; *Angew. Chem.* **2008**, *120*, 6266–6271.
- [9] a) K. C. Gwosch, J. K. Pape, F. Balzarotti, P. Hoess, J. Ellenberg, J. Ries, S. W. Hell, *Nat. Methods* **2020**, *17*, 217–222; b) F. Balzarotti, Y. Eilers, K. C. Gwosch, A. H. Gynna, V. Westphal, F. D. Stefani, J. Elf, S. W. Hell, *Science* **2017**, *355*, 606–612.
- [10] V. N. Belov, C. A. Wurm, V. P. Boyarskiy, S. Jakobs, S. W. Hell, *Angew. Chem. Int. Ed.* **2010**, *49*, 3520–3523; *Angew. Chem.* **2010**, *122*, 3598–3602.
- [11] G. A. Krafft, W. R. Sutton, R. T. Cummings, *J. Am. Chem. Soc.* **1988**, *110*, 301–303.
- [12] B. Roubinet, M. Bischoff, S. Nizamov, S. Yan, C. Geisler, S. Stoldt, G. Y. Mitronova, V. N. Belov, M. L. Bossi, S. W. Hell, *J. Org. Chem.* **2018**, *83*, 6466–6476.
- [13] a) L. M. Wysocki, J. B. Grimm, A. N. Tkachuk, T. A. Brown, E. Betzig, L. D. Lavis, *Angew. Chem. Int. Ed.* **2011**, *50*, 11206–11209; *Angew. Chem.* **2011**, *123*, 11402–11405; b) V. N. Belov, G. Y. Mitronova, M. L. Bossi, V. P. Boyarskiy, E. Heibisch, C. Geisler, K. Kolmakov, C. A. Wurm, K. I. Willig, S. W. Hell, *Chem. Eur. J.* **2014**, *20*, 13162–13173; c) J. B. Grimm, B. P. English, H. Choi, A. K. Muthusamy, B. P. Mehl, P. Dong, T. A. Brown, J. Lippincott-Schwartz, Z. Liu, T. Lionnet, L. D. Lavis, *Nat. Methods* **2016**, *13*, 985–988; d) J. B. Grimm, T. Klein, B. G. Kopeck, G. Shtengel, H. F. Hess, M. Sauer, L. D. Lavis, *Angew. Chem. Int. Ed.* **2016**, *55*, 1723–1727; *Angew. Chem.* **2016**, *128*, 1755–1759.
- [14] J. G. Danzl, S. C. Sidenstein, C. Gregor, N. T. Urban, P. Ilgen, S. Jakobs, S. W. Hell, *Nat. Photonics* **2016**, *10*, 122–128.
- [15] G. Lukinavičius, K. Umezawa, N. Olivier, A. Honigmann, G. Yang, T. Plass, V. Mueller, L. Reymond, I. R. Corrêa, Jr., Z.-G. Luo, C. Schultz, E. A. Lemke,

- P. Heppenstall, C. Eggeling, S. Manley, K. Johnsson, *Nat. Chem.* **2013**, *5*, 132–139.
- [16] a) G. Kostiuk, J. Bucevičius, R. Gerasimaitė, G. Lukinavičius, *J. Phys. D: Appl. Phys.* **2019**, *52*, 504003; b) T. Stephan, A. Roesch, D. Riedel, S. Jakobs, *Sci. Rep.* **2019**, *9*, 12419.
- [17] a) R. G. Dyer, K. D. Turnbull, *J. Org. Chem.* **1999**, *64*, 7988–7995; b) G. E. Negri, T. J. Deming, *ACS Macro Lett.* **2016**, *5*, 1253–1256.
- [18] C. Dennison, R. Lovrien, *Protein Expression Purif.* **1997**, *11*, 149–161.
- [19] a) J. Sjögren, W. B. Struwe, E. F. J. Cosgrave, P. M. Rudd, M. Stervander, M. Allhorn, A. Hollands, V. Nizet, M. Collin, *Biochem. J.* **2013**, *455*, 107–118; b) B. Ramakrishnan, P. K. Qasba, *J. Biol. Chem.* **2002**, *277*, 20833–20839.

Manuscript received: October 21, 2020

Accepted manuscript online: October 23, 2020

Version of record online: November 26, 2020

2.4. Manuscript III: MINSTED

Published on March 15, 2021 in Nature Photonics.

"**MINSTED fluorescence localization and nanoscopy.** Michael Weber, Marcel Leutenegger, Stefan Stoldt, Stefan Jakobs, Tiberiu S. Mihalia, Alexey N. Bukevich and Stefan W. Hell, *Nat. Photonics* **2021**, DOI: 10.1038/s41566-021-00774-2" is published under the terms of the Creative Commons CC BY licence.

Contribution

Together with Marcel Leutenegger, I designed and implemented the localization algorithm, built the setup and analyzed the data. I prepared the samples, together with Stefan Stoldt for the cell samples, and performed the measurements. Stefan W. Hell, Marcel Leutenegger and myself wrote the manuscript.



OPEN

MINSTED fluorescence localization and nanoscopy

Michael Weber^{1,4}, Marcel Leutenegger^{1,4}, Stefan Stoldt^{1,2}, Stefan Jakobs^{1,2}, Tiberiu S. Mihaila¹, Alexey N. Butkevich² and Stefan W. Hell^{1,3}✉

We introduce MINSTED, a fluorophore localization and super-resolution microscopy concept based on stimulated emission depletion (STED) that provides spatial precision and resolution down to the molecular scale. In MINSTED, the intensity minimum of the STED doughnut, and hence the point of minimal STED, serves as a movable reference coordinate for fluorophore localization. As the STED rate, the background and the required number of fluorescence detections are low compared with most other STED microscopy and localization methods, MINSTED entails substantially less fluorophore bleaching. In our implementation, 200–1,000 detections per fluorophore provide a localization precision of 1–3 nm in standard deviation, which in conjunction with independent single fluorophore switching translates to a ~100-fold improvement in far-field microscopy resolution over the diffraction limit. The performance of MINSTED nanoscopy is demonstrated by imaging the distribution of Mic60 proteins in the mitochondrial inner membrane of human cells.

To resolve fluorophores that are far closer than the diffraction limit, all lens-based fluorescence nanoscopy methods have to make adjacent fluorophores discernible during registration and identify their coordinates with high precision. The elegance of STED microscopy^{1,2} derives from the fact that both tasks are performed in one go by the doughnut-shaped STED beam. By confining the fluorescence ability to a sub-diffraction-sized region around its central minimum, the STED doughnut beam both singles out the fluorophores that happen to be located in this region and establishes their position. The fluorescence ability and therefore the region defined by the STED doughnut are well described by the effective point-spread-function (E-PSF) of the STED microscope³, a Gaussian of full-width-half-maximum (FWHM) $d \approx \lambda / (2NA\sqrt{1 + I/I_s})$. Here λ , NA, I and I_s denote the wavelength of the STED beam, the numerical aperture of the lens, the focal peak intensity at the doughnut crest and the intensity that reduces the fluorescence ability by half, respectively. Thus, scanning the sample with co-aligned (typically sub-nanosecond pulsed) excitation and STED beams separates fluorophores that are further apart than d and also locates them with the standard deviation $\sigma_E \approx 0.42d$.

Interestingly, if d becomes as small as the fluorophore itself (1–2 nm), which is theoretically possible for $I > 10^4 I_s$, all fluorophores will be prevented from fluorescing except the one that happens to be located right at the central doughnut minimum. At this conceptual limit without background, detecting just a single photon per fluorophore renders a perfect image, because a single detection within a given time span verifies the presence of a fluorophore at a coordinate perfectly defined by the doughnut. No other super-resolution fluorescence concept can make emitted photons as informative as STED microscopy and its close derivatives⁴.

Unfortunately, separating and locating the emitters in one go comes at a cost. Since fluorescence blocking by STED typically entails intensities of $I_s \approx 1\text{--}10 \text{ MW cm}^{-2}$, discerning fluorophores closer than $d = 20 \text{ nm}$ requires $I > 100 I_s \approx 0.1\text{--}1 \text{ GW cm}^{-2}$. Apart from the fact that applying such intensities to excited fluorophores promotes bleaching, doughnut minima are rarely $< 0.01 I$ in practice³ due to residual alignment errors and aberrations. For $I > 100 I_s$, this means that the intensity at the minimum exceeds I_s , which also

degrades the fluorescence probability at the targeted coordinate and thus the fluorophore separation at distances well below 20 nm.

Here we introduce MINSTED nanoscopy, a STED-based super-resolution fluorescence microscopy method that can provide molecule-size (1–3 nm) spatial resolution. This breakthrough has become possible by not requiring the STED doughnut to separate fluorophores (at small distances); its role is rather to establish the fluorophore's position. Although we give up some of the elegance of the original STED concept, we obtain a fluorescence microscopy method whose resolution can be tuned from the diffraction limit down to the size of the fluorophores themselves. Compared with most other advanced STED and super-resolution methods⁴, MINSTED nanoscopy and the pertinent MINSTED localization entail less bleaching and reach the molecular scale with much fewer detected photons than achieved by popular camera-based techniques.

Results

MINSTED principle. To separate fluorophores at nanometre distances, MINSTED nanoscopy employs fluorophores that are transferred from an inactive (off) to an active (on) state and back. In the active state the fluorophore can be optically excited and de-excited by stimulated emission as in the concept called protected STED⁵. However, in MINSTED nanoscopy only one fluorophore within a diffraction-limited region is switched on at any given time, meaning that its coordinate is initially unknown across diffraction length scales^{6,7}. The subsequent localization with the STED beam is greatly facilitated by the fact that the central minimum of the doughnut defines a coordinate to which the unknown coordinate of the fluorophore can be related. In the subsequent text, we refer to the position of the doughnut minimum as the ‘doughnut position’. Since it can be steered with beam deflectors at sub-nanometre precision, the doughnut position can be used for finding the position of the fluorophore in a sample: the closer it is to the fluorophore, the lower is the STED probability and the more probable is fluorescent emission. Evidently, the doughnut position entailing minimal STED must be identical with the fluorophore coordinate, hence the name MINSTED.

¹Department of NanoBiophotonics, Max Planck Institute for Biophysical Chemistry, Göttingen, Germany. ²Clinic of Neurology, University Medical Center Göttingen, Göttingen, Germany. ³Department of Optical Nanoscopy, Max Planck Institute for Medical Research, Heidelberg, Germany. ⁴These authors contributed equally: Michael Weber, Marcel Leutenegger. ✉e-mail: stefan.hell@mpibpc.mpg.de

In contrast to the related concept called MINFLUX⁸, searching for the doughnut position with minimal STED is tantamount to searching for the position where the fluorescence is maximal. Yet this does not imply maximizing emission per se. First, the absolute emission rate is freely adjustable via the excitation beam power. Second, and more importantly, placing the doughnut minimum on top of the fluorophore to maximize the emission is neither required nor desired. Since the E-PSF is a Gaussian function, moving the E-PSF maximum in close proximity to the fluorophore does not provide the most precise localization per number of detected photons^{8,9}. To find the peak of a Gaussian E-PSF it is in principle more photon-efficient to shift the peak aside and detect the rare, and hence more position-informative, photons generated at the Gaussian tail^{8,9}. Unfortunately, the fluorescence photons from the tail are usually covered by the background signal, rendering localization with diffraction-limited Gaussian excitation beams unattractive for most applications. In MINSTED, however, we narrow the E-PSF down, leave the diffraction limit behind and make all detected photons more informative in general. While a 'STED microscopy of $d=1\text{ nm}$ ' is still hard to reach with normal fluorophores, the localization precision σ continues to scale with d/\sqrt{N} . The number of detected photons N needed for reaching a certain σ decreases quadratically with decreasing d . Inserting the expression for d actually shows that $\sigma \propto 1/\sqrt{NI}$. Thus, MINSTED can shift the demand for many photons from N to I , that is from the photon-poor fluorescence to the photon-rich doughnut beam. Only those fluorescence photons that indicate the position of the fluorophore with respect to that of the doughnut are required.

Importantly, whilst making the doughnut more intense and zooming in on the fluorophore position, the doughnut can be translated so that the fluorophore always experiences intensities of the order of I_s and avoids the intensities $I \gg I_s$ that are found around the doughnut crest^{10,11}. As we show in this paper, the unique combination of all these factors bestows MINSTED nanoscopy with molecule-size precision and resolution.

MINSTED implementation, localization algorithm and simulations. We implemented MINSTED in a confocal scanning microscope with electro-optic deflectors (EODs) and galvanometer mirrors for fast and slow scanning in the focal plane, respectively (Fig. 1a). After identifying an individual fluorophore by scanning fleetingly over the sample and estimating its position with 5–10 detections, the co-aligned excitation and STED beams were circled around a position estimate C_i with a radius $R_i \approx d_i/2$. Both C_i and R_i were updated after each photon detection i (Fig. 1b). Starting at $i=0$ with a diffraction-limited E-PSF diameter d_0 given for $I=0$, the scan centre C_i was shifted by a fraction α of R_i toward the doughnut position, that is the E-PSF maximum, when detecting the next photon ($i+1$). In other words, the doughnut minimum was moved tentatively closer to the fluorophore. This measure allowed us to sharpen the E-PSF by increasing the doughnut intensity I_i and reduce R_i by a factor γ at the same time, so that the ensuing smaller d_i left the ratio R_i/d_i essentially unchanged. Therefore, despite the progressively higher I_i and the steeper E-PSF slope, the fluorophore constantly experienced moderate doughnut intensities in the ballpark of I_s (Fig. 1c). A reduction of 3% per photon detection ($\gamma=0.97$) of d_i and a step size of 15% of the scan radius ($\alpha=0.15$) were typically used. We also set a limit on the minimal radius R_{\min} and on the highest doughnut intensity I_{\max} . During the circular scanning, the synchronously steered galvanometer mirrors ensured that the scan centre C_i , that is the position estimate of the fluorophore, remained projected onto the confocal detector. As we zoomed in on the fluorophore, the precision σ improved with decreasing d_i whilst the average emission rate remained largely constant.

To assess the optimal ratio R_i/d_i , we simulated the precision σ expected for different R_i/d_i , intensity steps I_i and peak

signal-to-background ratios (SBRs) (Fig. 2). The SBR is a crucial parameter defined as the maximum detection rate from a fluorophore divided by a uniform detection rate in the sample. For zero background and a given number of detections N , a Gaussian E-PSF achieves a higher precision when R_i/d_i is large. However, in the practical range $5 < \text{SBR} < 50$ and for $N=100$ detections, $R_i/d_i=0.5$ is a better choice (Fig. 2a) because in the presence of the background the value of σ becomes smaller when the emitter is closer to the E-PSF maximum and provides more photons. The step size α has several effects on the distribution of the centre positions C_i and hence on the position estimate. A small α increases the N needed to reduce the distance between C_i and the fluorophore, and to converge to a final centre distribution (Fig. 2b). A larger α helps to approach the fluorophore quickly, but the weaker correlation amongst the successive C_i positions bears the risk of not converging at a low SBR. Furthermore, the reduction of d_i and R_i by a factor γ is tightly connected to the best step size α . Making α larger implies that $1-\gamma$ can also be larger than 3%. Increasing α and decreasing γ entails that the number N_c of detections needed to reach the final d_{\min} becomes smaller. For a low SBR the risk of ultimately missing the fluorophore position grows, as expected (Fig. 2b; see also Supplementary Figs. 1–4 and Supplementary Video 1).

Altogether, a simulation of 500 localizations as a function of a finite number of detections N showed that the chosen parameters should provide a robust and precise localization. As the doughnut scan centre homes in on the emitter, the C_i series serves as the permanently updated position estimate of the emitter. After reaching d_{\min} at $i=N_c$ and until reaching $i=N$, the coordinate average $\bar{C}_N = C_{N_c \leq i \leq N}$ was our localization result. The simulation reveals the importance of the counts up to about N_c for zooming in and reducing the N required for a certain σ . It also confirms that σ scales with $d_{\min}/\sqrt{N-N_c+1}$ (Fig. 2c). Concretely, $d_{\min}=40\text{ nm}$ is predicted to yield $\sigma \approx 3\text{ nm}$ with only $N=100$ photon detections.

Experimental MINSTED localization precision. To test these predictions, we localized immobilized individual Atto 647N fluorophores on coverslips¹² using MINSTED with $d_{\min} \approx 40\text{ nm}$. Driven by each detection i , the scan centre progressed toward the fluorophore and ultimately meandered around the estimated final coordinate (Fig. 3a,b and Supplementary Video 2). Recording many of these traces for many fluorophores allowed us to explore the attainable precision. The fluorophores were localized multiple times and the localization precision was analysed between the different localizations of the same molecule. To attribute localizations to individual fluorophores, we clustered localizations that were $\leq 25\text{ nm}$ apart. Only sets with more than five localizations were analysed and the scan centres C_i were regarded as the fluorophore coordinate estimates for $N < N_c$, as in the simulations. Once $d_{\min}=40\text{ nm}$ was reached, the 'meandering' positions C_i were averaged to \bar{C}_i until the specified N and hence \bar{C}_N was reached. Within each localization cluster, the estimated final coordinates were calculated at multiple photon numbers to establish σ as a function of N .

Our experiments show that σ decreases rapidly with decreasing d_i until d_{\min} is achieved at $N_c \approx 60$ (Fig. 3c). For $N > N_c$, the precision σ follows the $1/\sqrt{N-N_c+1}$ dependence (compare Fig. 2c) until it deviates from the simulation at about $\sigma < 2\text{ nm}$. This deviation is likely due to residual drifts of the fluorophore and/or the setup. The measured σ at around $N=10$ is slightly better than the previously simulated values, because the 5–10 detections gained from the initial fluorophore identification by galvo-scanning provided $\sigma_0 \approx 60\text{ nm}$ right at the outset. Consideration of this σ_0 resulted in an excellent agreement between the simulated and experimental σ as a function of N (Fig. 3c). Since we cannot exclude residual movement of fluorophores on distances substantially less than the standard deviation σ_c of C_i , we can safely assert that in our experiments MINSTED reached $\sigma=2\text{--}3\text{ nm}$ with just $N=200$ detections.

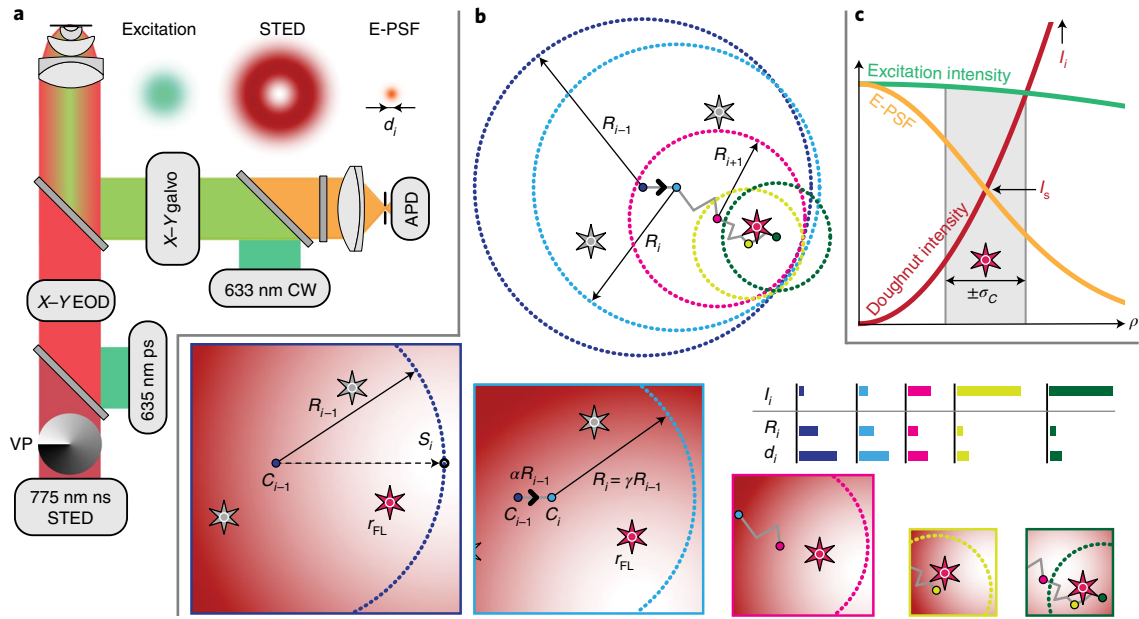


Fig. 1 | Principles of MINSTED localization. **a**, STED setup with co-aligned pulsed lasers for excitation and STED at 635 and 775 nm, respectively, and a vortex phase plate (VP) for helical phase modulation converting the STED beam into a doughnut; the inserts sketch the excitation and STED probability in the lens focal plane, along with that of the fluorescence (E-PSF). The 633 nm CW laser was used for fluorophore pre-identification in the focal plane, while the X-Y galvo unit also maintained the optical conjugation of the confocal avalanche photodiode (APD) detector to the centre C_i of the circular scan performed by the electro-optical lateral deflector (X-Y EOD). **b**, The active fluorophore (red among grey stars), located at unknown position r_{FL} , was localized by circular X-Y scans. For each photon detection i , the centre C_i was shifted by a fraction α of the radius R_i toward the doughnut minimum S_i . Simultaneously, R_i and the FWHM d_i of the E-PSF were scaled by $\gamma < 1$. The centre C_i thus converges to the fluorophore position (grey line) as indicated in the lower panels that also sketch relevant parts of the doughnut for some detections during the homing-in process. Once a minimum radius R_{min} (yellow) is reached, only C_i is updated and the localization terminated after the fluorophore becomes inactive (N detections). The column diagrams illustrate the decrease of R_i and of d_i with increasing doughnut intensity I_i . **c**, Normalized probability of excitation (green) and fluorescence detection (E-PSF, yellow) as a function of radial distance ρ from the focal point, along with a non-normalized intensity profile of the STED beam doughnut (red). Although I_i is constantly increased during the localization to sharpen the E-PSF, the intensity experienced by the fluorophore remains about I_s within the $\pm\sigma_C$ position range of the centre positions C_i highlighted in grey.

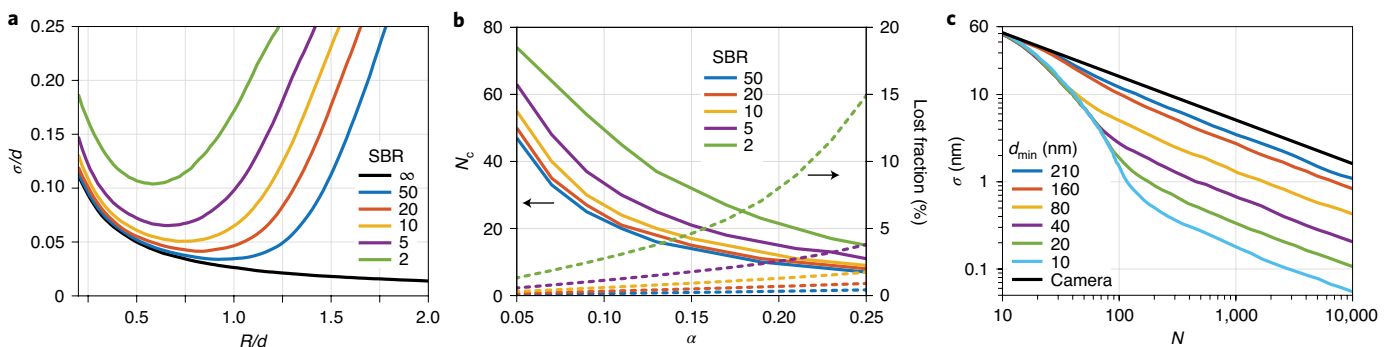


Fig. 2 | Simulation of MINSTED localization with $N = 100$ detected photons. **a**, Localization precision σ with different ratios of scan radius R to FWHM d of the STED microscope's Gaussian E-PSF with the SBR as the parameter. While the hypothetical infinite SBR case calls for R maximization (black line), the presence of the background enforces $0.5d \leq R \leq d$. For large R the information provided by the detection of a single photon is masked by the background, whereas for a small R it is masked by the many other photon detections connected with an E-PSF maximum of finite d . In the localization process, the values of R and d are updated for every photon count i to the specific values R_i and d_i , respectively. **b**, Detections N_c necessary until the distribution of scan centre positions C_i converges to a final distribution (with static d); percentage of simulations with centre positions C_i further than d away from the fluorophore and hence classified as lost. **c**, Localization precision σ as a function of total number of detections N with d_{min} as the parameter.

Next, we measured σ obtained after d_{min} had been reached. Since the total number of detections before bleaching typically exceeded 1,000 per fluorophore, we split the resultant C_i traces into segments of different sizes M and calculated the standard deviations σ_M of the localization in these segments. To avoid boundary artefacts, we explored the

range $N - N_c > 25$. In agreement with the simulations, the measurements again followed the $1/\sqrt{N - N_c + 1}$ relation and the linear dependence on d_{min} (Fig. 3d and Supplementary Fig. 5). To highlight the latter, we also scaled the measured σ_M to $d_{min} = 200$ nm so that any difference from the linear dependence could be noticed in the overlay.

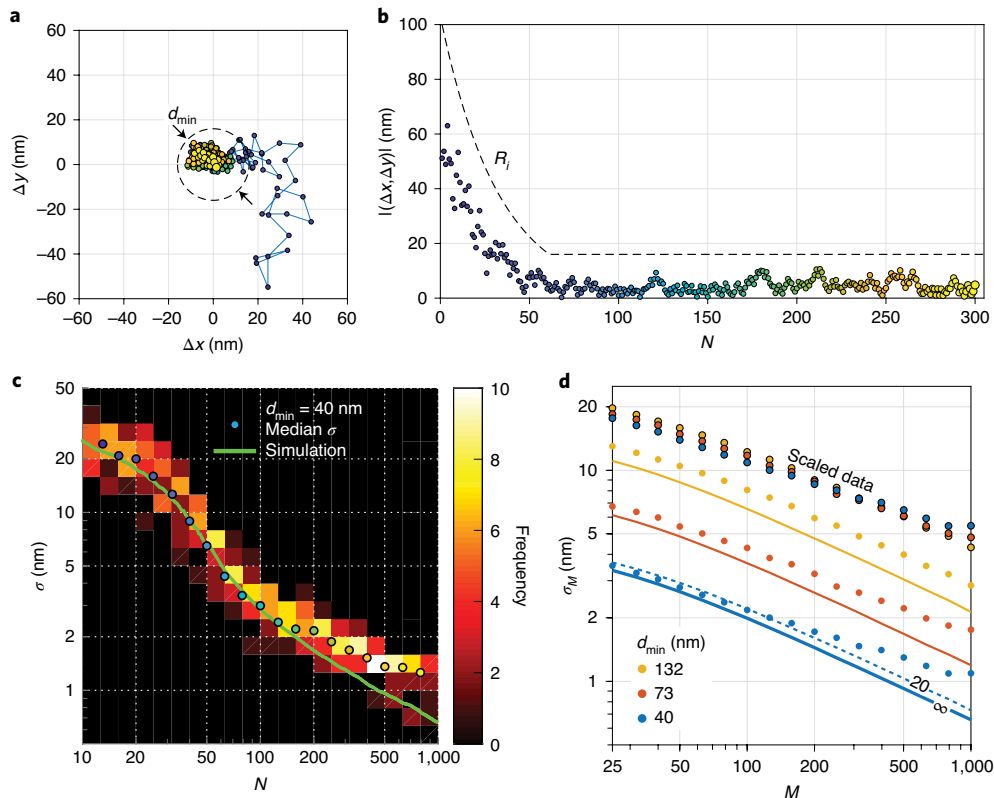


Fig. 3 | MINSTED localization of single fluorophores. **a**, Localization trace from the first $i=1$ (blue) to the last detection $i=300$ (yellow) with the final scan circle (dashed line) around the estimated (x,y) position. **b**, Scan radius R_i (dashed line), distance $(\Delta x, \Delta y)$ from the final estimated position to the scan centre C_i (points) from $i=1$ (blue) to $i=300$ (yellow) detections. **c**, Histogram of precision σ of grouped localization traces and their median σ showing good agreement with simulation. **d**, Measured precision σ_M (derived from segments of M detections measured after d_{\min} had been reached) showing how the increase in STED doughnut power improves the precision in linear proportion to d_{\min} , which is also confirmed by the overlap of data points when all points are scaled to $d_{\min}=200$ nm for comparison. Solid lines show simulation results for $\text{SBR} = \infty$, the dashed line for $\text{SBR} = 20$ as indicated. Note the logarithmic display in **c** and **d**.

At $\sigma < 3$ nm, the measured σ deviates from the simulations as before. However, the data show that at $d_{\min} = 40$ nm, 1,000 detected photons yield molecule-size precisions $\sigma \approx 1$ nm. If residual movements of the stage or the fluorophore could be avoided, ~ 500 detections at $\text{SBR} = 20$ would suffice for $\sigma \leq 1$ nm. Indeed, comparison of the measured precision with that simulated for the ideal $\text{SBR} = \infty$ case shows improved agreement for smaller d_{\min} , indicating that the STED doughnut not only improves the information of the detected photons by confining their origin in space, but also by suppressing the background.

MINSTED fluorescence nanoscopy in cells. The separation of emitters in MINSTED nanoscopy requires fluorophores that can be transferred from a lasting state that is non-responsive to excitation light into a semi-stable state leading to fluorescence upon excitation. Silicon rhodamine (SiR) fluorophores with two unsubstituted photoactivatable *ortho*-nitrobenzyl (ONB) caging groups proved suitable for MINSTED because photoactivation at the 355 nm wavelength activated the SiR fluorophores enabling STED at a wavelength of 775 nm with no concurrent two-photon activation¹³.

To demonstrate its potential for biological imaging, we used MINSTED nanoscopy to image the mitochondrial inner membrane protein Mic60 in chemically fixed human cells¹⁴. The mitochondrial inner membrane folds into cristae, large membrane invaginations that increase the surface area of this membrane. Mic60 is enriched at crista junctions¹⁵, which are round or slit-like structures that connect the crista membranes with the mitochondrial inner boundary membrane that is parallel to the mitochondrial outer membrane.

Immunolabelling of cultured human U-2 OS cells with ONB-2SiR-labelled primary anti-Mic60 antibodies allowed us to compare MINSTED nanoscopy with confocal and STED images recorded after activation of ONB-2SiR (Fig. 4). Confocal microscopy was unable to provide details of the distribution of Mic60 in the mitochondria (Fig. 4a). Featuring a resolution of about 60 nm, the recorded STED images demonstrated a clustering of Mic60, but failed to resolve individual emitters (Fig. 4b). By contrast, MINSTED accomplished this feat (Fig. 4c,d), recording 1.8–2.4 raw localizations per second and resolving individual fluorophores with a median precision of $\sigma = 2.1$ nm (Supplementary Fig. 6).

Figure 4c,d was reconstructed from 49% of the raw localizations; 48% of the raw localizations were dropped because they were too dim ($N - N_c < 250$) and a further 3% were dropped because they showed an excessive σ , that is they did not converge. We observed that consecutive multiple localizations of the same fluorophore were limited to a few percent of all localizations: 56% of the *raw* localizations were observed within two scans of the image area from the previous localization, but only 4.7% of those were located within less than 20 nm distance. Although 6.3% of the filtered localizations were observed within two scans and were within 20 nm of the previous localization, only 1% fell within the < 2 nm distance. Hence, we can conclude that only a few fluorophores were localized and rendered multiple times.

For this study, we relied on primary antibodies that were labelled by azide modification of the glycans on the antibody heavy chain, so that the distance between the antibody binding site and the fluoro-

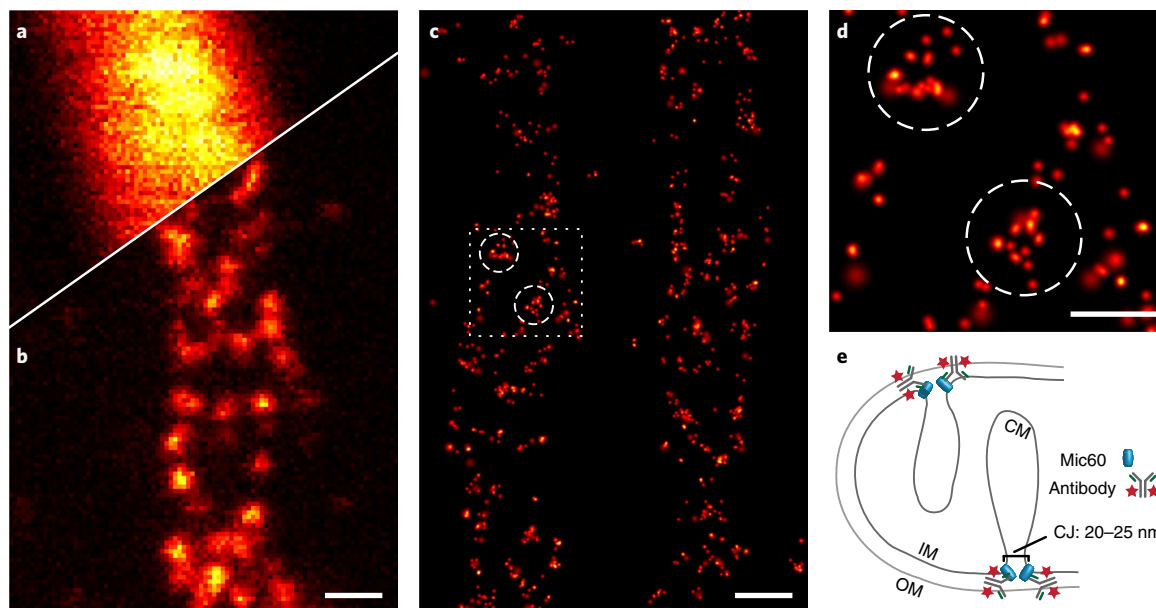


Fig. 4 | MINSTED nanoscopy of mitochondrial protein Mic60. **a, b** Confocal (**a**) and STED (**b**) images with $d \approx 60$ nm of the same mitochondrion taken after simultaneous activation of all fluorophores. **c**, MINSTED nanoscopy image of similar mitochondria resolving the Mic60 clusters (3,607 localizations acquired in 33 min, 1,766 localizations with $N - N_c \geq 200$ detections and $d_{\min} = 54$ nm). **d**, Excerpts of data as indicated in **c**. **e**, Schematic of the presumed localization of Mic60 in the mitochondrial inner membrane. IM, inner membrane; OM, outer membrane; CM, crista membrane; CJ, crista junction. Scale bars: **a–c**, 200 nm; **d**, 100 nm.

phore was as small as 6–10 nm (PDB ID code: 1HZH (ref. 16)). The localization precision of individual fluorophores was three times higher than this distance, highlighting the limits set by the labels on extracting biological information at the single-digit nanoscale. Since fluorescence microscopy cannot reveal anything but the fluorophores in the sample, our results show that MINSTED reaches the conceptual limits of this imaging modality. Nevertheless, our two-dimensional MINSTED data provide valuable insights about the nanoscale distribution of Mic60 in mitochondria. We repeatedly recorded a circular arrangement of Mic60 in mitochondria using MINSTED (Fig. 4d), which is in excellent agreement with the current understanding of Mic60 forming small ring-like assemblies at cristae junctions¹⁷. With future three-dimensional implementations of MINSTED, complex structures such as those found in the mitochondrial inner membrane should be accessible in detail.

Discussion

Under the provision that adjacent fluorophores are sequentially active and hence separable, MINSTED nanoscopy can deliver molecule-scale resolution like its MINFLUX counterpart¹⁸. However, in MINSTED a resolution of $\sigma = 2$ nm or $d = 4.7$ nm is attained with a total of just 200 detections, in close agreement with the simulations. The reason is that the STED doughnut suppresses spurious signal from the neighbourhood of the targeted fluorophore, rendering the MINSTED images (Fig. 4) almost background-free.

Another strength of the described MINSTED implementation is that the photon-by-photon update of the localization removes virtually all bias due to inaccurate assumptions on the background or doughnut shape. Furthermore, the unequivocal repositioning of the doughnut centre in the right direction allows for an aggressive reduction of d_i and hence also of N . Once d_{\min} is reached, each subsequent photon refines the scan centre C_i and lowers the uncertainty on the position estimate \bar{C}_N . In fact, continuous updating of C_i tracks the fluorophore until it bleaches or switches off. As it provides the most photon-efficient localization so far, MINSTED will also be useful for tracking rapidly moving emitters. Our MINSTED

protocol can be further refined by dynamically adapting R_i/d_i in response to the background.

Besides, MINSTED is able to single out individual fluorophores if any other active fluorophore is at least $d_i + (1 + 2\alpha)R_i$ away; with our typical parameters this distance amounts to about $1.8d_i$. In contrast to MINFLUX, for MINSTED only a sub-diffraction region around the targeted fluorophore must remain free of other active fluorophores when $d_{\min} \ll d_0$. Evidently, future MINSTED research will include multiple colour channels using spectrally shifted fluorophores, three-dimensional recordings using three-dimensional doughnuts and technically more sophisticated implementations with adaptable doughnut arrays or sets of standing waves (also known as structured illumination).

The selective spatial targeting of the doughnut minimum constitutes a fundamental difference from earlier applications of STED microscopy to single-fluorophore localization, whereby the doughnut is scanned laterally across the focal plane to map out the E-PSF centroid rendered by each fluorophore^{12,19,20}. This established combination of single fluorophores and STED works reliably only for bleaching-resilient emitters, such as nitrogen-vacancy centres¹⁹, or for low doughnut intensities, because the intense doughnut crest usually bleaches the fluorophore before the whole E-PSF is acquired. Moreover, precise rendering of the E-PSF is typically compromised by the tendency of the fluorophores to blink. In MINSTED, although the doughnut intensity is constantly increased, bleaching and blinking aggravation is avoided. For attaining nanometre spatial resolution, MINSTED nanoscopy requires neither intensities of $>10^4 I_s$, nor doughnut minima of $<1\%$ since the on/off separation of spatially tight fluorophores is not performed by the doughnut but by the on/off switching of individual fluorophores. However, the doughnut brings about the advantage that it additionally assists the on/off separation at sub-diffraction length scales.

Seeking a fluorescence minimum, as in MINFLUX, has a conceptual advantage over localizing with a Gaussian E-PSF unless the background comes into play. When narrowing the search range by increasing the doughnut intensity, the excitation doughnut in MINFLUX⁸ is more prone to worsening background levels than is

the STED doughnut in MINSTED. MINFLUX trades off the SBR for a smaller fluorophore-to-doughnut distance, as long as the deterioration in localization precision due to the lower SBR is overcompensated by the improvement gained from the smaller distance. In MINSTED, however, the fluorophore is exposed to nearly the same excitation and STED intensity throughout the process, irrespective of the fluorophore-to-doughnut distance. As a result, compared with MINFLUX, MINSTED experiences substantially reduced variations in the fluorescence signal and SBR. In fact, we found that higher STED doughnut intensities at 775 nm keep the background low, even for small d_{\min} values. For this reason, MINSTED is currently on a par with or even outperforms MINFLUX in key aspects.

In most of our MINSTED imaging, d_{\min} was not reduced below 40 nm because a higher STED beam power would have increasingly destabilized the system by heating. Requiring a STED beam is an added complexity of MINSTED compared with MINFLUX, but the precision σ values achievable with either of the two molecule-scale resolution approaches will ultimately depend on the background. In any case, by featuring excellent background suppression, MINSTED should become substantially faster and handle higher densities of fluorophores than most super-resolution methods in the future.

Finally, the introduction of MINSTED underscores that the idea of optically injecting a movable reference coordinate is transformative in the art of the localization of emitters. In conjunction with on/off state separation, MINSTED enlarges the scope of far-field fluorescence nanoscopy with molecule-size resolution, which, due to its 100-fold improvement over the diffraction limit, is poised to break new ground.

Online content

Any methods, additional references, Nature Research reporting summaries, source data, extended data, supplementary information, acknowledgements, peer review information; details of author contributions and competing interests; and statements of data and code availability are available at <https://doi.org/10.1038/s41566-021-00774-2>.

Received: 30 October 2020; Accepted: 1 February 2021;

Published online: 15 March 2021

References

- Hell, S. W. & Wichmann, J. Breaking the diffraction resolution limit by stimulated emission: stimulated-emission-depletion fluorescence microscopy. *Opt. Lett.* **19**, 780–782 (1994).
- Klar, T. A., Jakobs, S., Dyba, M., Egner, A. & Hell, S. W. Fluorescence microscopy with diffraction resolution barrier broken by stimulated emission. *Proc. Natl Acad. Sci. USA* **97**, 8206–8210 (2000).
- Westphal, V. & Hell, S. W. Nanoscale resolution in the focal plane of an optical microscope. *Phys. Rev. Lett.* **94**, 143903 (2005).
- Hell, S. W. Far-field optical nanoscopy. *Science* **316**, 1153–1158 (2007).
- Danzl, J. G. et al. Coordinate-targeted fluorescence nanoscopy with multiple off states. *Nat. Photonics* **10**, 122–128 (2016).
- Betzig, E. et al. Imaging intracellular fluorescent proteins at nanometer resolution. *Science* **313**, 1642–1645 (2006).
- Rust, M. J., Bates, M. & Zhuang, X. Sub-diffraction-limit imaging by stochastic optical reconstruction microscopy (STORM). *Nat. Methods* **3**, 793–796 (2006).
- Balzarotti, F. et al. Nanometer resolution imaging and tracking of fluorescent molecules with minimal photon fluxes. *Science* **355**, 606–612 (2017).
- Levi, V., Ruan, Q., Kis-Petikova, K. & Gratton, E. Scanning FCS, a novel method for three-dimensional particle tracking. *Biochem. Soc. Trans.* **31**, 997–1000 (2003).
- Göttfert, F. et al. Strong signal increase in STED fluorescence microscopy by imaging regions of subdiffraction extent. *Proc. Natl Acad. Sci. USA* **114**, 2125–2130 (2017).
- Heine, J. et al. Adaptive-illumination STED nanoscopy. *Proc. Natl Acad. Sci. USA* **114**, 9797–9802 (2017).
- Kasper, R. et al. Single-molecule STED microscopy with photostable organic fluorophores. *Small* **6**, 1379–1384 (2010).
- Weber, M. et al. Photoactivatable fluorophore for STED microscopy and bioconjugation technique for hydrophobic labels. *Chem. Eur. J.* **27**, 451–458 (2021).
- Pfanner, N. et al. Uniform nomenclature for the mitochondrial contact site and cristae organizing system. *J. Cell Biol.* **204**, 1083–1086 (2014).
- Jans, D. C. et al. STED super-resolution microscopy reveals an array of MINOS clusters along human mitochondria. *Proc. Natl Acad. Sci. USA* **110**, 8936–8941 (2013).
- Saphire, E. O. et al. Crystal structure of a neutralizing human IgG against HIV-1: a template for vaccine design. *Science* **293**, 1155–1159 (2001).
- Pape, J. K. et al. Multicolor 3D MINFLUX nanoscopy of mitochondrial MICOS proteins. *Proc. Natl Acad. Sci. USA* **117**, 20607–20614 (2020).
- Gwosch, K. C. et al. MINFLUX nanoscopy delivers 3D multicolor nanometer resolution in cells. *Nat. Methods* **17**, 217–224 (2020).
- Rittweger, E., Han, K. Y., Irvine, S. E., Eggeling, C. & Hell, S. W. STED microscopy reveals crystal colour centres with nanometric resolution. *Nat. Photonics* **3**, 144–147 (2009).
- Puthukodan, S., Murtezi, E., Jacak, J. & Klar, T. A. Localization STED (LocSTED) microscopy with 15 nm resolution. *Nanophotonics* **9**, 783–792 (2020).

Publisher's note Springer Nature remains neutral with regard to jurisdictional claims in published maps and institutional affiliations.



Open Access This article is licensed under a Creative Commons Attribution 4.0 International License, which permits use, sharing, adaptation, distribution and reproduction in any medium or format, as long as you give appropriate credit to the original author(s) and the source, provide a link to the Creative Commons license, and indicate if changes were made. The images or other third party material in this article are included in the article's Creative Commons license, unless indicated otherwise in a credit line to the material. If material is not included in the article's Creative Commons license and your intended use is not permitted by statutory regulation or exceeds the permitted use, you will need to obtain permission directly from the copyright holder. To view a copy of this license, visit <http://creativecommons.org/licenses/by/4.0/>.

© The Author(s), under exclusive licence to Springer Nature Limited 2021

Methods

MINSTED setup. The setup consists of an epi-fluorescence microscope with a dual-channel confocal laser scanning system using a Leica $\times 100/1.4\text{NA}$ oil-immersion objective lens. Two galvanometer mirrors and pupil relay optics allowed for rapid beam scanning over a quadratic sample area of about $100\ \mu\text{m}$ extent (x, y). A continuous-wave (CW) HeNe laser provided fluorescence excitation at the $633\ \text{nm}$ wavelength for rapid overview. A single-photon counting module detected the fluorescence light in the $650\text{--}750\ \text{nm}$ range. A confocal pinhole with a diameter of 0.5 Airy units blocked out-of-focus light. For STED microscopy and single-molecule localization, an additional illumination path without moving parts was implemented. Two electro-optic deflectors with pupil relay systems featured beam scanning within a square image area of about $2.6\ \mu\text{m}$ extent. A $635\ \text{nm}$ pulsed diode laser delivered excitation pulses of about $100\ \text{ps}$ duration, whereas a $775\ \text{nm}$ pulsed fibre laser provided STED pulses of about $1\ \text{ns}$ duration. A vortex phase plate imprinted a 2π phase ramp on the phase front of the STED beam and a polarization controller converted it to circular polarization to shape the STED beam into a doughnut profile. A laser at $355\ \text{nm}$ wavelength illuminated the STED image area to photoactivate the fluorophores. All laser beam powers were modulated with short response times of several microseconds. The sample was mounted on an $X\text{--}Y\text{--}Z$ -piezo positioning stage whose position was locked by a sample-tracking system. For this purpose, the position of fiducial markers was monitored with infrared light from a super-luminescent light-emitting diode and fast CMOS cameras. The tracking system issued the closed-loop control signals to cancel the sample drift. The MINSTED microscope was fully controlled by an FPGA board and a custom control program. Our software ran diffraction-limited overview scans using only the galvanometer beam scanner as well as high-resolution STED image scans and single-molecule localizations using both scanners synchronously. For STED imaging and localization, a time gate blocked the early fluorescence detections during the STED pulses. A graphical user interface allowed definition of the measurement parameters and retrieval of the measurement results.

Immobilization of Atto 647N fluorophores. Atto 647N molecules were sparsely distributed and immobilized on cover slides as described in ref. ⁸. A flow channel, consisting of a cleaned coverslip glued to a microscope slide with double-sided scotch tape, was rinsed with $100\ \mu\text{l}$ phosphate-buffered saline (PBS; $137\ \text{mM}$ NaCl, $2.7\ \text{mM}$ KCl, pH 7.4). The channel was filled with $15\ \mu\text{l}$ biotinylated bovine serum albumin (biotinylated BSA; A8549, Sigma Aldrich) $0.5\ \text{mg}\ \text{ml}^{-1}$ in PBS. After 4 min of incubation, the channel was flushed with $100\ \mu\text{l}$ PBS and filled with $15\ \mu\text{l}$ streptavidin (11721666001, Sigma Aldrich) $0.5\ \text{mg}\ \text{ml}^{-1}$ in PBS. After an incubation time of 4 min, the channel was flushed with $100\ \mu\text{l}$ PBS and filled with $15\ \mu\text{l}$ of $200\ \text{pM}$ hybridized biotin-DNA/Atto647N-DNA in PBS⁸. After 4 min of incubation, the channel was flushed with $100\ \mu\text{l}$ PBS and filled with 0.01% (w/v) poly-L-lysine (P8920, Sigma Aldrich) in PBS for 10 min. After flushing with $100\ \mu\text{l}$ PBS, the channel was filled with $15\ \mu\text{l}$ freshly diluted silica shelled silver nanoplates (SPSH1050, nanoComposix) $2.5\ \mu\text{g}\ \text{ml}^{-1}$ in PBS. After 10 min of incubation the channel was flushed with PBS again, filled with $15\ \mu\text{l}$ ROXS buffer²¹ and sealed with epoxy glue (Hysol, Locktite).

Antibody conjugation. The labelling of the antibody using glycan modification and strain-promoted click chemistry, together with the synthesis of the dye used was as described previously¹³. In short, the rabbit monoclonal antibody (ab245764, Abcam) was modified with azide groups using a commercial enzyme system (GlyClick, Genovis). After the modification, $250\ \mu\text{g}$ antibody in $200\ \mu\text{l}$ Tris-buffered saline (TBS; $20\ \text{mM}$ Tris HCl, $150\ \text{mM}$ NaCl, pH 7.6) was mixed with $50\ \mu\text{l}$ dimethylformamide containing $50\ \mu\text{g}$ dibenzylcyclooctyne dye and stirred overnight. The free dye was removed via phase extraction by adding $600\ \mu\text{l}$ distilled water, $90\ \mu\text{l}$ saturated $(\text{NH}_4)_2\text{SO}_4$ solution and $900\ \mu\text{l}$ *tert*-butanol, vortexing and separating the phases after a short centrifugation pulse. The aqueous phase (about $600\ \mu\text{l}$) was diluted using $600\ \mu\text{l}$ TBS. The labelled antibodies were aliquoted and stored at -20°C .

Cell labelling. The human osteosarcoma cell line U-2 OS was obtained from the European Collection of Authenticated Cell Cultures (ECACC; cat. no. 92022711, lot 17E015) and cultivated on coverslips in McCoy's medium (Thermo Fisher Scientific) supplemented with 10% (v/v) fetal bovine serum (Thermo Fisher Scientific), 1% (v/v) sodium pyruvate (Sigma Aldrich) and penicillin-streptomycin (Sigma Aldrich). The cells were fixed using 8% (w/v) paraformaldehyde in PBS for 5 min, permeabilized with 0.5% (w/v) Triton X-100 for 5 min and quenched with $100\ \text{mM}$ NH_4Cl in PBS for 5 min. The fixed cells were washed with PBS, blocked with 2% (w/v) BSA in PBS and treated with the primary antibody in the same buffer for 1 h, washed with 2% (w/v) BSA in PBS, treated with a secondary goat anti-rabbit antibody conjugated with Alexa 647 as counterstain for MINSTED and washed with PBS. The cells were incubated with freshly diluted silica shelled silver nanoplates (SPSH1050, nanoComposix) $2.5\ \mu\text{g}\ \text{ml}^{-1}$ in PBS for 10 min and washed with PBS again.

Cell imaging. The confocal and STED images were recorded using a commercial Abberior Instruments Expert Line microscope equipped with a $775\ \text{nm}$ $40\ \text{MHz}$ STED laser and a $640\ \text{nm}$ excitation laser after activation with a spectrally broad

$405\ \text{nm}$ light-emitting diode as described in ref. ¹³. For MINSTED, the labelled cells were incubated with freshly diluted silica shelled silver nanoplates in PBS for 20 min and then washed with PBS. The samples were mounted with buffer ($20\ \text{mM}$ HEPES, $150\ \text{mM}$ NaCl, pH 7) using Twinstil (Picodent). Before MINSTED, the cells were selected based on the counterstain signal and the Alexa 647 dyes were bleached using low-power STED light. The localization routine was started without the excitation laser to equilibrate the temperature in the immersion oil and sample, which were warmed up by the STED laser. After 10 s, the excitation laser was enabled and the caged dyes were sparsely activated using $355\ \text{nm}$ light when searching for another active fluorophore. Over the duration of the measurement, the ultraviolet laser power was slowly increased to keep the activation rate constant. The imaging was stopped when no further molecules could be activated.

Data analysis. The localizations were analysed based on the centre positions $C_{i \geq N_c}$ at d_{min} . The localizations were further selected with a maximum filter on the standard deviation σ_c of the C_i , together with a minimum filter on the number of detected photons N . The precision of each localization was estimated as described in the Supplementary Information and validated by simulations (Supplementary Fig. 3). The image was rendered with the estimated precision lower-bounded to $3\ \text{nm}$.

Reporting summary. Further information on research design is available in the Nature Research Reporting Summary linked to this article.

Data availability

The data that support the plots within this paper and other findings of this study are available from the corresponding author upon reasonable request. Sample data to generate Figs. 2b and 3a,b,d; Supplementary Figs. 1–3 and 5; and Supplementary Videos 1 and 2 is available in the supplementary archive.

Code availability

The simulation code to generate Figs. 2b and 3a,b,d; Supplementary Fig. 1–3, 5; and Supplementary Videos 1 and 2 is available in the supplementary archive.

References

- Vogelsang, J. et al. A reducing and oxidizing system minimizes photobleaching and blinking of fluorescent dyes. *Angew. Chem. Int. Ed.* **47**, 5465–5469 (2008).

Acknowledgements

We thank R. Schmidt (now Abberior Instruments GmbH) for contributions to early versions of the software and the setup. We are also grateful to F. Werner, T. Staudt and J. Keller-Findeisen for discussions on the localization statistics and for complementary calculations, as well as to K. Gwosch and F. Balzarotti for discussions about MINFLUX. T. Khan, H. Shojai and V. N. Belov supported us with the design and synthesis of fluorophores. We acknowledge E. Rothermel for preparing samples, T. Gilat and M. Roose for technical support. Funding by the German Federal Ministry of Education and Research (BMBF) in the project 'New fluorescence labels for protected- and multi-colour-STED microscopy (STEDlabel)' (no. 13N14122, to S.W.H.) and by the European Research Council Advanced Grant 835102 (to S.J.) is gratefully acknowledged. T.S.M. was supported by a Fulbright Research scholarship.

Author contributions

M.L. and M.W. designed and implemented the specific localization algorithm and performed the simulation analysis with critical input from S.W.H. The setup was built by M.L. and M.W., and M.L. wrote the software, including the real-time control of the setup. M.W. prepared the samples and performed the measurements. S.S. provided mitochondria samples. A.N.B. synthesized dyes for preliminary tests. T.S.M. explored various labelling techniques. M.W. and M.L. analysed the data with feedback from S.W.H. The fundamentals of the MINSTED concept were outlined by S.W.H., who also initiated and supervised its exploration. S.W.H., M.L. and M.W. wrote the manuscript. All authors contributed to the manuscript and the supplementary information either through discussions or directly.

Competing interests

S.W.H. benefits from intellectual property on the described localization and nanoscopy owned by the Max Planck Society.

Additional information

Supplementary information The online version contains supplementary material available at <https://doi.org/10.1038/s41566-021-00774-2>.

Correspondence and requests for materials should be addressed to S.W.H.

Peer review information *Nature Photonics* thanks the anonymous reviewers for their contribution to the peer review of this work.

Reprints and permissions information is available at www.nature.com/reprints.

Reporting Summary

Nature Research wishes to improve the reproducibility of the work that we publish. This form provides structure for consistency and transparency in reporting. For further information on Nature Research policies, see our [Editorial Policies](#) and the [Editorial Policy Checklist](#).

Statistics

For all statistical analyses, confirm that the following items are present in the figure legend, table legend, main text, or Methods section.

n/a Confirmed

- The exact sample size (n) for each experimental group/condition, given as a discrete number and unit of measurement
- A statement on whether measurements were taken from distinct samples or whether the same sample was measured repeatedly
- The statistical test(s) used AND whether they are one- or two-sided
Only common tests should be described solely by name; describe more complex techniques in the Methods section.
- A description of all covariates tested
- A description of any assumptions or corrections, such as tests of normality and adjustment for multiple comparisons
- A full description of the statistical parameters including central tendency (e.g. means) or other basic estimates (e.g. regression coefficient) AND variation (e.g. standard deviation) or associated estimates of uncertainty (e.g. confidence intervals)
- For null hypothesis testing, the test statistic (e.g. F , t , r) with confidence intervals, effect sizes, degrees of freedom and P value noted
Give P values as exact values whenever suitable.
- For Bayesian analysis, information on the choice of priors and Markov chain Monte Carlo settings
- For hierarchical and complex designs, identification of the appropriate level for tests and full reporting of outcomes
- Estimates of effect sizes (e.g. Cohen's d , Pearson's r), indicating how they were calculated

Our web collection on [statistics for biologists](#) contains articles on many of the points above.

Software and code

Policy information about [availability of computer code](#)

Data collection

Data analysis

For manuscripts utilizing custom algorithms or software that are central to the research but not yet described in published literature, software must be made available to editors and reviewers. We strongly encourage code deposition in a community repository (e.g. GitHub). See the Nature Research [guidelines for submitting code & software](#) for further information.

Data

Policy information about [availability of data](#)

All manuscripts must include a [data availability statement](#). This statement should provide the following information, where applicable:

- Accession codes, unique identifiers, or web links for publicly available datasets
- A list of figures that have associated raw data
- A description of any restrictions on data availability

Field-specific reporting

Please select the one below that is the best fit for your research. If you are not sure, read the appropriate sections before making your selection.

Life sciences Behavioural & social sciences Ecological, evolutionary & environmental sciences

For a reference copy of the document with all sections, see [nature.com/documents/nr-reporting-summary-flat.pdf](https://www.nature.com/documents/nr-reporting-summary-flat.pdf)

Life sciences study design

All studies must disclose on these points even when the disclosure is negative.

Sample size	<i>Describe how sample size was determined, detailing any statistical methods used to predetermine sample size OR if no sample-size calculation was performed, describe how sample sizes were chosen and provide a rationale for why these sample sizes are sufficient.</i>
Data exclusions	No data were excluded from the analysis unless specified in the manuscript.
Replication	All light microscopy experiments were done at least in triplicate.
Randomization	No extra randomization was required as the cells used for imaging showed similar labeling of the Mic60 protein.
Blinding	Proof-of-principle experiments were performed on randomly located single molecules. All other experiments were performed on samples whose detailed features were unknown. Simulations and calculations were used as controls.

Reporting for specific materials, systems and methods

We require information from authors about some types of materials, experimental systems and methods used in many studies. Here, indicate whether each material, system or method listed is relevant to your study. If you are not sure if a list item applies to your research, read the appropriate section before selecting a response.

Materials & experimental systems		Methods	
n/a	Involvement in the study	n/a	Involvement in the study
<input type="checkbox"/>	<input checked="" type="checkbox"/> Antibodies	<input checked="" type="checkbox"/>	<input type="checkbox"/> ChIP-seq
<input type="checkbox"/>	<input checked="" type="checkbox"/> Eukaryotic cell lines	<input checked="" type="checkbox"/>	<input type="checkbox"/> Flow cytometry
<input checked="" type="checkbox"/>	<input type="checkbox"/> Palaeontology and archaeology	<input checked="" type="checkbox"/>	<input type="checkbox"/> MRI-based neuroimaging
<input checked="" type="checkbox"/>	<input type="checkbox"/> Animals and other organisms		
<input checked="" type="checkbox"/>	<input type="checkbox"/> Human research participants		
<input checked="" type="checkbox"/>	<input type="checkbox"/> Clinical data		
<input checked="" type="checkbox"/>	<input type="checkbox"/> Dual use research of concern		

Antibodies

Antibodies used	Anti-Mitofilin antibody [EPR8749], Rabbit, monoclonal, abcam, ab245764
Validation	Anti-Mitofilin antibody [EPR8749], Rabbit, monoclonal, abcam, ab245764. The antibody was validated on Mic60/mitofilin knock out cell lines.

Eukaryotic cell lines

Policy information about [cell lines](#)

Cell line source(s)	U-2 OS (ECACC 92022711): ECACC, Porton Down, Salisbury, UK; Cat no. 92022711, Lot. 17E015
Authentication	Cells were checked for morphology by light microscopy.
Mycoplasma contamination	Cell culture was regularly tested for mycoplasma contamination by PCR. Additionally, stainings with DAPI against DNA were used to exclude extranuclear DNA.
Commonly misidentified lines (See ICLAC register)	n/a

3. Discussion

The combination of STED and single molecule localization has been demonstrated for non-switchable emitters like organic fluorophores [16] or nitrogen vacancy centers in diamond [14]. To use this combination for imaging applications, an emitter with a long lasting dark state is needed that is unaffected by the STED light. The switching ability of the fluorophore in combination with good applicability in STED microscopy and high molecular brightness excludes most of the commonly used fluorophores for STED microscopy or single molecule localization microscopy. All dyes routinely used in STED microscopy are non-switchable, and the switchable dyes used for PALM or STORM microscopy are mostly un-stable in STED microscopy. The most used dye for STORM microscopy, AlexaFluor 647, is switched into a long lasting off-state by the nucleophilic attack of a thiol on the positively charged cyanine fluorophore when it is in a triplet state. AlexaFluor 647 is generally unsuitable for STED microscopy due to high bleaching induced by STED light already at moderate intensity. The same switching mechanism can be used for xanthenic dyes as well, which are commonly used STED fluorophores. Different dyes have been tested with this switching mechanism, but the nucleophilic attack on the central carbon atom of a xanthenic structure is more sterically hindered than the one on the very accessible conjugated chain of cyanines. Therefore, only a subpopulation of xanthenic dyes are switched to the dark state before bleaching. Although single molecule switching was achieved in combination with STED, the loss of fluorophores due to bleaching before switching turned out to be too severe and only useable for imaging applications with overabundance of fluorophores, such as primary and secondary antibody labelled samples. The large separation between the molecule of interest and the fluorophores and the large distribution of this separation questions the meaningfulness of single-digit nanometric resolution on these types of samples. Xanthenic fluorophores can also be transformed to a photoactivatable version by introducing a diazoketone group in the center of the chromophore [17], which leads to a disturbance of the conjugated system. Through the absorption of UV photons, the

molecule undergoes a Wolff rearrangement, which results in either a fluorescent carboxy fluorophore or in a non-fluorescent by-product. Due to this unavoidable side reaction and a reported instability towards two-photon activation by STED light [17], this class of fluorophores was discarded after initial tests. Therefore, diarylethene variants were synthesized with a reduced cycloreversion quantum yield to increase the number of emitted photons per switching cycle. Although this fluorophore class was never used in STED microscopy, the thermal stability of their on- and off-state and high number of switching cycles makes them interesting fluorophores for MINSTED.

The number of emitted photons per cycle by the diarylethene variants was increased by approximately one order of magnitude, enabling the use of these fluorophores for STORM microscopy. Unexpectedly, the excitation also resulted in a sparse on-switching of the dyes. Although this behavior was not detrimental for the STORM imaging, it is an undesired action that could interfere with the imaging if more control over the on-state distribution is needed. The slow off-switching diarylethenes were tested for STED microscopy to investigate their usability for MINSTED. Although a resolution improvement was achieved, the fluorophores showed a dramatically enhanced off-switching under STED light. The slow-switching diarylethenes under STED light showed the same off-switching speed as the fast switchers. The latter were only slightly accelerated in their switching. This can be explained by the energy landscape of the off-switching mechanism as reported in [18]. The off-switching through the first excited state is hampered by an energy barrier. By exciting the electron from the first excited state to the second excited state, this energy barrier can be overcome, resulting in an enhanced off-switching quantum yield. This behavior is only observed with sequential absorption, since the relaxation after the first excitation is needed to be able to reach vibrational modes in the second excited state, which are assisting in getting over the energy barrier. A direct excitation into these vibrational modes from the ground state is not possible due to the unfavorable Franck Condon factors. Even though the enhanced off-switching inhibits the use of diarylethenes for MINSTED, this process could be used to enhance the control over these fluorophores for other microscopy techniques. Since diarylethenes were considered non-optimal for MINSTED, photoactivatable xanthenic fluorophores, which rely on photocleavable *ortho*-Nitrobenzyl groups, were synthesized for this type of microscopy.

The new fluorophore ONB-2SIR is a photoactivatable siliconrhodamine with both high stability towards two-photon activation by 775 nm STED light and good applicability

for STED microscopy. ONB-2SIR is, to our knowledge, the first photoactivatable fluorophore with negligible two-photon activation by the high intensity STED light at 775 nm wavelength. This not only enabled its use for MINSTED microscopy, but also provided valuable features for multi-channel STED measurements. A STED microscope typically supports a few color channels. A photoactivatable fluorophore like ONB-2SIR can provide an additional channel by activating and imaging it in the same spectral channel as another fluorophore, which must be imaged and photobleached beforehand. Since the caged fluorophores absorb neither the excitation nor the STED light, they are protected from bleaching. Due to its intrinsic low water solubility, the dye can only be used for antibody labelled samples, which was enabled by our new conjugation and purification protocol. A coupling to nanobodies led to precipitation. Self-labelling enzymes like Halo-, Clip- or Snap-Tag suffered from a low labelling efficiency and from the dye sticking to membranes. The use of a glycan-labelled antibody is not only beneficial to control the degree of labelling to inhibit precipitation, but it also results in a defined distance between the binding site of the antibody and the fluorophore position, which is of particular interest for localizing fluorophores with single-digit nanometric uncertainty. Primary antibodies labelled by this protocol feature a much smaller and more homogeneous spacing between the binding site and the fluorophore than what the primary and secondary antibody labelling strategy would yield. The separation is comparable to the one of proteins endogenously tagged with green fluorescent protein and sensed by a nanobody, but it is still larger than with self-labelling enzymes or directly targeting nanobodies.

The combination of single-molecule switching and STED microscopy in MINSTED achieves 2nm localization precision with only 200 detected photons in total for nearly background-free single-molecule samples and an effective PSF limited to 40nm FWHM. In cellular samples a median resolution of 2.1nm was achieved by averaging the central positions when a median number of 1238 photons were detected with the smallest effective PSF. These values highlight the strength of the concept of combining single-molecule switching with STED and the efficient single-photon update scheme, which makes MINSTED a powerful tool to achieve very high localization precision. Compared to the closely related MINFLUX microscopy, MINSTED does not draw its resolution improvement from bringing the fluorophore closer to the excitation minimum, but from sharpening the effective PSF while keeping the excitation level of the emitter and its emission rate constant. On samples with a background proportional to the excitation intensity, this results in a decreasing SBR for smaller L in MINFLUX, while the SBR stays constant in the case of MINSTED. If the

background can be suppressed by the STED light, MINSTED even improves the SBR for smaller effective PSFs as it has been observed in the case of single-molecule samples. This gives MINSTED a fundamental advantage over MINFLUX in samples with insufficient SBR or in densely labelled samples, where signal from adjacent fluorophores can be suppressed by the STED light. Additionally, the region in which only one emitter must be active to perform an unbiased localization scales down with the effective PSF in MINSTED.

Despite its theoretical advantages, a MINSTED microscope is technically more demanding, since the high intensity of the STED laser results in apparent sample displacements due to heating of the optical system and the immersion oil. Additionally, MINSTED demands switching fluorophores that are suitable for STED microscopy as well, which is a major challenge. Therefore, the selection of fluorophores applicable in MINSTED is up to now quite limited and currently ONB-2SIR achieves the best performance in MINSTED. For MINFLUX a much larger pool of fluorophores is available. As the achievable resolution of both methods ultimately depends on the specific properties of the method, the fluorophore and the sample, a direct comparison purely by the achievable resolution is rather meaningless.

Since our implementation of MINSTED is based on a photon-by-photon decision, the point where the intensities of the effective PSFs on the opposite sides of the circular scan trajectory are equal is always dragged to the emitter position. With undistorted PSFs, this point is in the center of the circular scan pattern, but can be displaced in the case of aberrated PSFs. If fixed positions were to be used as sampling points and the emitter position were calculated based on the detections at these points, the aberrated PSF could lead to localization artifacts and the effective PSF therefore should always be measured in each experiment to compensate this. By adjusting the center position with each detected photon, aberrated PSFs or a wrong estimation of the FWHM of the effective PSF including ellipticity mainly worsen the localization precision but do not lead to localization artifacts. Any offsets between the averaged center position of the scan pattern and the position of emitter due to an asymmetrical effective PSF would result in the same displacement for all localizations, which only shifts the final image. Another advantage of a single detection driven update of the center position is that the emitter is constantly tracked and therefore the same localization algorithm can be used for tracking of moving emitters.

The achieved localization uncertainty in MINSTED was substantially smaller than the sep-

aration between the antibody binding site and the fluorophores. As fluorescence microscopy can only image the fluorophores, the separation between the fluorophore and the protein or structure of interest has to be considered when interpreting the localizations. Since all commonly used labelling techniques suffer from either a low affinity, a low specificity, a large separation between label and target, or a combination of these, the labelling currently sets a limit for the practically relevant resolution in cellular samples. Therefore, new labelling techniques are needed to make full use of the resolution in cellular samples beyond the one achieved with MINSTED microscopy. The demonstrated localization precision allows to fully exploit the common labelling techniques like primary antibody, nanobody or self-labelling enzymes. The newly developed fluorophore ONB-2SIR unfortunately only supports the use of labelled primary antibody. Its use in nanobodies or self-labelling enzymes is inhibited by its low water-solubility and its stickiness.

In the case of labelled antibodies, the low water-solubility and stickiness of the dye can be circumvented by using an enzyme based glycan labelling, hydrolysis-stable strained click chemistry for attaching the fluorophore, and a phase separation purification technique to remove the lipophilic unbound dye. This new labelling and purification protocol can also be used for other low water-soluble fluorophores or for attaching other complex molecules like pharmaceuticals to antibodies. The optimization of dyes with respect to water solubility and stickiness is important during the development of fluorophores for fluorescence microscopy. By bypassing these issues with the presented labelling and purification strategy, the dyes could first be selected by their photophysical properties. Besides enabling the application of a wider range of dyes that were previously considered unsuitable due to their low water solubility or stickiness, the new protocol also allows to test dyes for their applicability in fluorescence microscopy before aiming for sufficient water solubility. Since most of the bleaching in STED microscopy occurs in the high intensity regions of the STED beam, scanning only points near the minimum of the donut beam allows to use high STED intensities and achieves a high resolution without extensive bleaching. This so-called MINFIELD concept could be used in combination with tightly confined activation to scan small areas with high resolution without bleaching the dyes outside this region and reconstructing the whole field of view by image stitching. The low water solubility of ONB-2SIR could probably be compensated by the use of more elaborate chemical modifications.

Besides the need to increase the number of emitted photons per cycle, the lacking water solubility was the main challenge in making diarylethenes applicable for single-molecule

localization microscopy. Without the new labelling and purification technique at hand at that time, the water solubility had to be increased by the addition of carboxy groups. These additions led to an increase of the cycloreversion quantum yield, which resulted in a more than tenfold-reduced number of emitted photons per cycle. Although these values were measured in methanol, the water insoluble variants could still have advantageous properties in aqueous media if attached to antibodies using the new protocol.

Although the new diarylethenes with reduced cycloreversion quantum yield and therefore higher number of emitted photons per cycle are not usable for STED microscopy due to their enhanced cycloreversion through a sequential absorption of excitation and STED light, their properties in combination with this enhanced off-switching mechanism could be very interesting for other microscopy applications. Using only single photon off-switching, diarylethenes can be either designed to emit a high number of photons or to switch off fast. The switching mechanism making use of the higher excited states could be exploited to convert per design slow switching diarylethenes rapidly into their non-fluorescent open form. This multimodal switching of diarylethenes is relatively close to the ideal situation of photoswitchable fluorophores, where activation, de-activation and fluorescence are driven by specific laser wavelengths. For example, emitters outside the region of interest could be switched effectively into the open form to reduce the background for single-molecule localization microscopy.

The main focus of this research on a microscopy method combining the strength of single-molecule localization microscopy and STED, was highly supported by the development of a fluorophore specifically designed for this microscopy technique. The development of better water-soluble photoactivatable fluorophores should enable a larger variety of labelling strategies. Besides the use of photoactivatable organic fluorophores, switchable fluorescent proteins could be used. Especially for living samples, the incorporation of fluorescent proteins is much easier compared to organic fluorophores. Since near-infrared fluorescent proteins usable with a 775 nm STED laser suffer from a low fluorescence quantum yield, a different STED laser wavelength would be required. The brightest fluorescent proteins are emitting between 470 nm and 620 nm. Therefore, a STED wavelength in the green to red is needed for these proteins.

4. Summary

The new MINSTED microscopy technique relies on localizing single emitters with STED. For this purpose different fluorophores have been developed to address the demands of MINSTED. The first class of fluorophores, diarylethenes, are photoswitchable dyes with thermodynamically stable on- and off-states. Since the excitation wavelength also drives the off-switching, the dyes were chemically modified to reduce the quantum yield of this process. This allows the fluorophores to emit more photons before switching off and together with solubilizing chemical modifications, enabled their use in STORM microscopy. Under illumination with STED light, the diarylethenes showed an accelerated off-switching, which has been shown in the literature to stem from a large cycloreversion quantum yield in the second excited state. Since this side process cannot be avoided in STED microscopy, the number of detected photons from single diarylethene molecules was low. Therefore silicon-rhodamines, a well-suited dye family for STED microscopy, was converted into a photoactivatable fluorophore by adding photocleavable groups, which forces the chromophore into its non-absorbing lactone form. The absorption of the photocleavable group was shifted into the UV to reduce the activation by two-photon absorption of the STED light. The final compound ONB-2SIR shows only a very small two-photon activation by the STED laser. This was highlighted by using the fluorophore as an additional color channel after imaging and bleaching a spectrally similar dye. To circumvent the low water-solubility of ONB-2SIR, a new conjugation and purification protocol was developed, which relies on exchanging the hydrolysis-sensitive NHS-esters during conjugation with hydrolysis-stable strained click chemistry, on enzyme-based glycan labelling and on purifying the labelled antibody by aqueous-organic phase separation. The new microscopy technique MINSTED applied ONB-2SIR to individually activate SIR and localize it with STED. Our MINSTED implementation searched for active emitters in the confocal overview scans. Upon detection of 5-10 photons, this active fluorophore was further localized with circular scans with a diameter equal to the FWHM of the effective PSF. With each detected photon, the center

position of the scan was moved towards the position of detection by a fraction of the scan radius and the STED intensity was increased, which resulted in the scan diameter being reduced as well. The reduction of the effective PSF and scan diameter was continued for each detection until a predefined minimal effective PSF and therefore minimal scan diameter was reached. For all further detections, only the center position of the circular scan was updated. The position of the emitter was estimated by averaging the center positions at minimal effective PSF. Since the position estimation was based on a much smaller effective PSF compared to conventional camera based localization, a localization precision of 2 nm was achieved with only 200 detected photons for immobilized molecules. MINSTED was used to localize ONB-2SIR attached to primary antibody against MIC60 on chemically fixed cells with a median localization precision of 2.1 nm. MINSTED not only achieves single-digit nanometric localization precision, but it is also the only localization based nanoscopy method not relying on a diffraction-limited PSF. This allows to suppress the signal from emitters nearby and to reduce the background, which increases the localization precision and reduces the probability of miss-localizations. Additionally, the resolution can be tuned all the way from diffraction-limited to single-digit nanometric by using STED and MINSTED. All these features make MINSTED a very robust nanoscopy method for achieving localization precision down to the molecular size of the fluorophore.

5. Acknowledgement

First, I would like to thank Prof. Stefan Hell for giving me the opportunity to work on this very interesting topic in his department and for his great advice and support throughout the thesis. I thank Roman Schmidt, Mark Bates and especially Marcel Leutenegger for their help within the different projects throughout my studies. I really appreciate the support by Steffen Sahl, Jan Keller-Findeisen and Volker Westphal. I am particularly grateful for the aid of Vladimir Belov, Alexey Butkevich and Jonas Bucevicius, who deeply revised my chemistry knowledge and guided me through chemical problems. Additionally, I thank Heydar Shojaei, Gyuzel Mitronova, Kakishi Uno, Grazvydas Lukinavicius and Ruta Gerasimaite for their help. The biological samples would not have been possible without the generous support by Prof. Stefan Jakobs, Stefan Stoldt, Christian Brueser, Nickels Jensen and other members of the research group of mitochondrial structure and dynamics. Special thanks go to the technical staff of the department and the chemistry facility, notably Jaydev Jethwa, Ellen Rothermel, Tanja Koenen, Rita Schmitz-Salue, Sylvia Löbermann, Marco Roose, Stefanie Kruse and Sarah Leondarakis.

Last but not least, I would like to thank my wife Rachel and my family for their everlasting support and company during my studies.

6. Supporting Information

6.1. Manuscript I: Photoswitchable Diarylethenes

Fluorescent Photoswitchable Diarylethenes for Biolabeling and Single Molecule Localization Microscopies with Optical Superresolution

Benoît Roubinet^a, Michael Weber^a, Heydar Shojaei^a, Mark Bates^a, Mariano L. Bossi^a, Vladimir N. Belov^{a*}, Masahiro Irie^{b*}, and Stefan W. Hell^{a*}

^aDepartment of Nanobiophotonics, Max Planck Institute for Biophysical Chemistry, Am Fassberg 11, 37077 Göttingen, Germany

^bResearch Center for Smart Molecules, Department of Chemistry, Rikkyo University, Nishi-Ikebukuro 3-34-1, Toshimaku, Tokyo, Japan

Supporting information

1. Abbreviations	3
2. Synthesis.....	3
2.1 Liquid chromatography	3
2.2 Preparation of boronic esters.....	4
Di- <i>tert</i> -butyl 5-bromo-2-methoxyisophthalate (S1).....	4
3,5-Di(<i>tert</i> -butoxycarbonyl)-4-methoxyphenylboronic acid pinacol ester (C).....	4
Tetra- <i>tert</i> -butyl 5-bromo-2-methoxybenzene 1,3-bis-(carbonyl- <i>N</i> -iminodiacetate) (S2).....	5
2.3 Symmetric DAE derivative	6
Compound 3	6
2.4 Asymmetric DAEs	8
General Procedure A1 (GP A1): “the first Suzuki-Miyaura cross-coupling”	10
General Procedure A2 (GP A2): “the second Suzuki-Miyaura cross-coupling”	10
General Procedure B (GP B): “Benzothiophene oxidation”	10
General Procedure C (GP C): “Cleavage of <i>tert</i> -butyl esters”	10
Compound S3b.....	11
Compound S4a	11
Compound S4b.....	12
Compound S5a	12
Compound S5b.....	13
Compound S6a	13
Compound S6b.....	14
Compound 7-Me.....	14
Compound 7-Et	15
Compound S7.....	16
Compound S8.....	16

Compound 8	17
Compound S9	17
Compound S10	18
Compound S11	18
Compound 10	19
Compound S12	20
Compound S13	20
3. Immunolabeling and fluorescence imaging	22
3.2 Photoswitching of bioconjugates.....	22
3.3 Immunolabeling protocol	22
3.4 Confocal images	23
3.5 Superresolution (PALM/STORM) imaging.....	24
3.5.1 STORM Microscope:	24
3.5.2 Detected photons per switching event.....	26
3.5.3 Photoinduced control of the amount of events per frame Fourier ring correlation analysis of the images	29
3.6 Photoswitching fatigue resistance of compounds 4-Et and 11 at the ensemble level, in methanol and aqueous buffered solutions	28
3.7 Fourier ring correlation analysis of the images	29
3.8 Imaging in "blinking buffer".....	29
4. NMR spectra and RP-HPLC traces of symmetric dimethoxy DAEs derivatives: compounds 3, 4-Me and 4-Et	30
Compound 3	30
Compound 4-Me.....	32
Compound 4-Et	34
5. NMR spectra and RP-HPLC traces of asymmetric DAEs derivatives.....	38
Compound S5a	38
Compound S5b.....	40
Compound S6a	41
Compound S6b.....	43
Compound 7-Me.....	44
Compound 7-Et	46
Compound S7	48
Compound S8	49
Compound 8	51

Compound S10	53
Compound S11	54
Compound 10	56
Compound S12	58
Compound S13	59
Compound 11	61
6. References	64

1. Abbreviations

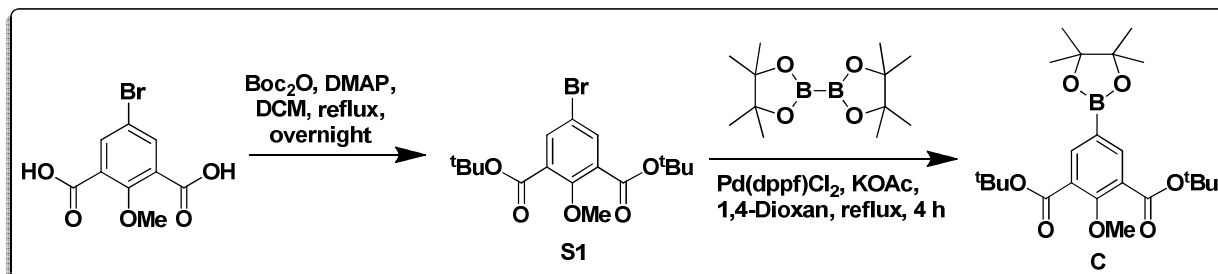
The following abbreviations are used in the text of the *Supplementary Information*: anti-parallel (*ap*), aqueous (aq.), argon (Ar), bis(pinacolato)diboron (b(pin)₂), di-*tert*-butyl dicarbonate (Boc₂O), broad (br.), closed form (CF), 3-chloroperbenzoic acid (*m*-CPBA), diarylethene (DAE), dichloromethane (DCM), 4-(*N,N*-dimethylamino)pyridine (DMAP), *N,N*-dimethylformamide (DMF), dimethyl sulfoxide (DMSO), degree of labeling (DOL), 1-ethyl-3-(3-dimethylaminopropyl)carbodiimide (EDC), electrospray ionization (ESI), ethyl acetate (EtOAc), ethanol (EtOH), high performance liquid chromatography (HPLC), high resolution mass spectrometry (HR-MS), potassium acetate (KOAc), *N*-hydroxysuccinimide (NHS), nuclear magnetic resonance (NMR), open form (OF), parallel (*p*), phosphate buffer saline (PBS), reverse phase (RP), room temperature (r.t.), saturated (sat.), 2-dicyclohexylphosphino-2',6'-dimethoxybiphenyl (SPhos), triethylamine (TEA), tetrahydrofuran (THF), trifluoroacetic acid (TFA), thin layer chromatography (TLC), ultraviolet (UV), visible (vis).

2. Synthesis

2.1 Liquid chromatography

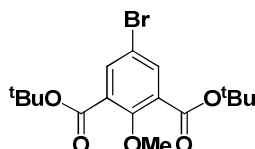
The following columns (cartridges) and solvent systems were used for analytical and preparative separations. **System A**: RP-HPLC (Eurosphere II, 100-5 C₁₈ column, 5 μm, 4.0×150 mm) with CH₃CN and 0.05% aq. TFA (pH ~ 2.0) [linear gradient from 30% to 70% of CH₃CN in 20 min] at a flow rate of 1.2 mL/min; UV-vis detection with diode array and at 254 nm (OF) and 460 nm (CF). **System B**: automated flash purification on Biotage Isolera One (ISO-1EW) device (cartridge PF-C₁₈-HC, 30 μM, with 20 g of RP-C₁₈ silica gel) with the following eluent: 0.1% aq. TFA / CH₃CN, 7:3, at a flow rate of 20 mL/min for 15 min; UV detection at 254 nm. **System C**: System A with a linear gradient from 60% to 90% of CH₃CN in 15 min at a flow rate of 1.2 mL/min. **System D**: System B with the following eluent: 0.1% aq. TFA / CH₃CN, 3:7, at a flow rate of 20 mL/min for 15 min. **System E**: System B with the following eluent: 0.1% aq. TFA / CH₃CN, 1:1, at a flow rate of 20 mL/min for 15 min. **System F**: RP-HPLC (Eurosphere II, 100-5 C₁₈ column, 5 μm, 4.0×150 mm) with CH₃CN and 0.1% aq. TFA (pH ~ 1.5) [30% ACN: 0 – 3 min, then linear gradient from 30% to 100% of CH₃CN in 12 min] at a flow rate of 1.2 mL/min; UV-vis detection with diode array and at 254 nm (OF) and 470 nm (CF).

2.2 Preparation of boronic esters



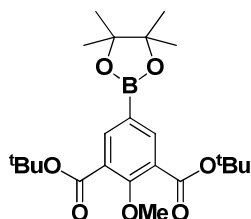
Scheme S1. Preparation of pinacol ester of 3,5-di(*tert*-butoxycarbonyl)-4-methoxyphenylboronic acid.

Di-*tert*-butyl 5-bromo-2-methoxyisophthalate (S1)



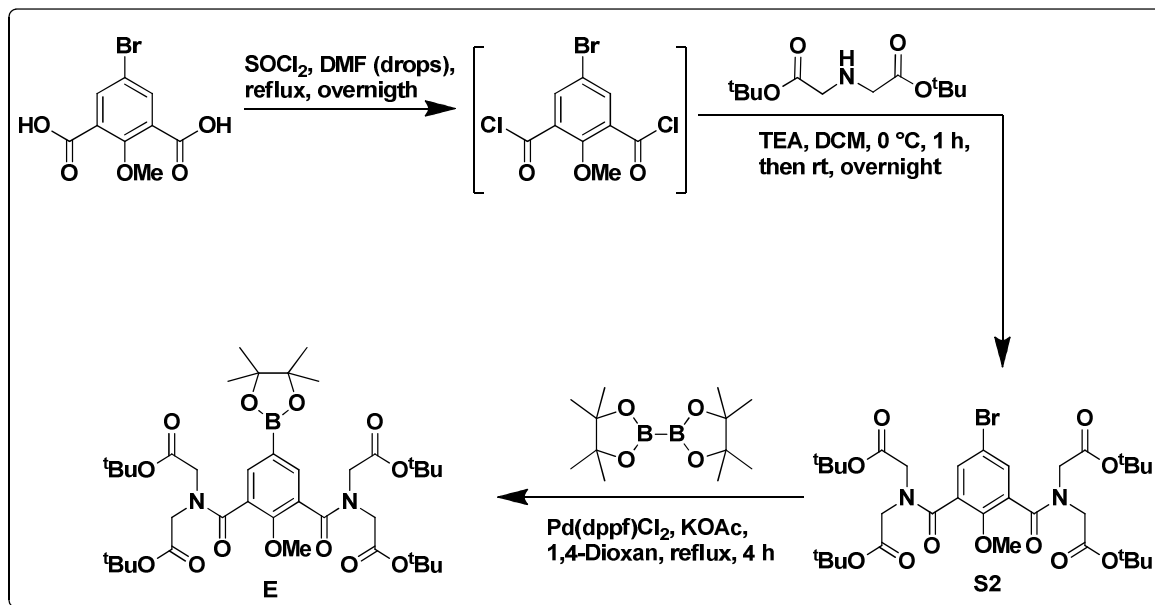
To a solution of 5-bromo-2-methoxyisophthalic acid¹ (300 mg, 1.10 mmol) and DMAP (27 mg, 0.22 mmol, 0.2 equiv.) in a mixture of DCM (5 mL) and DMF (0.2 mL), Boc_2O (720 mg, 3.30 mmol, 3 equiv.) was added in one portion, and stirred at reflux overnight. Then, the resulting mixture was washed thrice with a sat. NaHCO_3 solution (3×35 mL), brine (50 mL), dried over MgSO_4 and concentrated under vacuum. The residue was purified by flash chromatography on a silica gel (*n*-hexane/EtOAc, with a gradient from 100:0 to 90:10) to afford the title compound **S1** as viscous colorless oil (327 mg, 77% yield). R_f (*n*-hexane/EtOAc, 9:1, v/v) = 0.8. ^1H NMR (400 MHz, CDCl_3): δ = 7.86 (s, 2 H), 3.89 (s, 3 H), 1.59 (s, 18 H). ^{13}C NMR (101 MHz, CDCl_3): δ = 164.0, 157.7, 136.5, 130.5, 115.9, 82.7, 63.7, 28.3. HR-MS (ESI, positive mode): 409.0627 [$\text{M}+\text{Na}$, ^{79}Br]⁺, 411.0609 [$\text{M}+\text{Na}$, ^{81}Br]⁺ (found), 411.0601 (calculated for $\text{C}_{17}\text{H}_{23}\text{BrNaO}_5$, [$\text{M}+\text{Na}$, ^{81}Br]⁺).

3,5-Di(*tert*-butoxycarbonyl)-4-methoxyphenylboronic acid pinacol ester (C)



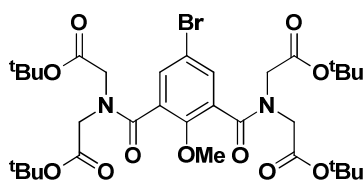
In a sealed tube purged with Ar, compound **S1** (300 mg, 0.78 mmol), bis-pinacolato diboron ($\text{b}(\text{pin})_2$; 237 mg, 0.93 mmol, 1.2 equiv.), KOAc (23 mg, 2.40 mmol, 3 equiv.), $\text{Pd}(\text{dppf})\text{Cl}_2$ (19 mg, 23 μmol , 0.03 equiv.) were combined, and dry 1,4-dioxan (5 mL) was added. The reaction mixture was purged with Ar for further 5 min (Ar bubbling) and stirred at reflux (bath temp. 80 °C) for 2 h. After removal of volatile materials in vacuum, EtOAc (30 mL) was added, and

the reaction mixture was washed with brine (2×30 mL), dried over Na₂SO₄, concentrated under reduced pressure and subjected to column chromatography on silica gel (*n*-hexane/EtOAc, with a gradient from 100:0 to 70:30) to afford the boronic pinacol ester **C** as a white solid (201 mg, 60% yield). *R*_f (*n*-hexane/EtOAc, 4:1, v/v) = 0.8. ¹H NMR (400 MHz, CDCl₃): δ = 8.13 (s, 2 H), 3.90 (s, 3 H), 1.59 (s, 18 H), 1.33 (s, 12 H). ¹³C NMR (101 MHz, CDCl₃): δ = 165.8, 160.4, 139.9 (*overlap of 2 signals*), 128.3, 84.3, 82.0, 63.5, 28.3, 25.0. ESI-MS, positive mode: *m/z* (rel. int., %) = 457.1 (100) [M+Na]⁺ (found), 457.3 (calculated for C₂₃H₃₅BNaO₇, [M+Na]⁺).



Scheme S2. Pinacolato 3,5-bis[*N,N*-di-(*tert*-butoxycarbonylmethyl)]carbamoyl-4-methoxyphenyl boronate.

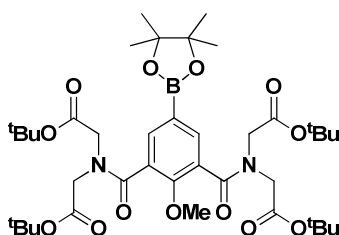
Tetra-*tert*-butyl 5-bromo-2-methoxybenzene 1,3-bis-(carbonyl-*N*-iminodiacetate) (**S2**)



To a solution of 5-bromo-2-methoxyisophthalic acid¹ (552 mg, 2.0 mmol), SOCl₂ (1.5 mL, 20.0 mmol, 10 equiv.) and few drops of DMF were added, and the reaction mixture was refluxed overnight with stirring. An excess of thionyl chloride was removed by distillation, the residue co-evaporated twice with DCM was used directly in the next step. This acyl chloride was dissolved in 35 mL of dry DCM, and a solution of TEA (0.81 mL, 6.0 mmol, 3 equiv.) and di-*tert*-butyl iminodiacetate² (1.03 g, 4.2 mmol, 2.1 equiv.) was added dropwise at 0 °C. After stirring overnight at r.t., the mixture was filtered, the filtrate was washed thrice with a saturated aq. solution of NaHCO₃ (3×35 mL), dried over MgSO₄, concentrated under reduced pressure and subjected to flash chromatography on silica gel (*n*-hexane/EtOAc, with a gradient from 100:0 to

80:20). The title compound **S2** was isolated as a white solid (1.0 g, 69% yield). R_f (*n*-hexane/EtOAc, 7:3, v/v) = 0.67. $^1\text{H NMR}$ (400 MHz, CDCl_3): δ = 7.43 (s, 2 H), 4.54 (m, 2 H), 3.90 (m, 9 H), 1.48 (s, 18 H), 1.42 (s, 18 H). $^{13}\text{C NMR}$ (101 MHz, CDCl_3): δ = 167.6, 167.4, 164.4, 133.4, 132.4, 130.4, 115.7, 82.4, 82.3, 51.7, 50.6, 47.7, 28.2, 28.1. ESI-MS, positive mode: m/z (rel. int., %; *the octa-carboxylic acid was also detected*), 505.1 (100) $[\text{M}+\text{H}, ^{79}\text{Br}]^+$, 506.9 (100) $[\text{M}+\text{H}, ^{81}\text{Br}]^+$ (found), 506.2 (calculated for $\text{C}_{17}\text{H}_{18}\text{BrN}_2\text{O}_{11}$, $[\text{M}+\text{H}, ^{81}\text{Br}]^+$), 751.2 (60) $[\text{M}+\text{Na}, ^{79}\text{Br}]^+$, 753.3 (60) $[\text{M}+\text{Na}, ^{81}\text{Br}]^+$ (found), 752.6 (calculated for $\text{C}_{33}\text{H}_{49}\text{BrN}_2\text{NaO}_{11}$, $[\text{M}+\text{Na}, ^{81}\text{Br}]^+$).

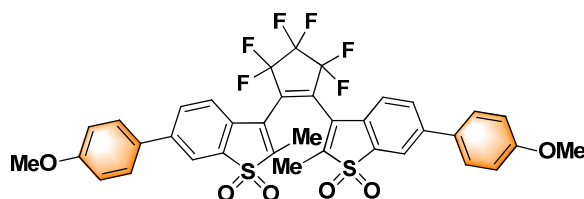
Pinacolato 3,5-bis[*N,N*-di-(*tert*-butoxycarbonylmethyl)]carbamoyl-4-methoxyphenyl boronate (**E**)



In a sealed tube purged with Ar, compound **S2** (300 mg, 0.41 mmol), bis-pinacolato diboron ($\text{b}(\text{pin})_2$; 125 mg, 0.50 mmol, 1.2 equiv.), KOAc (121 mg, 1.23 mmol, 3 equiv.), and $\text{Pd}(\text{dppf})\text{Cl}_2$ (10 mg, 12 μmol , 0.03 equiv.) were combined in dry 1,4-dioxan (5 mL). The reaction mixture was purged with Ar for 5 min (Ar bubbling) and stirred at reflux (bath temp. 80 $^\circ\text{C}$) for 4 h. After removal of volatile materials in vacuum, EtOAc (30 mL) was added, and the reaction mixture was washed with brine (2 \times 30 mL), dried over Na_2SO_4 , concentrated under reduced pressure and subjected to column chromatography on silica gel (*n*-hexane/EtOAc, with a gradient from 100:0 to 70:30) to afford the title compound **E** as a white solid (186 mg, 58% yield). R_f (*n*-hexane/EtOAc, 7:3, v/v) = 0.51. $^1\text{H NMR}$ (400 MHz, CDCl_3): δ = 7.72 (s, 2 H), 4.53 (m, 2 H), 3.93 (m, 9 H), 1.47 (s, 18 H), 1.40 (s, 18 H), 1.23 (s, 12 H). $^{13}\text{C NMR}$ (101 MHz, CDCl_3): δ = 169.6, 168.0, 137.2, 136.3, 128.7, 127.4, 84.0, 82.6, 82.0, 51.7, 47.9, 28.2, 28.1, *methyl signals of pinacol residue are masked by strong singlets of tert-butyl groups*. ESI-MS, positive mode: m/z (rel. int., %) = 799.7 (100) $[\text{M}+\text{Na}]^+$ (found), 799.7 (calculated for $\text{C}_{39}\text{H}_{61}\text{BN}_2\text{NaO}_{13}$, $[\text{M}+\text{Na}]^+$).

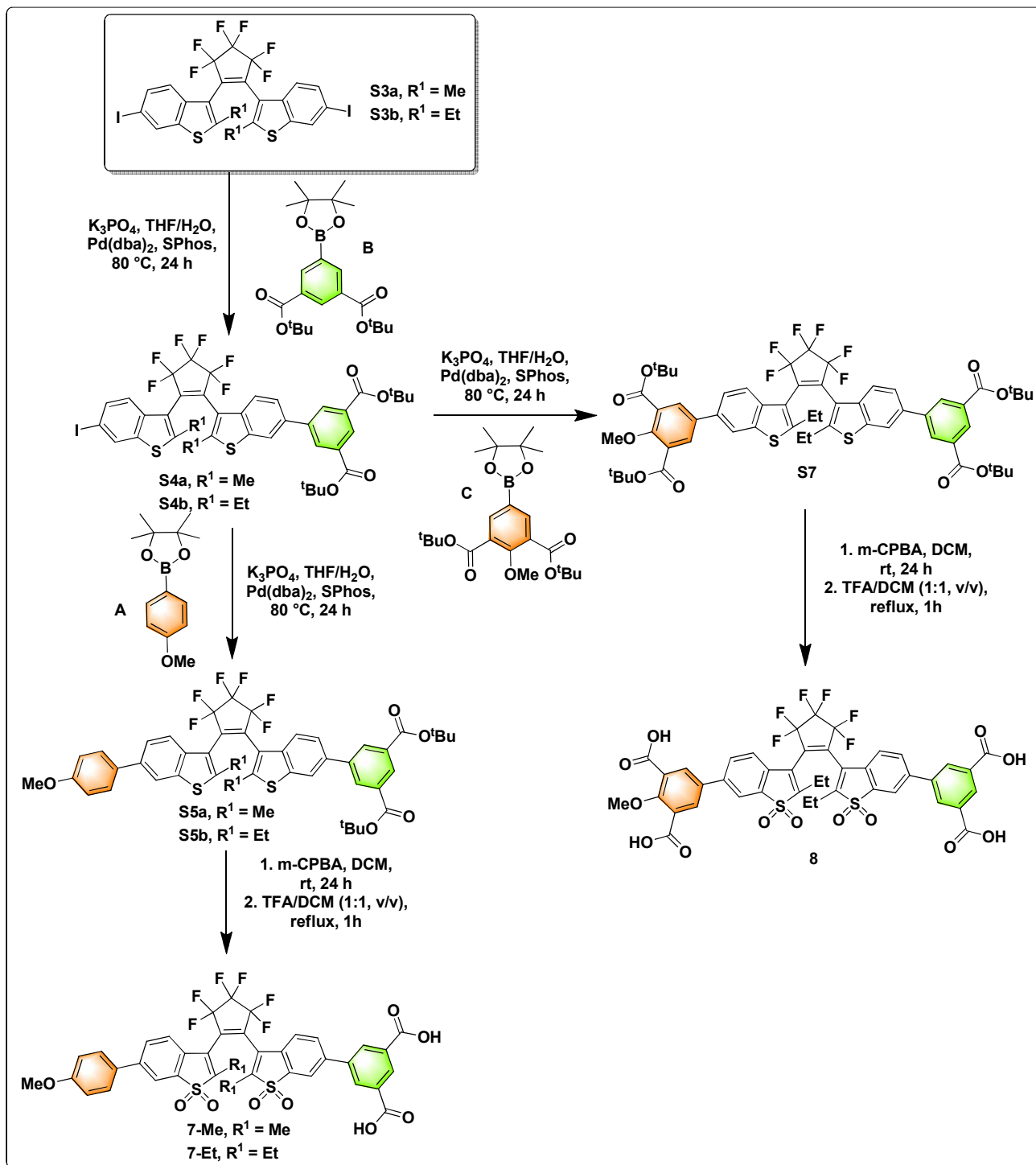
2.3 Symmetric DAE derivative

Compound 3

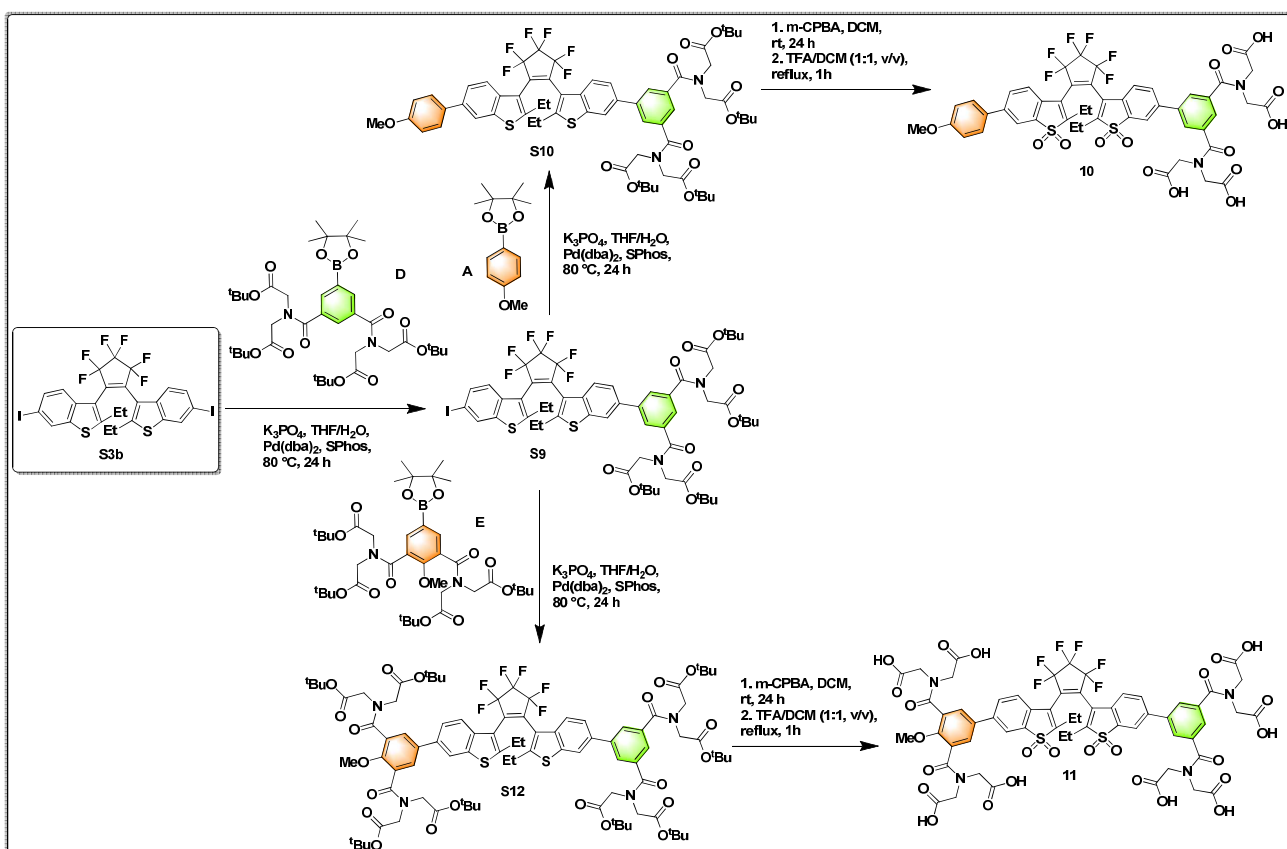


To a solution of 1,2-bis(2-methyl-6-iodobenz[a]thiophen-1,1-dioxide-3-yl)perfluorocyclopentene³ (123 mg, 0.16 mmol) in a mixture of Toluene/EtOH (3.5 mL, 6:1, v/v), (*p*-methoxyphenyl)boronic acid (68 mg, 0.45 mmol, 2.8 equiv.), Na₂CO₃ solution (2 M, 0.2 mL, 2.5 equiv.), and Pd(PPh₃)₄ (9 mg, 7.80 μmol, 5 mol %) were added; the suspension was purged for 5 min with Ar (Ar “bubbling”) and stirred 12 h at reflux (bath temperature = 100 °C). After cooling down, the reaction mixture was filtered through a pad of Silica, washed with Et₂O, and concentrated under reduced pressure. The residue was then purified by flash chromatography on silica gel (*n*-hexane/EtOAc, with a gradient from 90:10 to 70:30) to afford compound **3** as a red solid (53 mg, 45% yield). *The closed isomer (≈ 10%) is produced during the preparation of this dye (see NMR spectra).* *ap:p* = 55:45. ¹H NMR (400 MHz, CDCl₃): δ = 7.93 (s, 1.1 H, *ap*), 7.88 (s, 0.9 H, *p*), 7.75 (d, *J* = 8.0 Hz, 1.1 H, *ap*), 7.59 (d, *J* = 8.0 Hz, 0.9 H, *p*), 7.53 (d, *J* = 8.5 Hz, 2.2 H, *ap*), 7.45 (d, *J* = 8.5 Hz, 1.8 H, *p*), 7.21 (s, 1.1 H, *ap*), 7.19 (s, 0.9 H, *p*), 7.03 (d, *J* = 8.5 Hz, 2.2 H, *ap*), 6.96 (d, *J* = 8.5 Hz, 1.8 H, *p*), 3.87 (s, 3.3 H, *ap*), 3.84 (s, 2.7 H, *p*), 2.23 (s, 2.8 H, *p*), 2.09 (s, 3.2 H, *ap*). ¹³C NMR (126 MHz, CDCl₃): δ = 160.6 *ap*, 160.6 *p*, 144.2 *ap*, 144.0 *p*, 143.0 *p*, 142.8 *ap*, 136.1 *ap*, 136.1 *p*, 131.6 *ap*, 131.4 *p*, 130.5 *ap*, 130.5 *p*, 128.4 *ap*, 128.4 *p*, 127.5 *p*, 127.3 *ap*, 124.1 *ap*, 124.0 *p*, 122.9 *ap*, 122.8 *p*, 121.0 *ap*, 120.9 *p*, 114.9 *ap*, 114.8 *p*, 55.6 *p/ap*, 9.1 *ap*, 9.0 *p*. ¹⁹F NMR (376 MHz, CDCl₃): δ = -109.86 (m, 4.0 F, *p/ap*), -131.97 (m, 2.0 F, *p/ap*). HR-MS (ESI, positive mode): 762.1388 [M+NH₄]⁺ (found), 762.1413 (calculated for C₃₇H₃₀F₆NO₆S₂, [M+NH₄]⁺).

2.4 Asymmetric DAEs



Scheme S3. Synthesis of asymmetric DAEs as “di- and tetra-acids”



Scheme S4. Synthesis of asymmetric DAEs as "tetra- and octa-acids"

General Procedure A1 (GP A1): “the first Suzuki-Miyaura cross-coupling”

To a solution of 1,2-bis(2-alkyl-6-iodobenz[a]thiophen-3-yl)perfluorocyclopentene³⁻⁴ (1 equiv., amount: 0.1 – 0.2 mmol) in a mixture of THF/H₂O (4 mL, 3:1, v/v), arylboronic ester (1 equiv.), K₃PO₄ (3 equiv.), SPhos (0.1 equiv.) and Pd(dba)₂ (0.1 equiv.) were added; the suspension was purged for 5 min with Ar (Ar “bubbling”) and stirred 4 h at reflux (bath temperature = 80 °C). Then, the reaction mixture was diluted with EtOAc, washed with brine (3 × 25 mL), dried over Na₂SO₄ and concentrated under reduced pressure. The residue was purified by flash chromatography on silica gel (*n*-hexane/EtOAc) to afford the desired “mono-substituted monoiodide” DAE as a purple viscous semi-solid.

General Procedure A2 (GP A2): “the second Suzuki-Miyaura cross-coupling”

To a solution of “mono-substituted monoiodide” (GP A1) (amount: 20 - 70 μmol) in a mixture of THF/H₂O (4 mL, 3:1, v/v), arylboronic ester (3 equiv.), K₃PO₄ (3 equiv.), SPhos (0.1 equiv.) and Pd(dba)₂ (0.095 equiv.) were added; the suspension was purged for 5 min with Ar (Ar “bubbling”) and stirred 4 h at reflux (bath temperature = 80 °C). Then, the reaction mixture was diluted with EtOAc, washed with brine (3 × 25 mL), dried over Na₂SO₄ and concentrated under reduced pressure. The residue was purified by flash chromatography on silica gel (*n*-hexane/EtOAc) to afford the desired asymmetric DAE as a white solid.

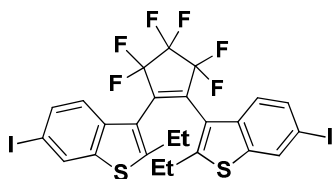
General Procedure B (GP B): “Benzothiophene oxidation”

To a solution of asymmetric DAE (GP A2) (amount: 10 - 40 μmol) in DCM (2 mL), *m*-CPBA (9 equiv.) was added, and the reaction mixture was stirred 24 h at r.t. Then the reaction mixture was diluted with DCM, washed with a *sat.* NaHCO₃ solution (20 mL), brine (35 mL), dried over MgSO₄, and concentrated under reduced pressure. The residue was purified by flash chromatography on silica gel (*n*-hexane/EtOAc) to afford the desired oxidized compound as an orange solid.

General Procedure C (GP C): “Cleavage of *tert*-butyl esters”

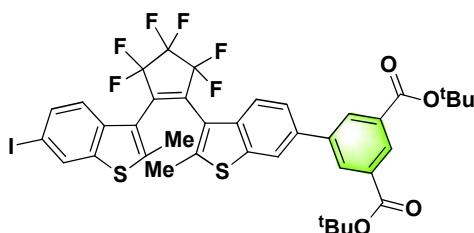
The oxidized DAE (amount: 10 - 30 μmol) was dissolved in a mixture of TFA/DCM (4 mL, 1:1, v/v) and stirred for 1 h at reflux. Then the reaction mixture was concentrated in vacuum and subjected to flash chromatography using a RP-C₁₈ cartridge. The product-containing fractions were pooled and lyophilized to give the desired compound as an amorphous orange solid.

Compound S3b



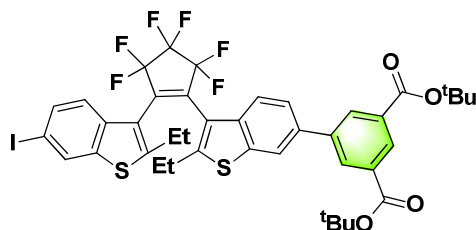
The synthesis of this diiodide DAE was performed according to a published procedure⁵. Iodine (258 mg, 1.02 mmol, 0.9 equiv.) and H₅IO₆ (35 mg, 0.39 mmol, 0.35 equiv.) was added to a stirred solution of 1,2-bis(2-ethyl-benz[a]thiophen-3-yl)perfluorocyclopentene (560 mg, 1.13 mmol) in AcOH (37.5 mL), H₂SO₄ (750 μL), and water (1.8 mL), and the mixture was stirred for 3 h at 70 °C in the open air. The reaction mixture was poured into 100 mL of ice-water, diluted with EtOAc (100 mL), washed with a sat. solution of NaHCO₃ and brine, dried over MgSO₄, and concentrated under reduced pressure. The residue was purified by column chromatography on silica gel (100 % *n*-hexane) to afford the “diiodo-sulfide” DAE as a white solid (306 mg, 36%). *ap:p* = 60:40. This compound was used in the next step without further purification (purity over 85% determined by NMR). *R*_f (*n*-hexane) = 0.40. HR-MS (ESI, negative mode): 746.8599 [M-H]⁻ (found), 746.8614 (calculated for C₂₅H₁₅F₆I₂S₂, [M-H]⁻).

Compound S4a



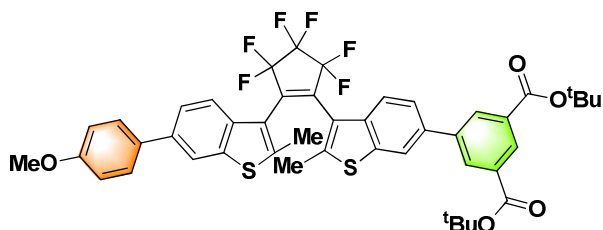
Compound S4a was synthesized from 1,2-bis(2-methyl-6-iodobenz[a]thiophen-3-yl)perfluorocyclopentene³ (100 mg, 0.14 mmol) according to GP A1, and purified by column chromatography on silica gel (*n*-hexane/EtOAc, with a gradient from 100:0 to 90:10); 43 mg, 36% yield. This compound was used in the next step without further purification (purity over 85% determined by NMR). *R*_f (*n*-hexane/EtOAc, 9:1, v/v) = 0.30. HR-MS (ESI, positive mode): 893.0659 [M+Na]⁺ (found), 893.0661 (calculated for C₃₉H₃₃F₆INaO₄S₂, [M+Na]⁺).

Compound S4b



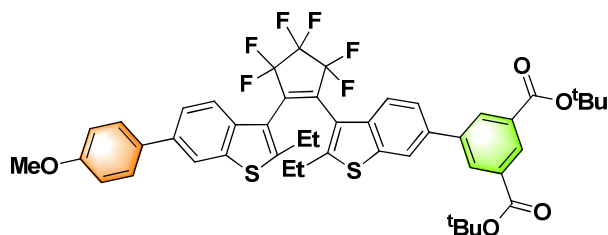
Compound **S4b** was synthesized from 1,2-bis(2-ethyl-6-iodobenz[thiophen-3-yl])perfluorocyclopentene⁴ (120 mg, 0.16 mmol) according to GP A1, and purified by column chromatography on silica gel gel (*n*-hexane/EtOAc, with a gradient from 100:0 to 90:10); 60 mg, 42% yield. This compound was used in the next step without further purification (purity over 85% determined by NMR). R_f (*n*-hexane/EtOAc, 9:1, v/v) = 0.35. HR-MS (ESI, positive mode): 921.0963 [M+Na]⁺ (found), 921.0974 (calculated for C₄₁H₃₇F₆INaO₄S₂, [M+Na]⁺).

Compound S5a



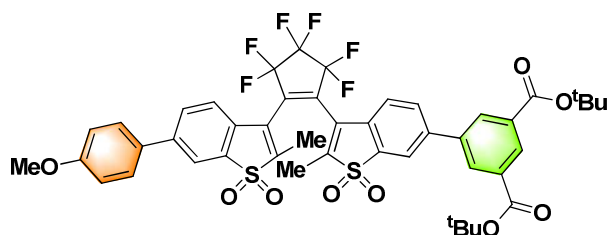
Compound **S5a** was synthesized from compound **S4a** (43 mg, 0.049 mmol) according to GP A2, and purified by column chromatography on silica gel gel (*n*-hexane/EtOAc, with a gradient from 100:0 to 80:20); 26 mg, 62% yield. R_f (*n*-hexane/EtOAc, 9:1, v/v) = 0.24. $ap:p = 65:35$. ¹H NMR (400 MHz, CDCl₃): $\delta = 8.57$ (br. t, $J = 1.6$ Hz, 0.6 H, *ap*), 8.52 (br. t, $J = 1.6$ Hz, 0.4 H, *p*), 8.41 (d, $J = 1.6$ Hz, 1.2 H, *ap*), 8.31 (d, $J = 1.6$ Hz, 0.8 H, *p*), 7.98 (d, $J = 1.6$ Hz, 0.6 H, *ap*), 7.88 (d, $J = 1.6$ Hz, 0.4 H, *p*), 7.86 (d, $J = 1.6$ Hz, 0.6 H, *ap*), 7.78 – 7.39 (m, 6.4 H, *p/ap*), 7.00 (d, $J = 8.6$ Hz, 1.2 H, *ap*), 6.93 (d, $J = 8.6$ Hz, 0.8 H, *p*), 3.86 (s, 1.9 H, *ap*), 3.82 (s, 1.1 H, *p*), 2.54 (s, 1.0 H, *p*), 2.52 (s, 1.0 H, *p*), 2.28 (s, 2.0 H, *ap*), 2.26 (s, 2.0 H, *ap*), 1.65 (s, 12.0 H, *ap*), 1.61 (s, 6.0 H, *p*). ¹³C NMR (101 MHz, CDCl₃): $\delta = 165.1, 159.4, 159.4, 144.0, 143.5, 142.8, 141.0, 139.2, 139.2, 138.1, 137.6, 137.1, 136.1, 133.2, 133.1, 133.0, 131.9, 130.6, 129.4, 129.3, 129.1, 128.5, 128.4, 128.4, 124.3, 124.2, 124.1, 122.7, 122.7, 122.5, 122.4, 122.2, 120.8, 120.6, 120.0, 119.8, 119.4, 119.2, 119.1, 114.5, 114.5, 114.4, 82.0, 81.9, 55.5, 55.5, 28.3, 28.3, 15.5, 15.4$. ¹⁹F NMR (376 MHz, CDCl₃): $\delta = -110.0$ (m, 4.0 F, *p/ap*), -132.8 (m, 2.0 F, *p/ap*). HR-MS (ESI, positive mode): 873.2126 [M+Na]⁺ (found), 873.2114 (calculated for C₄₆H₄₀F₆NaO₅S₂, [M+Na]⁺).

Compound S5b



Compound **S5b** was synthesized from compound **S4b** (60 mg, 0.067 mmol) according to GP A2, and purified by column chromatography on silica gel gel (*n*-hexane/EtOAc, with a gradient from 100:0 to 80:20); 36 mg, 61% yield. R_f (*n*-hexane/EtOAc, 9:1, v/v) = 0.32. *ap:p* = 60:40. $^1\text{H NMR}$ (400 MHz, CDCl_3): δ = 8.57 (br. t, J = 1.6 Hz, 0.6 H, *ap*), 8.52 (br. t, J = 1.6 Hz, 0.4 H, *p*), 8.41 (d, J = 1.6 Hz, 1.2 H, *ap*), 8.31 (d, J = 1.6 Hz, 0.8 H, *p*), 8.01 (d, J = 1.6 Hz, 0.6 H, *ap*), 7.90 (d, J = 1.6 Hz, 0.4 H, *p*), 7.88 (d, J = 1.6 Hz, 0.6 H, *ap*), 7.80 – 7.39 (m, 6.4 H, *p/ap*), 6.99 (d, J = 8.8 Hz, 1.2 H, *ap*), 6.93 (d, J = 8.8 Hz, 0.8 H, *p*), 3.86 (s, 2.2 H, *ap*), 3.82 (s, 0.8 H, *p*), 2.96 (m, 0.6 H, *p/ap*), 2.77 (m, 2.0 H, *p/ap*), 2.50 (m, 1.4 H, *p/ap*), 1.65 (s, 12.0 H, *ap*), 1.61 (s, 6.0 H, *ap*), 1.34 (m, 2.4 H, *p*), 0.87 (m, 3.6 H, *ap*). $^{13}\text{C NMR}$ (101 MHz, CDCl_3): δ = 165.1, 165.1, 159.5, 159.4, 151.8, 151.2, 150.6, 150.1, 143.5, 141.1, 141.0, 139.1, 139.1, 139.0, 138.9, 138.2, 137.9, 137.6, 137.5, 137.1, 136.9, 136.0, 134.9, 133.2, 133.2, 133.1, 133.0, 131.9, 131.9, 130.6, 129.4, 129.4, 129.3, 129.3, 129.1, 128.5, 128.5, 128.4, 128.4, 125.6, 124.3, 124.2, 124.1, 124.0, 122.7, 122.7, 122.4, 122.4, 122.3, 120.9, 120.8, 120.1, 120.0, 118.1, 117.9, 117.8, 114.5, 114.4, 82.0, 81.9, 55.5, 55.5, 28.3, 28.3, 23.6, 23.5, 23.3, 23.2, 16.1, 16.1, 15.6, 15.6. $^{19}\text{F NMR}$ (376 MHz, CDCl_3): δ = -110.3 (m, 4.0 F, *p/ap*), -132.7 (m, 2.0 F, *p/ap*). HR-MS (ESI, positive mode): 901.2389 $[\text{M}+\text{Na}]^+$ (found), 901.2427 (calculated for $\text{C}_{48}\text{H}_{44}\text{F}_6\text{NaO}_5\text{S}_2$, $[\text{M}+\text{Na}]^+$).

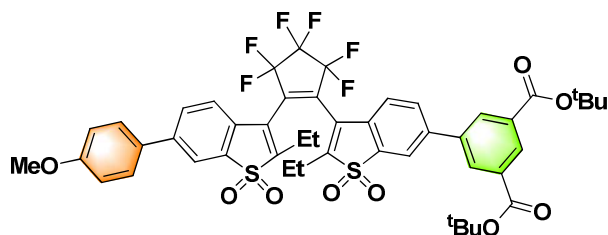
Compound S6a



Compound **S6a** was synthesized from **S5a** (26 mg, 0.031 mmol) according to GP B, and purified by column chromatography on silica gel gel (*n*-hexane/EtOAc, with a gradient from 100:0 to 80:20); 21 mg, 75% yield. R_f (*n*-hexane/EtOAc, 4:1, v/v) = 0.35. *ap:p* = 50:50. $^1\text{H NMR}$ (400 MHz, CDCl_3): δ = 8.63 (s, 0.5 H, *ap*), 8.58 (s, 0.5 H, *p*), 8.35 (d, J = 1.6 Hz, 1.0 H, *ap*), 8.27 (d, J = 1.6 Hz, 1.0 H, *p*), 8.01 - 7.85 (m, 3.0 H, *p/ap*), 7.76 (dd, J = 1.6 Hz and 7.7 Hz, 0.5 H, *p*), 7.71 (dd, J = 1.6 Hz and 7.7 Hz, 0.5 H, *ap*), 7.64 – 7.39 (m, 3.0 H, *p/ap*), 7.20 (d, J = 8.0 Hz, 1.0 H, *p/ap*), 7.00 (d, J = 8.0 Hz, 1.0 H, *p*), 6.95 (d, J = 8.0 Hz, 1.0 H, *ap*), 3.87 (s, 1.5 H, *ap*), 3.83 (s, 1.5 H, *p*), 2.26 (s, 1.5 H, *p*), 2.23 (s, 1.5 H, *p*), 2.12 (s, 1.5 H, *ap*), 2.10 (s, 1.5 H, *ap*), 1.65 (s, 9.0 H, *ap*), 1.61 (s, 9.0 H, *p*). $^{13}\text{C NMR}$ (101 MHz, CDCl_3): δ = 164.6, 160.6, 144.5, 144.3,

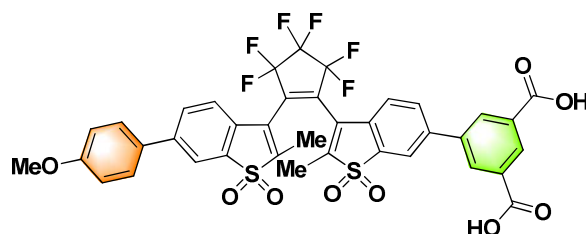
144.1, 143.9, 143.6, 142.8, 142.6, 138.5, 136.3, 136.1, 134.8, 133.9, 133.6, 133.5, 132.6, 132.4, 131.6, 131.6, 131.5, 131.5, 130.8, 130.8, 130.5, 130.4, 130.0, 129.1, 128.9, 128.4, 128.4, 127.5, 127.3, 124.0, 123.8, 123.1, 122.9, 122.7, 121.7, 121.5, 121.1, 120.9, 114.9, 114.8, 82.4, 55.6, 28.3, 14.3, 14.3. ^{19}F NMR (376 MHz, CDCl_3): $\delta = -109.6$ (m, 4.0 F, *p/ap*), -132.0 (m, 2.0 F, *p/ap*). HR-MS (ESI, positive mode): 937.1917 $[\text{M}+\text{Na}]^+$ (found), 937.1910 (calculated for $\text{C}_{46}\text{H}_{40}\text{F}_6\text{NaO}_9\text{S}_2$, $[\text{M}+\text{Na}]^+$).

Compound S6b



Compound **S6b** was synthesized from **S5b** (35 mg, 0.040 mmol) according to GP B, and purified by column chromatography on silica gel gel (*n*-hexane/EtOAc, with a gradient from 100:0 to 80:20); 18 mg, 50% yield. R_f (*n*-hexane/EtOAc, 4:1, v/v) = 0.28. *ap:p* = 55:45. ^1H NMR (400 MHz, CDCl_3): $\delta = 8.63$ (br. t, $J = 1.5$ Hz, 0.6 H, *ap*), 8.58 (br. t, $J = 1.5$ Hz, 0.4 H, *p*), 8.35 (d, $J = 1.6$ Hz, 1.2 H, *ap*), 8.27 (d, $J = 1.6$ Hz, 0.8 H, *p*), 8.04 - 7.85 (m, 3 H, *p/ap*), 7.77 (dd, $J = 1.8$ and 8.0 Hz, 0.6 H, *ap*), 7.70 (dd, $J = 1.8$ and 8.0 Hz, 0.4 H, *p*), 7.64 - 7.39 (m, 3 H, *p/ap*), 7.24 (d, $J = 7.4$ Hz, 0.6 H, *ap*), 7.24 (d, $J = 7.4$ Hz, 0.4 H, *p*), 7.01 (d, $J = 8.8$ Hz, 1.2 H, *ap*), 6.95 (d, $J = 8.8$ Hz, 0.8 H, *p*), 3.87 (s, 1.7 H, *ap*), 3.83 (s, 1.3 H, *p*), 2.63 (m, 2.8 H, *p/ap*), 2.45 (m, 1.2 H, *p/ap*), 1.64 (s, 11 H, *ap*), 1.61 (s, 7 H, *p*), 1.43 (m, 2.7 H, *p*), 1.11 (m, 3.3 H, *ap*). ^{13}C NMR (101 MHz, CDCl_3): $\delta = 164.7$, 164.7, 160.6, 160.6, 149.1, 148.8, 148.2, 147.8, 4144.3, 144.2, 142.8, 142.7, 138.5, 138.5, 136.8, 136.8, 136.6, 136.6, 134.8, 134.0, 133.6, 133.5, 132.5, 132.2, 131.6, 131.6, 131.3, 131.1, 130.8, 130.8, 130.5, 130.5, 130.4, 130.0, 129.0, 128.9, 128.5, 128.4, 128.4, 127.4, 127.3, 123.5, 123.4, 123.3, 123.2, 122.9, 121.3, 120.6, 114.9, 114.8, 82.4, 82.4, 55.6, 55.5, 28.3, 28.3, 19.5, 19.4, 19.4, 19.3, 12.1, 12.0, 11.9, 11.8. ^{19}F NMR (376 MHz, CDCl_3): $\delta = -109.9$ (m, 4.0 F, *p/ap*), -132.1 (m, 2.0 F, *p/ap*). HR-MS (ESI, positive mode): 965.2202 $[\text{M}+\text{Na}]^+$ (found), 965.2223 (calculated for $\text{C}_{48}\text{H}_{44}\text{F}_6\text{NaO}_9\text{S}_2$, $[\text{M}+\text{Na}]^+$).

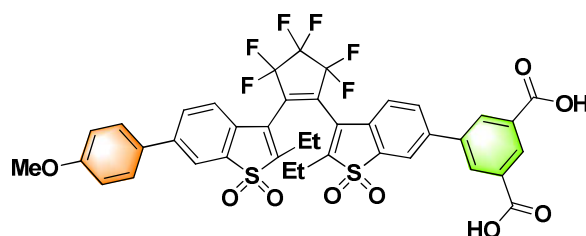
Compound 7-Me



Compound **7-Me** was synthesized from **S6a** (21 mg, 0.023 mmol) according to GP C, and purified by flash chromatography using a RP-C18 cartridge (system D); 8 mg, 43% yield. *ap:p* =

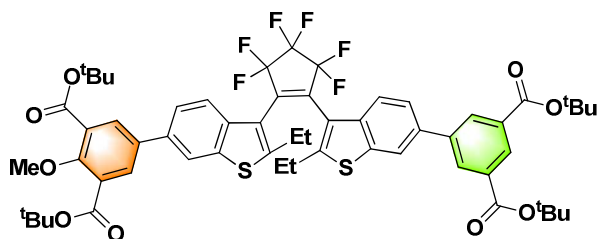
50:50. ^1H NMR (400 MHz, DMF- d_7): δ = 8.71 (br. t, J = 1.6 Hz, 0.5 H, p), 8.66 (m, 1.0 H, p/ap), 8.62 (m, 1.0 H, p/ap), 8.60 (d, J = 1.6 Hz, 0.5 H, ap), 8.54 (m, 1.0 H, p/ap), 8.37 (d, J = 1.6 Hz, 0.5 H, p), 8.31 (m, 1.0 H, p/ap), 8.17 (m, 1.0 H, p/ap), 8.02 (m, 1.5 H, p/ap , masked by the signal of the residual CH-protons in DMF- d_7), 7.89 (m, 2.0 H, p/ap), 7.76 (m, 1.0 H, p/ap), 7.12 (d, J = 8.8 Hz, 1.0 H, ap), 7.05 (d, J = 8.8 Hz, 1.0 H, p), 3.89 (s, 1.2 H, p), 3.85 (s, 1.8 H, ap), 2.39 (s, 1.5 H, p), 2.38 (s, 1.5 H, p), 2.32 (s, 3.0 H, ap). ^{13}C NMR (126 MHz, DMF- d_7): δ = 167.8, 167.8, 162.0, 161.9, 145.5, 144.8, 143.5, 143.4, 140.3, 140.2, 137.4, 137.3, 135.0, 134.7, 134.1, 134.0, 133.4, 133.4, 133.2, 131.7, 131.3, 129.9, 129.9, 128.3, 125.8, 125.7, 125.5, 124.6, 124.5, 123.0, 122.8, 121.6, 121.5, 116.0, 115.9, 56.5, 56.5, 9.8, 9.5. ^{19}F NMR (376 MHz, DMF- d_7): δ = -109.2 (m, 4.0 F, p/ap), -130.2 (m, 2.0 F, p/ap). HR-MS (ESI, negative mode): 801.0671 $[\text{M-H}]^-$ (found), 801.0693 (calculated for $\text{C}_{38}\text{H}_{23}\text{F}_6\text{O}_9\text{S}_2$, $[\text{M-H}]^-$). HPLC (system C): t_{R} = 9.3 min (93% HPLC area, open form); 11.5 min (1% HPLC area, closed form).

Compound 7-Et



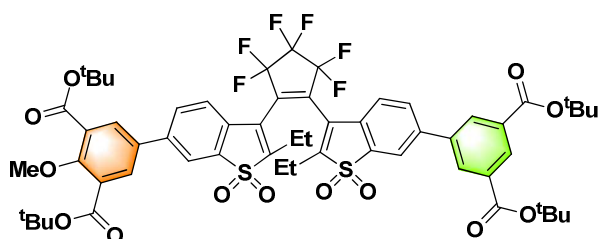
Compound **7-Et** was synthesized from **S6b** (18 mg, 0.019 mmol) according to GP C, and purified by flash chromatography using a RP-C18 cartridge (system D); 9 mg, 57% yield. $ap:p$ = 60:40. ^1H NMR (500 MHz, DMF- d_7): δ = 8.71 (br. t, J = 1.6 Hz, 0.6 H, ap), 8.66 (m, 0.8 H, p), 8.63 (d, J = 1.6 Hz, 0.6 H, ap), 8.56 (d, J = 1.6 Hz, 0.4 H, p), 8.54 (d, J = 1.6 Hz, 0.6 H, p), 8.37 (d, J = 1.8 Hz, 0.6 H, ap), 8.34 (d, J = 1.8 Hz, 0.4 H, p), 8.33 (d, J = 1.8 Hz, 0.4 H, p), 8.25 (d, J = 1.8 Hz, 0.6 H, p), 8.18 (m, 1.0 H, p/ap), 8.02 (m, 2.0 H, p/ap , overlaps with the signal of the residual CH-protons in DMF- d_7), 7.89 (m, 2 H, p/ap), 7.76 (m, 1.0 H, p/ap), 7.13 (d, J = 9.7 Hz, 1.2 H, ap), 7.05 (d, J = 9.7 Hz, 0.8 H, p), 3.90 (s, 1.8 H, ap), 3.85 (s, 1.2 H, p), 2.82 (m, 2.4 H, p/ap), 2.64 (m, 1.6 H, p/ap), 1.41 (m, 2.6 H, p), 1.08 (m, 3.4 H, ap). ^{13}C NMR (126 MHz, DMF- d_7): δ = 167.5, 167.5, 161.7, 161.6, 150.5, 150.2, 149.4, 149.3, 144.7, 144.7, 143.4, 143.3, 140.0, 139.9, 137.6, 137.5, 137.5, 137.3, 134.7, 134.3, 133.8, 133.7, 133.1, 133.1, 132.9, 131.4, 131.4, 131.0, 130.9, 129.6, 129.6, 129.6, 129.5, 128.0, 127.8, 126.1, 125.8, 125.6, 124.1, 124.0, 122.4, 122.2, 121.0, 120.9, 115.7, 115.6, 56.2, 56.2, 20.1, 20.0, 20.0, 19.9, 12.8, 12.7, 12.6, 12.4. ^{19}F NMR (471 MHz, DMF- d_7): δ = -109.8 (m, 4.0 F, p/ap), -130.7 (m, 2.0 F, p/ap). HR-MS (ESI, positive mode): 853.0956 $[\text{M}+\text{Na}]^+$ (found), 853.0971 (calculated for $\text{C}_{40}\text{H}_{28}\text{F}_6\text{NaO}_9\text{S}_2$, $[\text{M}+\text{Na}]^+$). HPLC (system B): t_{R} = 10.8 min (91% HPLC area, open form); 12.5 min (1% HPLC area, closed form).

Compound S7



Compound **S7** was synthesized from **S4b** (42 mg, 48.2 μmol) according to GP A2, and purified by column chromatography on silica gel gel (*n*-hexane/EtOAc, with a gradient from 100:0 to 80:20); 28 mg, 54% yield. R_f (*n*-hexane/EtOAc, 9:1, v/v) = 0.20. *ap:p* = 65:35. ^1H NMR (400 MHz, CDCl_3): δ = 8.55 (bt, J = 1.6 Hz, 0.6 H, *ap*), 8.50 (bt, J = 1.6 Hz, 0.4 H, *p*), 8.40 (d, J = 1.6 Hz, 1.2 H, *ap*), 8.31 (d, J = 1.6 Hz, 0.8 H, *p*), 8.03 - 7.99 (m, 2.0 H, *p/ap*), 7.96 - 7.91 (m, 2.0 H, *p/ap*), 7.85 - 7.60 (m, 3.0 H, *p/ap*), 7.50 (dd, J = 1.8 Hz & 8.5 Hz, 0.6 H, *ap*), 7.43 (dd, J = 1.8 Hz & 8.5 Hz, 0.4 H, *ap*), 3.95 (s, 1.0 H, *p*), 3.94 (s, 2.0 H, *ap*), 2.95 (m, 0.6 H, *p/ap*), 2.78 (m, 2.0 H, *p/ap*), 2.50 (m, 1.4 H, *p/ap*), 1.64 (m, 38.4 H, *p/ap*), 0.88 (t, J = 6.6 Hz, 3.6 H, *ap*). ^{13}C NMR (101 MHz, CDCl_3): Due to co-elution of this compound with the starting boronic ester (compound C), it was not possible to interpret the ^{13}C NMR spectrum. ^{19}F NMR (376 MHz, CDCl_3): δ = -110.2 (m, 4.0 F, *p/ap*), -130.7 (m, 2.0 F, *p/ap*). ESI-MS, negative mode: m/z (rel. int., %) = 465.7 (100) $[\text{M}-2\text{H}+\text{K}]^-$ (found), 465.5 (calculated for $\text{C}_{42}\text{H}_{27}\text{KF}_6\text{O}_9\text{S}_2$, $[\text{M}-2\text{H}+\text{K}]^-$, premature cleavage of tert-butyl substituents occurred during this analysis).

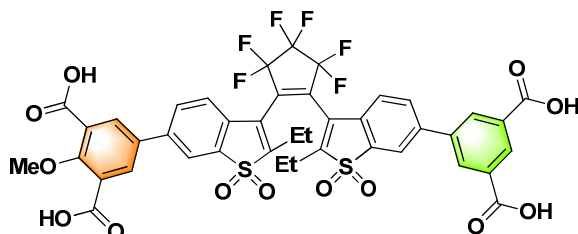
Compound S8



Compound **S8** was synthesized from compound **S7** (28 mg, 25.9 μmol) according to GP B, and purified by column chromatography on silica gel gel (*n*-hexane/EtOAc, with a gradient from 100:0 to 80:20); 18 mg, 60% yield. R_f (*n*-hexane/EtOAc, 9:1, v/v) = 0.15. *ap:p* = 60:40. ^1H NMR (400 MHz, CDCl_3): δ = 8.62 (bt, J = 1.6 Hz, 0.6 H, *ap*), 8.58 (bt, J = 1.6 Hz, 0.4 H, *p*), 8.35 (d, J = 1.6 Hz, 1.2 H, *ap*), 8.27 (d, J = 1.6 Hz, 0.8 H, *p*), 8.10 - 7.95 (m, 4.0 H, *p/ap*), 7.92 - 7.86 (m, 1.4 H, *p/ap*), 7.82 (dd, J = 1.7 and 8.0 Hz, 0.6 H, *ap*), 7.72 (dd, J = 1.8 and 8.0 Hz, 0.4 H, *p*), 7.66 (dd, J = 1.8 and 8.0 Hz, 0.4 H, *p*), 7.59 (m, 1.2 H, *p/ap*), 3.96 (s, 1.8 H, *ap*), 3.91 (s, 1.2 H, *p*), 2.62 (m, 2.7 H, *p/ap*), 2.45 (m, 1.3 H, *p/ap*), 1.65 (s, 11.0 H, *ap*), 1.63 (s, 11.0 H, *ap*), 1.60 (s, 7.0 H, *p*), 1.58 (s, 7.0 H, *p*), 1.44 (m, 2.6 H, *p*), 1.11 (m, 3.4 H, *ap*). ^{13}C NMR (101 MHz, CDCl_3): δ = 165.0, 165.0, 164.7, 164.6, 159.1, 159.0, 149.2, 149.0, 148.8, 148.8, 142.8, 142.7, 142.5, 142.4, 138.5, 138.4, 136.8, 136.8, 134.8, 133.9, 133.6, 133.5, 133.2, 133.2, 132.5, 132.3, 132.2, 132.1, 132.0, 131.6, 131.6, 130.9, 130.8, 130.4, 130.0, 129.8, 129.6, 129.0, 128.8, 128.6,

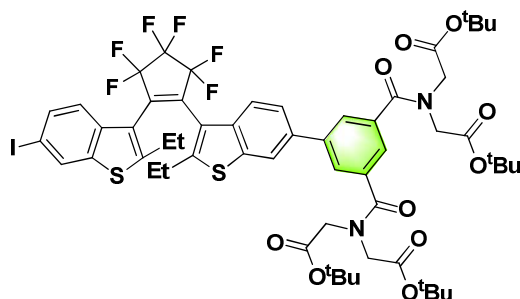
128.5, 123.4, 123.3, 123.1, 123.0, 121.3, 121.3, 121.0, 121.0, 82.8, 82.7, 82.4, 82.4, 63.8, 63.7, 28.3, 28.3, 19.5, 19.4, 12.0, 11.8. ^{19}F NMR (376 MHz, CDCl_3): $\delta = -109.9$ (m, 4.0 F, *p/ap*), -132.2 (m, 2 F, *p/ap*). ESI-MS, positive mode: m/z (rel. int., %) = 1166.2 (100) $[\text{M}+\text{Na}]^+$ (found), 1166.2 (calculated for $\text{C}_{58}\text{H}_{60}\text{F}_6\text{NaO}_{13}\text{S}_2$ $[\text{M}+\text{Na}]^+$).

Compound 8



Compound **8** was synthesized from compound **S8** (18 mg, 15.7 μmol) according to GP C, and purified by flash chromatography using a RP-C18 cartridge (system E); 5 mg, 35% yield. *ap:p* = 60:40. ^1H NMR (500 MHz, DMF-d_7): $\delta = 8.71$ (br. t, $J = 1.6$ Hz, 0.6 H, *ap*), 8.64 (m, 2.4 H, *p/ap*), 8.60 (d, $J = 1.8$ Hz, 0.6 H, *ap*), 8.56 (d, $J = 1.8$ Hz, 0.4 H, *ap*), 8.53 – 8.48 (m, 1.0 H, *p/ap*), 8.36 (m, 1.0 H, *p/ap*), 8.33 (dd, $J = 1.8$ and 8.0 Hz, 0.6 H, *ap*), 8.29 (dd, $J = 1.8$ and 8.0 Hz, 0.4 H, *p*), 8.23 (m, 1.0 H, *p/ap*), 8.17 (dd, $J = 1.8$ and 8.0 Hz, 0.4 H, *p*), 8.12 (dd, $J = 1.8$ and 8.0 Hz, 0.6 H, *ap*), 8.02 (m, 1.0 H, *p/ap*, overlaps with the residual proton signals of DMF-d_7), 7.90 (d, $J = 8.0$ Hz, 0.6 H, *ap*), 7.86 (d, $J = 8.0$ Hz, 0.4 H, *p*), 4.00 (s, 1.8 H, *ap*), 3.94 (s, 1.2 H, *p*), 2.87 - 2.62 (m, 4.0 H, *p/ap*, overlaps with the residual proton signals of DMF-d_7), 1.42 (m, 2.4 H, *p*), 1.09 (m, 3.6 H, *ap*). ^{13}C NMR (126 MHz, DMF-d_7): $\delta = 167.9, 167.5, 159.8, 150.5, 150.3, 150.2, 150.0, 143.4, 143.2, 142.9, 142.8, 141.0, 140.0, 139.8, 137.6, 137.6, 137.4, 137.4, 134.7, 134.4, 134.2, 134.0, 133.9, 133.8, 133.8, 133.1, 133.0, 131.3, 130.6, 130.5, 130.1, 129.6, 129.4, 129.2, 129.0, 125.8, 123.9, 123.9, 122.4, 122.3, 122.2, 121.9, 121.9, 64.2, 64.1, 20.1, 20.0, 12.7, 12.5, 12.5, 12.4$. ^{19}F NMR (471 MHz, DMF-d_7): $\delta = -109.7$ (m, 4.0 F, *p/ap*), -130.8 (m, 2.0 F, *p/ap*). HR-MS (ESI, positive mode): 941.0748 $[\text{M}+\text{Na}]^+$ (found), 941.0768 (calculated for $\text{C}_{42}\text{H}_{28}\text{F}_6\text{NaO}_{13}\text{S}_2$, $[\text{M}+\text{Na}]^+$). HPLC (system A): $t_R = 13.1$ min (4% peak area, closed form), 13.7 min (96% peak area, open form).

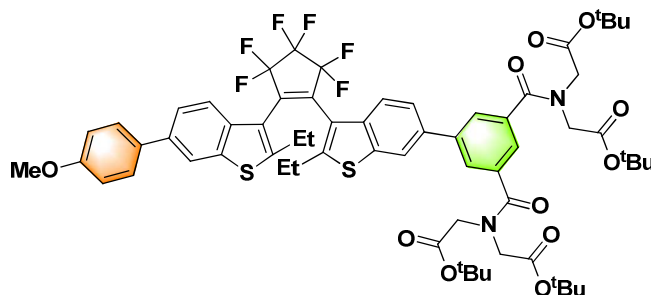
Compound S9



Compound **S9** was synthesized from 1,2-bis(2-ethyl-6-iodobenz[*a*]thiophen-3-yl)perfluorocyclopentene⁴ (100 mg, 0.134 mmol) according to GP A1, and purified by column

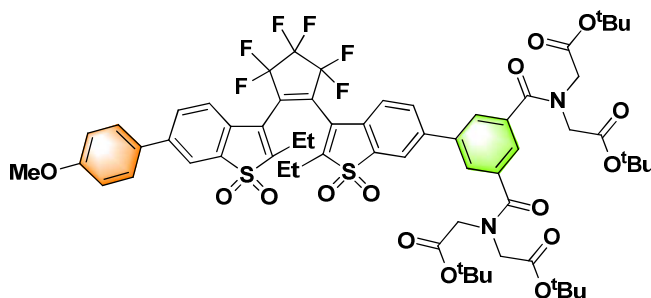
chromatography on silica gel gel (*n*-hexane/EtOAc, with a gradient from 100:0 to 70:30); 42 mg, 25% yield. This compound was used in the next step without further purification (HPLC area of the main peak 85%). R_f (*n*-hexane/EtOAc, 4:1, v/v) = 0.5. HR-MS (ESI, positive mode): 1263.2767 [M+Na]⁺ (found), 1263.2765 (calculated for C₅₇H₆₃F₆IN₂NaO₁₀S₂, [M+Na]⁺).

Compound S10



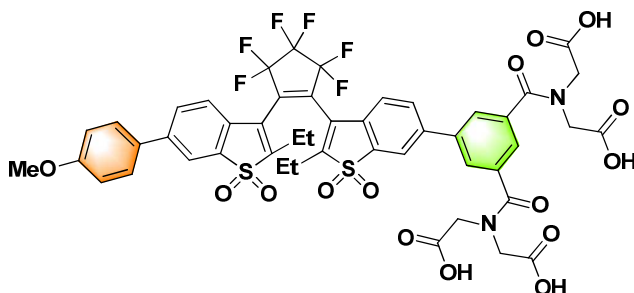
Compound S10 was synthesized from compound S9 (39 mg, 24.2 μmol) according to GP A2, and purified by column chromatography on silica gel gel (*n*-hexane/EtOAc, with a gradient from 100:0 to 60:40); 20 mg, 53% yield. R_f (*n*-hexane/EtOAc, 4:1, v/v) = 0.35. *ap:p* = 70:30. ¹H NMR (400 MHz, CDCl₃): δ = 7.92 (d, *J* = 1.6 Hz, 0.7 H, *ap*), 7.88 (d, *J* = 1.6 Hz, 0.7 H, *ap*), 7.83 (d, *J* = 1.6 Hz, 0.3 H, *p*), 7.79 (m, 1.0 H, *p/ap*), 7.78 (d, *J* = 1.6 Hz, 0.3 H, *p*), 7.71 (d, *J* = 2.2 Hz, 0.7 H, *ap*), 7.69 (m, 1.3 H, *p/ap*), 7.65-7.54 (m, 4.0 H, *p/ap*), 7.50 – 7.38 (m, 2.0 H, *p/ap*), 7.00 (d, *J* = 8.8 Hz, 1.4 H, *ap*), 7.93 (d, *J* = 8.8 Hz, 0.6 H, *p*), 4.21 (s, 1.1 H, *ap*), 4.20 (s, 1.1 H, *ap*) 4.18 (s, 0.4 H, *p*), 4.16 (s, 0.4 H, *p*), 3.99 (s, 2.7 H, *p/ap*), 3.93 (s, 1.0 H, *p/ap*), 3.86 (s, 2.0 H, *p/ap*), 3.81 (s, 0.8 H, *p/ap*), 2.95 - 2.74 (m, 2.6 H, *p/ap*), 2.45 (m, 1.4 H, *p/ap*), 1.50 (s, 13.0 H, *ap*), 1.48 (s, 5.0 H, *p*), 1.37 (s, 13.0 H, *ap*), 1.32 (m, 1.8 H, *p*), 1.27 (s, 5.0 H, *p*), 0.84 (m, 4.2 H, *ap*). ¹³C NMR (126 MHz, CDCl₃): δ = 171.5, 168.7, 168.6, 168.3, 168.2, 159.8, 159.7, 152.3, 151.0, 142.0, 142.0, 139.4, 139.4, 139.3, 139.2, 138.6, 137.9, 137.9, 137.4, 137.0, 136.9, 135.8, 135.8, 133.5, 133.5, 128.8, 128.7, 127.5, 127.5, 124.5, 124.5, 124.4, 124.3, 124.2, 124.0, 123.0, 123.0, 122.8, 122.7, 122.5, 121.1, 121.0, 120.4, 120.3, 118.2, 118.1, 114.8, 114.7, 83.4, 83.3, 82.6, 82.6, 55.9, 55.8, 52.9, 52.8, 48.9, 28.6, 28.6, 28.4, 28.2, 23.9, 23.6, 23.5, 16.5, 16.4, 16.0, 15.8. ¹⁹F NMR (376 MHz, CDCl₃): δ = -110.3 (m, 4.0 F, *p/ap*), -132.8 (m, 2.0 F, *p/ap*). HR-MS (ESI, positive mode): 1243.4219 [M+Na]⁺ (found), 1243.4217 (calculated for C₆₄H₇₀F₆N₂NaO₁₁S₂, [M+Na]⁺).

Compound S11



Compound **S11** was prepared from **S10** (20 mg, 16.4 μmol) according to GP B, and purified by column chromatography on silica gel gel (*n*-hexane/EtOAc, with a gradient from 100:0 to 60:40) 18 mg, 86% yield. R_f (*n*-hexane/EtOAc, 4:1, v/v) = 0.28. *ap:p* = 60:40. ^1H NMR (400 MHz, CDCl_3): δ = 8.06 (bt, J = 1.8 Hz, 0.6 H, *ap*), 7.98 (bt, J = 1.8 Hz, 0.4 H, *p*), 7.96 (d, J = 1.7 Hz, 0.6 H, *ap*), 7.93 (d, J = 1.7 Hz, 0.4 H, *p*), 7.88 (d, J = 1.7 Hz, 0.6 H, *ap*), 7.85 (d, J = 1.7 Hz, 0.6 H, *ap*), 7.84 (d, J = 1.7 Hz, 0.4 H, *p*), 7.82 (d, J = 1.7 Hz, 0.4 H, *p*), 7.78 (m, 1.6 H, *p/ap*), 7.75 (d, J = 1.7 Hz, 0.4 H, *p*), 7.70 (d, J = 1.5 Hz, 0.6 H, *ap*), 7.66 (dd, J = 1.7 Hz & 8.0 Hz, 0.4 H, *p*), 7.62 – 7.60 (m, 3.0 H, *p/ap*), 7.45 (m, 1.0 H, *p/ap*), 7.01 (d, J = 8.8 Hz, 1.2 H, *ap*), 6.96 (d, J = 8.8 Hz, 0.8 H, *p*), 4.18 (m, 4.4 H, *p/ap*), 3.96 (s, 2.6 H, *ap*), 3.90 (s, 1.0 H, *p*), 3.87 (s, 1.8 H, *ap*), 3.83 (s, 1.2 H, *p*), 2.68 - 2.52 (m, 3.0 H, *p/ap*), 2.43 – 2.35 (m, 1.0 H, *p/ap*), 1.50 (s, 11.0 H, *ap*), 1.48 (s, 7.0 H, *p*), 1.41 (m, 13.4 H, *p/ap*), 1.32 (s, 7.0 H, *p*), 1.07 (m, 3.6 H, *ap*). ^{13}C NMR (126 MHz, CDCl_3): δ = 170.7, 168.3, 168.2, 167.8, 167.8, 160.6, 160.6, 149.4, 149.1, 148.2, 147.8, 144.3, 142.2, 142.1, 139.1, 139.1, 137.2, 137.1, 137.0, 137.0, 136.6, 136.5, 134.8, 133.8, 132.4, 132.1, 131.6, 131.3, 131.2, 130.5, 130.4, 130.3, 130.0, 129.2, 128.4, 128.4, 128.4, 125.3, 125.1, 123.5, 123.4, 123.2, 123.1, 123.0, 122.8, 120.9, 120.7, 120.6, 114.9, 114.8, 83.3, 83.2, 82.4, 55.6, 55.5, 52.6, 52.5, 48.6 48.6, 28.3, 28.3, 28.1, 28.0, 19.5, 19.4, 19.3, 19.2, 12.1, 12.0, 11.9, 11.7. ^{19}F NMR (376 MHz, CDCl_3): δ = -109.9 (m, 4.0 F, *p/ap*), -132.3 (m, 2.0 F, *p/ap*). HR-MS (ESI, positive mode): 1307.4004 $[\text{M}+\text{Na}]^+$ (found), 1307.4014 (calculated for $\text{C}_{64}\text{H}_{70}\text{F}_6\text{N}_2\text{NaO}_{15}\text{S}_2$, $[\text{M}+\text{Na}]^+$).

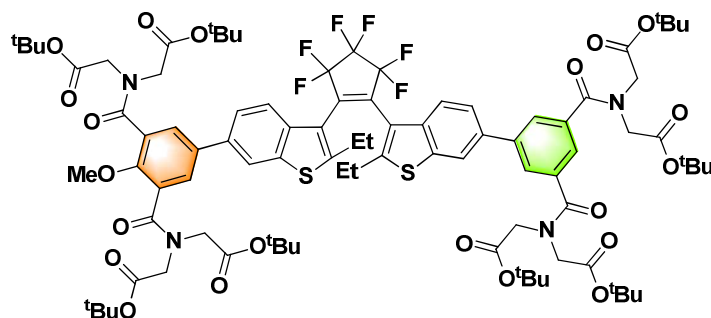
Compound 10



Compound **10** was prepared from **S11** (18 mg, 14.0 μmol) according to GP C, and purified by flash chromatography using a RP-C18 cartridge (system E); 7 mg, 47% yield. *ap:p* = 60:40. ^1H NMR (500 MHz, DMF-d_7): δ = 8.49 (d, J = 1.8 Hz, 0.6 H, *ap*), 8.38 (m, 1.0 H, *p/ap*), 8.23 (m, 0.8 H, *p/ap*), 8.17 (dd, J = 8.1 and 1.8 Hz, 0.6 H, *ap*), 8.11 (dd, J = 8.0 and 1.8 Hz, 0.4 H, *ap*), 8.03 – 7.94 (m, 2.6 H, *p/ap*, overlaps with the signal of the residual CH -protons in DMF-d_7), 7.89 (m, 2.0 H, *p/ap*), 7.84 (m, 1.0 H, *p/ap*), 7.79 (d, J = 8.1 Hz, 0.4 H, *p*), 7.74 (d, J = 8.1 Hz, 0.6 H, *ap*), 7.55 (br. t, J = 1.5 Hz, 0.6 H, *ap*), 7.51 (br. t, J = 1.5 Hz, 0.4 H, *ap*), 7.14 (d, J = 8.9 Hz, 1.2 H, *ap*), 7.05 (d, J = 8.9 Hz, 0.8 H, *p*), 4.36 (s, 2.5 H, *ap*), 4.35 (m, 1.5 H, *p*), 4.33 (s, 2.5 H, *ap*), 4.27 (s, 1.5 H, *p*), 3.90 (s, 1.7 H, *ap*), 3.85 (s, 1.3 H, *p*), 2.85 – 2.70 (m, 2.5 H, *p/ap*, overlaps with the signal of the residual CH_3 -protons in DMF-d_7), 2.61 (m, 1.5 H, *p/ap*), 1.41 (m, 2.5 H, *p*), 1.03 (m, 3.5 H, *ap*). ^{13}C NMR (126 MHz, DMF-d_7): δ = 172.4, 171.8, 171.7, 171.5, 162.0, 161.9, 150.7, 150.4, 149.6, 149.5, 144.9, 143.6, 143.4, 139.9, 139.8, 138.7, 138.6, 137.8,

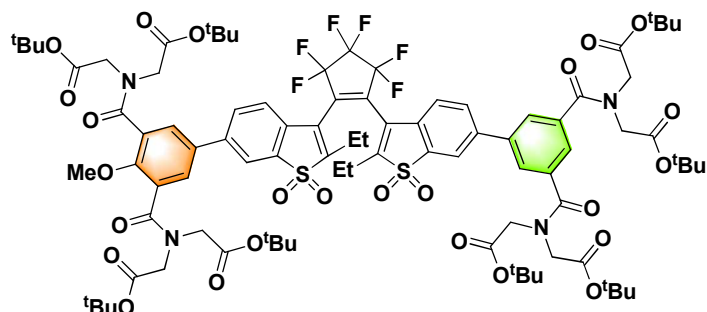
137.8, 137.6, 137.5, 134.8, 134.4, 133.4, 133.1, 131.2, 131.1, 129.9, 129.8, 129.8, 129.7, 128.2, 127.9, 127.9, 126.7, 126.6, 126.3, 126.0, 125.8, 124.3, 124.2, 122.3, 122.1, 121.2, 121.1, 116.0, 115.9, 56.4, 56.4, 53.1, 53.0, 49.3, 49.2, 20.3, 20.3, 20.1, 20.1, 13.0, 12.9, 12.7, 12.6. ^{19}F NMR (471 MHz, DMF-d_7): $\delta = -109.7$ (m, 4.0 F, *p/ap*), -130.7 (m, 2.0 F, *p/ap*). HR-MS (ESI, negative mode): 1059.1510 $[\text{M-H}]^-$ (found), 1059.1545 (calculated for $\text{C}_{48}\text{H}_{37}\text{F}_6\text{N}_2\text{O}_{15}\text{S}_2$, $[\text{M-H}]^-$). HPLC (system A): $t_{\text{R}} = 15.4$ min (90% peak area, open form); 16.7 min (2% peak area, closed form).

Compound S12



Compound **S12** was prepared from **S9** (90 mg, 72.5 μmol) according to GP A2, and purified by column chromatography on silica gel (*n*-hexane/EtOAc, with a gradient from 100:0 to 60:40) 83 mg, 65% yield. R_f (*n*-hexane/EtOAc, 3:2, v/v) = 0.52. *ap:p* = 70:30. ^1H NMR (400 MHz, CDCl_3): $\delta = 7.92$ (d, $J = 1.7$ Hz, 0.7 H, *ap*), 7.84 (m, 0.6 H, *p*), 7.79 (d, $J = 1.6$ Hz, 1.4 H, *ap*), 7.72 - 7.43 (m, 6.0 H, *p/ap*), 7.40 - 7.29 (m, 1.6 H, *p/ap*), 7.11 - 7.04 (m, 0.7 H, *p/ap*), 4.64 - 4.45 (m, 2.0 H, *p/ap*), 4.26 - 4.15 (m, 3.0 H, *p/ap*), 4.07 - 3.80 (m, 14.0 H, *p/ap*), 3.00 - 2.62 (m, 2.0 H, *p/ap*), 2.47 - 2.33 (m, 1.5 H, *p/ap*), 1.51 - 1.46 (m, 36.0 H, *p/ap*), 1.42 - 1.30 (m, 37.6 H, *p/ap*), 0.90 - 0.80 (m, 4.4 H, *ap*). ^{13}C NMR (126 MHz, CDCl_3): $\delta = 171.0, 169.2, 168.2, 168.0, 168.0, 167.9, 167.8, 167.8, 151.4, 141.5, 138.9, 138.9, 138.1, 136.5, 135.3, 129.8, 127.1, 124.0, 123.7, 122.5, 122.4, 120.6, 117.6, 82.9, 82.1, 82.1, 81.9, 52.4, 51.6, 51.6, 48.4, 23.0, 23.0, 15.4, 15.4$. ^{19}F NMR (471 MHz, CDCl_3): $\delta = -110.2$ (m, 4.0 F, *p/ap*), -132.9 (m, 2.0 F, *p/ap*). HR-MS (ESI, positive mode): 1785.7057 $[\text{M}+\text{Na}]^+$ (found), 1785.7057 (calculated for $\text{C}_{90}\text{H}_{112}\text{F}_6\text{N}_4\text{NaO}_{21}\text{S}_2$, $[\text{M}+\text{Na}]^+$).

Compound S13



Compound **S13** was synthesized from **S12** (70 mg, 39.7 μmol) according to GP B, and purified by column chromatography on silica gel gel (*n*-hexane/EtOAc, with a gradient from 100:0 to 60:40); 36 mg, 50% yield. R_f (*n*-hexane/EtOAc, 3:2, v/v) = 0.45. $ap:p$ = 65:35. ^1H NMR (400 MHz, CDCl_3): δ = 8.03 - 7.70 (m, 6.35 H, *p/ap*), 7.66 - 7.47 (m, 3.65 H, *p/ap*), 7.28 - 7.19 (m, 1.0 H, *p/ap*, overlaps with the signal of the residual CH-protons in CDCl_3), 4.61 - 4.41 (m, 2.0 H, *p/ap*), 4.26 - 4.13 (m, 4.0 H, *p/ap*), 4.05 - 3.81 (m, 13.0 H, *p/ap*), 2.67 - 2.47 (m, 2.4 H, *p/ap*), 2.39 - 2.26 (m, 1.6 H, *p/ap*), 1.52 - 1.44 (m, 38.0 H, *p/ap*), 1.40 - 1.28 (m, 36 H, *p/ap*), 1.07 - 0.97 (m, 4.0 H, *ap*). ^{19}F NMR (376 MHz, CDCl_3): δ = -109.8 (m, 4.0 F, *p/ap*), -132.2 (m, 2.0 F, *p/ap*). HR-MS (ESI, positive mode): 1849.6860 $[\text{M}+\text{Na}]^+$ (found), 1849.6853 (calculated for $\text{C}_{90}\text{H}_{112}\text{F}_6\text{N}_4\text{NaO}_{25}\text{S}_2$, $[\text{M}+\text{Na}]^+$).

3. Immunolabeling and fluorescence imaging

3.2 Photoswitching of bioconjugates

To ensure that the DAEs bound to proteins were still photochemically active, diluted samples (in MeOH and PBS; pH = 7.4) of the bioconjugates were placed into a 1 cm path quartz cuvette and irradiated under conditions similar to the conditions used for photoswitching of the free dyes, in MeOH and PBS. Photoisomerizations of the probes in both directions (with 365 nm light (OF→CF) and 470 nm (CF→OF) light) were observed, with the concomitant changes in fluorescence emission (Figure S1).

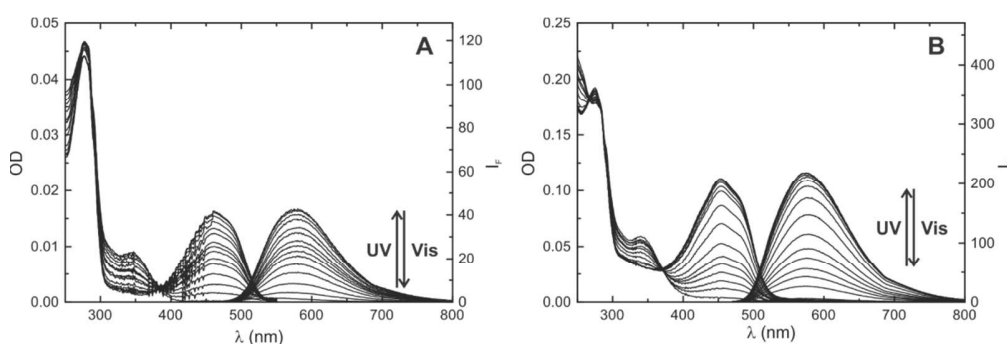


Figure S1. Absorption and emission changes upon irradiation of two representative bioconjugates of **4-Et** (DOL = 3, A) and **11** (DOL = 5, B) in PBS (pH = 7.4). Diluted samples in a 1 cm-path quartz cuvette were irradiated under continuous stirring. Typical irradiation light powers were around 20–30 mW. Absorption and emission spectra were recorded after each irradiation step (10–60 s).

3.3 Immunolabeling protocol

Vero cell samples cells were grown on standard cover slips and then fixed with previously cooled (-20 °C) methanol for 5 min, and blocked with 5% (w/v) BSA in PBS pH = 7.4 (blocking buffer). Then the cells were incubated with a primary antibody at r.t. for 1 h, followed by three washing steps of 5 min each with blocking buffer. The cells were then incubated at r.t. for 1 h with the labelled bioconjugates (typical dilutions of 1:50 to 1:100 from the purified bioconjugate), washed again (5 min each step) three times with blocking buffer and, finally, with mounting medium (PBS, pH 7.4). The samples were mounted with PBS (pH = 7.4) in concave microscopy slides and sealed with a silicone resin (Picodent Twinsil) to prevent leakage. As primary antibodies (Abcam, Cambridge, UK), mouse and rabbit anti- α -tubulin, mouse anti-NUP 153, and rabbit anti-vimentin were used.

3.4 Confocal images

Standard confocal images were acquired in a commercial Leica TCS SP5 confocal microscope. Images (Figures S2 and S3) were recorded with 488 nm excitation, after a short (ca. 1-5 s) and low-intensity wide-field pre-activation with ~366 nm light, from the mercury lamp. Detection was collected between 520 and 670 nm. A fading of the signal was observed after one or several consecutive scans of the same area, due to the isomerization (CF→OF) induced by the excitation light (a process competing with fluorescence emission of the probe). The signal can be recovered with another pre-activation pulse, and thus further imaging of the same area can be repeated several times.

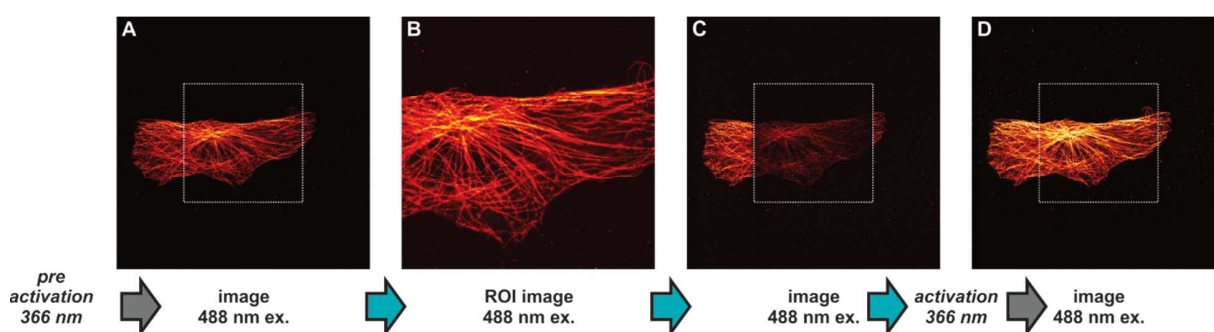


Figure S2. Confocal imaging with a 4-Et bioconjugate. First, an overview of a cell was recorded (A). Then, an image of the ROI (boxed area in A) was acquired (B). The pixel size in B is smaller than in A, C-D, and thus markers received a higher light dose. The following overview image (C) shows the fading of the signal in the ROI. The signal is recovered (D) after a short exposition (a few seconds) to UV light (wide-field illumination of a Hg lamp selected with a filter), which demonstrates that the fading was due to the cycloreversion of the DAE markers.

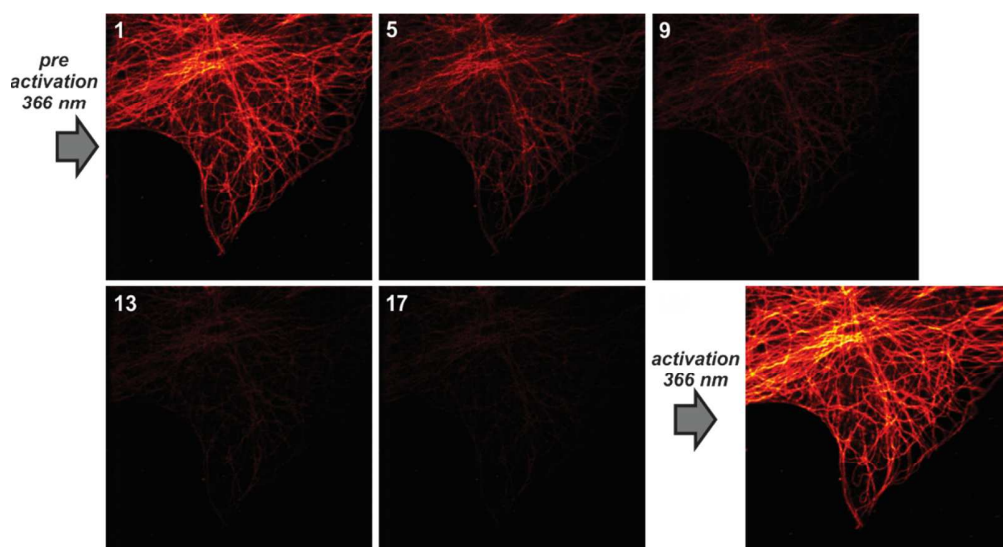


Figure S3. Confocal imaging with a 11 bioconjugate. A total of 17 frames were successively acquired on the same FOV (frames 1, 5, 9, 13, and 17 are shown). The sample was then exposed for a few seconds to UV light (wide-field illumination of a Hg lamp selected with a filter), and a new frame was acquired. Exact same imaging settings were used for all frames.

3.5 Superresolution (PALM/STORM) imaging

3.5.1 STORM Microscope:

The microscope (Figure S4) is based on a commercial microscope stand (Olympus IX71) and imaging was carried out using a 100 x 1.4 NA oil-immersion objective (OB: Olympus UPLSAPO 100XO). Excitation light sources included a 488 nm Argon laser (L 488: Innova 70C Argon filled, Coherent, ~ 0.5 kW/cm²), and a 375 nm laser diode (L 375: CUBE 375, Coherent, ~ 13 W/cm²). The 488 nm was modulated using an acousto-optic tunable filter (AOTF: PCAOM VIS, Crystal Technology). The 375 nm beam was combined into the excitation beam path after the AOTF by a dichroic mirror (Di01-R405-25x36, Semrock), and was modulated using its own digital & analog modulation inputs. The combined beams were expanded and cropped using an aperture, in order to achieve a relatively flat illumination profile, before being focused to the back focal plane of the objective lens, such that the light beam reaching the sample is collimated. The lateral position of the excitation beam focus in the objective was adjusted using a translation stage in the excitation beam path, such that the illumination could be brought in to a total-internal-reflection (TIRF) configuration.

A quad band dichroic mirror (ZT405/488/561/640rpc, Chroma) was used to separate the incoming excitation light from the outgoing fluorescence. The fluorescence was further filtered using a quad band notch filter (NF01-405/488/557/640-25x5.0-D, Semrock) and a band-pass filter (FF01-582/75-25, Semrock). The fluorescence image of the sample was relayed through a telescope and detected using an EMCCD camera (IXON+ DU860, Andor Technologies).

Sample focus was maintained during imaging using a custom-built focus lock system. An infrared laser beam was introduced into the microscope through the right side port and coupled into the optical path using a dichroic mirror (900SPRDC, Chroma). The beam was focused to the back focal plane of the objective and the focal position was adjusted to bring the beam into TIRF at the water-glass interface in the sample. The position of the reflected beam was monitored using a quadrant-photodiode and this provided a measure of the sample position above the objective lens. The objective lens position was then continuously adjusted using a piezo positioner (MIPOS 250, Piezo Jena). Residual infrared light was blocked in the detection path using a short-pass filter (FF01-842/SP-25, Semrock).

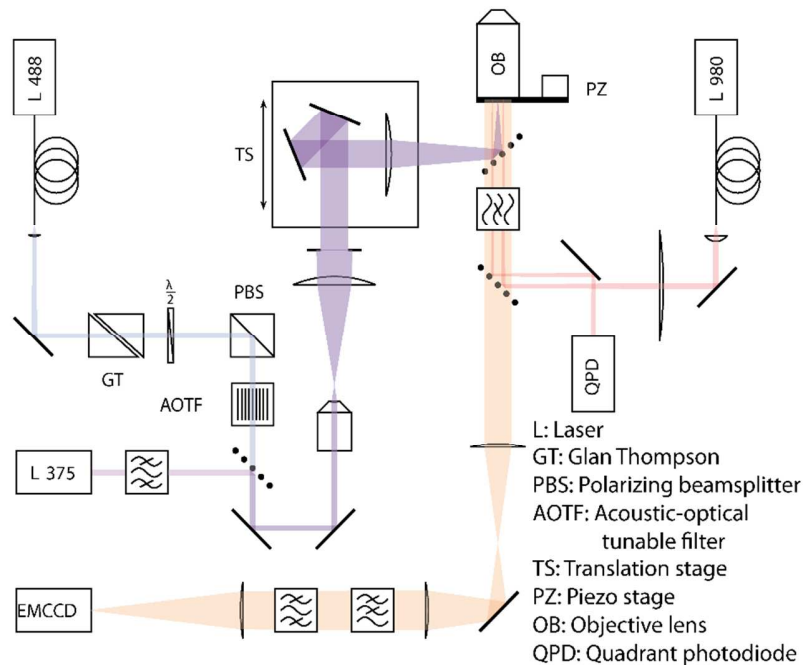


Figure S4. Schematic representation of the microscope used, a custom-build wide field microscope with a TIRF illumination system.

3.5.2 Detected photons per switching event

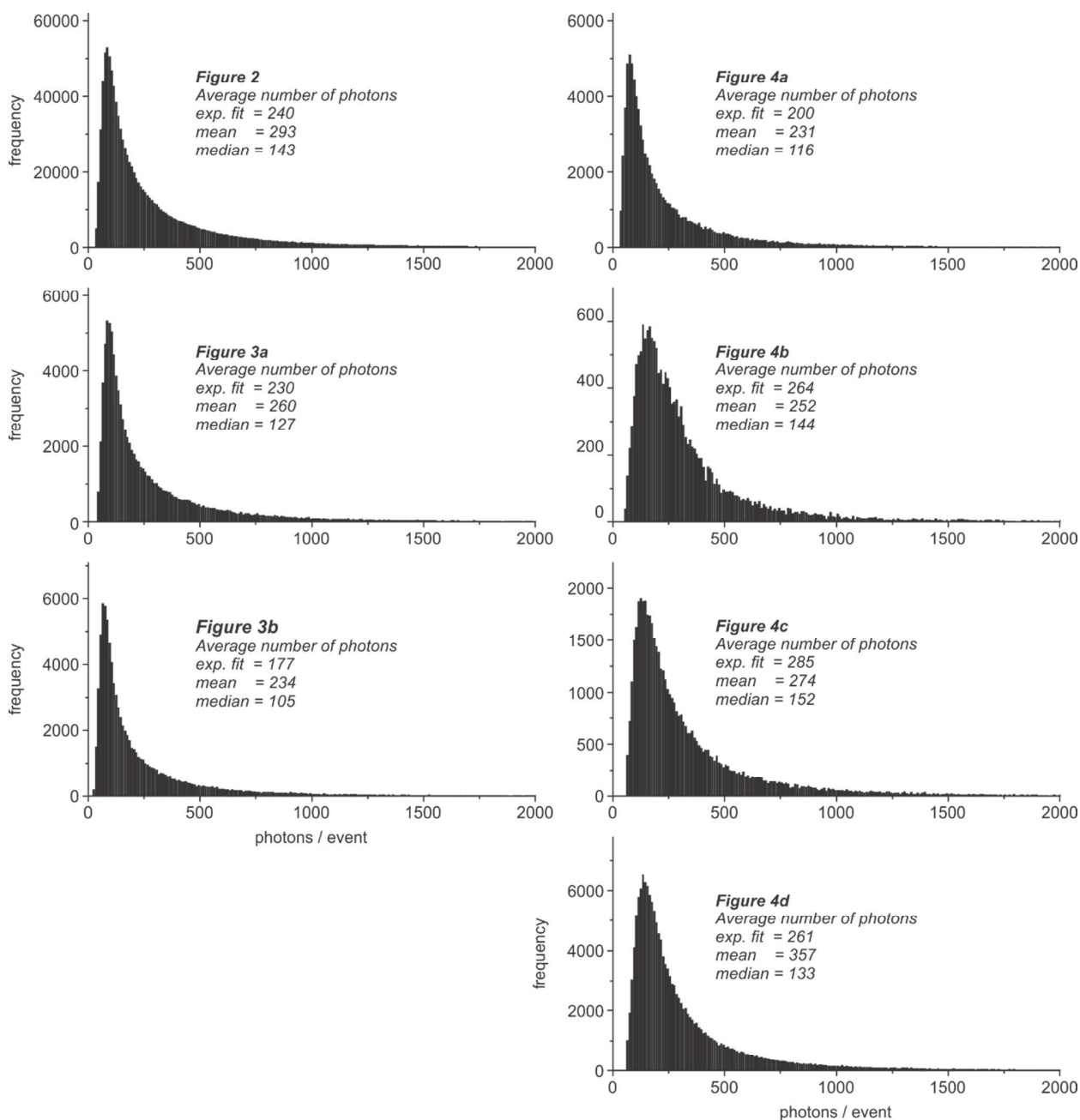


Figure S5. Histogram of detected photons per switching event, generated from every single molecule localized and used to reconstruct superresolution images presented in the text (Figures 2 – 4). The average values reported for each case were calculated from a mono-exponential fit, as in Dempsey *et al.* (6). When calculating the mean or median value, only photon counts on the right side of the distribution (larger than the maximum of the histogram) were considered.

3.5.3 Photoinduced control of the amount of events per frame

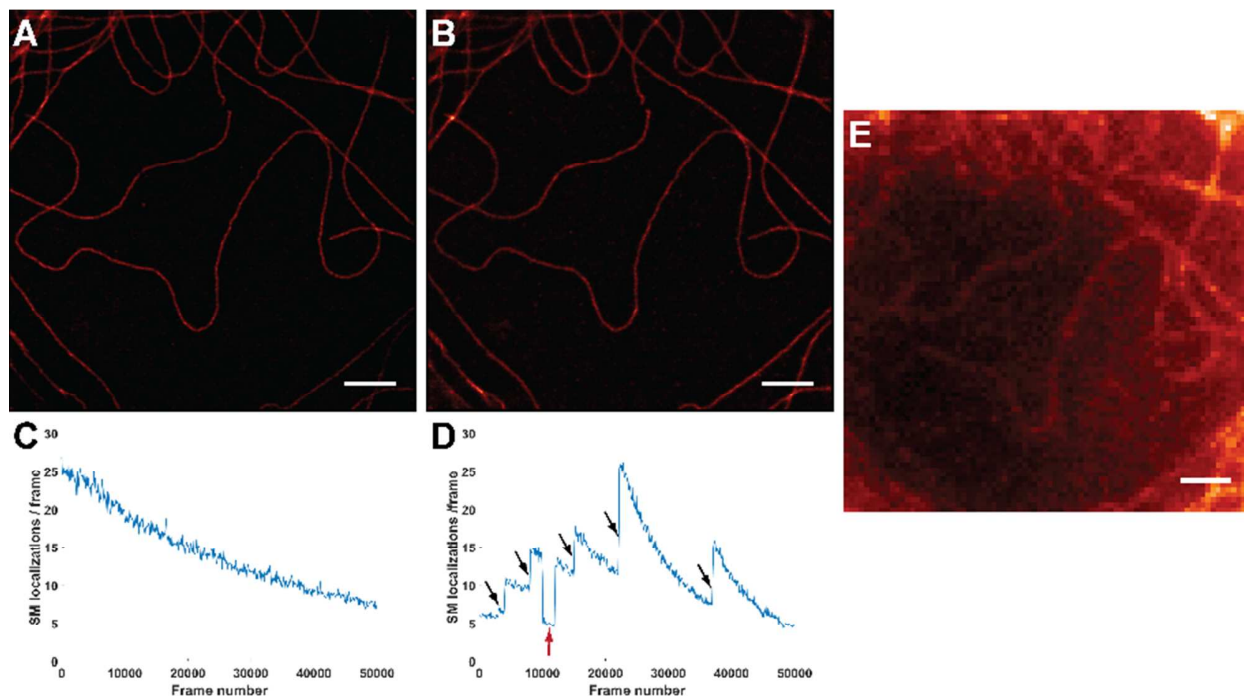


Figure S6. Superresolution images (STORM) without (A) and with activation light of 375 nm (B), of Vero cells immunostained with a primary antibody against tubulin and a secondary antibody labelled with compound **4-Et** (DOL = 3.5). Mounting media used was PBS pH = 7.4. No photoactivation (only excitation at 488 nm) was used in the first 50000 frames; slow photobleaching is evidenced by an exponential decay of the detected events per frame (C). Then, the activation laser was enabled at low power and increased stepwise, as indicated by black arrows in (D). The activation laser was disabled for ca. 2000 frames (red arrow); spontaneous activations is still present, but at a lower rate than in the presence of photoactivation (the latter is ~3-fold higher). At the end of the image acquisition, the activation laser was considerable increased beyond the condition to achieve a sparse distribution but enough to achieve a wide field image; a frame (only 10 ms integration) is shown in (E). This demonstrates the remaining amount of usable markers after 100000 frames. The inhomogeneity of the bleaching is also appreciated. Scale-bars: 2 μ m.

3.6 Photoswitching fatigue resistance of compounds 4-Et and 11 at the ensemble level, in methanol and aqueous buffered solutions

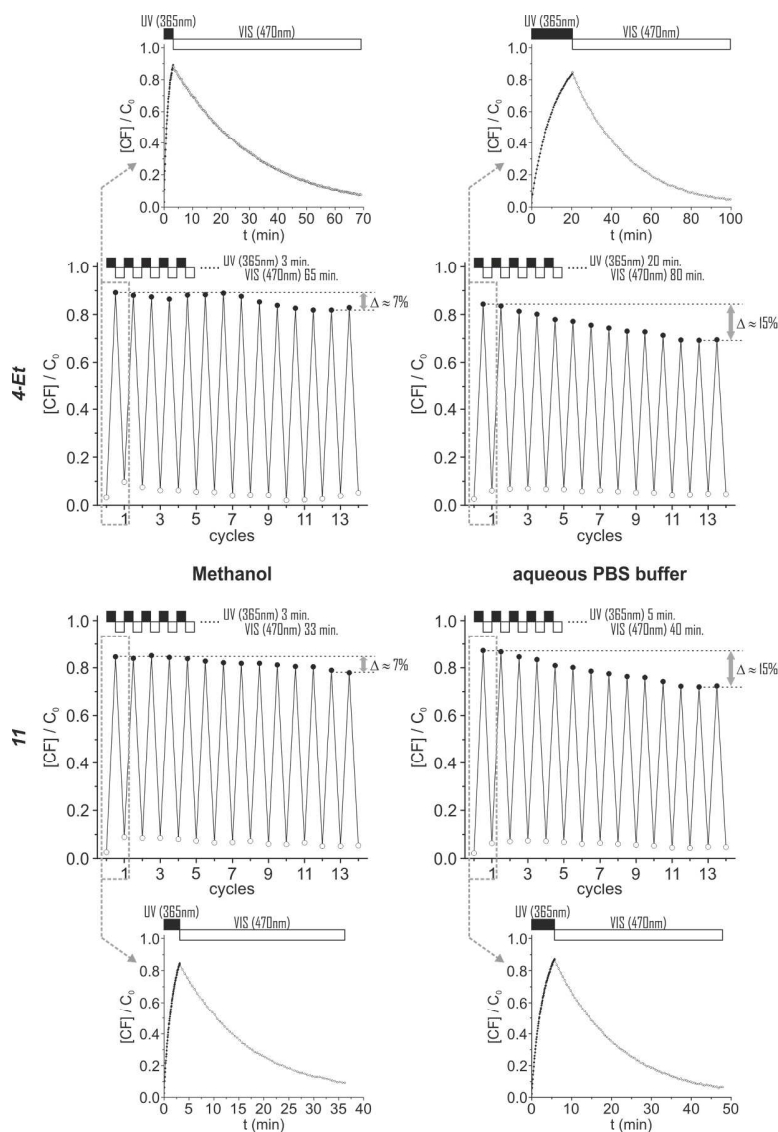


Figure S7. Photoswitching fatigue resistance of compounds 4-Et and 11 in methanol and aqueous PBS. Solutions of each compound (OF) were freshly prepared ($c_0 = 4\text{--}5\ \mu\text{M} = [\text{OF}] + [\text{CF}]$). The samples (3 mL) were irradiated under continuous stirring with UV light (365 nm), until 85–90% conversion to the CF ($\alpha_{\text{CF}} = [\text{CF}]/c_0 > 0.85$) was achieved, and then irradiated with visible light (470 nm), until the reaction was reversed to a conversion below 10 % ($\alpha_{\text{CF}} < 0.10$). The intensity of the irradiation sources ($20\ \text{mW}/\text{cm}^2$ and $35\ \text{mW}/\text{cm}^2$ for UV and visible light, respectively) was the same in all experiments. The time required for each semi-cycle was found ($t_{\text{UV}} = 3\text{--}20\ \text{min}$ and $t_{\text{VIS}} = 33\text{--}80\ \text{min}$) and used for repeating the photoconversion for 14 full cycles (in total, 8 – 23 hours of irradiation was required for each solution). The degree of conversion was evaluated by measuring the absorption of the closed form in the visible range using a single beam spectrometer. The amount of compound irreversibly photobleached after 14 cycles was very similar for both compounds, and amounted to 7% in methanol, and 15 % in PBS ($\pm 2\%$). From this experiment, we can conclude that these compounds can endure in average several tens of cycles, determined from the number of cycles needed to photobleach half of the initial dye amount.

3.7 Fourier ring correlation analysis of the images

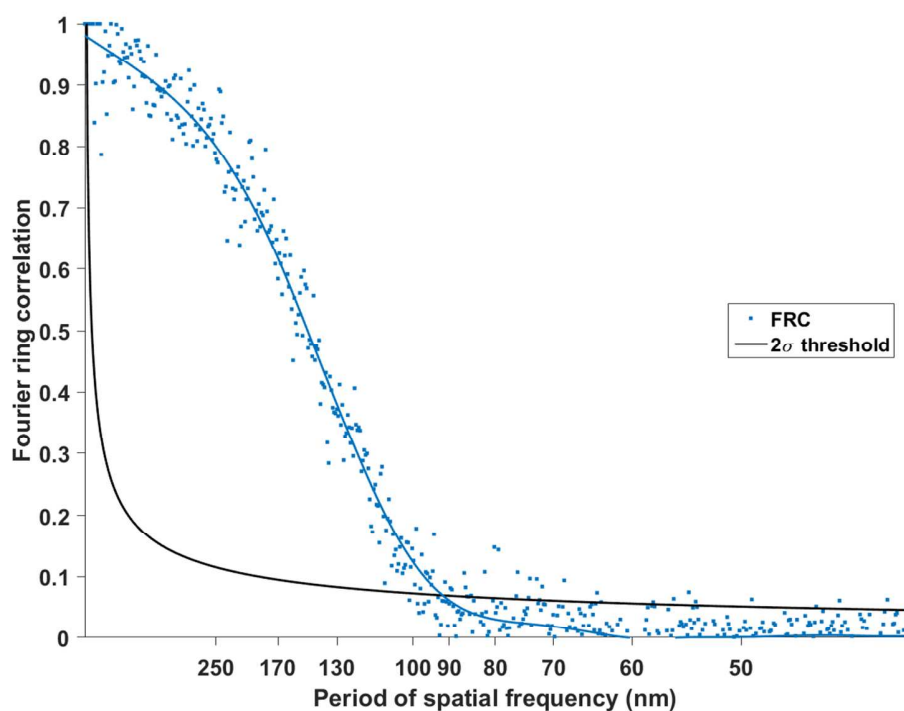


Figure S8. Fourier ring correlation (FRC) of the localizations presented in Figure 2; a smoothed FRC curve is shown as a solid blue line within the noisy FRC data (blue dots). The resolution of the image is estimated from the intersection between the FRC and the 2σ threshold, yielding a value of around 90 nm.

3.8 Imaging in “blinking buffer”

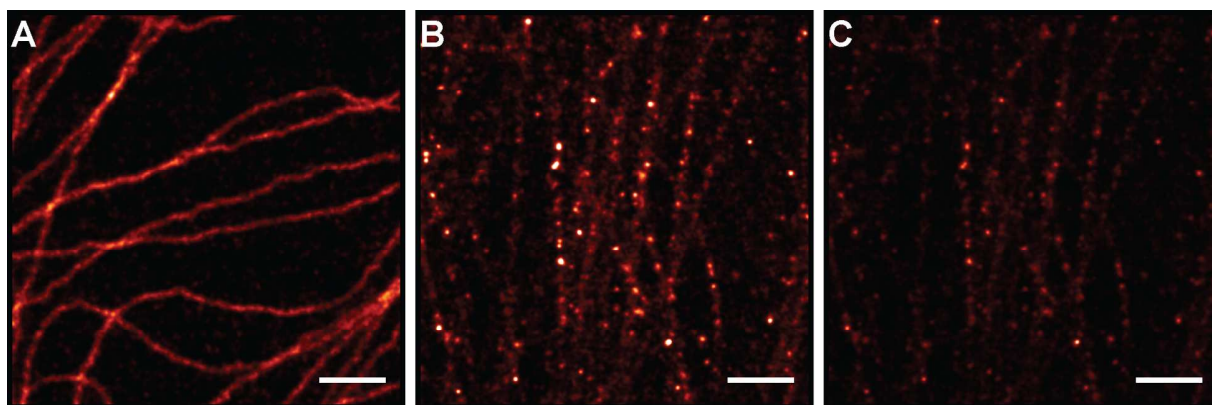
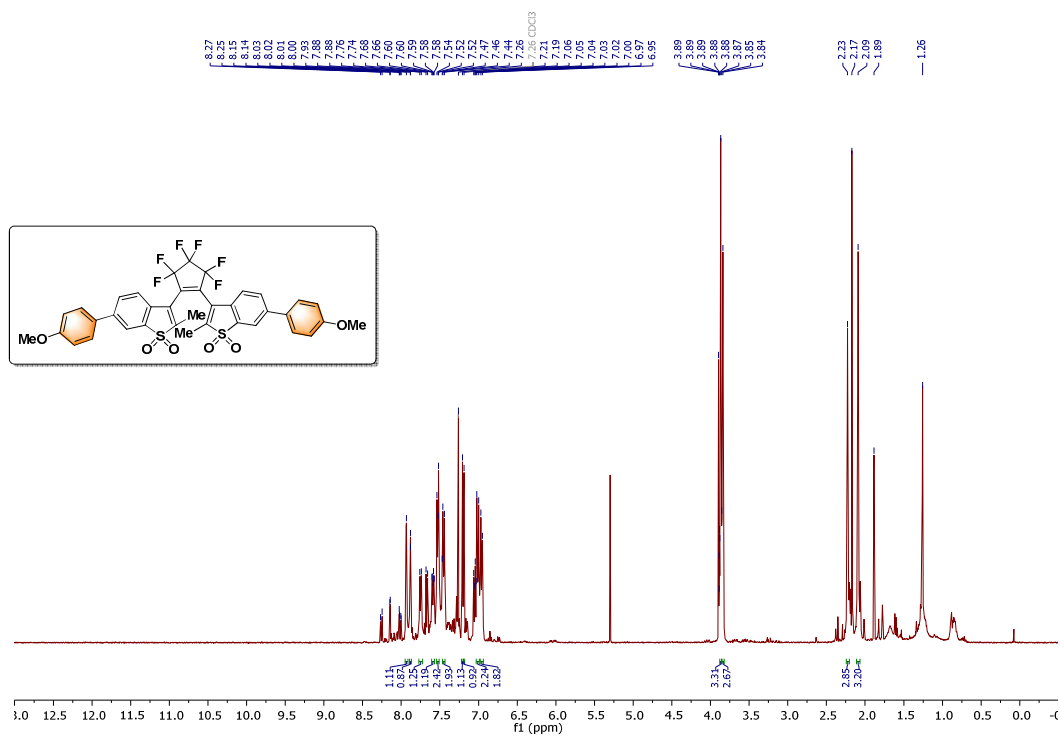


Figure S9. Superresolution images (STORM) of Vero cells immunolabeled with primary antibody against tubulin and secondary antibodies conjugated with compound 4-Et in (A) PBS pH = 7.4 and (B-C) in blinking buffer without UV activation. The image in B is the same as in C, with a saturated colormap. The blinking buffer (TRIS pH = 8.0) contained an enzymatic oxygen scavenger system and β -mercaptoethylamine. Scale-bars: 1 μ m.

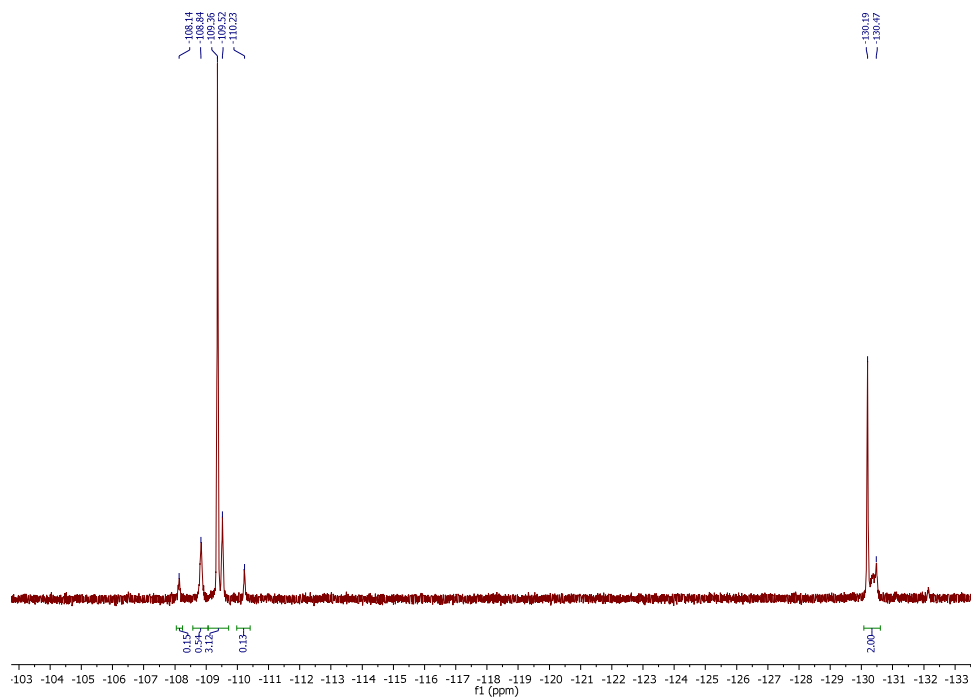
4. NMR spectra and RP-HPLC traces of symmetric dimethoxy DAEs derivatives: compounds 3, 4-Me and 4-Et

Compound 3

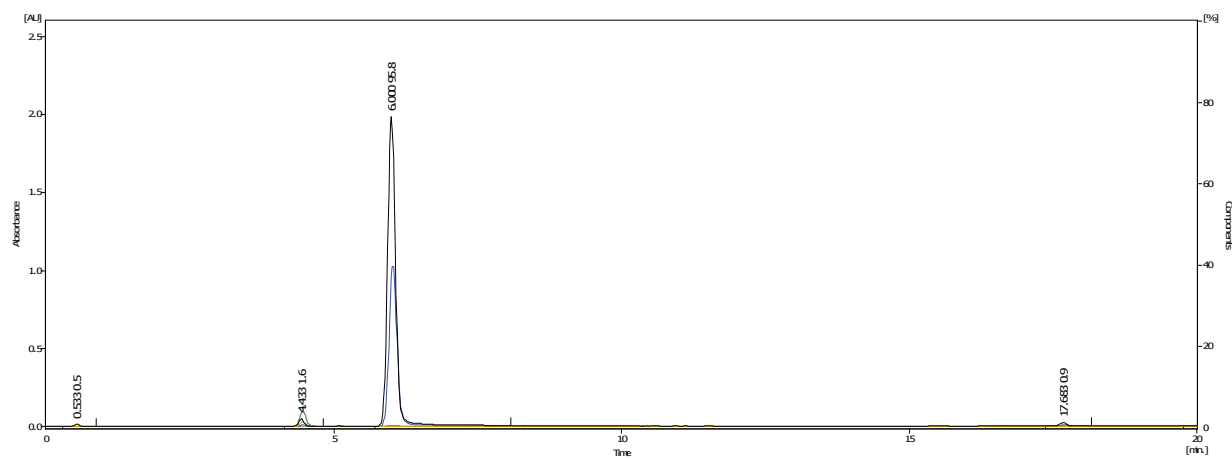
¹H NMR spectrum in CDCl₃ (400 MHz)



^{19}F NMR spectrum in DMF- d_7 (376 MHz)

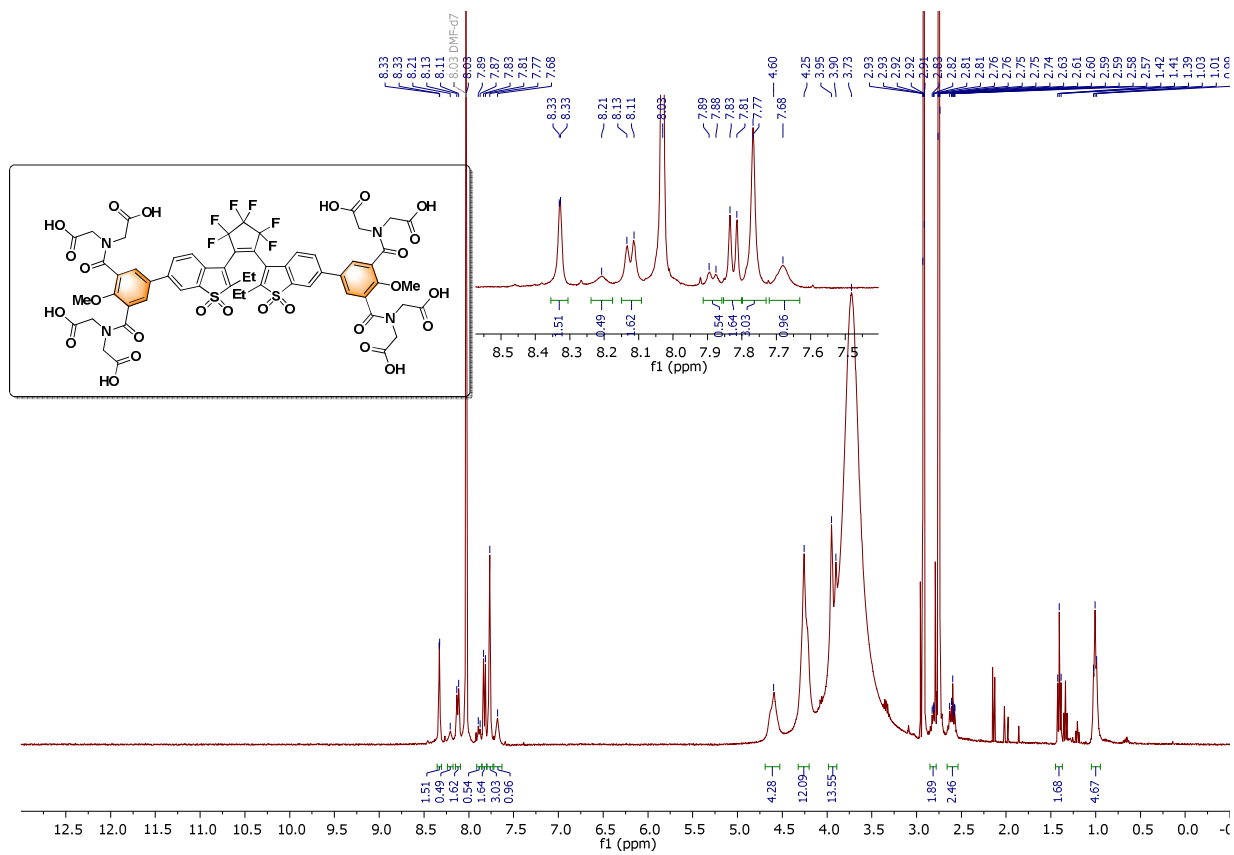


RP-HPLC elution profile (system A)

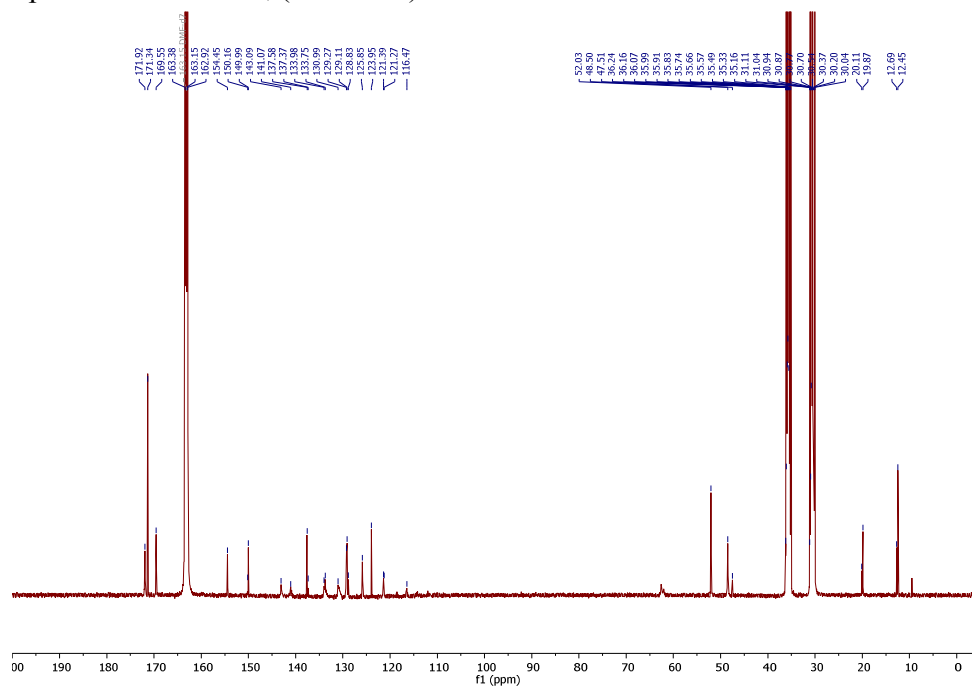


Compound 4-Et

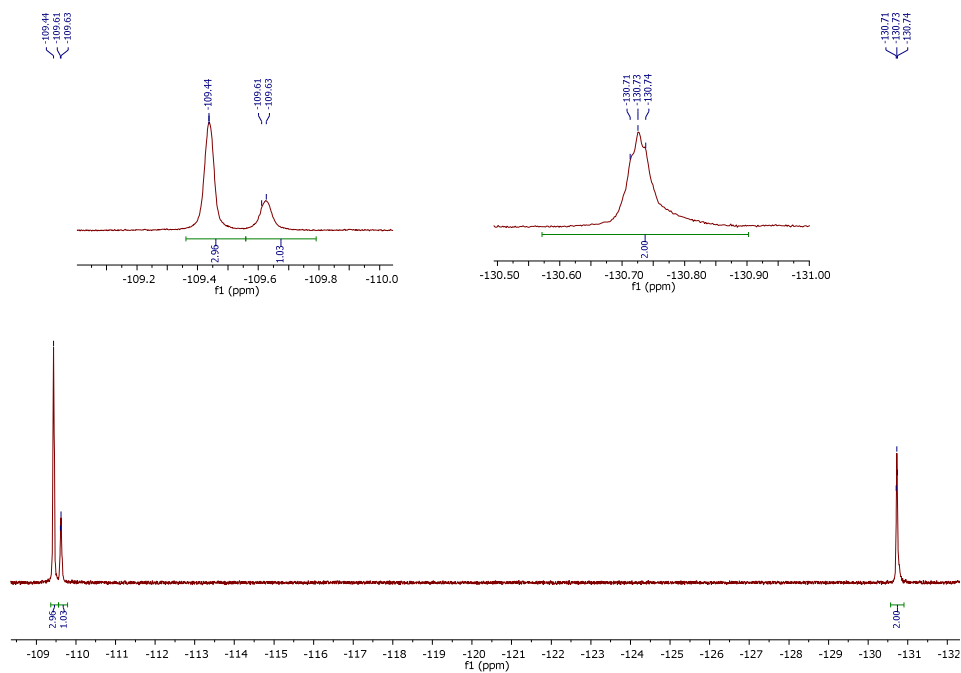
^1H NMR spectrum in DMF- d_7 (400 MHz)



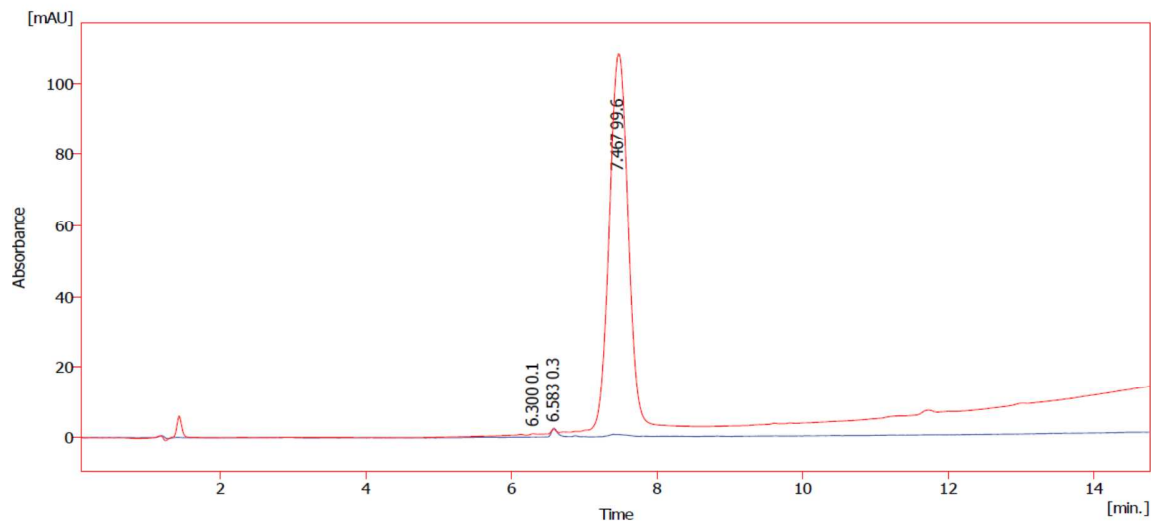
^{13}C NMR spectrum in DMF- d_7 (126 MHz)



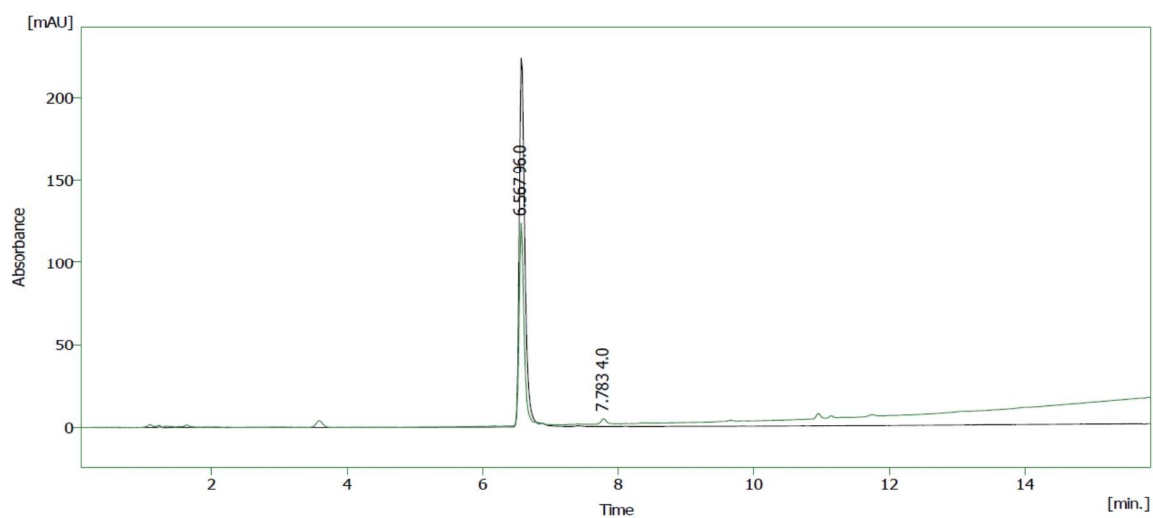
^{19}F NMR spectrum in DMF- d_7 (376 MHz)



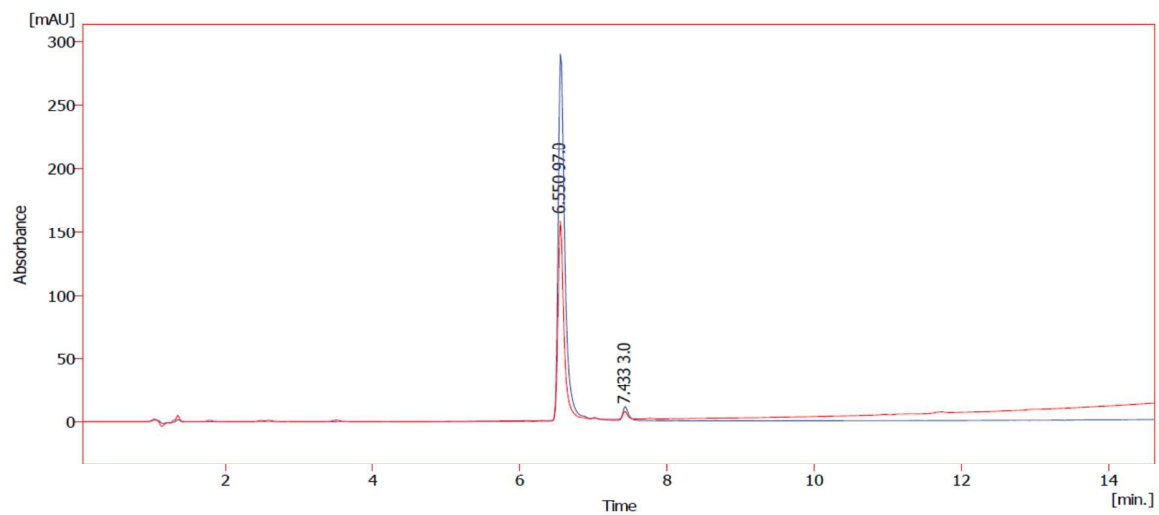
RP-HPLC elution profile (system F); “open-ring” isomer – red trace (254 nm), “closed-ring” isomer – blue trace (470 nm):



RP-HPLC elution profile (system F); “closed-ring” isomer showing green trace (254 nm) and black trace (470 nm) was isolated by HPLC and immediately analyzed in CD₃OD:



RP-HPLC elution profile (system F): “closed-ring” isomer in CD₃OD solution after storing for 3 weeks in the dark at room temperature; relative intensities of the red (254 nm) and blue (470 nm) traces indicate that the peak with $t_R = 7.43$ min is not an “open-ring” isomer:

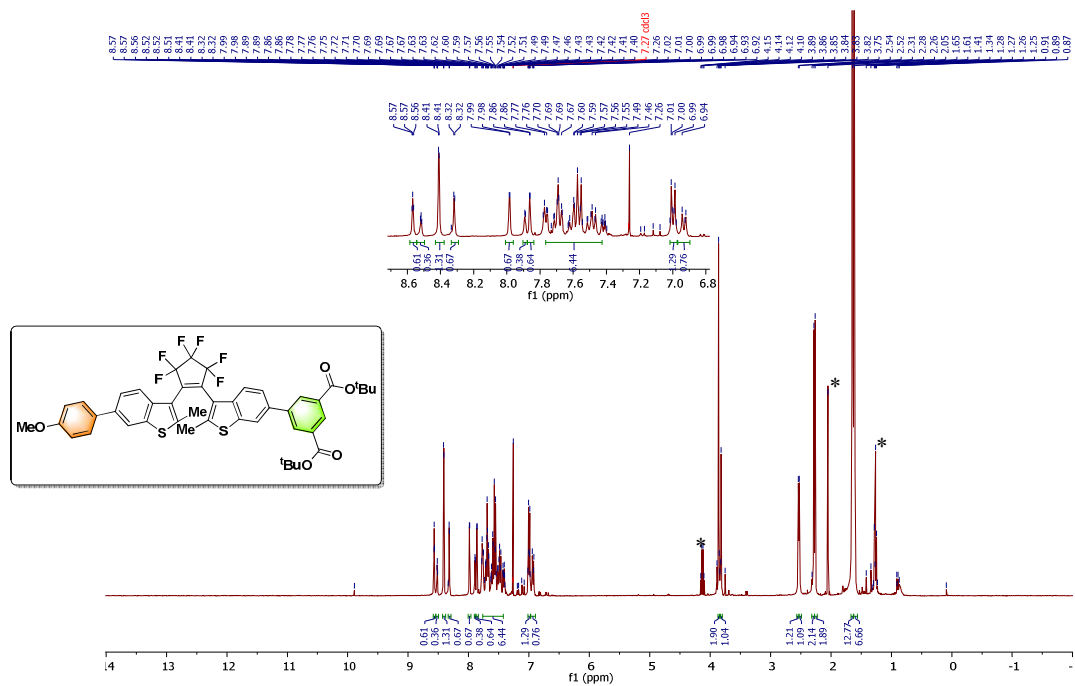


5. NMR spectra and RP-HPLC traces of asymmetric DAEs derivatives

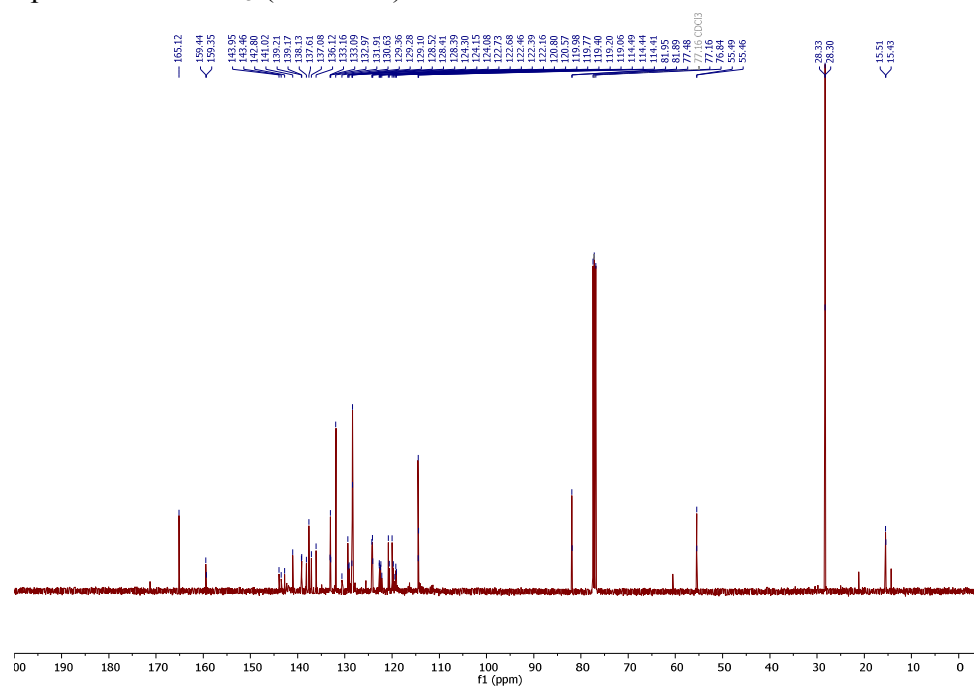
Compound S5a

^1H NMR spectrum in CDCl_3 (400 MHz)

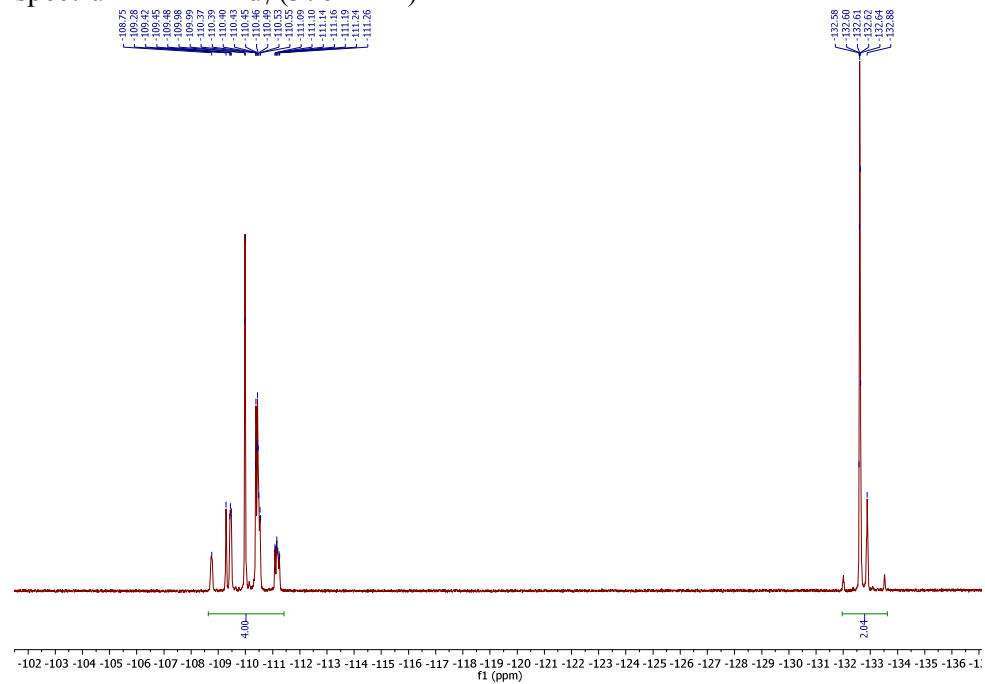
* peaks assigned to residual EtOAc



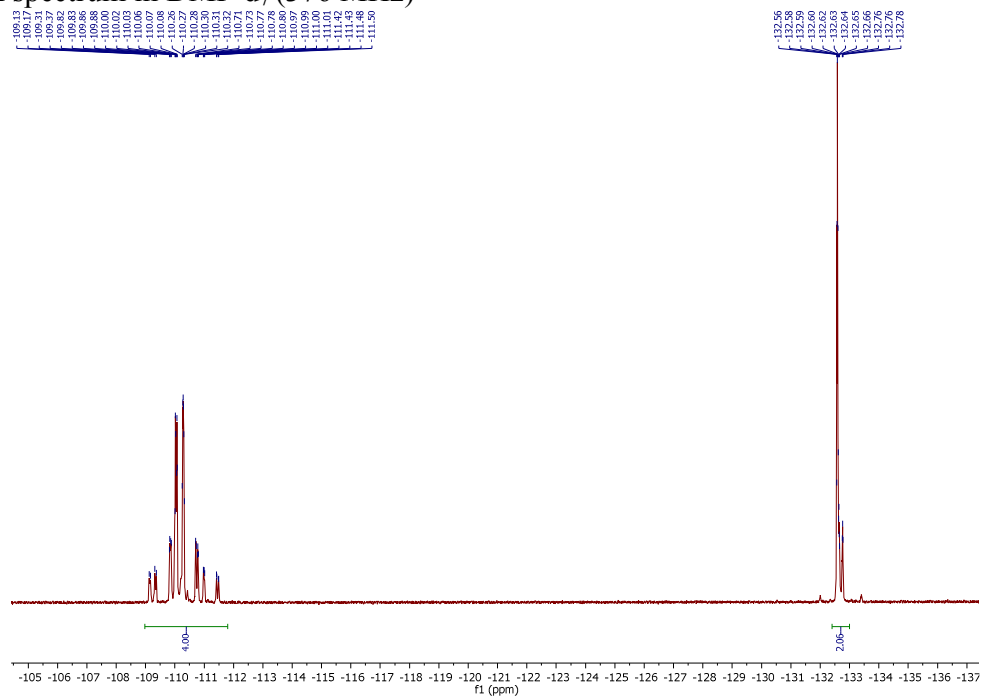
^{13}C NMR spectrum in CDCl_3 (101 MHz)



^{19}F NMR spectrum in DMF-d_7 (376 MHz)



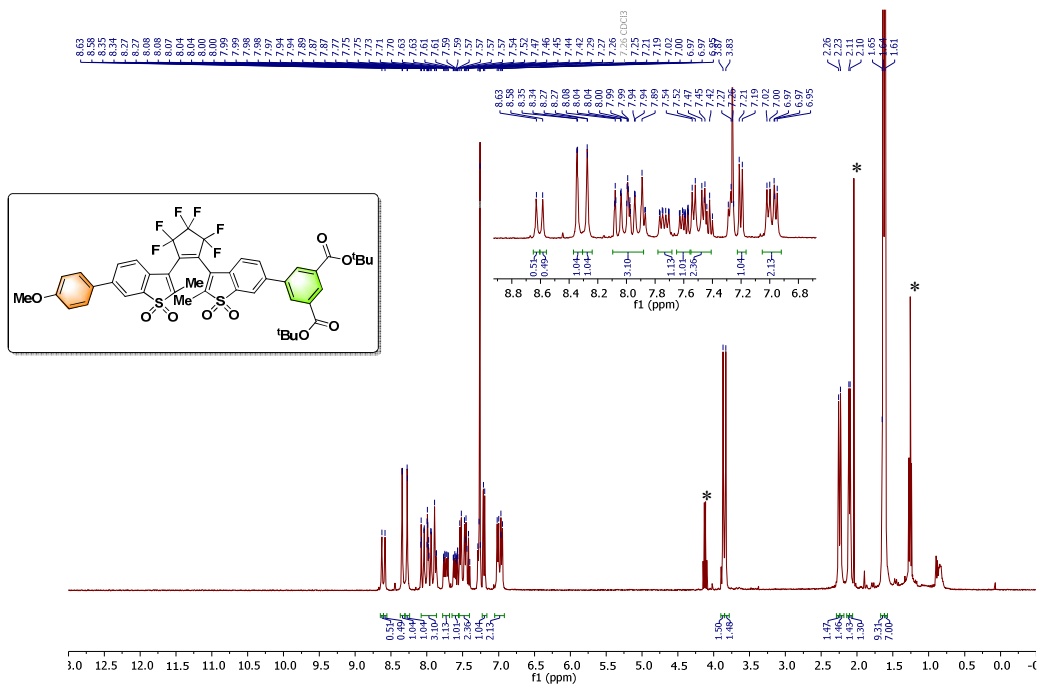
¹⁹F NMR spectrum in DMF-d₇ (376 MHz)



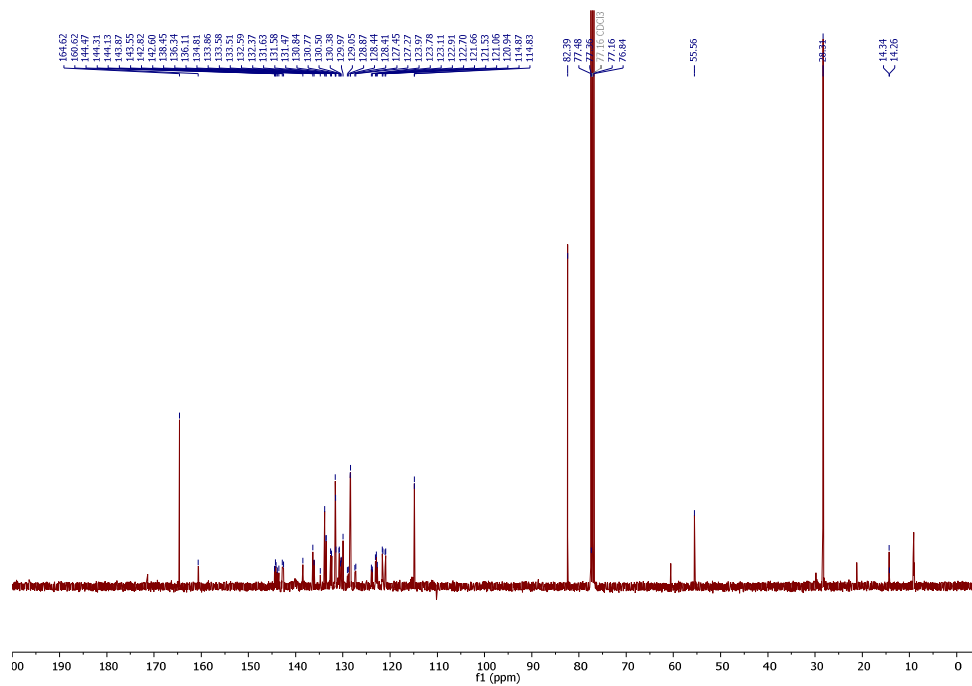
Compound S6a

¹H NMR spectrum in CDCl₃ (400 MHz)

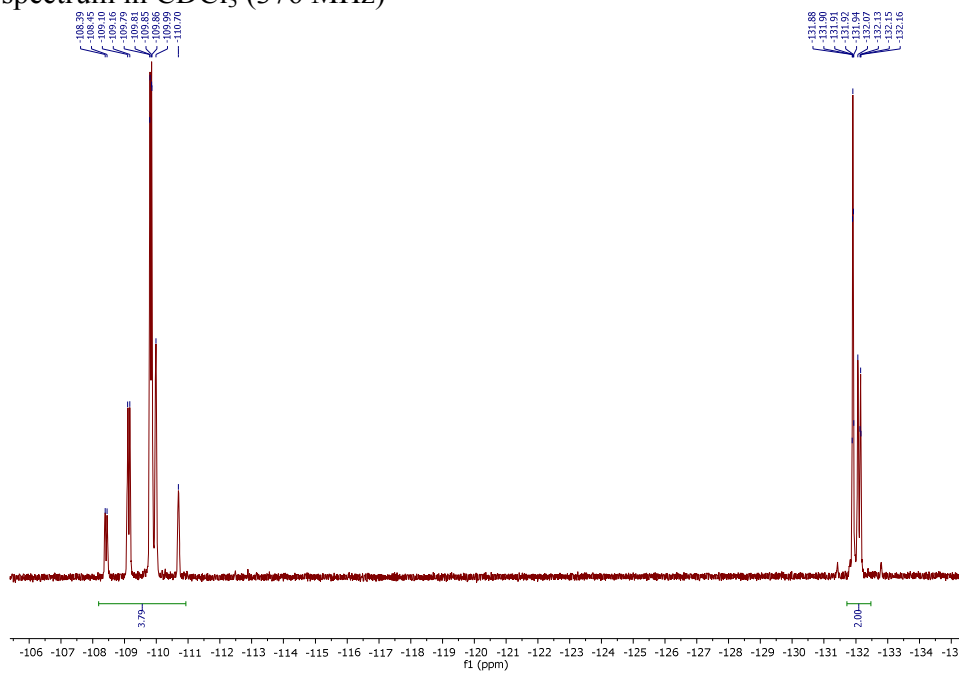
* peaks assigned to residual EtOAc



^{13}C NMR spectrum in CDCl_3 (101 MHz)

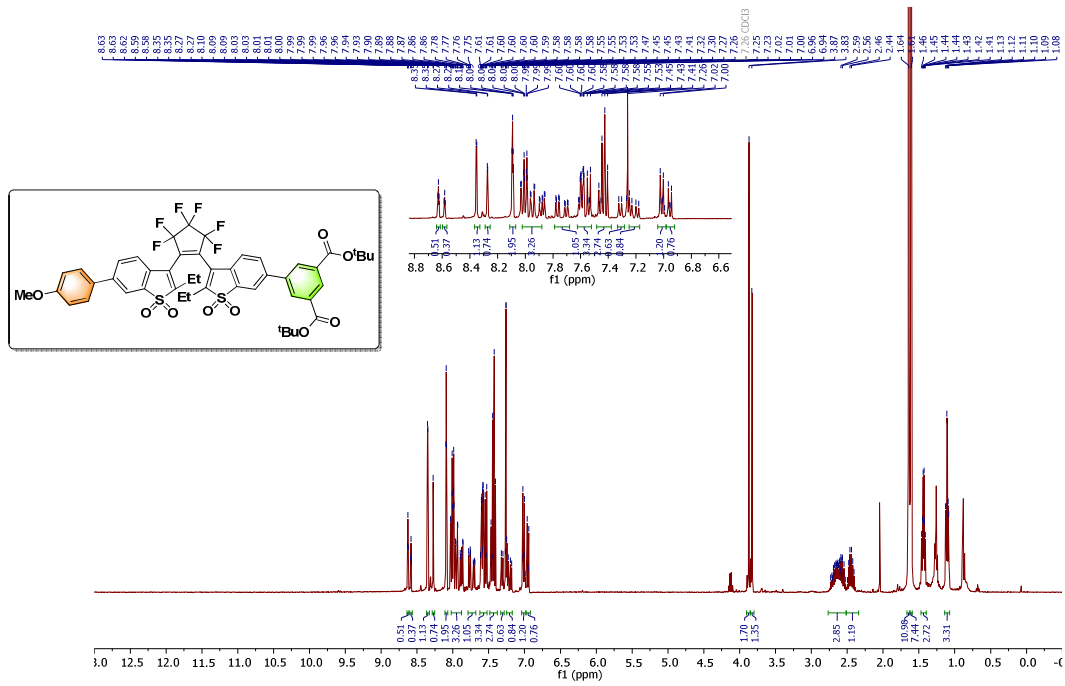


^{19}F NMR spectrum in CDCl_3 (376 MHz)

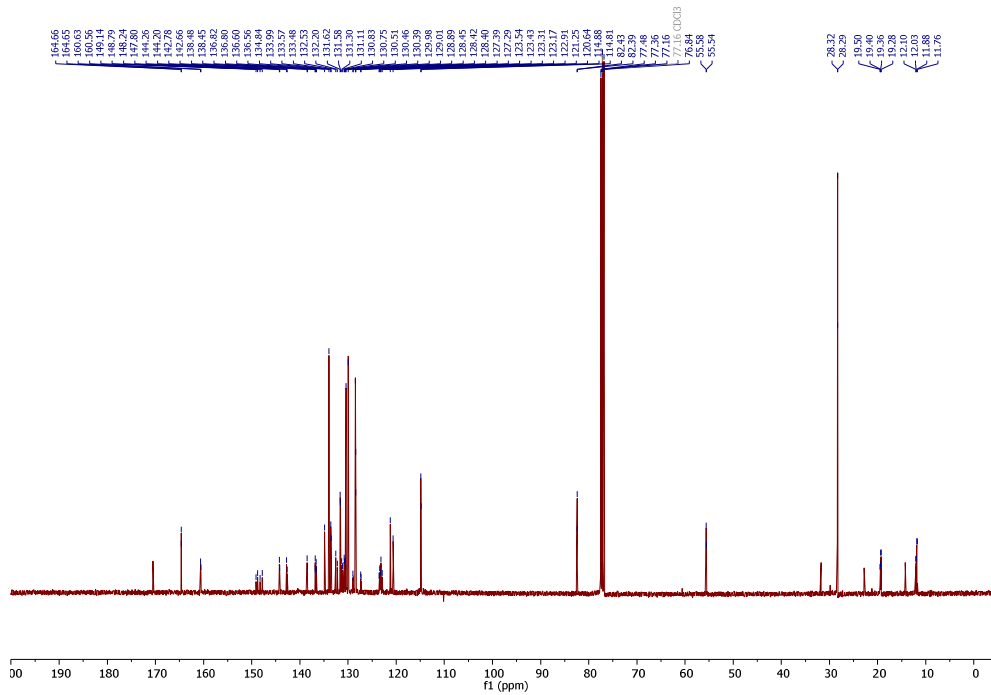


Compound S6b

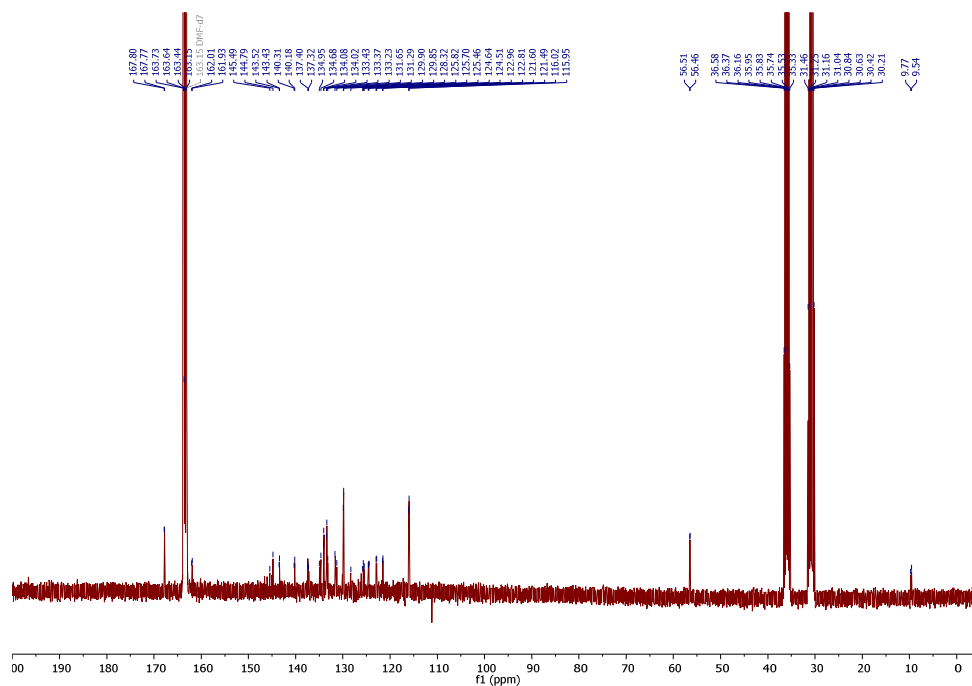
¹H NMR spectrum in CDCl₃ (400 MHz)



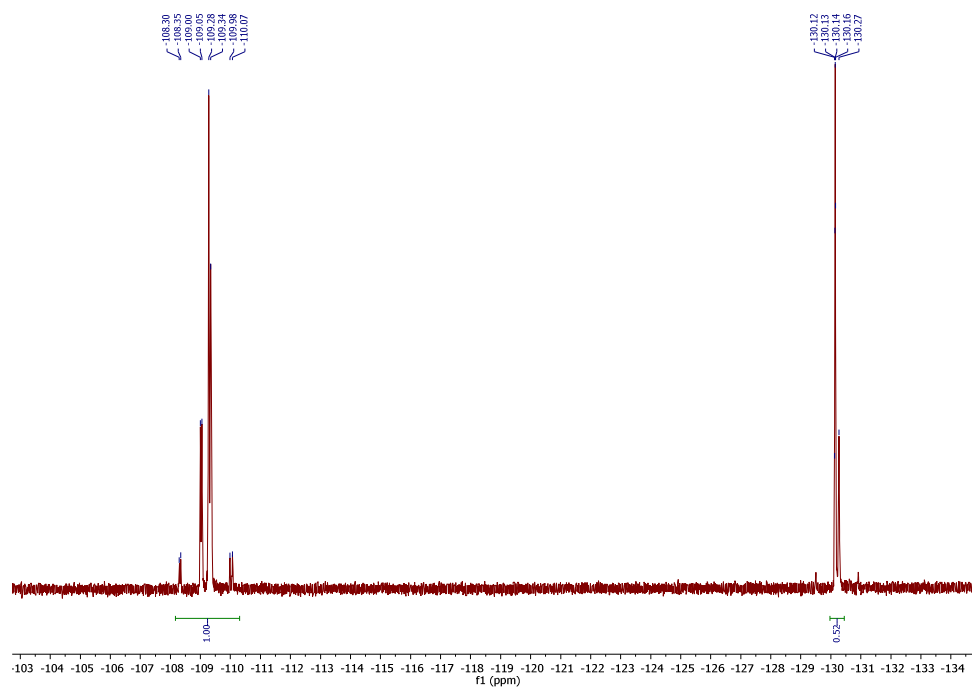
¹³C NMR spectrum in CDCl₃ (101 MHz)



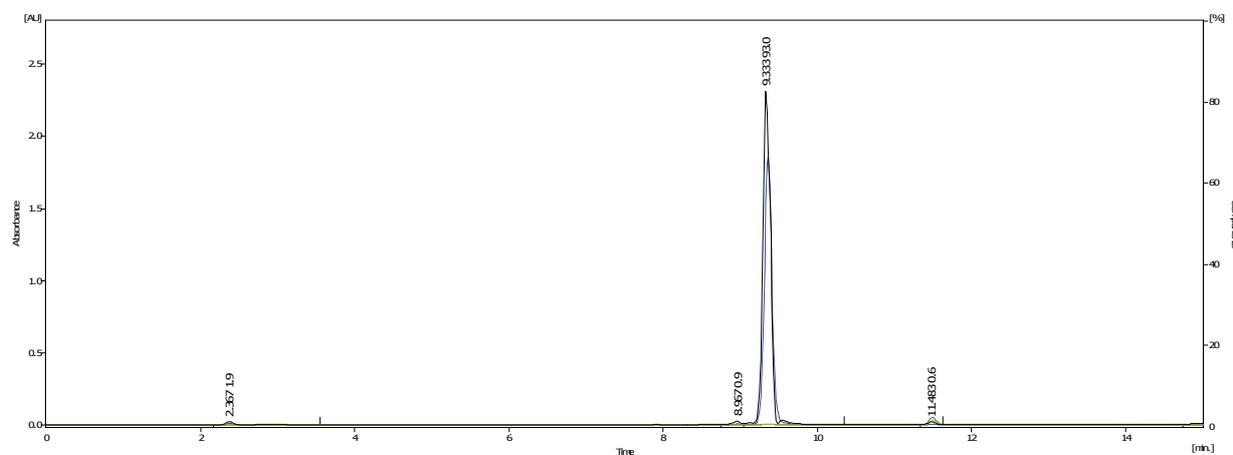
^{13}C NMR spectrum in DMF- d_7 (126 MHz)



^{19}F NMR spectrum in DMF- d_7 (376 MHz)

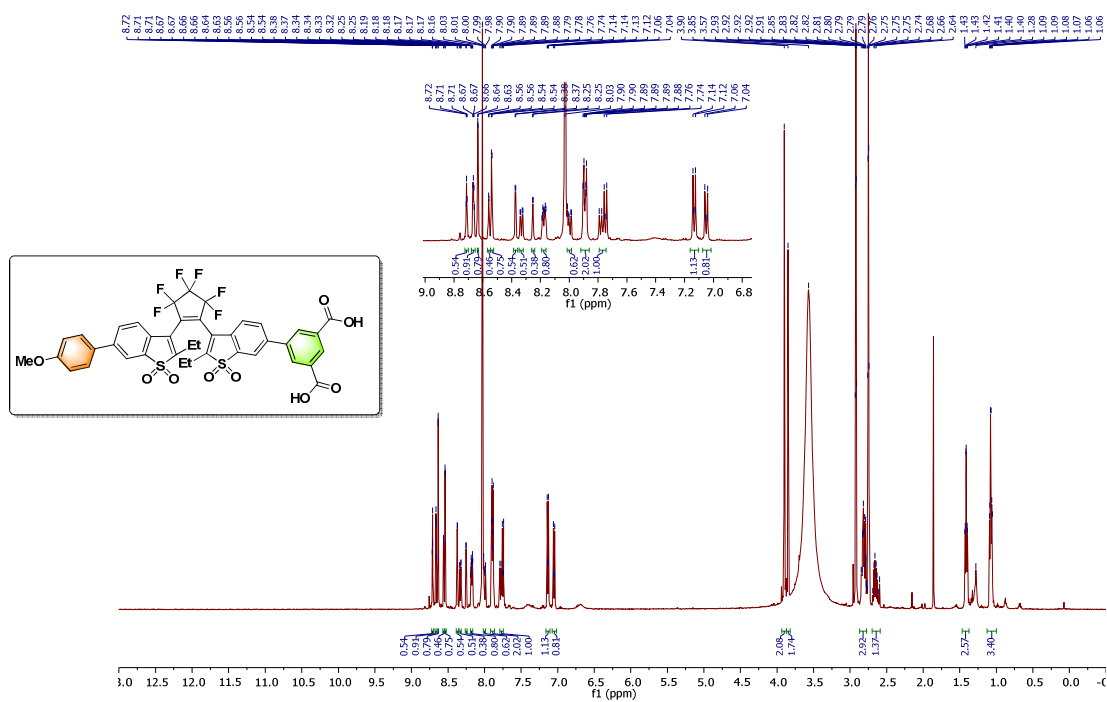


RP-HPLC elution profile (system C)

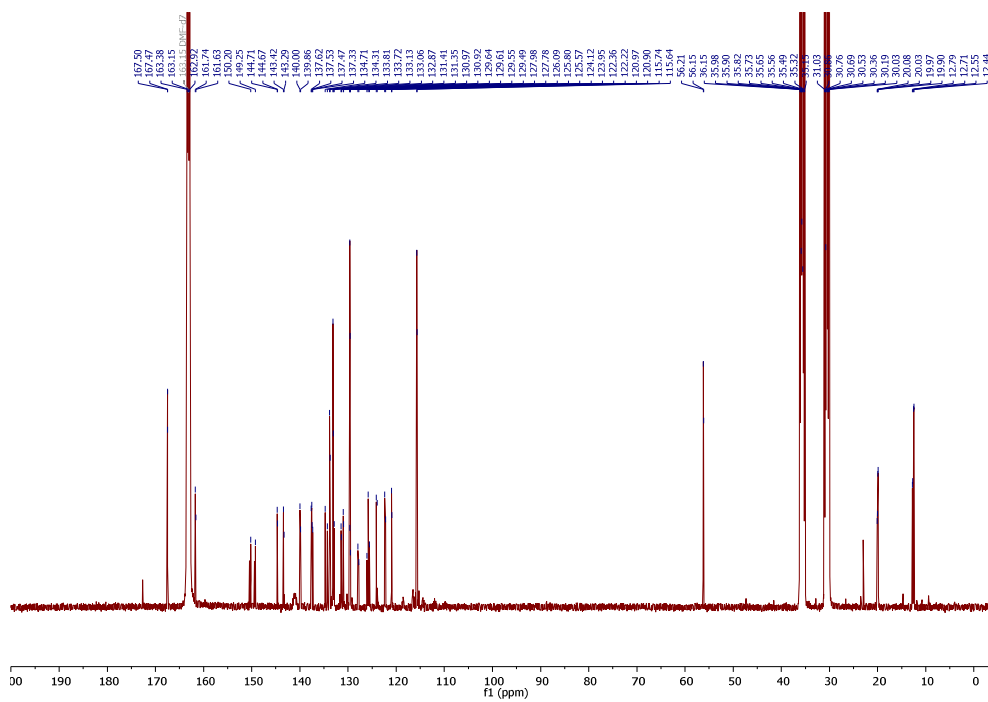


Compound 7-Et

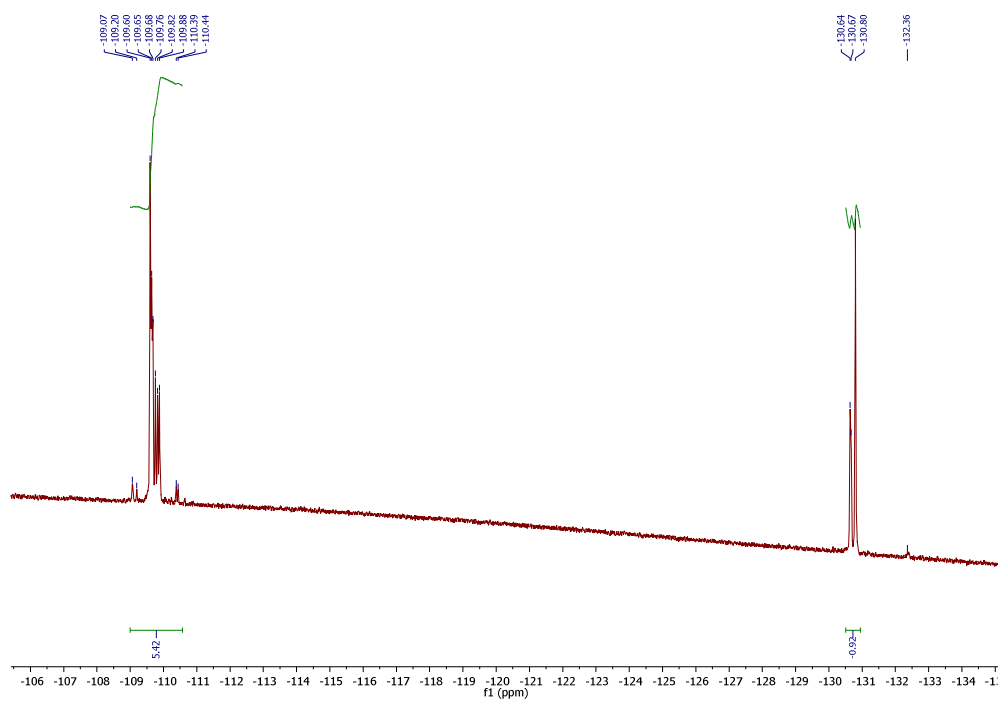
^1H NMR spectrum in DMF-d_7 (500 MHz)



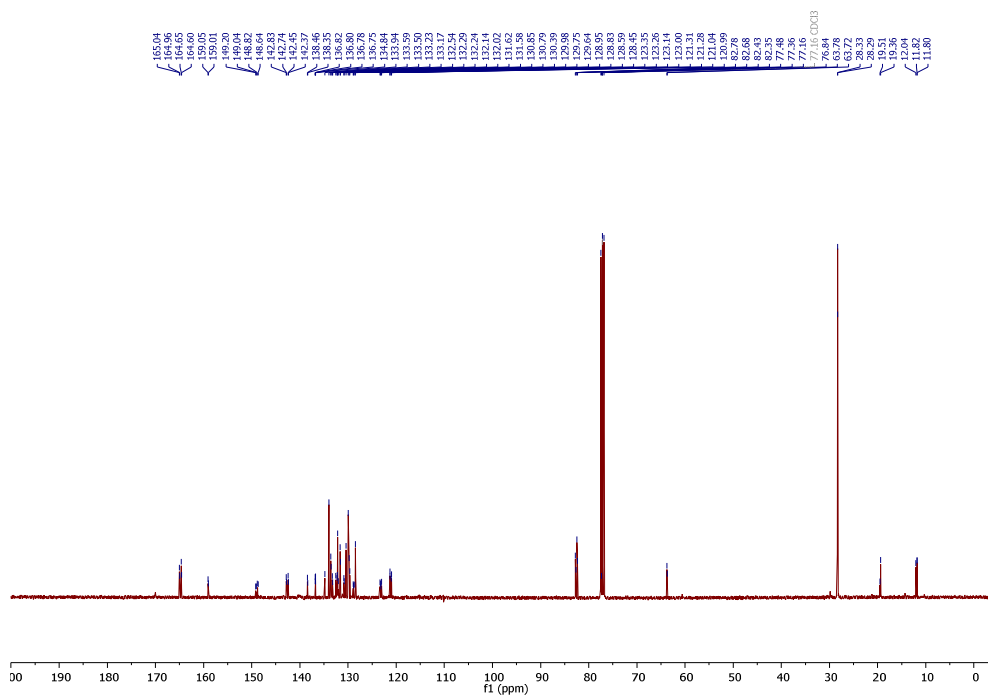
^{13}C NMR spectrum in DMF- d_7 (126 MHz)



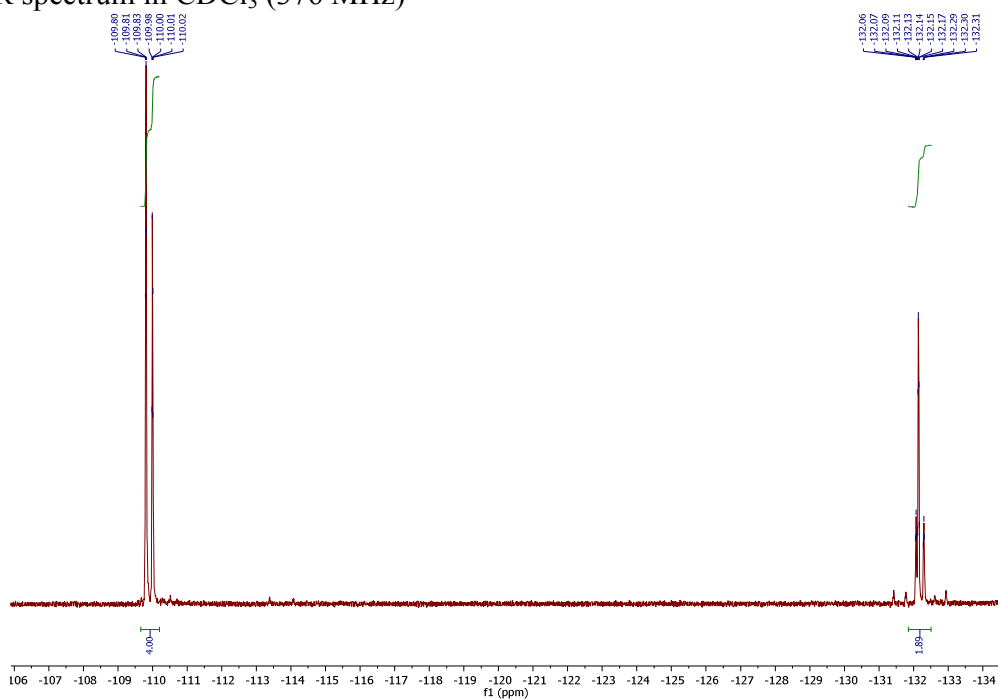
^{19}F NMR spectrum in DMF- d_7 (471 MHz)



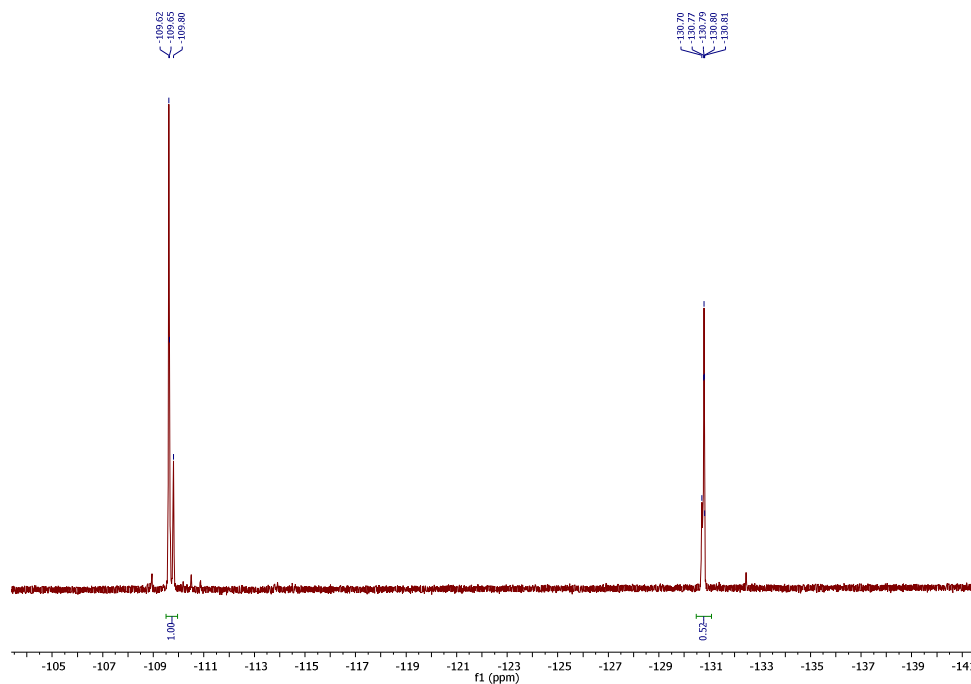
^{13}C NMR spectrum in CDCl_3 (101 MHz)



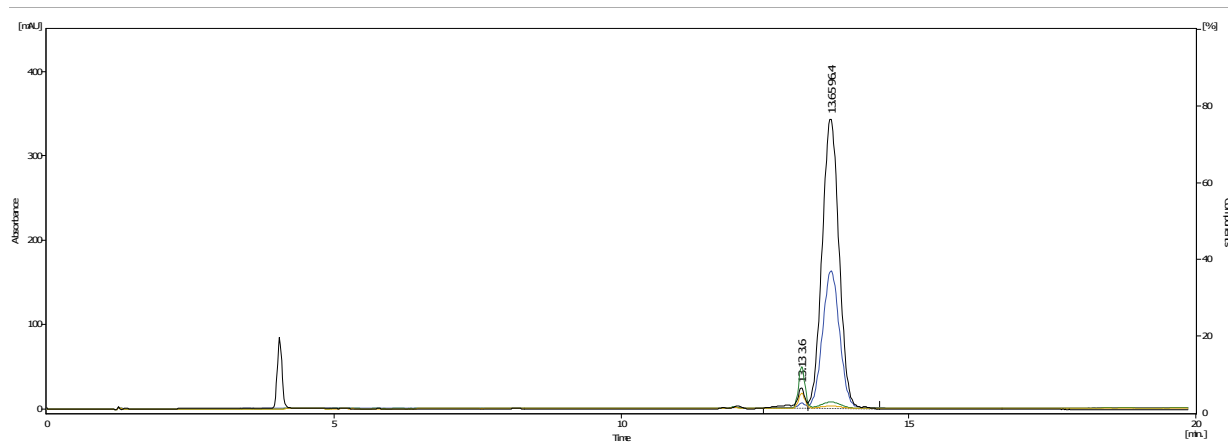
^{19}F NMR spectrum in CDCl_3 (376 MHz)



^{19}F NMR spectrum in DMF- d_7 (471 MHz)

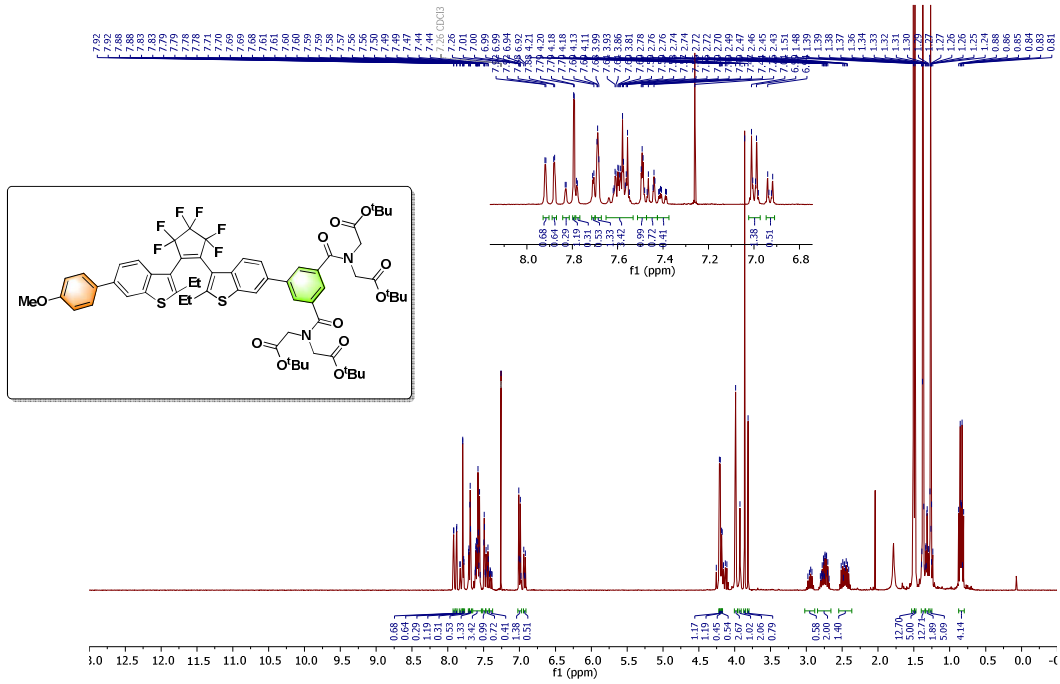


RP-HPLC elution profile (system A)

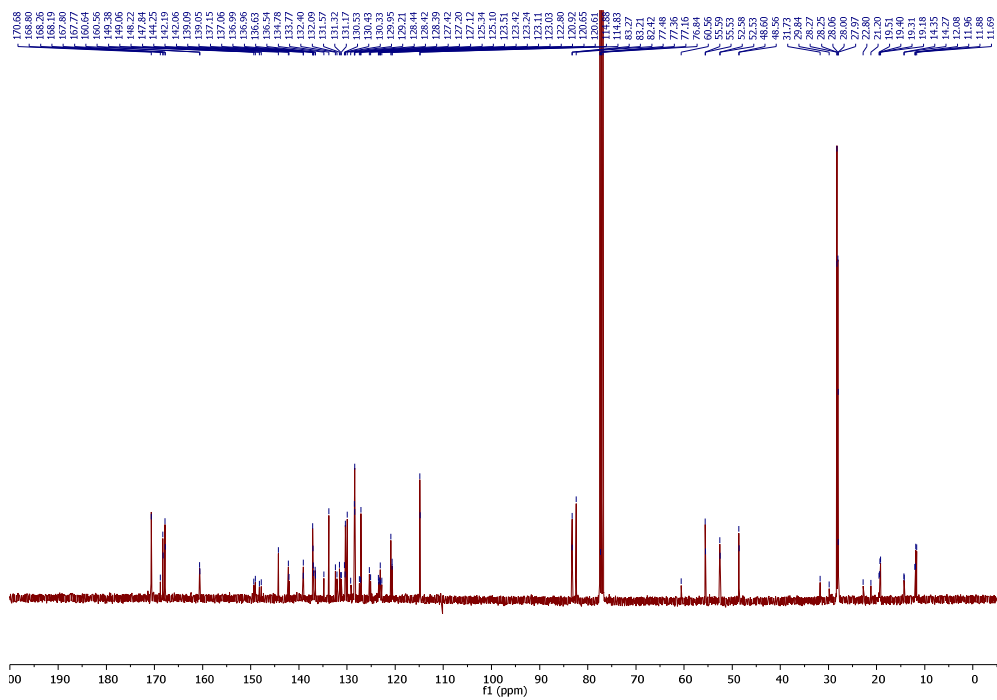


Compound S10

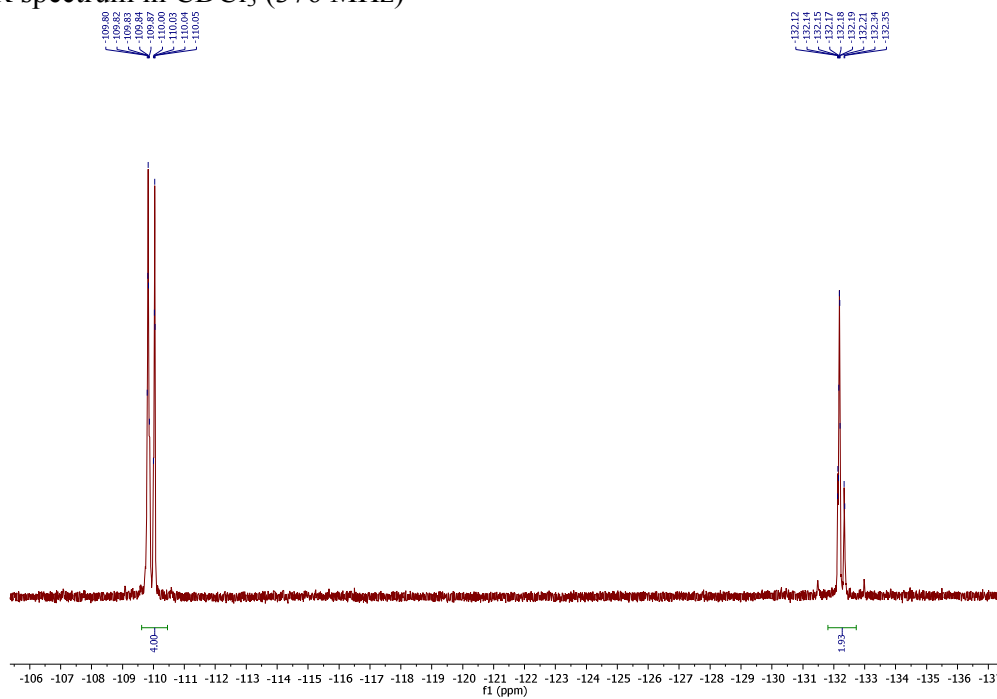
¹H NMR spectrum in CDCl₃ (400 MHz)



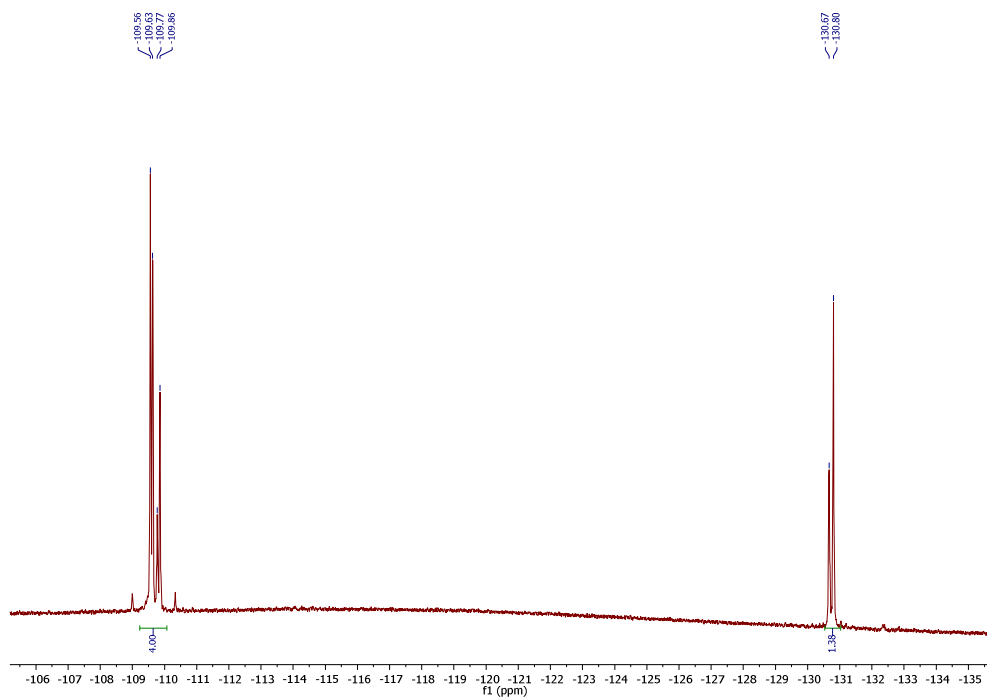
¹³C NMR spectrum in CDCl₃ (101 MHz)



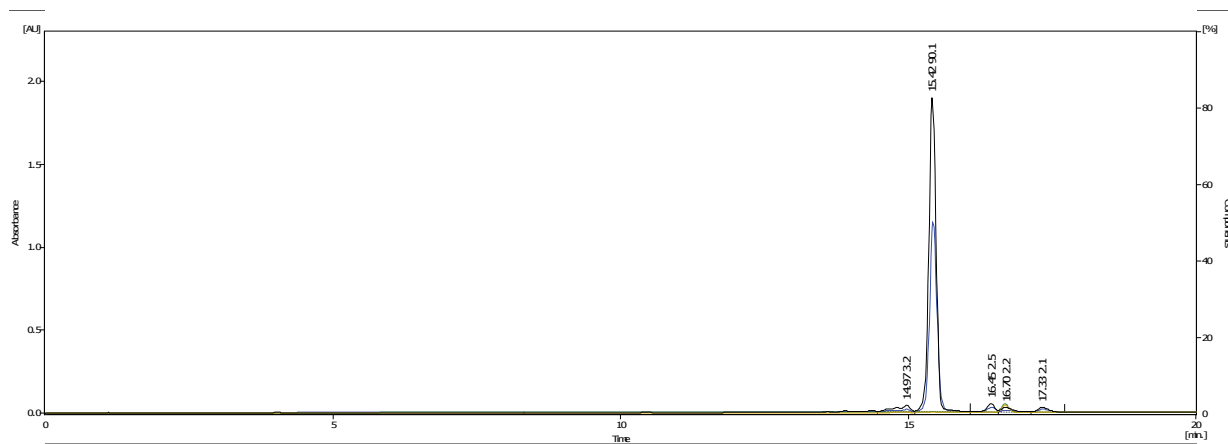
¹⁹F NMR spectrum in CDCl₃ (376 MHz)



^{19}F NMR spectrum in DMF- d_7 (471 MHz)

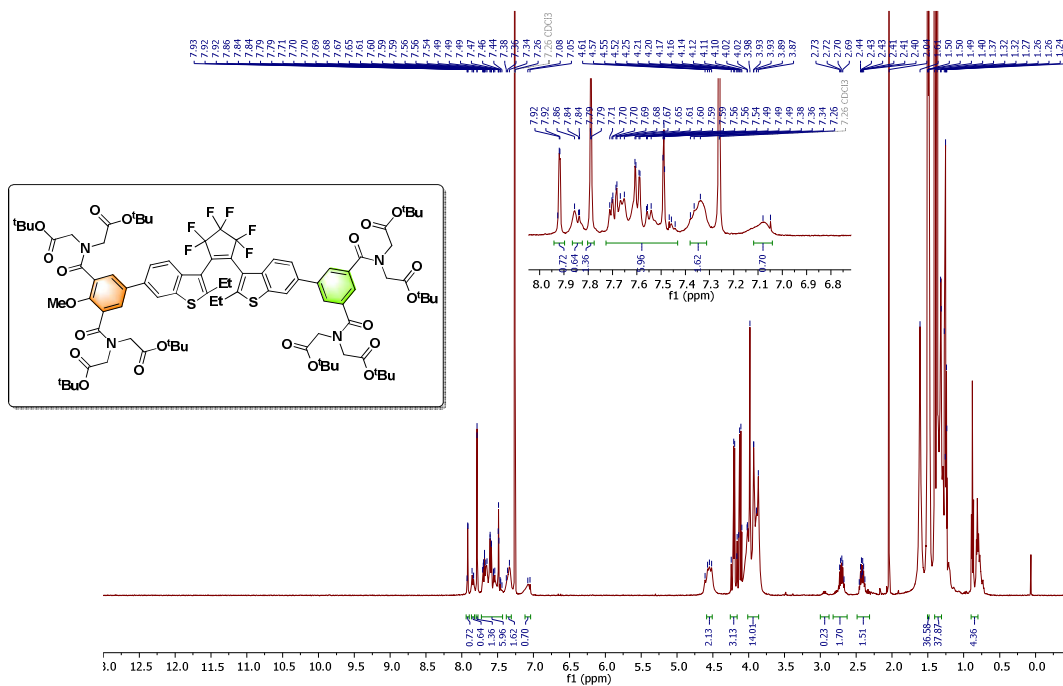


RP-HPLC elution profile (system A)

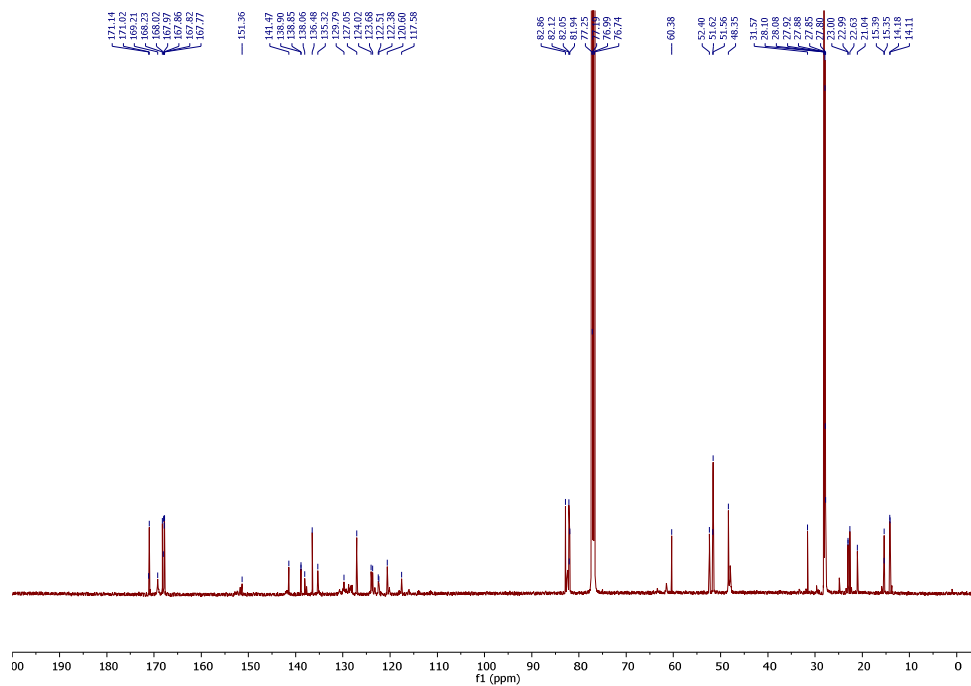


Compound S12

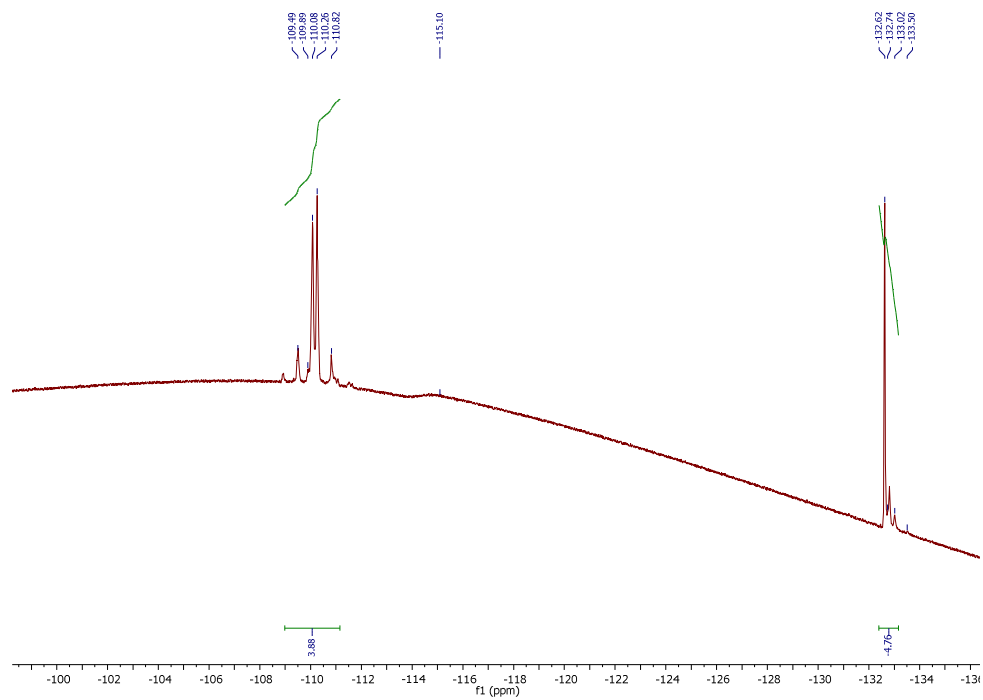
^1H NMR spectrum in CDCl_3 (500 MHz)



^{13}C NMR spectrum in CDCl_3 (126 MHz)

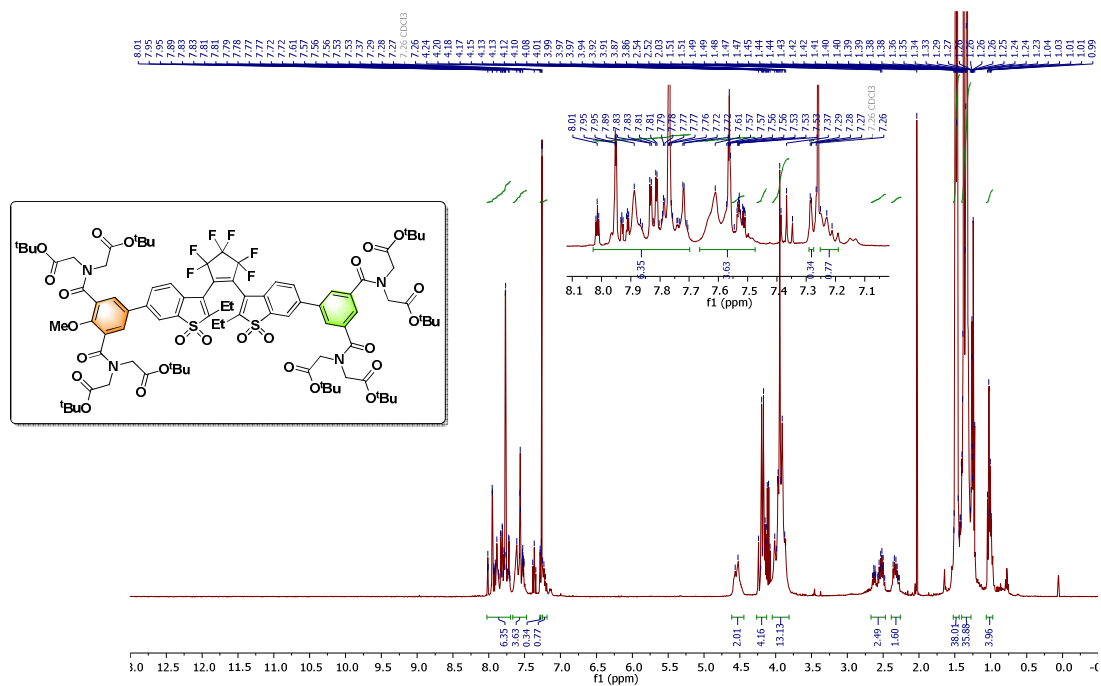


^{19}F NMR spectrum in CDCl_3 (471 MHz)

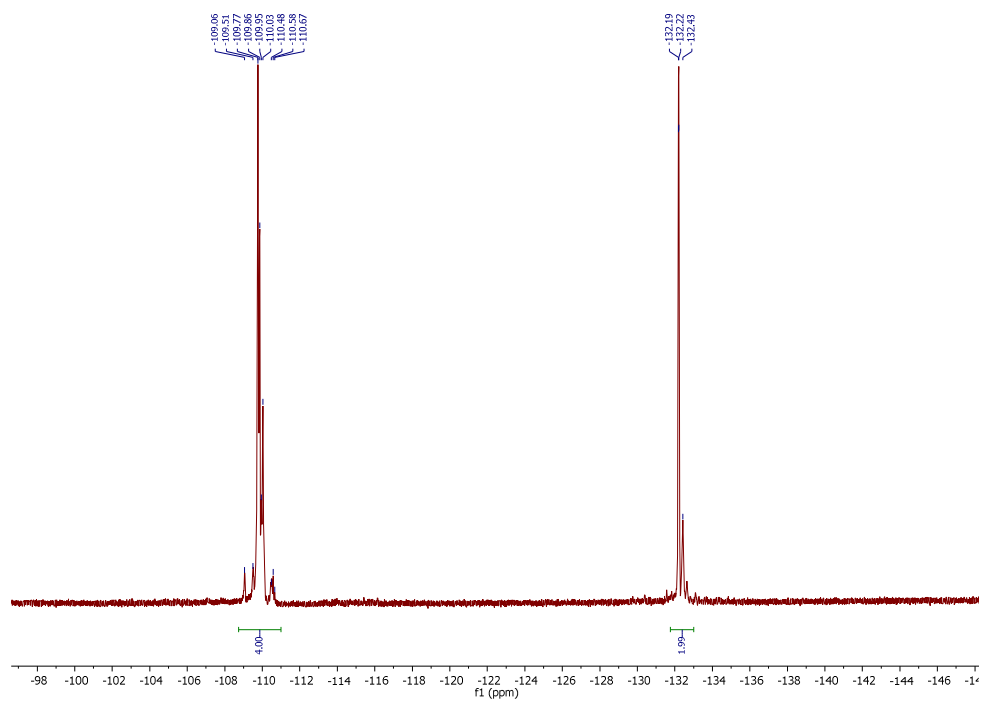


Compound S13

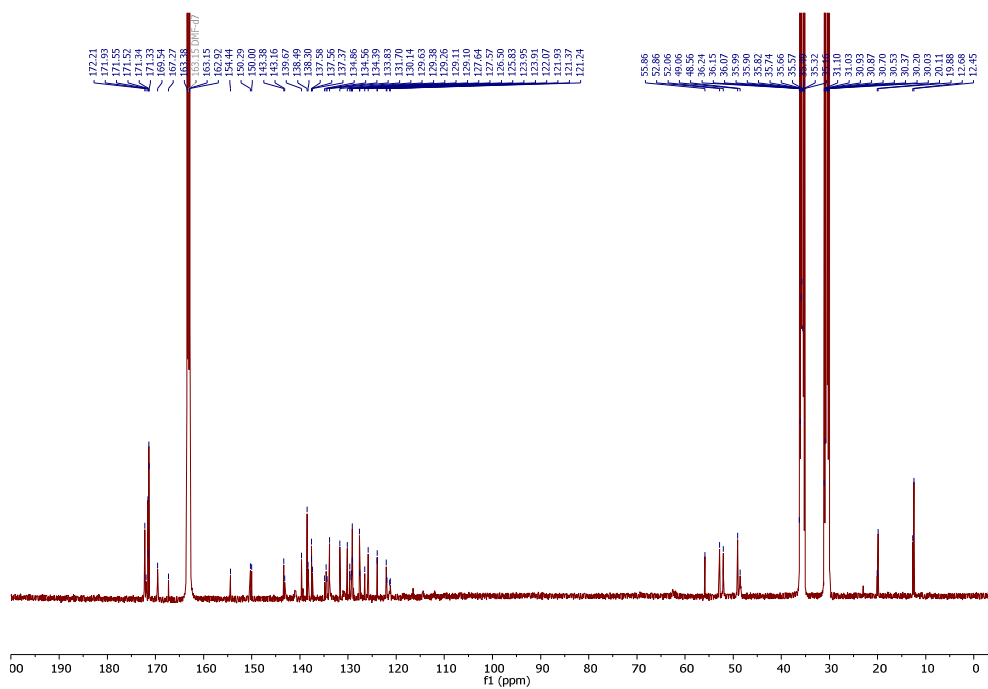
^1H NMR spectrum in CDCl_3 (400 MHz)



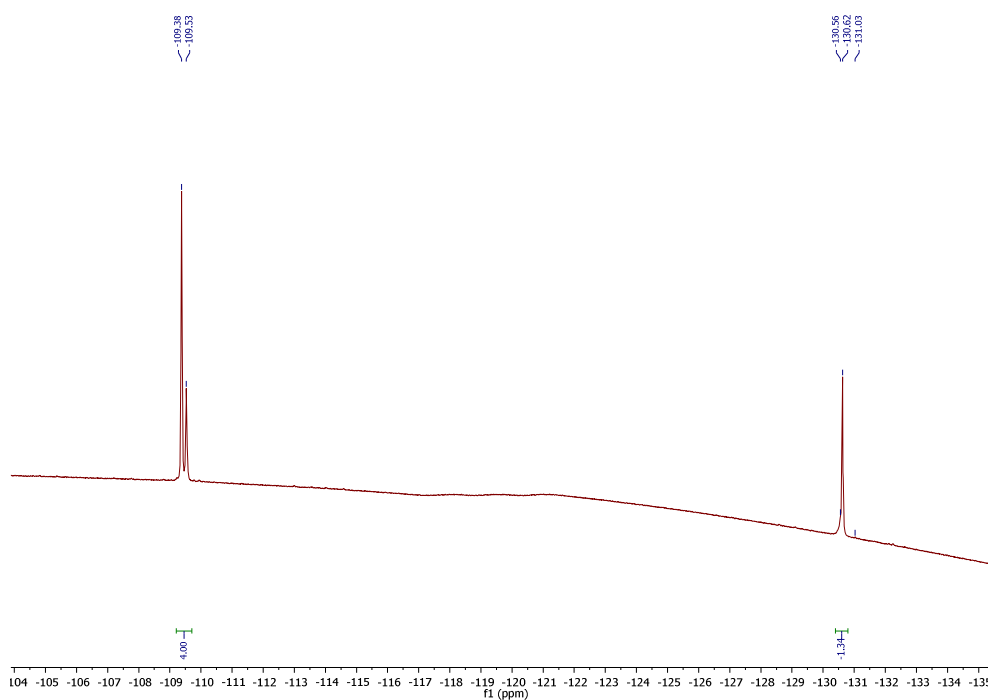
^{19}F NMR spectrum in CDCl_3 (376 MHz)



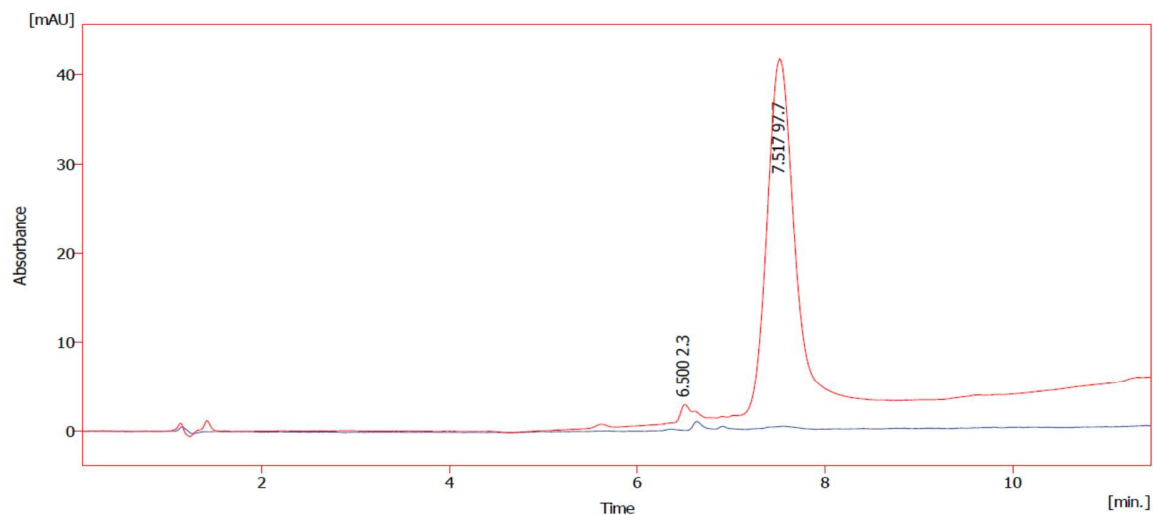
^{13}C NMR spectrum in DMF- d_7 (126 MHz)



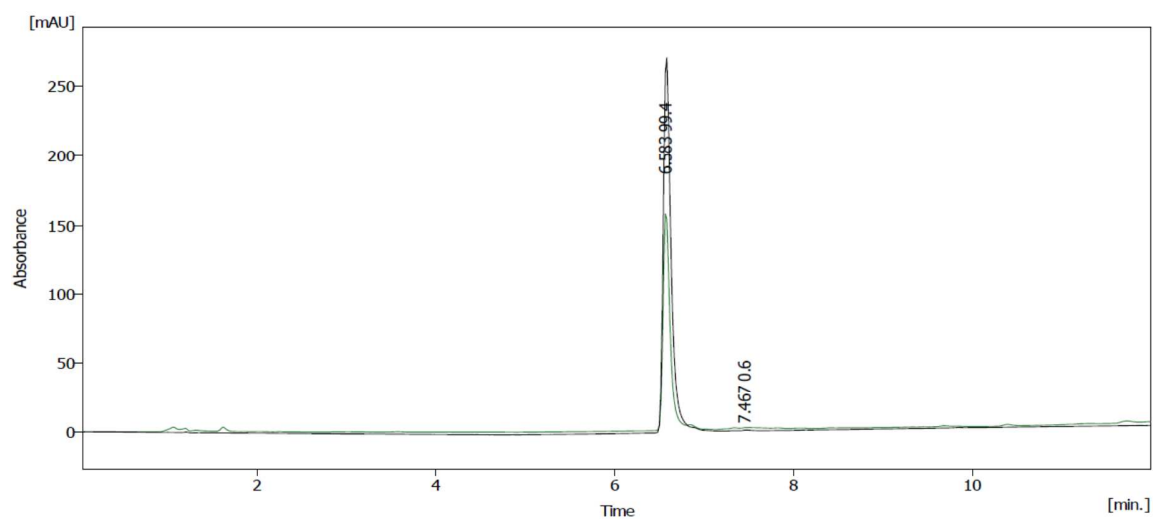
^{19}F NMR spectrum in DMF- d_7 (471 MHz)



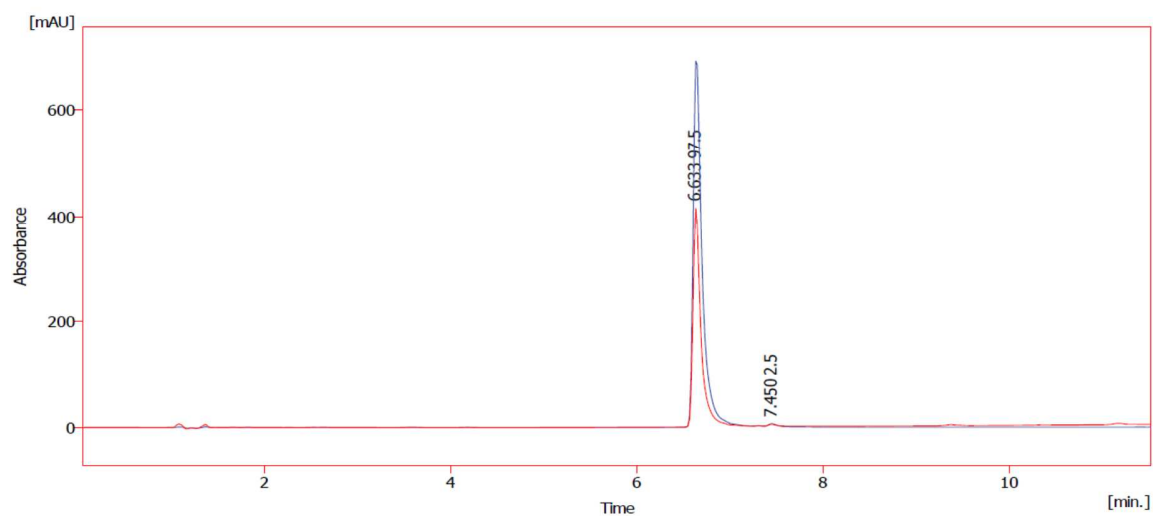
RP-HPLC elution profile (system F); “open-ring” isomer – red trace (254 nm); “closed-ring” isomer – blue trace (470 nm):



RP-HPLC elution profile (system F); “closed-ring” isomer, which shows green trace (254 nm) and black trace (470 nm), was isolated by HPLC and immediately analyzed in CD₃OD:



RP-HPLC elution profile (system F): “closed-ring” isomer dissolved in CD₃OD after storing for 3 weeks in the dark at room temperature; red trace (254 nm) and blue trace (470 nm)



6. References

- (1) Li, F.; Basile, V. M.; Pekarek, R. T.; Rose, M. J., *ACS Appl. Mater. Interfaces* **2014**, *6*, 20557-20568.
- (2) Paramelle, D.; Cantel, S.; Enjalbal, C.; Amblard, M.; Forest, E.; Heymann, M.; Geourjon, C.; Martinez, J.; Subra, G., *Proteomics* **2009**, *9*, 5384-5388.
- (3) Gillanders, F.; Giordano, L.; Diaz, S. A.; Jovin, T. M.; Jares-Erijman, E. A., *Photochem. Photobiol. Sci.* **2014**, *13*, 603-612.
- (4) Uno, K.; Niikura, H.; Morimoto, M.; Ishibashi, Y.; Miyasaka, H.; Irie, M., In situ preparation of highly fluorescent dyes upon photoirradiation. *J. Am. Chem. Soc.* **2011**, *133* (34), 13558-13564.
- (5) Matsuda, K.; Irie, M., *Chem. Eur. J.* **2001**, *7*, 3466-3473.
- (6) Dempsey, G. T.; Vaughan, J. C.; Chen, K. H.; Bates, M.; Zhuang, X. W. *Nat. Methods* **2011**, *8*, 1027-1036.

6.2. Manuscript II: Photoactivatable Siliconrhodamine

Chemistry–A European Journal

Supporting Information

Photoactivatable Fluorophore for Stimulated Emission Depletion (STED) Microscopy and Bioconjugation Technique for Hydrophobic Labels

Michael Weber,^[a] Taukeer A. Khan,^[a] Lukas J. Patalag,^[a, c] Mariano Bossi,^[b]
Marcel Leutenegger,^[a] Vladimir N. Belov,^[a] and Stefan W. Hell*^[a, b]

Table of Contents

Experimental Procedures	2
Scheme S1 and S2	4
Experimental procedures and analytical data	5
Scheme S3	8
Experimental procedures and analytical data	9
Scheme S4	11
Experimental procedures and analytical data	11
Scheme S5	14
Experimental procedures and analytical data	15
Supplementary figures	16
¹ H and ¹³ C NMR and HPLC spectra	22
Supplementary references	35

Experimental Procedures

Thin layer chromatography: Analytical TLC (normal phase) was performed on Merck Millipore ready-to-use aluminium sheets coated with silica gel 60 (F₂₅₄). Compounds were detected by exposing TLC plates to UV-light (254 or 366 nm).

Preparative flash column chromatography: Flash column chromatography was performed using regular silica gel 60 (40–63 μm) from Macherey-Nagel, or cartridges from Interchim (PF-SIHC, 15 μM, 25 or 40 g SiO₂), or Teledyne Isco (RediSepRf, 35 μM, 24 or 40 g SiO₂). Automated separations were performed with an Isolera One system (Biotage AG, Sweden) using the type of cartridge and solvent gradient indicated.

High-performance liquid chromatography: Analytical HPLC was performed on a Knauer Azura liquid chromatography system with a binary P 6.1L pump, UV diode array detector DAD 6.1L, an injection valve with a 20 μL loop and two electrical switching valves V 2.1S with 6-port multiposition valve head. Analytical columns: Knauer Eurospher II 100-5 C18, 5 μm, 150×4 mm or Interchim Uptisphere Strategy C18-HQ, 10 μm, 250×4.6 mm, flow rate 1.2 mL/min, unless stated otherwise.

Preparative HPLC was performed on an Interchim puriFlash 4250 2X preparative HPLC/Flash hybrid system (Interchim) with a 5 mL injection loop, a 200-600 nm UV-Vis detector and an integrated ELSD detector. Preparative column: Interchim Uptisphere Strategy C18-HQ 10 μm, 250×21.2 mm, flow rate: 20 mL/min, unless specified otherwise.

NMR spectra were recorded at 25°C with an Agilent 400-MR spectrometer at 400 MHz (¹H), 376.4 MHz (¹⁹F), and 100.6 MHz (¹³C). ¹³C NMR spectra were also acquired with a Bruker Avance III HD 500 MHz (BBO Prodigy probe) instrument. Chemical shifts (δ) are reported in ppm. All ¹H spectra are referenced to tetramethylsilane (TMS; δ = 0 ppm) using the signals of added TMS (0.03% v/v) or the residual protons of CHCl₃ (7.26 ppm) in CDCl₃, CHD₂OD (3.31 ppm) for CD₃OD, DMSO-*d*₅ (2.50 ppm) for DMSO-*d*₆. ¹³C NMR spectra are referenced to TMS (δ = 0 ppm) using the signals of added TMS (0.03% v/v) or the solvent: CDCl₃ (77.16 ppm), CD₃OD (49.00 ppm), DMSO-*d*₆ (39.52 ppm). Multiplicities of signals are described as follows: s = singlet, d = doublet, t = triplet, q = quartet, p = pentet, m = multiplet or overlap of non-equivalent resonances; br = broad signal. Coupling constants (*J*) are given in Hz.

ESI-MS were recorded on a Varian 500-MS spectrometer (Agilent). ESI-HRMS were recorded on a MICROTOF spectrometer (Bruker) equipped with ESI ion source (Apollo) and direct injector with LC autosampler Agilent RR 1200.

Spectroscopy: Stocks solutions (2-3 mM) of compounds **1**-OMe-H, **2**-H-H, and **3**, were prepared in acetonitrile. Final dilutions for spectroscopic characterization and irradiation experiments were prepared in 1:1 mixtures of acetonitrile and phosphate buffer at a concentration of 10-20 μM. All measurements were performed in quartz cuvettes with four clear faces (Hellma GmbH & Co.). Absorption and emission spectra were recorded in a Cary Series UV-Vis-NIR Spectrophotometer (Agilent Technologies), and a Cary Eclipse Fluorescence Spectrophotometer (Agilent Technologies), respectively. Fluorescence lifetime was measured in a Fluorescence Lifetime Spectrometer (FluoTime 300, PicoQuant). Irradiation experiments were performed in a home-build setup^[1], using a 365 nm LED as irradiation source (M365-L2, Thorlabs), a Deuterium/Xenon lamp (DH-2000-BAL, Ocean Optics) as an illumination source and a diode array spectrometer (FLAME-S-UV-VIS-ES, Ocean Optics). The intensity of the irradiation light was calibrated with a chemical actinometer (Azobenzene in MeOH). The samples were kept at 20 °C and continuously stirred with a Peltier-based temperature control (Luma 40, Quantum Northwest, Inc.). The absorption of the samples was recorded at a right angle with respect to the irradiation source, at fixed irradiation intervals until complete conversion to the final product. At fixed intervals, a small amount of sample was extracted to perform LC-MS experiments (Shimadzu LCMS-2020).

Antibody Conjugation and Purification: All necessary chemicals for antibody conjugation were purchased from Sigma-Aldrich. For NHS-ester conjugated antibodies 400 μL (~1 mg) secondary goat anti rabbit antibody (111-005-003, Dianova) was mixed with 40 μL 1 M NaHCO₃ and 200 μL DMF premixed with 100 μg NHS-ester dye. After one hour reaction under rigorous stirring, the sample was purified using either a standard size exclusion purification with a PD-10 (GE Healthcare) column or by phase separation. For the phase separation purification 1.2 mL distilled water, 182 μL saturated (NH₄)₂SO₄ and 1.82 mL *tert*-butanol was added, quickly vortexed and separated into two phases after a short centrifugation pulse. The aqueous phase (~400 μL) was diluted to two times its volume with PBS. The conjugated antibodies were aliquoted and stored at -20 °C. The antibodies did not show any degradation even after months of storage at 5 °C.

To modify antibodies with azide-groups, 1 mg (~400 μL) secondary goat anti rabbit antibody was mixed with 40 μL 1 M NaHCO₃ and 1.32 μL DMSO premixed with 13.2 μg *N*-hydroxysuccinimidyl azidoacetate. The mixture was stirred for 1 h and purified using a PD-10 (GE Healthcare) size exclusion column. TBS was used as elution buffer. The glycan labelled antibodies (250 μg) were produced using the commercial GlyClick (Genovis) enzyme system and eluted in TBS (150 mM NaCl, 50 mM Tris-HCl, pH 7.6). To the final volume of 200 μL (1 mg *N*-hydroxysuccinimidyl azidoacetate modified antibodies or 250 μg glycan azide antibodies), 50 μL DMF and 50 μg of azide reactive DBCO-dye was added. The mixture was stirred over night at room temperature. Then it was diluted with 600 μL distilled water, 90 μL saturated (NH₄)₂SO₄ and 900 μL *tert*-butanol, quickly vortexed and separated into two phases after a short centrifugation pulse. The aqueous phase (~200 μL) was diluted to two times its volume with TBS. Optionally, the buffer can be exchanged using a regenerated cellulose MWCO spin filter (Microcon YM-50 50 kDa MWCO). The conjugated antibodies were aliquoted and stored at -20 °C.

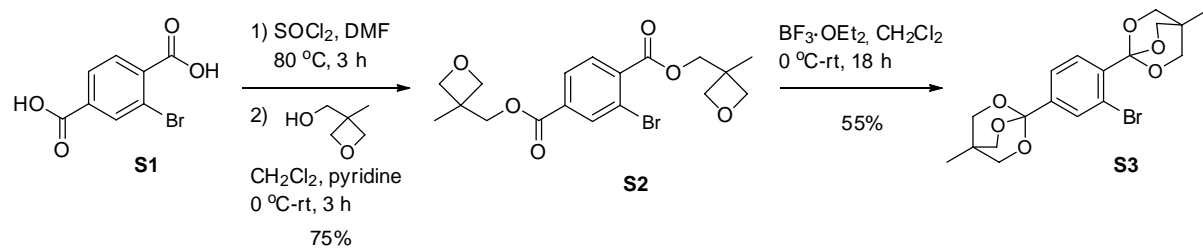
Cell fixation and staining: HeLa and U2OS cells were grown on coverslips and then fixed with 4% (w/v) paraformaldehyde for 15 min or with cold methanol (-20°C) for 4 min. The cells were permeabilized with 0.1% Triton X-100 in PBS for 5 min. After blocking with 2% (w/v) BSA in PBS, the cells were treated with antibodies diluted in the same buffer for 1 h. Between multiple antibody treatments, the cells were washed with 2% (w/v) BSA in PBS. The phalloidin conjugates were dissolved in DMSO and applied on the fixed cells for 1 h at a final concentration of ~100 µg/mL in PBS. The samples were mounted in PBS (wide-field, confocal and STED imaging) or 20 mM Hepes buffer (pH 7 + 150 mM NaCl) and sealed using silicon resin (TwinSeal Picodent). Used antibody: ATP-Synthase B (ab5432, Abcam), TOM 20 (sc-11415, SantaCruz), DNA (61014, Progen), alpha-Tubulin (ab18251, Abcam).

Imaging: The wide-field images were taken on a Leica DM6000 microscope (Leica HCX PI APO 100x/1.4-0.7 NA oil) using an A4 filter cube (Leica, excitation: 360/40 nm, detection: 470/40 nm) for activation and APC HC filter cube (AHF F36-540, excitation: 600/37 nm, detection: 675/67 nm) for imaging.

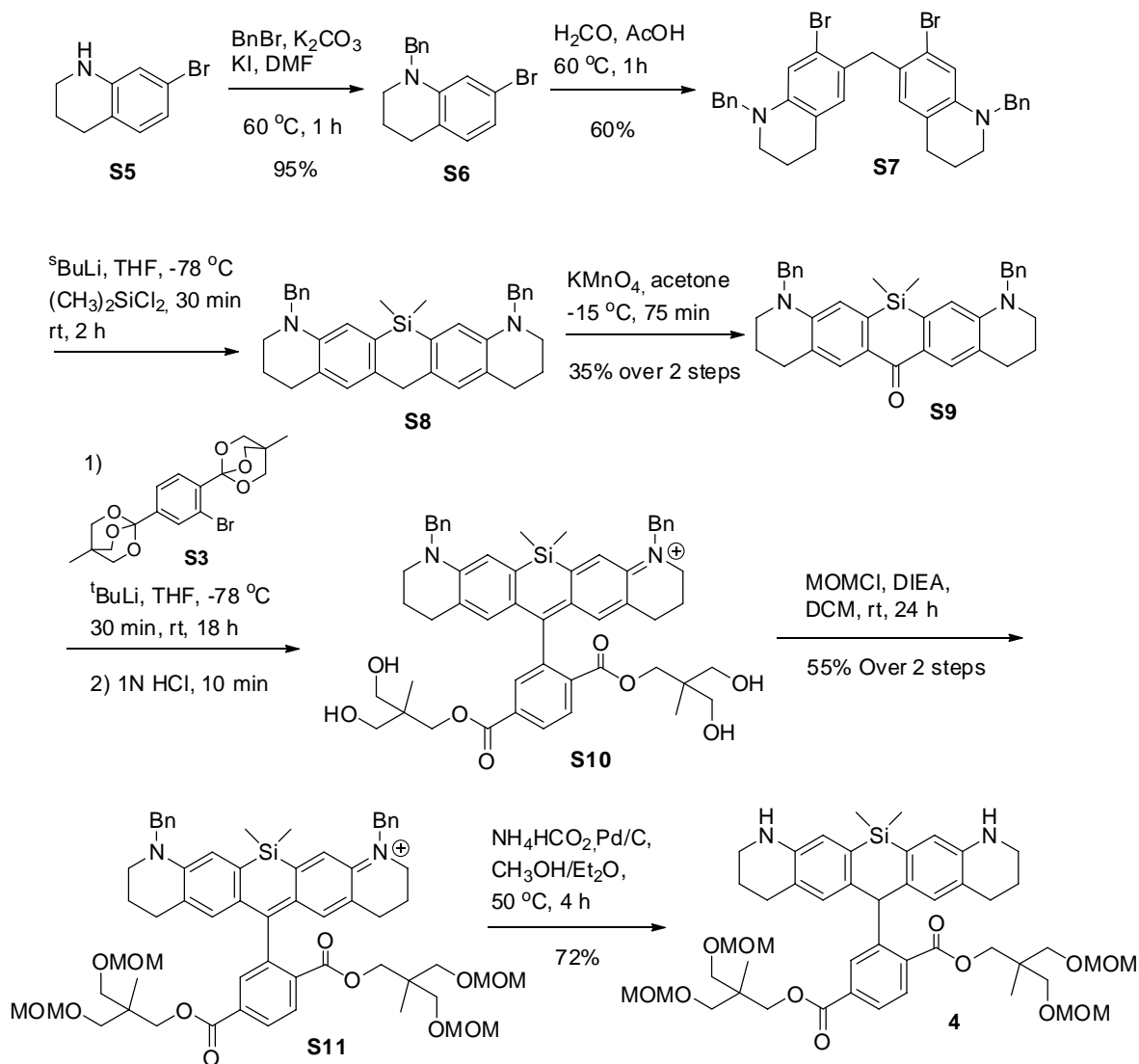
For the STED images a commercial Abberior Instruments Expert Line microscope equipped with a UPLANSAPO 100x/1.4 NA oil-immersion objective and a 775 nm 40 MHz STED laser of ~ 1.2 ns pulse duration was used. The fluorophores were excited with a 640 nm and a 561 nm 40 MHz pulsed laser and detected in two color channels 615/20 nm and 685/70 nm. Between the acquisitions of the multiplexed color channel, the sample was bleached using a 595 nm laser. The caged dyes were activated using a wide-field 405 nm led illumination (CoolLED) with a broad spectrum extending far below 400 nm.

The single molecule and PALM images were performed on a home-built microscope and analyzed as previously described^[2]. In brief, the sample was illuminated through an oil immersion objective (Olympus UPLANSAPO 100x/1.4 NA oil) using a 642 nm laser in total internal reflection (TIRF) mode and imaged onto an EMCCD camera using a bandpass emission filter (700/75 nm). The molecules were sparsely activated using a 405 nm laser.

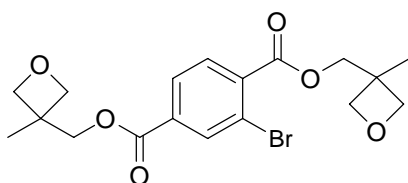
Results and Discussion



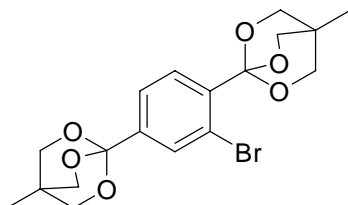
Scheme S1. Synthesis of orthoester **S3** and *o*-nitrobenzyl chloroformate **6**



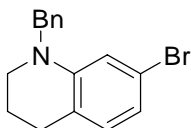
Scheme S2. Synthesis of leuco-Si-rhodamine **4**



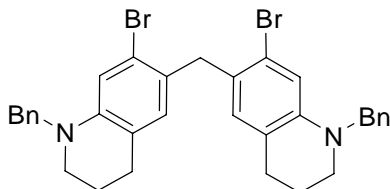
Bis((3-methyloxetan-3-yl)methyl) 2-bromoterephthalate (S2):^[3] A mixture of 2-bromoterephthalic acid (3.0 g, 12.2 mmol), thionyl chloride (10.0 mL), and DMF (2 drops) was stirred at reflux for 3 h. The mixture was concentrated in vacuum and co-evaporated twice with toluene. The crude acid chloride was taken up in CH₂Cl₂ (18 mL) and was added to a solution of 3-methyl-3-oxetanemethanol (3.12 g, 30.6 mmol, 2.5 eq) and pyridine (2.2 mL, 61 mmol, 5 eq) in CH₂Cl₂ (12 mL) at 0 °C, and stirred for 10 min. The ice bath was removed, and the reaction mixture was stirred at room temperature for 3 h. The reaction mixture was diluted with water and extracted with CH₂Cl₂ (3 x). The combined organic solutions were washed with brine, dried (Na₂SO₄), filtered, and evaporated. Flash chromatography (0–75% EtOAc/hexanes, linear gradient) afforded the diester (S2) as a colourless gum (4.90 g, 90%). The NMR spectra corresponded to the published data ^[3].



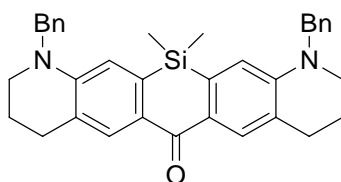
1,1'-(2-Bromo-1,4-phenylene)bis(4-methyl-2,6,7-trioxabicyclo[2.2.2]octane) (S3):^[3] A solution of diester, S2 (4.85 g, 11.7 mmol) in CH₂Cl₂ (30 mL) was cooled to 0 °C under nitrogen, BF₃·OEt₂ (0.81 mL, 5.9 mmol, 0.5 eq) was added; the reaction mixture was stirred for 10 min, allowed to warm to room temperature and stirred for 18 h. Et₃N (4 mL) was added, and the solution stirred for 15 min, concentrated in vacuum and purified by flash chromatography (0–20% EtOAc/hexanes, linear gradient, with constant 40% v/v CH₂Cl₂ and 1% Et₃N) to provide 2.8 g (57%) of S3 as a white solid. ¹H NMR (DMSO-*d*₆, 400 MHz) δ 7.63 (d, *J* = 8.3 Hz, 1H), 7.62 (d, *J* = 1.6 Hz, 1H), 7.42 (dd, *J* = 8.2, 1.7 Hz, 1H), 3.98 (s, 6H), 3.97 (s, 6H), 0.81 (s, 3H), 0.80 (s, 3H). Other analytical data were identical to the reported values ^[3].



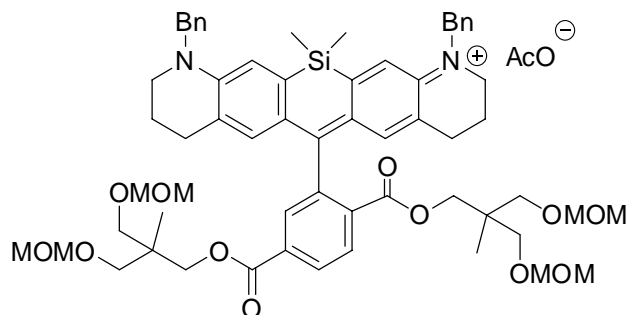
1-Benzyl-7-bromo-1,2,3,4-tetrahydroquinoline (S6): 7-Bromo-1,2,3,4-tetrahydroquinoline¹ (6.4 g, 30 mmol, 1 eq), benzyl bromide (4.0 mL, 36 mmol, 1.2 eq), K₂CO₃ (12.5 g, 90.5 mmol, 3 eq), and KI (1 g, 6 mmol, 0.2 eq) were combined in DMF (45 mL) and stirred at 60 °C for 6 h. The reaction mixture was diluted with water and extracted with EtOAc (3 x). The combined organic solutions were washed with water and brine, dried (Na₂SO₄), filtered, and concentrated in vacuo. Flash chromatography (0–15% Et₂O/hexanes, linear gradient) on regular SiO₂ (100 g) yielded compound S6² (8.4 g, 92%) as a gum that crystallized into an off-white, low-melting solid upon standing. ¹H NMR (CDCl₃, 400 MHz) δ 7.34 – 7.30 (m, 2H), 7.27 – 7.20 (m, 3H), 6.80 (d, *J* = 7.9 Hz, 1H), 6.66 (dd, *J* = 7.9, 1.9 Hz, 1H), 6.62 (d, *J* = 1.9 Hz, 1H), 4.44 (s, 2H), 3.38 – 3.30 (m, 2H), 2.73 (t, *J* = 6.3 Hz, 2H), 1.99 – 1.91 (m, 2H).



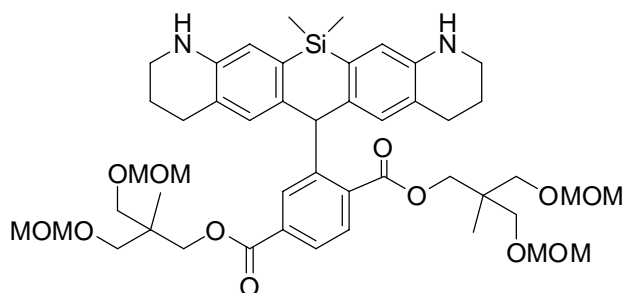
Bis(1-benzyl-7-bromo-1,2,3,4-tetrahydroquinolin-6-yl)methane (S7):^[4] 1-Benzyl-7-bromo-1,2,3,4-tetrahydroquinoline S6 (3.3 g, 10.9 mmol) was taken up in AcOH (15 mL). Formaldehyde (37% w/w in H₂O, 2.2 mL, 29 mmol, 2.7 eq) was added dropwise, and the solution stirred at 60 °C for 1 h. The reaction mixture was concentrated in vacuo to remove AcOH, diluted with saturated NaHCO₃, and extracted with EtOAc (3 x). The combined organic solvents were washed with saturated NaHCO₃ and brine, dried (Na₂SO₄), filtered, and evaporated. The residue was triturated with Et₂O to obtain a solid which was isolated by filtration, washed with Et₂O, and dried to provide S7 as an off-white solid^[3] (2.5 g, 75%). ¹H NMR (CDCl₃, 400 MHz) δ 7.37 – 7.29 (m, 4H), 7.26 – 7.24 (m, 6H), 6.72 (s, 2H), 6.64 (s, 2H), 4.43 (s, 4H), 3.88 (s, 2H), 3.28 (t, *J* = 6.3 Hz, 4H), 2.67 (t, *J* = 6.3 Hz, 4H), 1.97 – 1.91 (m, 4H).



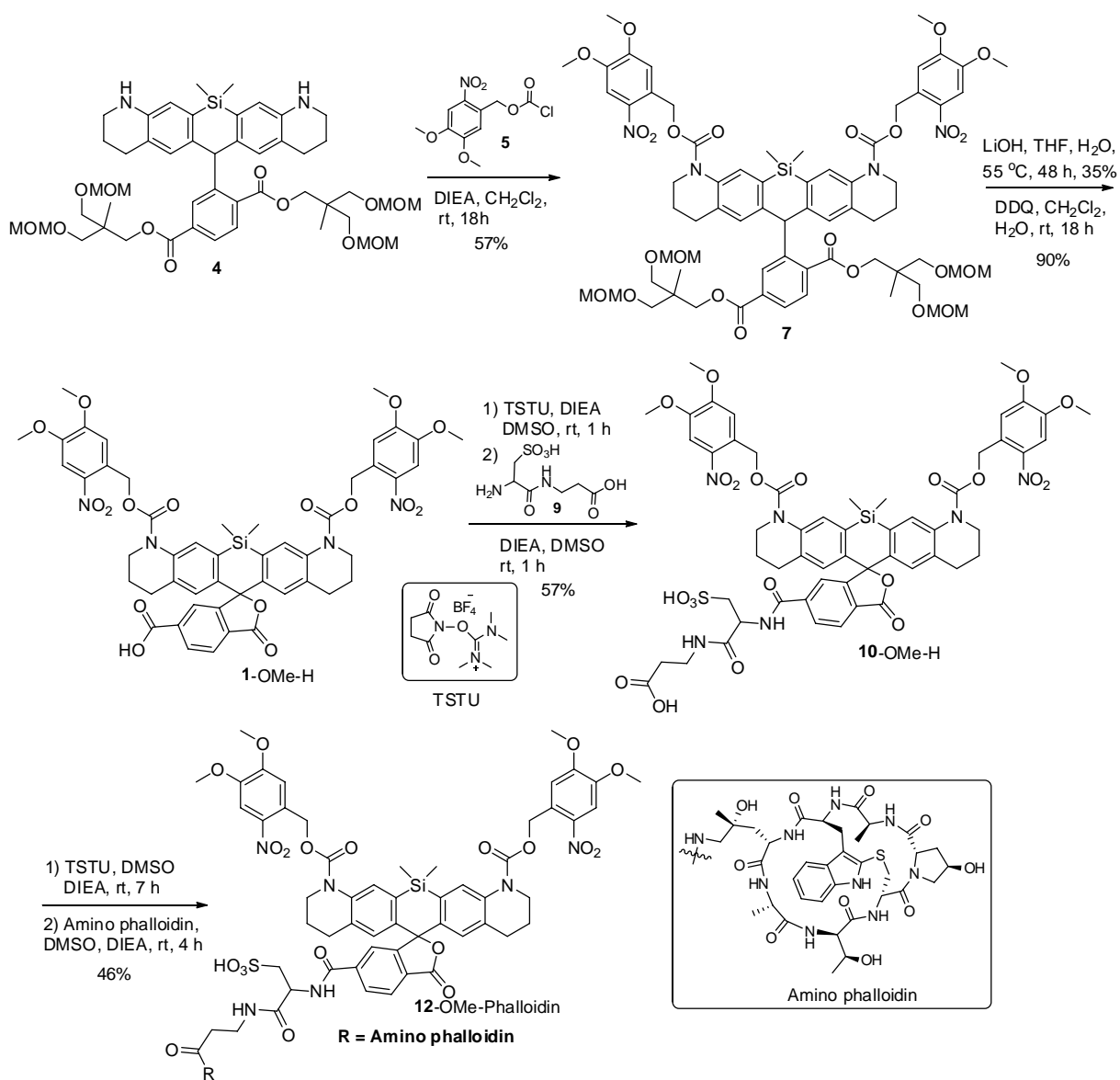
1,11-Dibenzyl-13,13-dimethyl-1,2,3,4,8,9,10,11-octahydrosilino[3,2-g:5,6-g']diquinolin-6(13H)-one (S9): A solution of dibromide **S7** (1.00 g, 1.62 mmol) in THF (ca. 10 mL) was cooled to $-78\text{ }^{\circ}\text{C}$ (in a dry ice – acetone bath) under nitrogen. *sec*-Butyllithium (1.4 M in cyclohexane, 3.5 mL, 4.9 mmol, 3.0 eq) was added, and the reaction mixture stirred at $-78\text{ }^{\circ}\text{C}$ for 30 min. Dichlorodimethylsilane (0.36 mL, 2.9 mmol, 1.8 eq) was then added dropwise. The dry ice – bath was removed, and the reaction mixture stirred at room temperature for 2 h. Then saturated aq. NH_4Cl was added carefully with stirring (5 mL), the reaction mixture diluted with water, and extracted with EtOAc (3 x). The combined organic solutions were washed with brine, dried (Na_2SO_4), filtered, and concentrated in vacuum to afford compound **S8** as a greenish-brown material. The crude substance (**S8**) was taken up in acetone (15 mL) and cooled to $-15\text{ }^{\circ}\text{C}$. KMnO_4 (513 mg, 3.2 mmol, 2 eq) was added in 4 equal portions at 15 min intervals (45 min in total) under vigorous stirring. After stirring for another 30 min at $-15\text{ }^{\circ}\text{C}$, the brown mixture was diluted with CH_2Cl_2 , filtered through Celite, and concentrated. Flash chromatography on silica gel (15 g, 5–40% EtOAc/hexanes, linear gradient) provided 319 mg (37% over 2 steps) of ketone (**S9**) as a yellow solid. ^1H NMR (CDCl_3 , 400 MHz) δ 8.10 (s, 2H), 7.33 – 7.28 (m, 4H), 7.25 – 7.21 (m, 6H), 6.56 (s, 2H), 4.57 (s, 4H), 3.45 – 3.42 (m, 4H), 2.88 (t, $J = 6.2$ Hz, 4H), 2.04 – 1.98 (m, 4H), 0.10 (s, 6H); ^{13}C NMR (CDCl_3 , 101 MHz) δ 185.09, 147.55, 138.5, 138.0, 130.6, 129.6, 128.7, 127.1, 126.6, 123.7, 113.6, 54.9, 50.2, 28.2, 22.0, -1.4. HRMS (ESI) calcd for $\text{C}_{35}\text{H}_{36}\text{N}_2\text{OSi}$ $[\text{M}+\text{H}]^+$ 529.2670, found 529.2669.



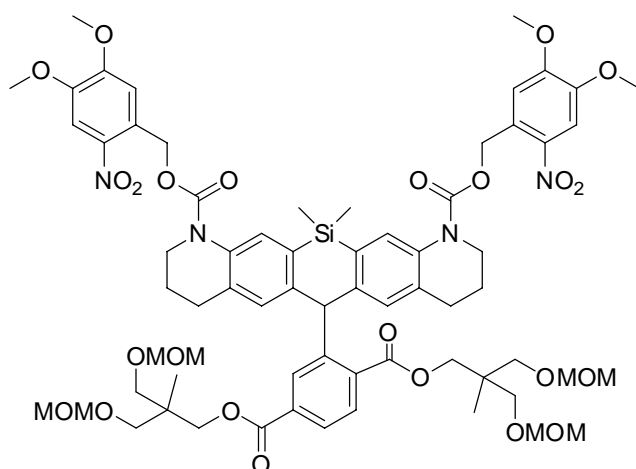
1,11-Dibenzyl-6-(2,5-bis((methoxymethoxy)-2-((methoxymethoxy)methyl)-2-methylpropoxy)carbonyl)phenyl)-13,13-dimethyl-2,3,4,8,9,10,11,13-octahydrosilino[3,2-g:5,6-g']diquinolin-1-ium acetate (S11): A solution of bromide **S3** (0.975 g, 2.36 mmol, 5 eq) in THF (58 mL) was cooled to $-78\text{ }^{\circ}\text{C}$ under nitrogen. *tert*-Butyllithium (1.7 M in pentane, 2.8 mL, 4.7 mmol, 10 eq) was added dropwise, and the reaction stirred for 30 min at $-78\text{ }^{\circ}\text{C}$. Then a solution of ketone **S9** (250 mg, 0.47 mmol, 1 eq) in THF (6 mL) was added dropwise. The reaction mixture was allowed to slowly warm to room temperature while stirring overnight (18 h). The reaction mixture was “quenched” by slow addition of 1 M aq HCl (13 mL), which caused an immediate colour change from pale orange to deep blue. After stirring for 10 min, the mixture was diluted with water and extracted with 15% *i*PrOH/ CHCl_3 (3 x). The combined organic solutions were dried (Na_2SO_4), filtered, and concentrated under vacuum. Silica gel chromatography (0–20% MeOH/ CH_2Cl_2 , linear gradient, with constant 1% v/v AcOH additive) provided the 3-hydroxy-2-(hydroxymethyl)-2-methylpropyl diester (**S10**) as a deep blue solid. Diester (**S10**) was taken up in CH_2Cl_2 (25 mL), *N,N*-diisopropylethylamine (1.2 mL, 7.1 mmol) and chloromethyl methyl ether (539 μL , 7.09 mmol) were added, and the reaction was stirred at room temperature for 24 h while protected from light. The solution was diluted with water and extracted with CH_2Cl_2 (3 x). The combined organic solution were dried (Na_2SO_4), filtered, and evaporated. The residue was purified by flash chromatography (0–10% MeOH/ CH_2Cl_2 , linear gradient, with constant 1% v/v AcOH additive) to afford 275.6 mg (55% over 2 steps) of **S11** as a dark blue solid. ^1H NMR (CD_3OD , 400 MHz) δ 8.32 (d, $J = 1.1$ Hz, 2H), 7.82 (s, 1H), 7.39 – 7.34 (m, 4H), 7.32 – 7.24 (m, 6H), 7.14 (s, 2H), 6.60 (s, 2H), 4.93 (AB quartet, $v_A = 1978$ Hz, $v_B = 1962$ Hz, $J_{AB} = 17.0$ Hz, 4H), 4.54 (s, 4H), 4.40 (s, 4H), 4.32 (s, 2H), 4.03 (s, 2H), 3.70 (t, $J = 5.7$ Hz, 4H), 3.48 (AB quartet, $v_A = 1399$ Hz, $v_B = 1386$ Hz, $J_{AB} = 9.4$ Hz, 4H), 3.23 (s, 6H), 3.21 (s, 6H), 3.15 (AB quartet, $v_A = 1267$ Hz, $v_B = 1258$ Hz, $J_{AB} = 9.4$ Hz, 4H), 2.53 (t, $J = 6.2$ Hz, 4H), 1.95 – 1.92 (m, 4H), 1.06 (s, 3H), 0.67 (s, 3H), 0.26 (s, 3H), 0.22 (s, 3H); ^{13}C NMR ($\text{MeOH}-d_4$, 101 MHz) δ 166.9, 165.1, 164.7, 151.7, 146.6, 140.2, 137.8, 136.1, 134.6, 133.4, 131.1, 130.9, 129.5, 128.7, 127.8, 127.5, 126.4, 125.1, 120.7, 96.3, 96.3, 69.9, 69.4, 67.8, 67.5, 55.1, 54.1, 54.0, 51.6, 39.3, 39.1, 27.0, 20.6, 16.5, 16.5, -2.6, -3.4; HRMS (ESI) calcd for $\text{C}_{61}\text{H}_{77}\text{N}_2\text{O}_{12}\text{Si}$ $[\text{M}]^+$ 1057.5240, found 1057.5245.



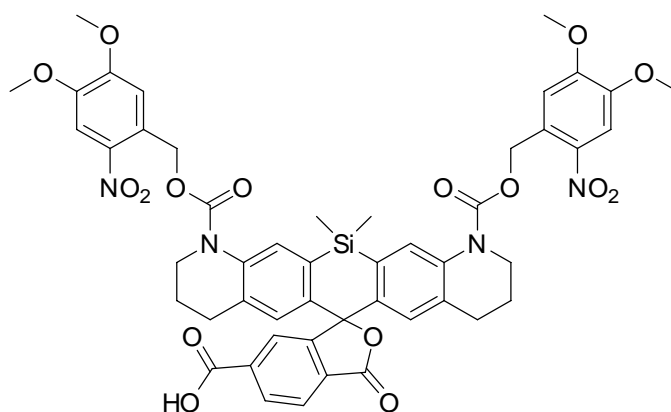
6-(2,5-Bis(3-(methoxymethoxy)-2-((methoxymethoxy)methyl)-2-methylpropoxy)carbonyl)phenyl)-13,13-dimethyl-2,3,4,8,9,10,11,13-octahydro-1H-silino[3,2-g:5,6-g']diquinoline (4): A two-neck round-bottom flask equipped with a reflux condenser was charged with Si-rhodamine **S11** (63 mg, 0.059 mmol). The flask was sealed and evacuated/backfilled with nitrogen (3 x). MeOH (6.6 mL) and Et₂O (2 mL) were added, followed by Pd/C (10% w/w, 30.5 mg, 29.5 μmol, 0.5 eq) and ammonium formate (55 mg, 0.88 mmol, 15 eq). Reaction mixture was stirred at 50 °C for 4 h, cooled to room temperature, and filtered through Celite. The filter-pad was washed with CH₂Cl₂, the filtrate concentrated in vacuo. Silica gel chromatography (10 g SiO₂, 5–50% EtOAc/hexanes, linear gradient) afforded 40 mg (76%) of compound **4** as a greenish-yellow gum. ¹H NMR (CDCl₃, 400 MHz) δ 7.72 – 7.62 (m, 3H), 6.85 (s, 2H), 6.70 (s, 2H), 6.37 (s, 1H), 4.62 (s, 4H), 4.53 (s, 4H), 4.46 (s, 2H), 4.14 (s, 2H), 3.56 (s, 4H), 3.40 (s, 4H), 3.34 (s, 6H), 3.31 – 3.21 (m, 4H), 3.26 (s, 6H), 2.73 – 2.51 (m, 4H), 1.93 – 1.77 (m, 4H), 1.16 (s, 3H), 0.98 (s, 3H), 0.60 (s, 3H), 0.40 (s, 3H). ¹³C NMR (CDCl₃, 101 MHz) δ 168.7, 165.4, 149.9, 137.8, 132.9, 132.8, 132.6, 131.6, 130.8, 129.4, 125.4, 123.9, 119.0, 96.8, 96.7, 96.6, 71.8, 70.2, 70.0, 68.0, 67.1, 55.2, 55.1, 42.0, 39.6, 39.5, 26.9, 22.0, 17.6, 17.4, 0.54, -0.47. HRMS (ESI) calcd for C₄₇H₆₆N₂O₁₂Si [M+H]⁺ 879.4458, found 879.4460.



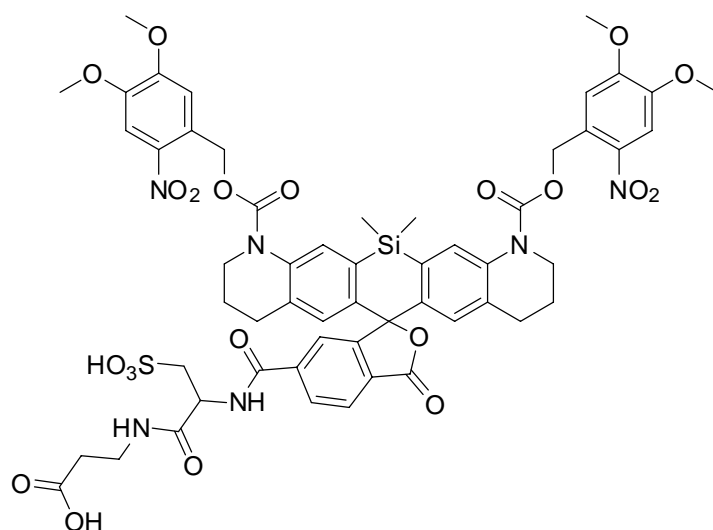
Scheme S3. NVOC2-QSiR-6-hydrophilizer-phalloidin conjugate.



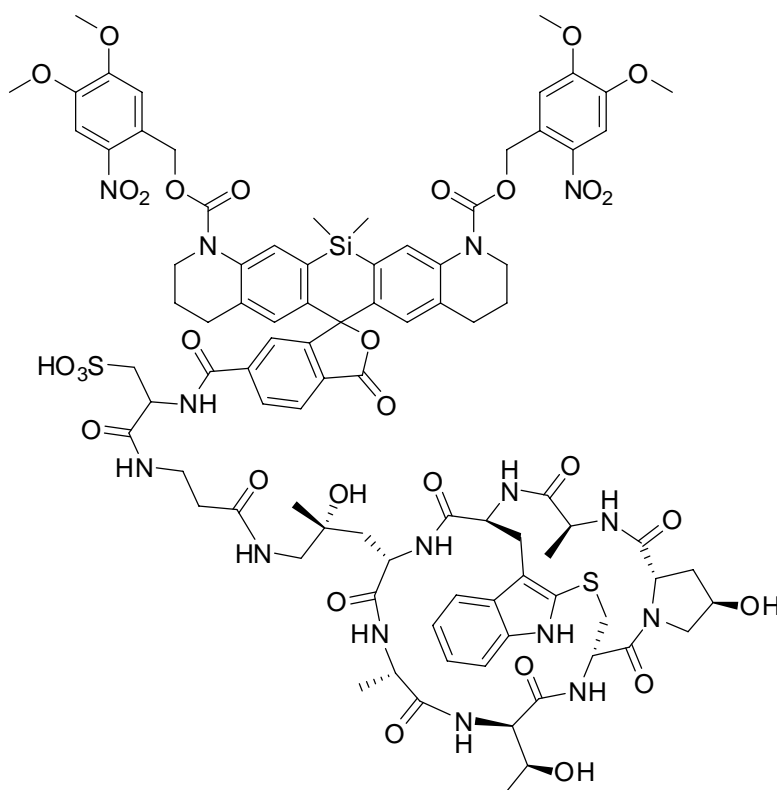
Compound 7: Compound **4** (120 mg, 0.137 mmol) was dissolved in CH_2Cl_2 (4 mL) under nitrogen. 4,5-Dimethoxy-2-nitrobenzyl chloroformate, **5** (151 mg, 0.546 mmol, 4 eq) in CH_2Cl_2 (2 mL) was added, followed by *N,N*-diisopropylethylamine (126 μL , 0.73 mmol, 5.3 eq). The reaction mixture was protected from light, stirred at room temperature for 18 h, diluted with 10% w/v aqueous citric acid and extracted with EtOAc (3x). The combined organic solutions were washed with brine, dried (MgSO_4), filtered, and evaporated. Flash chromatography (25 g SiO_2 , 10–100% EtOAc/hexanes, linear gradient, with constant 40% v/v CH_2Cl_2 additive) provided the compound **7** (106 mg, 57%) as a light orange foam. ^1H NMR (CDCl_3 , 400 MHz) δ 7.93 (s, 2H), 7.80 – 7.74 (m, 1H), 7.73 – 7.67 (m, 3H), 6.98 (s, 2H), 6.95 – 6.86 (m, 2H), 6.58 (s, 1H), 5.61 – 5.26 (m, 4H), 4.62 (s, 4H), 4.52 (s, 4H), 4.46 (s, 2H), 4.14 (s, 2H), 3.94 (s, 6H), 3.84 – 3.70 (m, 10H), 3.56 (s, 4H), 3.39 (s, 4H), 3.34 (s, 6H), 3.24 (s, 6H), 2.73 – 2.51 (m, 4H), 1.90 (p, J = 6.5 Hz, 4H), 1.15 (s, 3H), 0.97 (s, 3H), 0.60 (s, 3H), 0.32 (s, 3H); ^{13}C NMR (CDCl_3 , 126 MHz) δ 168.3, 165.1, 154.1, 153.3, 148.5, 148.2, 143.2, 140.0, 136.0, 133.2, 132.8, 132.6, 131.4, 129.8, 129.8, 127.5, 125.9, 110.7, 108.2, 96.7, 96.6, 70.2, 69.9, 68.1, 67.3, 64.5, 56.4, 56.2, 55.2, 55.1, 47.4, 45.0, 39.7, 39.5, 27.4, 23.2, 17.6, 17.4, 1.0, -0.8; HRMS (ESI) calcd for $\text{C}_{67}\text{H}_{84}\text{N}_4\text{O}_{24}\text{Si}$ [$\text{M}+\text{Na}$] $^+$ 1379.5137, found 1379.5122.



Compound 1-OMe-H: A vial was charged with compound **7** (52 mg, 38 μmol) and evacuated/backfilled with nitrogen (3 x). Freshly degassed THF (3.2 mL) and 1 M aq LiOH (0.9 mL, 0.8 mmol, 20 eq) were added, and the mixture was stirred at 55 $^\circ\text{C}$ for 48 h (protected from light). The reaction mixture was cooled to room temperature, acidified with 1 M HCl (3 mL), diluted with water, and extracted with CH_2Cl_2 (3 x). The organic solutions were dried (MgSO_4), filtered, and evaporated. The residue was purified by flash chromatography on silica gel (0–10% methanol in CH_2Cl_2) to get the di-acid target compound (13 mg, 35%) as an off-white solid which was used in the next step. The diacid was dissolved in 10:1 $\text{CH}_2\text{Cl}_2/\text{H}_2\text{O}$ (3.3 mL); DDQ (15 mg, 0.07 mmol, 5 eq) was added, and the reaction stirred at room temperature for 18 h (protected from light). The reaction mixture was concentrated to dryness and was purified by flash chromatography on silica gel (10 g, 0–5% methanol/ CH_2Cl_2 , linear gradient) to afford the caged dye **1-OMe-H** as an off-white solid (4.5 mg, 90%). Analytical HPLC: >98% purity (4.6 mm x 75 mm 2.6 μm C18 column; 1 μL injection; A/B 20:80 \rightarrow 100:0, A – acetonitrile, B – water + 0.05% trifluoroacetic acid; 10 min run; 1 mL/min flow. ^1H NMR ($\text{DMSO}-d_6$, 400 MHz) δ 8.11 – 8.01 (m, 2H), 7.93 (s, 2H), 7.71 (s, 2H), 7.60 (t, J = 1.0 Hz, 1H), 7.20 (s, 2H), 6.78 (s, 2H), 5.51 – 5.34 (m, 4H), 3.87 (s, 6H), 3.79 (s, 6H), 3.70 – 3.66 (m, 4H), 2.71 – 2.53 (m, 3H), 1.76 (p, J = 6.3 Hz, 4H), 0.31 (s, 3H), 0.19 (s, 3H). ^{13}C NMR ($\text{DMSO}-d_6$, 126 MHz) δ 169.2, 165.8, 155.0, 153.5, 154.0, 148.2, 140.0, 138.1, 137.7, 132.3, 130.7, 130.3, 128.8, 126.5, 125.8, 123.4, 112.5, 108.3, 88.6, 64.4, 56.2, 56.1, 44.6, 27.0, 22.5, -0.9, -1.0. HRMS (ESI) calcd for $\text{C}_{49}\text{H}_{46}\text{N}_4\text{O}_{16}\text{Si}$ [$\text{M}+\text{H}$] $^+$ 975.2751, found 975.2737.

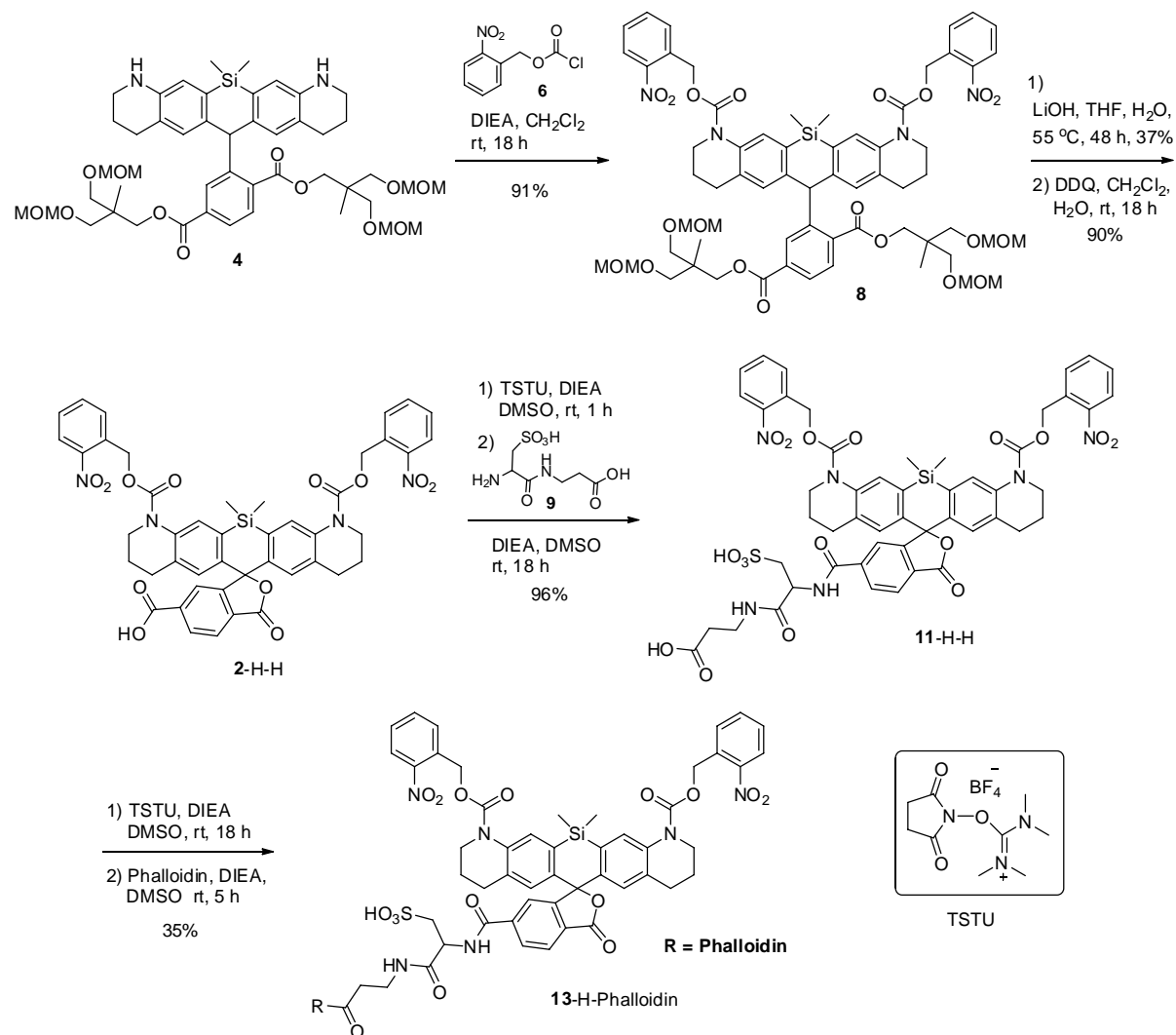


Compound 10-OMe-H: To a solution of acid **1-OMe-H** (2 mg, 2 μmol) in DMSO (200 μL) were added *N,N*-diisopropylethylamine (9.0 μL , 54 μmol) and TSTU (1.15 mg, 3.84 μmol). The reaction mixture was protected from light and stirred at room temperature for 1 h. To the NHS ester formed in the reaction mixture, a hydrophilizer linker, $\text{H}_2\text{NCH}(\text{CH}_2\text{SO}_3\text{H})\text{CONH}(\text{CH}_2)_2\text{CO}_2\text{H}$ (1.95 mg, 7.80 μmol), was added, and the reaction mixture kept for 15 min in the ultrasonic bath at room temperature (shaken from time to time). Water (20 μL) was added and the reaction mixture was stirred at room temperature for another 45 min. After complete conversion (HPLC control), the reaction was “quenched” by addition of acetic acid (3.6 μL , 62 μmol), frozen in a bath with acetone – dry ice mixture, dried by lyophilization and purified by prep. HPLC (Interchim, gradient A:B 70:30 \rightarrow 100:0 over 30 min, A – acetonitrile, B – water + 0.1% trifluoroacetic acid) to obtain compound **10-OMe-H** (1.4 mg 57%) as a colourless solid. 95% HPLC area (column 4.6 mm x 75 mm, 2.6 μm Kinetex C18 100; A/B 20:80 \rightarrow 100:0, A – acetonitrile, B – water + 0.05% trifluoroacetic acid; 10 min run; 1 mL/min flow). HRMS (ESI) calcd for $\text{C}_{55}\text{H}_{56}\text{N}_6\text{O}_{21}\text{SSi}$ [M-H]⁺ 1195.2916, found 1195.2945.

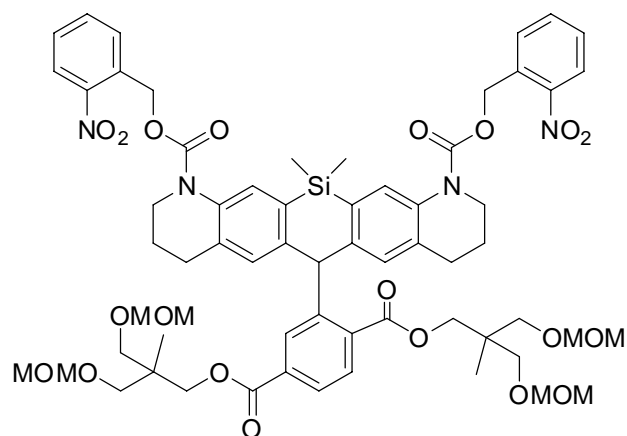


2 x NVOC-QSiR-6-h-aminophalloidin (12-OMe-Phalloidin): Compound **10-OMe-H** (0.4 mg, 0.3 μmol , 1 eq) was dissolved in DMSO (70 μL) and 10% *N,N*-diisopropylethylamine stock solution in DMSO (8.0 μL , 4.8 μmol) was added following by TSTU (0.4 mg, 1.2 μmol ; 3.3 μL of a stock solution containing 3.0 mg TSTU in 25 μL DMSO). The reaction mixture was protected from light and stirred at room temperature for 1 h. HPLC displayed ca. 90% conversion to the corresponding NHS ester. Then aminophalloidin (1.0 mg, 1.3 μmol) in DMSO (25 μL) and 10% *N,N*-diisopropylethylamine stock solution in DMSO (4.0 μL , 2.4 μmol) were added. The reaction mixture was stirred at room temperature for 4 h. After completion of the reaction (HPLC control), the reaction mixture was frozen,

lyophilized and purified by reverse phase HPLC (A/B 0:100 → 100:0 over 20 min, A – acetonitrile, B – water + 0.1% trifluoroacetic) to afford 0.3 mg (46%) of target compound **12-OME-Phalloidin**. Analytical HPLC: 95% HPLC area (4.6 mm x 75 mm, 2.6 μm, C18 column; 1 μL injection; A:B 20:80 → 100:0, A – acetonitrile, B – water + 0.05% trifluoroacetic acid; 10 min run; 1 mL/min flow). HRMS (ESI) calcd for C₉₀H₁₀₃N₁₅O₃₀S₂Si [M-H]⁺ 1964.6123, found 1964.6141.

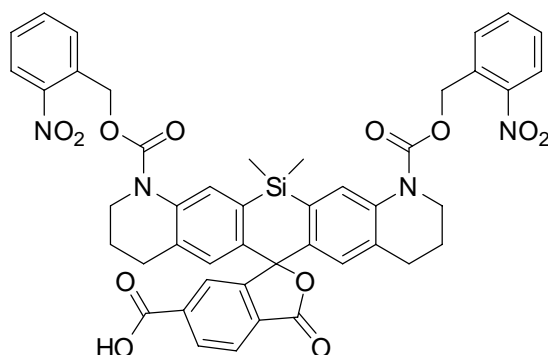


Scheme S4. Synthesis of phalloidin conjugate of dye **13** decorated with a hydrophilizer linker

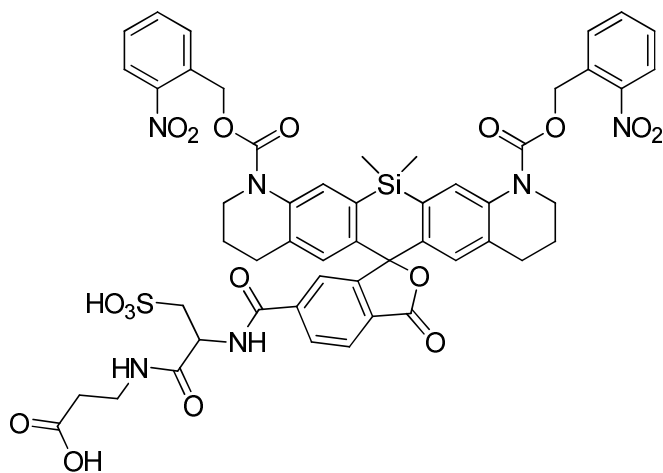


Bis[(2-nitrophenyl)methyl] 6-[2,5-bis({3-(methoxymethoxy)-2-[(methoxymethoxy)methyl]-2-methylpropoxy}carbonyl)phenyl]-13,13-dimethyl-3,4,8,9,10,13-hexahydrosilino[3,2-g:5,6-g']diquinoline-1,11(2H,6H)-dicarboxylate (8**):** Compound **4** (18 mg, 20.5

μmol) was dissolved in CH_2Cl_2 (1.0 mL) under nitrogen. The freshly prepared solution of 2-nitrobenzyl chloroformate^[5] (**6**) (17.6 mg, 81.6 μmol , 4 eq) in CH_2Cl_2 (0.5 mL) was added, followed by *N,N*-diisopropylethylamine (22 μL , 120 μmol , 6 eq). The reaction mixture was stirred at room temperature for 18 h (protected from light), diluted with 10% w/v aqueous citric acid and extracted with EtOAc (3 x). The combined organic solutions were washed with brine, dried (Na_2SO_4), filtered, and evaporated. The crude product was purified by flash chromatography on silica gel (25 g; 10–100% EtOAc/hexanes, linear gradient, with constant 40% v/v CH_2Cl_2 additive) provided **8** (23 mg, 91%) as an off-white solid. ^1H NMR (CDCl_3 , 400 MHz) δ 8.09 (dd, $J = 8.2, 1.3$ Hz, 2H), 7.93 (s, 2H), 7.82 – 7.72 (m, 2H), 7.70 (dd, $J = 8.1, 1.7$ Hz, 1H), 7.64 (td, $J = 7.6, 1.3$ Hz, 2H), 7.57 (dd, $J = 7.9, 1.5$ Hz, 2H), 7.49 – 7.45 (m, 2H), 7.01 (s, 2H), 6.61 (s, 1H), 5.62 (AB quartet, $\nu_A = 2255.85$ Hz, $\nu_B = 2241.63$ Hz, $J_{AB} = 14.8.0$ Hz, 4H), 4.62 (s, 4H), 4.51 (s, 4H), 4.47 (s, 2H), 4.14 (s, 2H), 3.83 – 3.71 (m, 4H), 3.57 (s, 4H), 3.39 (s, 4H), 3.34 (s, 6H), 3.24 (s, 6H), 2.73 – 2.57 (m, 4H), 1.92 – 1.86 (m, 4H), 1.16 (s, 3H), 0.97 (s, 3H), 0.60 (s, 3H), 0.34 (s, 3H); ^{13}C NMR (CDCl_3 , 101 MHz) δ 168.3, 165.1, 154.1, 148.6, 147.5, 143.3, 136.0, 133.8, 133.2, 132.8, 132.7, 132.6, 131.6, 131.3, 130.0, 129.8, 129.1, 128.6, 125.8, 125.0, 96.7, 96.6, 70.2, 69.9, 68.1, 67.3, 64.4, 55.2, 55.1, 47.5, 45.1, 39.7, 39.5, 27.4, 23.2, 17.6, 17.4, 0.31, -0.59; HRMS (ESI) calcd for $\text{C}_{63}\text{H}_{76}\text{N}_4\text{O}_{20}\text{Si}$ [$\text{M}+\text{Na}$]⁺ 1259.4714, found 1259.4713.

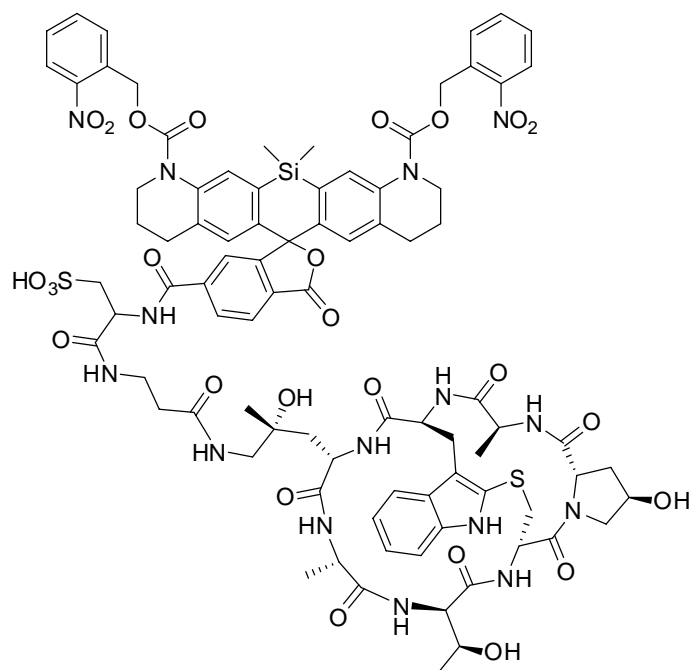


2 x 2-NBnOC-QSiR-6-Carboxylic acid (2-H-H): A vial was charged with **8** (23.4 mg, 18.9 μmol), sealed, and evacuated/backfilled with nitrogen (3 x). Freshly degassed THF (1.5 mL) and 1 M aq LiOH solution (0.40 mL, 0.38 mmol, 20 eq) were added, and the mixture was stirred at 55 °C for 48 h (protected from light). The reaction mixture was cooled to room temperature, acidified with 1 M HCl (1 mL), diluted with water, and extracted with CH_2Cl_2 (3 x). The combined organic solutions were dried (Na_2SO_4), filtered, and evaporated. The residue was purified by flash chromatography on silica gel (0–10% methanol in CH_2Cl_2) to get the desired leuco-diacid **2-H-H** (6.0 mg, 37%) as an off-white solid which was used in the next step. The di-acid (5.0 mg, 5.8 μmol , 1 eq) was dissolved in 10:1 $\text{CH}_2\text{Cl}_2/\text{H}_2\text{O}$ (1.1 mL); DDQ (6.6 mg, 29 μmol , 5 eq) was added, and the reaction mixture stirred at room temperature for 18 h (protected from light). The mixture was concentrated in vacuo and was purified by flash chromatography on silica gel (10 g; 0–5% methanol/ CH_2Cl_2 , linear gradient) to afford diacid **2-H-H** as an off-white solid (“closed” form, 4.5 mg, 90%). Analytical HPLC: >98% HPLC area (4.6 mm x 75 mm, 2.6 μm , C18 column; A:B 20:80 \rightarrow 100:0, A – acetonitrile, B – water + 0.05% trifluoroacetic acid; 10 min run; 1 mL/min flow; ^1H NMR ($\text{DMSO}-d_6$, 400 MHz) δ 8.11 (dd, $J = 8.1, 1.3$ Hz, 2H), 8.08 – 8.00 (m, 2H), 7.98 (s, 2H), 7.79 – 7.75 (m, 2H), 7.71 – 7.57 (m, 5H), 6.83 (s, 2H), 5.49 (AB quartet, $\nu_A = 2199.6$ Hz, $\nu_B = 2193.8$ Hz, $J_{AB} = 14$ Hz, 4H), 3.83 – 3.57 (m, 4H), 2.73 – 2.53 (m, 4H), 1.77 (m, 4H), 0.37 (s, 3H), 0.24 (s, 3H). ^{13}C NMR ($\text{DMSO}-d_6$, 101 MHz) δ 169.4, 165.8, 155.5, 153.4, 147.5, 138.2, 137.6, 134.1, 132.4, 131.4, 130.7, 130.5, 130.2, 129.9, 129.5, 128.8, 126.4, 125.6, 124.9, 123.2, 114.3, 88.5, 64.1, 44.7, 26.9, 22.4, -0.5, -0.7. HRMS (ESI) calcd for $\text{C}_{45}\text{H}_{38}\text{N}_4\text{O}_{12}\text{Si}$ [$\text{M}+\text{H}$]⁺ 855.2328, found 855.2318.

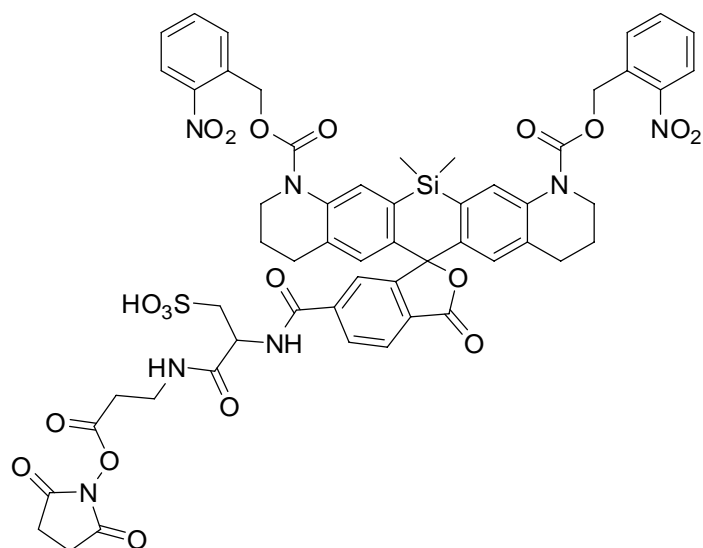


Compound 11-H-H: To a solution of acid **2-H-H** (4.1 mg, 4.8 μmol) and TSTU (2.9 mg, 9.6 μmol , 2 eq) in anhydrous DMSO (300 μL) was added *N,N*-diisopropylethylamine (21.9 μL , 125 μmol , 5 eq). The reaction mixture was protected from light and stirred at room

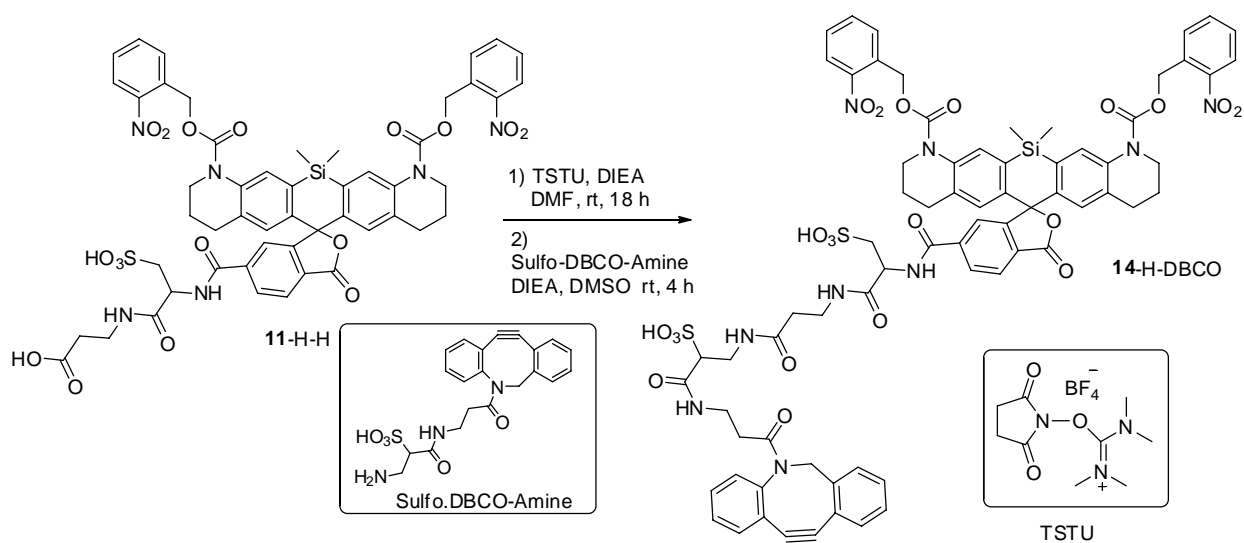
temperature for 1 h (monitored by HPLC). To NHS ester formed in the reaction mixture, hydrophilizer (**9**)^[6] (4.0 mg, 14.4 μmol) was added and the reaction mixture was sonicated in the ultrasonic bath at room temperature (shaken from time to time) for 15 min. Water (20 μL) was added and the reaction mixture was further stirred at room temperature for 18 h (monitored by HPLC). After completion of the reaction (HPLC control), 9 μL of acetic acid were added. The reaction mixture was frozen and dried by lyophilization. The residue was separated by prep. HPLC; A:B 20:80 \rightarrow 100:0 over 25 min (A – acetonitrile, B – water + 0.1% trifluoroacetic acid) to afford acid **11-H-H** (5 mg, 96%) as a solid. Analytical HPLC: >98% HPLC area, t_{R} = 6.1 min (column 4.6 mm x 75 mm, Kinetex 2.6 μm C18 100; 20 – 80% $\text{CH}_3\text{CN}/\text{H}_2\text{O}$, linear gradient, with constant 0.05% v/v TFA additive; 10 min run; 1 mL/min flow; HRMS (ESI) calcd for $\text{C}_{51}\text{H}_{48}\text{N}_6\text{O}_{17}\text{SSi}$ $[\text{M}-\text{H}]^+$ 1075.2493, found 1075.2505.



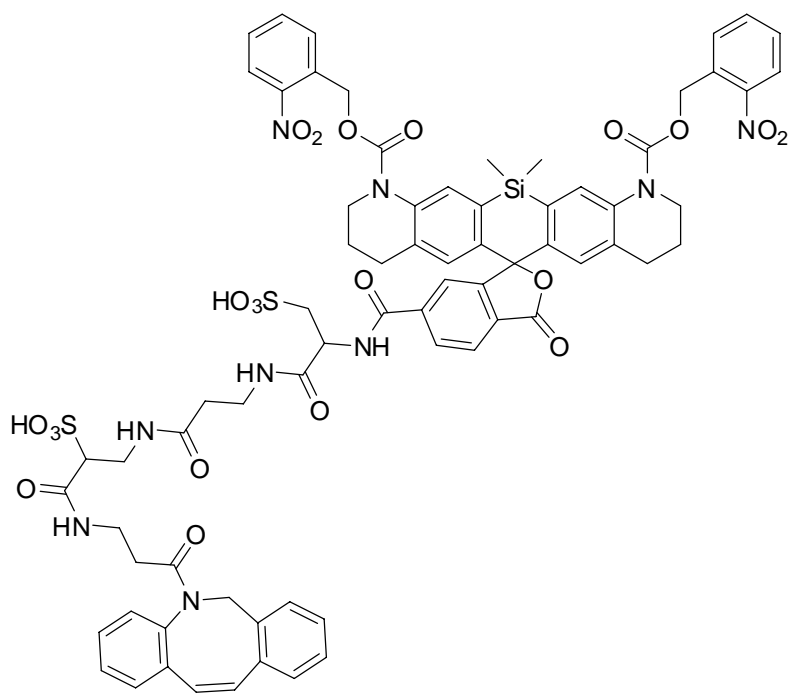
Compound 13-H-Phalloidin (R = *N*-hydroxysuccinimidyloxy / NH-phalloidin): Acid **11-H-H** (1.0 mg, 0.93 μmol , 1 eq) was combined with TSTU (0.56 mg, 1.86 μmol , 2 eq) and *N,N*-diisopropylethylamine (1.6 μL , 9.3 μmol , 10 eq), in anhydrous DMSO (300 μL), and the reaction mixture stirred at room temperature for 1 h (monitored by HPLC) and protected from light. HPLC analysis showed the degree of conversion to compound **11-H-Su** (t_{R} = 6.4 min) of ca. 90%; t_{R} = 6.4 min (for HPLC conditions, see compound **11-H-H**). $\text{C}_{55}\text{H}_{51}\text{N}_7\text{O}_{19}\text{SSi}$, $M = 1173.3$, $[\text{M}-\text{H}]^+$ found 1172.3. Aminophalloidin tosylate (1.0 mg, 1.0 μmol) was added, and the reaction mixture was stirred for additional 5 h at room temperature. The reaction mixture was frozen in a bath with dry ice and acetone and dried by lyophilization. The residue was purified by reverse phase HPLC (A:B = 0:100 \rightarrow 100:0 over 20 min, A – acetonitrile, B – water + 0.1% trifluoroacetic acid) to afford **13-H-Phalloidin** (600 μg , 35%) as a solid. Analytical HPLC: 95% area (250 x 4.6 mm, 10 μm , C18 column; Solvent A: water + 0.1% TFA; solvent B: ACN + 0.1% TFA. 0-3 min: 40% B, 3–15 min: 40–100% B; 20 min run; 1.2 mL/min flow); HRMS (ESI) calcd for $\text{C}_{86}\text{H}_{95}\text{N}_{15}\text{O}_{26}\text{S}_2\text{Si}$ $[\text{M}-\text{H}]^+$ 1844.5711, found 1844.5640.



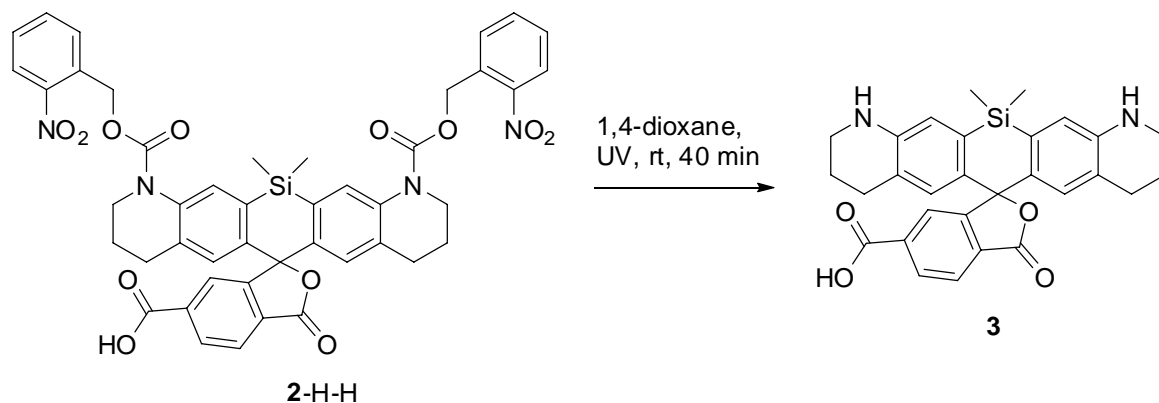
Compound 11-H-Su: For conjugation with antibodies, compound **11-H-Su** was generated with ca. 90% conversion from 0.29 mg (270 nmol) of compound **11-H-H** in dry DMSO (50 μ L) in the course of addition of 3.6 μ L (2.1 μ mol) of 10% *i*Pr₂Net in DMSO and 1.0 μ L of the stock solution of 3.0 mg TSTU in 25 μ L DMSO; reaction time 1 h.



Scheme S5. Synthesis of the sulfo-DBCO-amine conjugate of dye **14-H-DBCO** for "click chemistry".



2 x 2-NBnOC-QSiR-6-hydrophylizer-linker-Sulfo-DBC0 (14-H-DBC0): NHS ester of acid 11-H-H (2.0 mg, 1.7 μmol) was dissolved in anhydrous DMSO (300 μL), then *N,N*-diisopropylethylamine (4.2 μL , 23.8 μmol) and DBCO-amine (2.2 mg, 5.1 μmol) were added. The reaction mixture was stirred at room temperature for 4 h (protected from light), and the course of the reaction monitored by HPLC. The reaction mixture was frozen, dried by lyophilisation, and the residue purified by prep. HPLC (A/B 50:50 \rightarrow 90:10 over 20 min, A – acetonitrile, B – water + 20mM TEA-FA, pH-6.6) to afford compound **14-H-DBC0** (1.0 mg, 45%) as a solid. Analytical HPLC: >95% purity (4.6 mm x 75 mm 2.6 μm C18 column; 1 μL injection; 20–80 \rightarrow 100:0 $\text{CH}_3\text{CN}/\text{H}_2\text{O}$ TEA-FA 20 mM pH-4; 10 min run; 1 mL/min flow; HRMS (ESI) calcd for $\text{C}_{72}\text{H}_{67}\text{N}_9\text{O}_{21}\text{S}_2\text{Si}$ $[\text{M}-\text{H}]^+$ 1484.3589, found 1484.3609.



SiR (3): Compound **2-H-H** (3.0 mg, 3.5 μmol , 1 eq) was dissolved in 1,4-dioxane (3 mL). The solution in a quartz cuvette was irradiated with 365 nm UV lamp and stirred for 40 min. The reaction mixture was concentrated and the residue was subjected to prep. HPLC (A:B 0:100 \rightarrow 100:0 over 20 min, A – acetonitrile, B – water + 0.1% trifluoroacetic acid) to afford SiRhodamine (**3**) trifluoroacetate as a deep blue solid (700 μg , 40%). Analytical HPLC: >95% HPLC area (75 mm x 4.6 mm, 2.6 μm C18 column; Solvent A: ACN; solvent B: water + 0.05% TFA. A/B 0:15 \rightarrow 100:0 over 10 min run; 1 mL/min flow; ^1H NMR (CD_3OD , 400 MHz) δ 8.34 – 8.22 (m, 2H), 7.78 (dd, $J = 1.6, 0.6$ Hz, 1H), 6.98 (s, 2H), 6.56 (s, 2H), 3.48 – 3.44 (m, 4H), 2.48 (t, $J = 6.2$ Hz, 4H), 1.89 – 1.75 (m, 4H), 0.51 (s, 3H), 0.45 (s, 3H). ^{19}F NMR (CD_3OD , 376 MHz) δ -77.2 (s); HRMS (ESI) calcd for $\text{C}_{29}\text{H}_{28}\text{N}_2\text{O}_4\text{Si}$ $[\text{M}+\text{H}]^+$ 497.1891, found 497.1889.

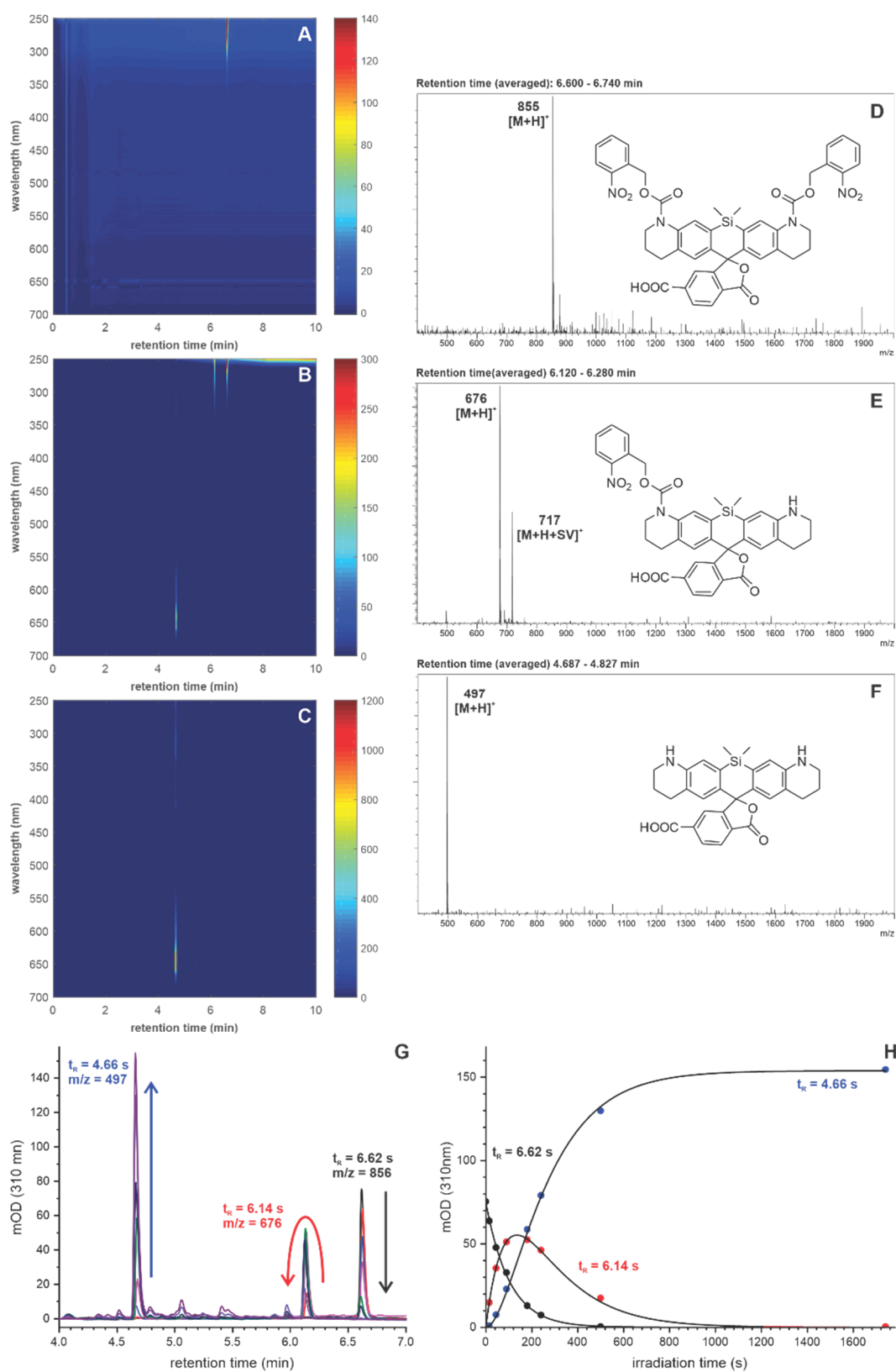


Figure S1. "Uncaging" (photoactivation) experiments with compound 2-H-H, in a 1:1 mixture of acetonitrile and phosphate buffer (100 mM, pH = 7). Small aliquots of the irradiated solution were extracted at specific times and analyzed by LC-MS. (A, B, C) 3D absorption maps in mOD of the starting solution (A), a partially photoactivated solution (B), and the solution obtained at the end of the experiment (C). (D, E, F) Mass spectra of the three main peaks observed in the chromatogram of (B), when the reaction was incomplete. (G) Chromatograms at different irradiation times; the wavelength for detection was selected arbitrarily, to obtain a reasonable absorption for all reactants. (H) Temporal evolution of the intensities of the three main peaks. The curves correspond to a global fit based on two consecutive reactions.

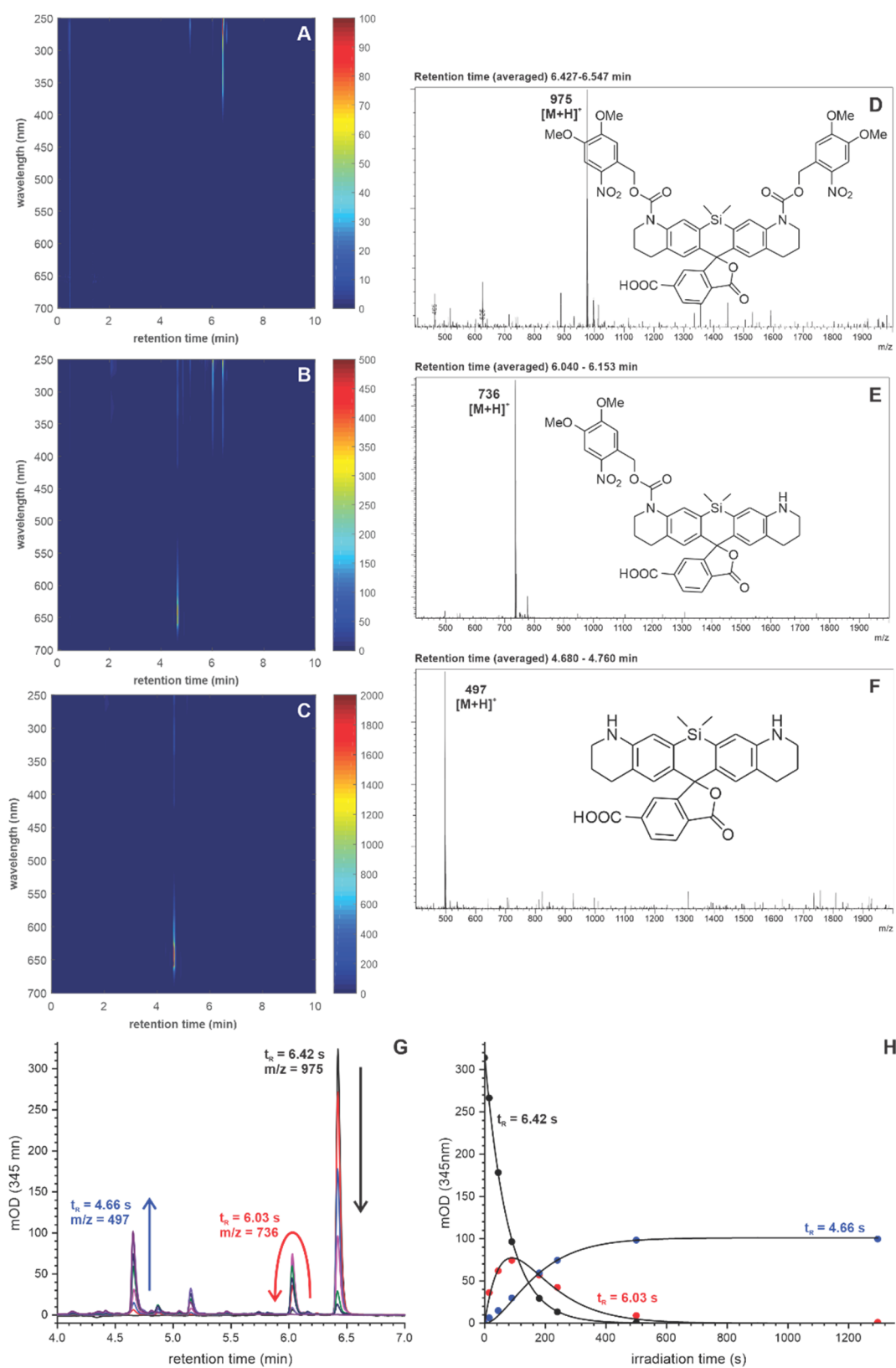


Figure S2. “Uncaging” (photoactivation) experiments with compound 1-OMe-H, in a 1:1 mixture of acetonitrile and phosphate buffer (100 mM, pH = 7). Small aliquots of the irradiated solution was extracted at specific times and analyzed by LC-MS. (A, B, C) 3D absorption maps in mOD of the starting solution (A), a partially photoactivated solution (B), and the solution obtained at the end of the experiment (C). (D, E, F) Mass spectra of the three main peaks observed in the chromatogram of (B), when the reaction was incomplete. (G) Chromatograms at different irradiation times; the wavelength for detection was selected arbitrarily, to obtain a reasonable absorption for all reactants. (H) Temporal evolution of the intensities of the three main peaks. The curves correspond to a global fit involving two consecutive reactions scheme.

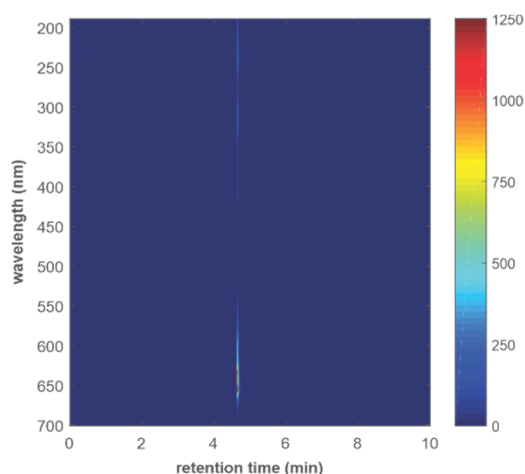


Figure S3. LC-MS (3D absorption map in mOD) of model compound **3** (free dye formed upon full photo-activation) recorded under the same conditions, as for the irradiated solutions of the two caged compounds (**2-H-H** and **1-OMe-H**).

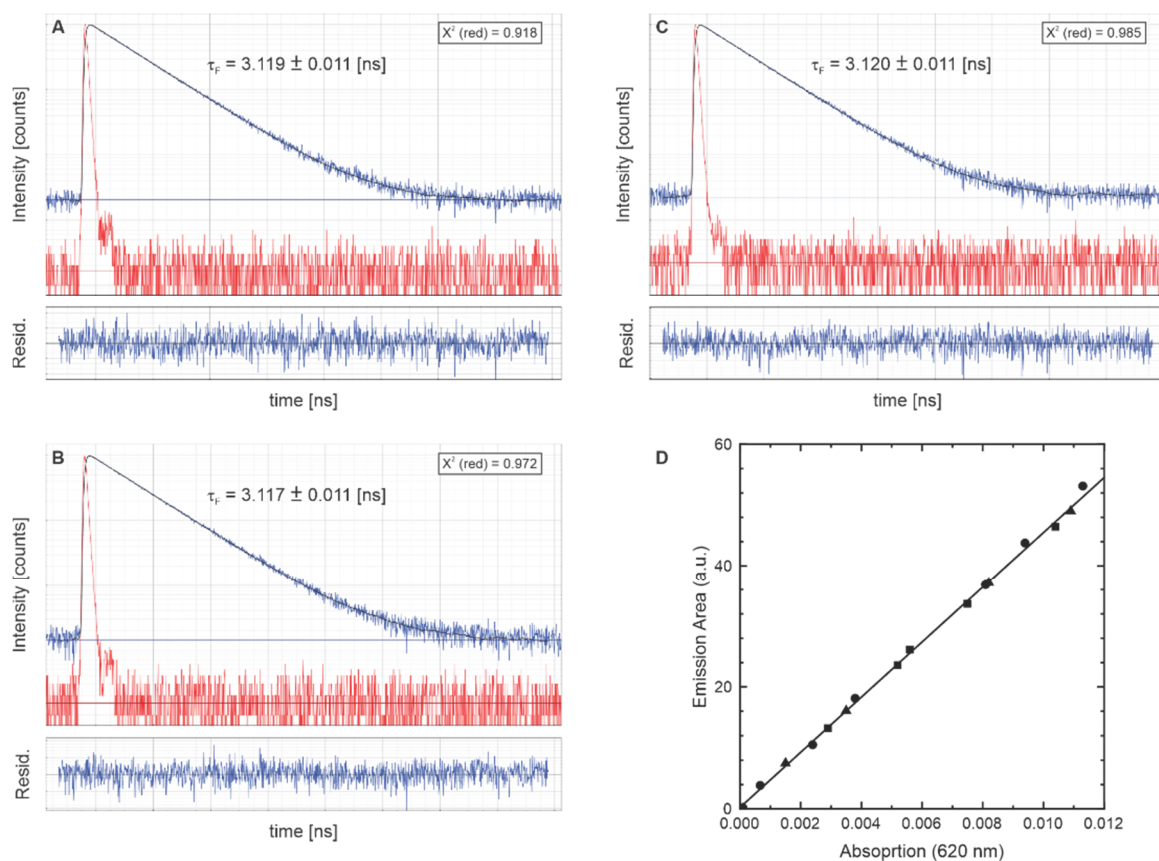


Figure S4. Fluorescence decays of the irradiated/partially "uncaged" compounds **1-OMe-H** (**A**) and **2-H-H** (**B**) in solutions and a diluted solution of compound **3** (**C**), in a 1:1 mixture of acetonitrile and phosphate buffer (100 mM, pH = 7). (**D**) The total integrated emission vs. the absorption at the excitation wavelength (620 nm) is shown for compounds **1-OMe-H** (triangles), **2-H-H** (circles) and **3** (squares), in the same solvent. For the "caged" (masked) compounds, starting solutions were stepwise irradiated, while the concentration for compound **3** was increased by additions of a stock solution. An emission quantum yield of 0,60 was calculated, using Nile Blue in ethanol as a reference dye ($\Phi_{\text{Fluo}} = 0.27$)^[7].

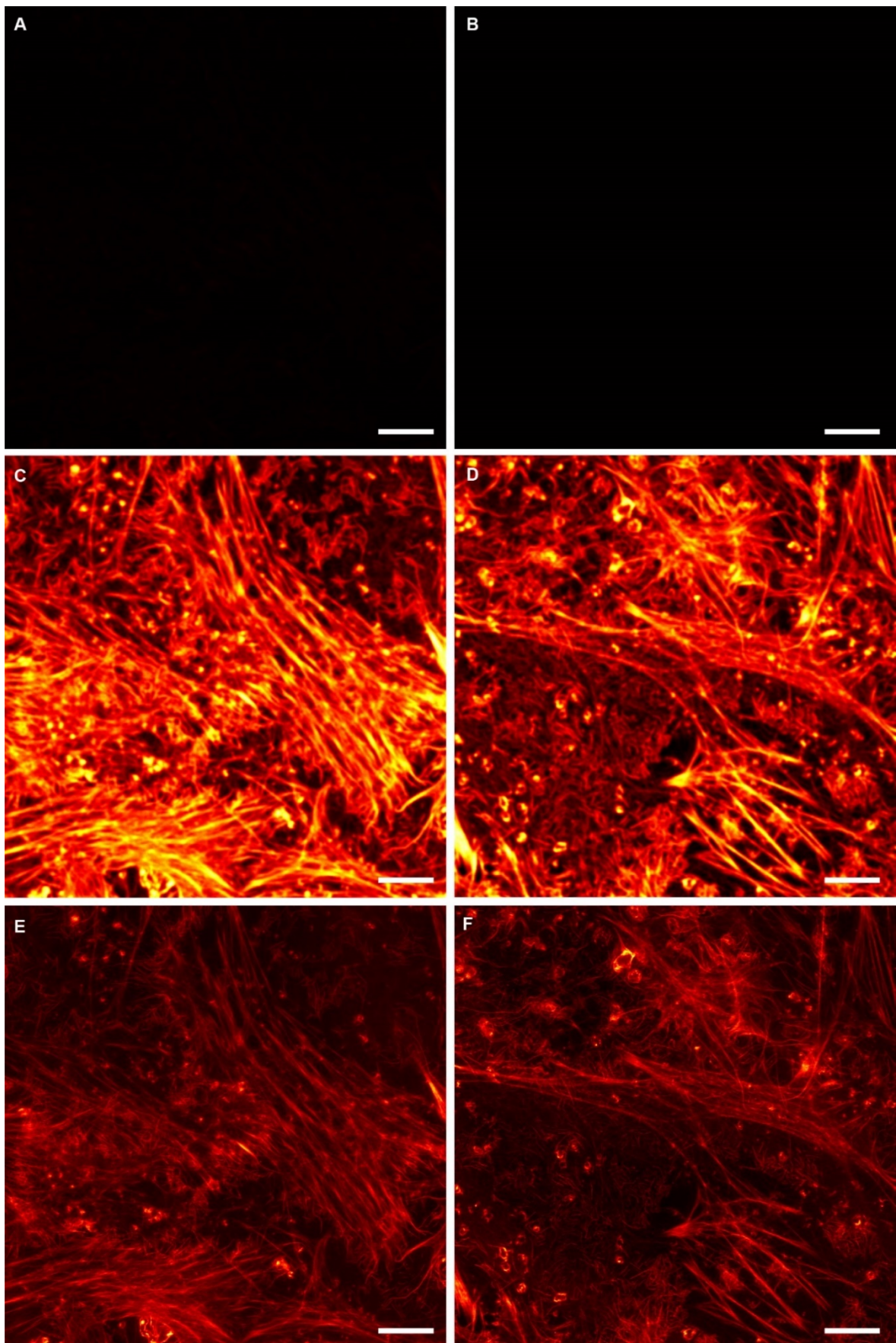


Figure S5. Confocal (A - D) and STED (E, F) images of fixed HeLa labelled with compounds 12-OMe-Phalloidin (A, C, E) and 13-H-Phalloidin (B, D, F) before UV activation (A, B), after UV activation (C - F). Confocal images share the same colormap. Scale-bars: 5 μ m

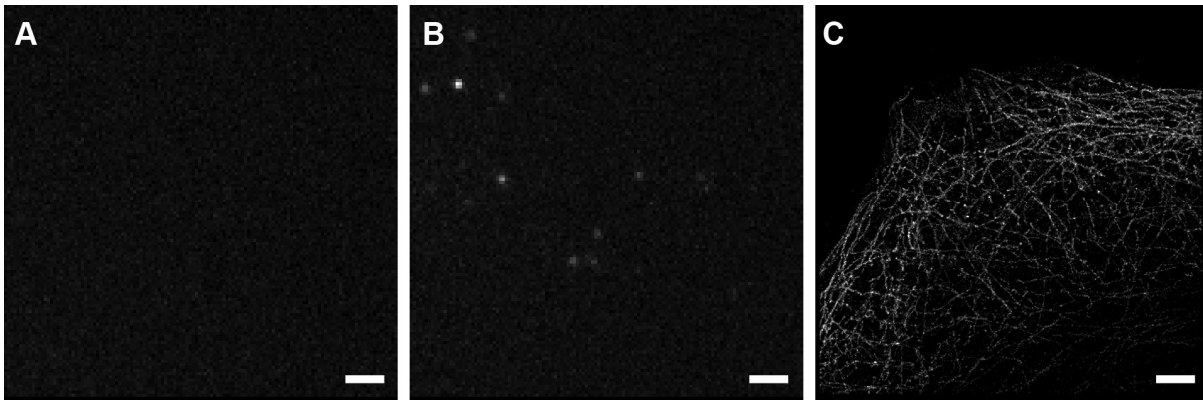


Figure S6. TIRF images of a PFA fixed HeLa cells immunostained with primary antibody against alpha-tubulin and secondary antibodies with compound **14-H-DBCO** without **A** and with **B** 405 nm UV activation. **C**: PALM image of the same area. Scale-bars: 2 μm

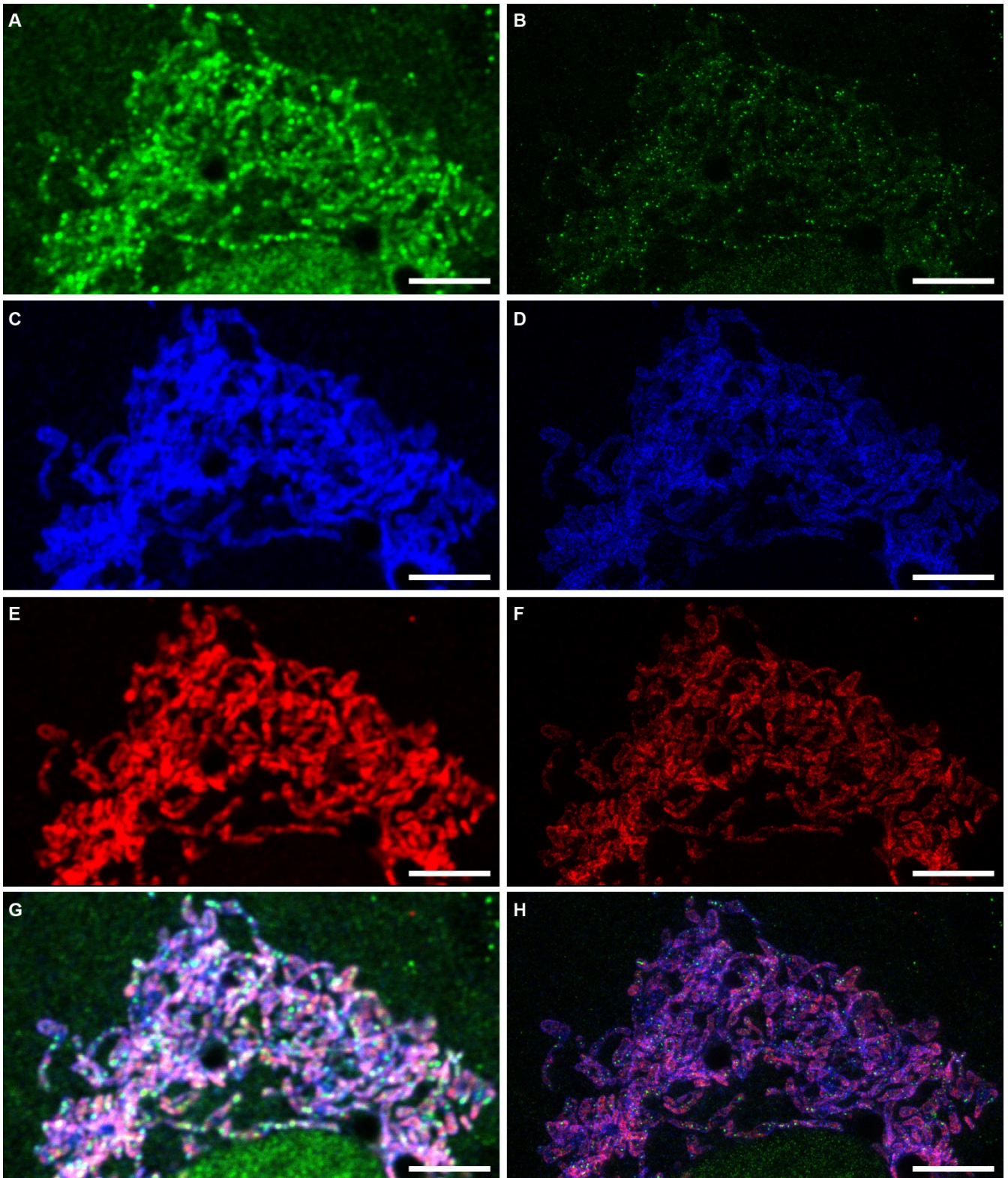
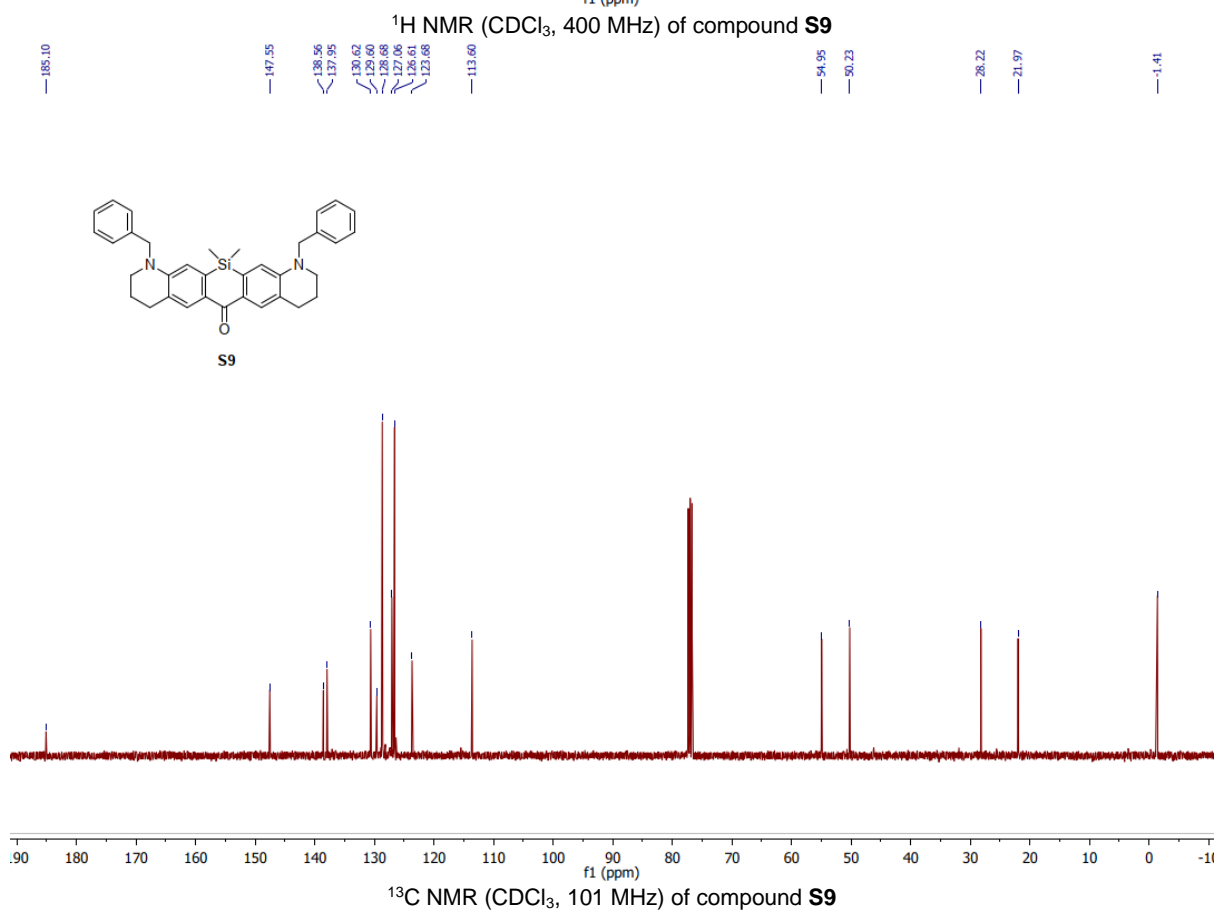
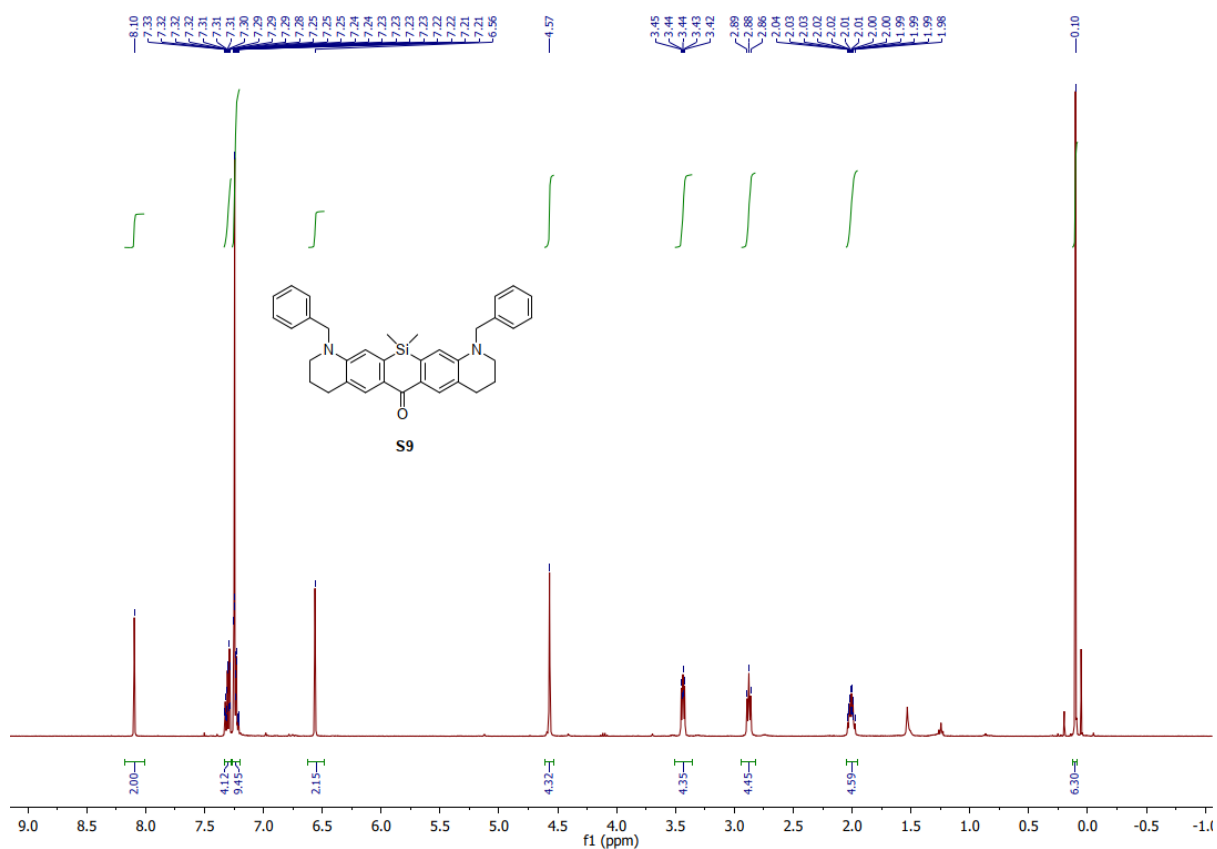
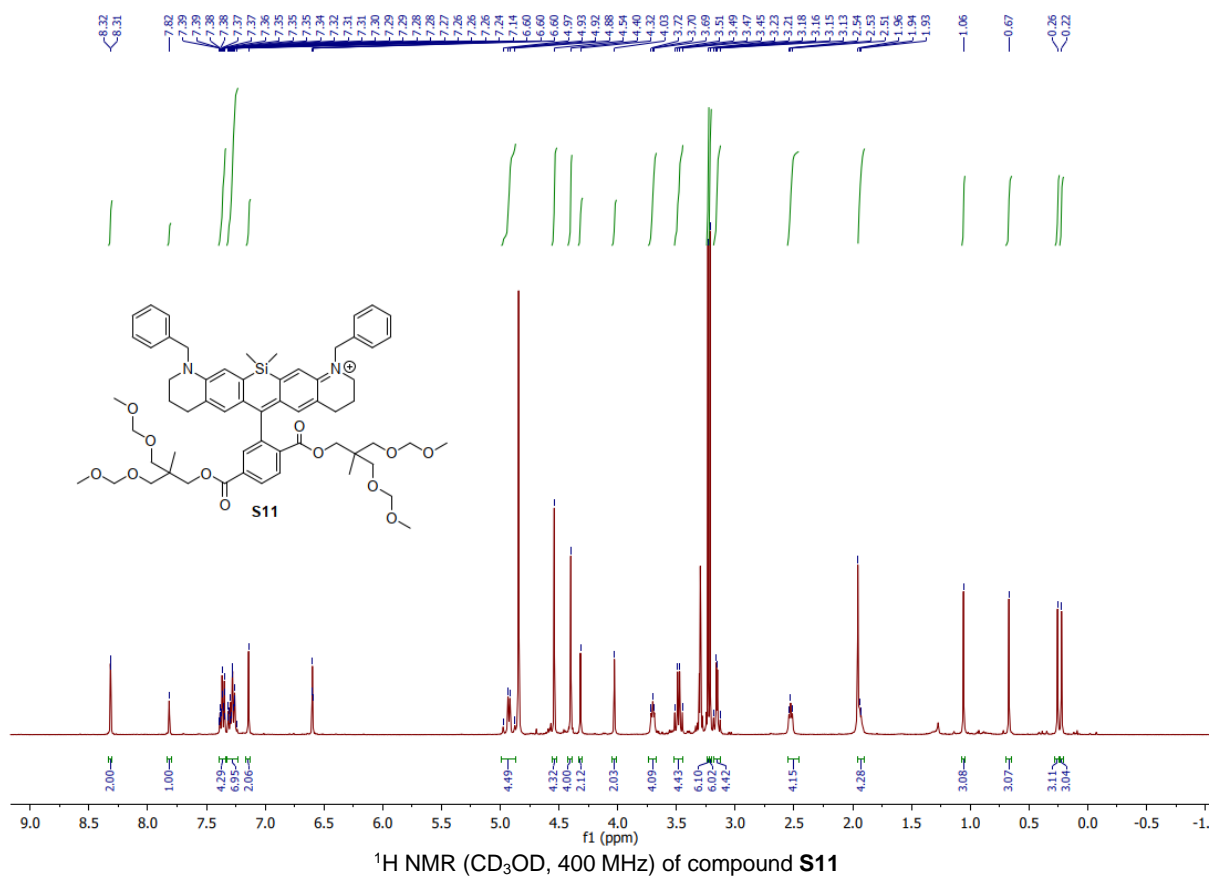
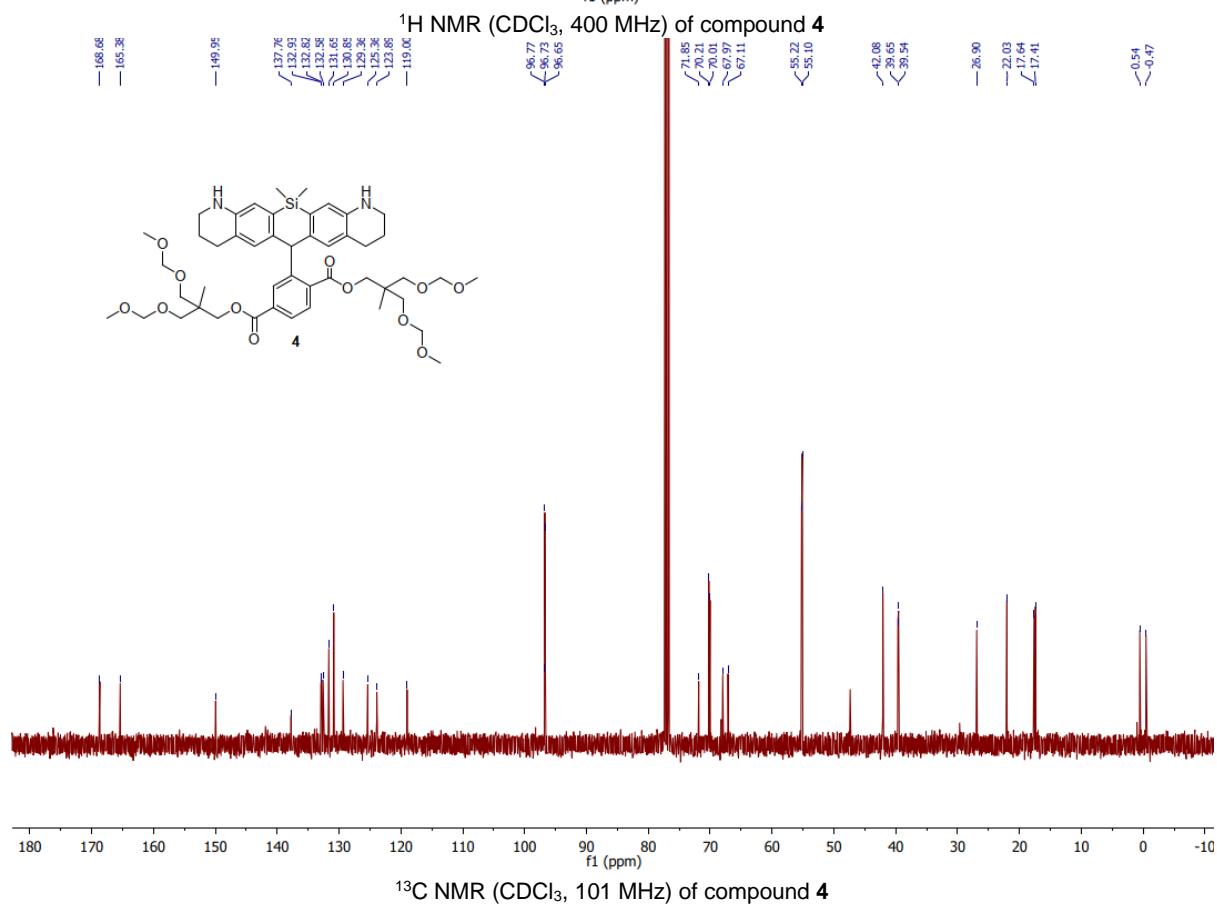
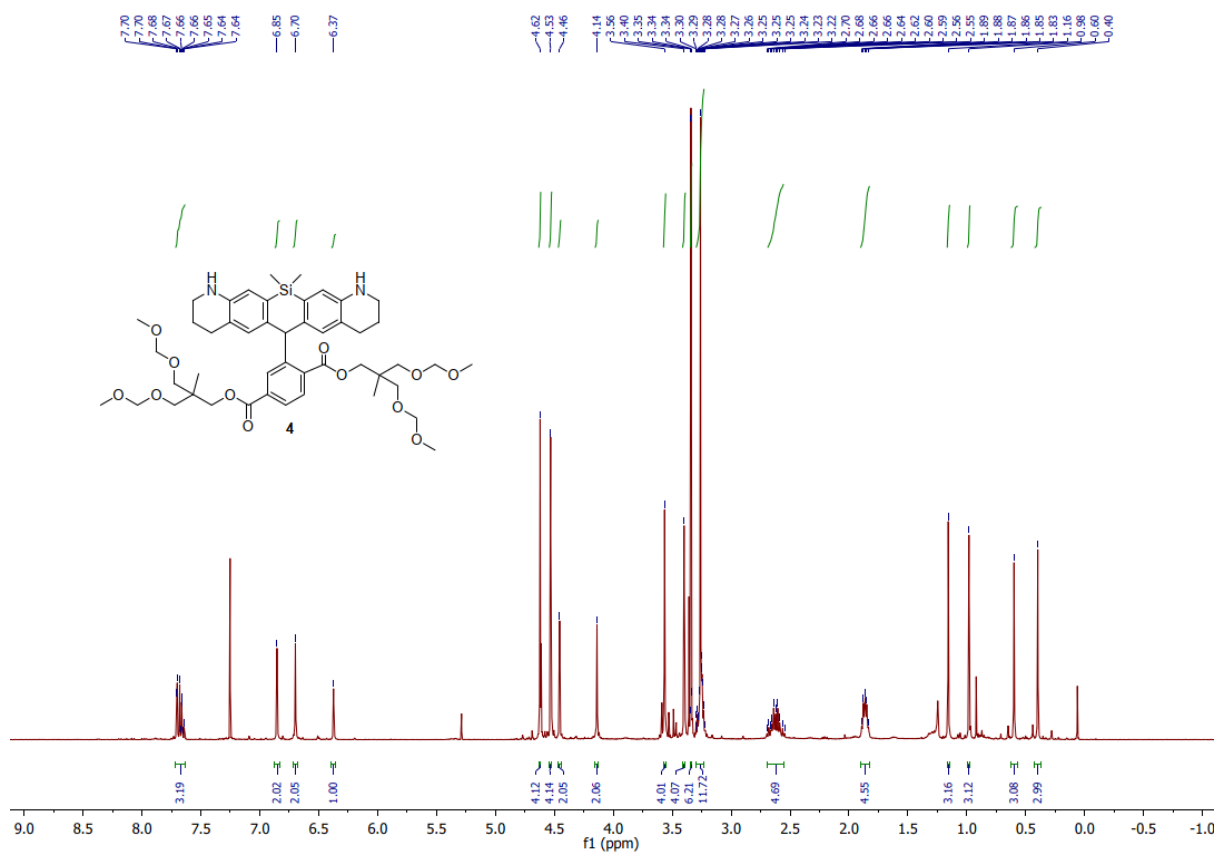
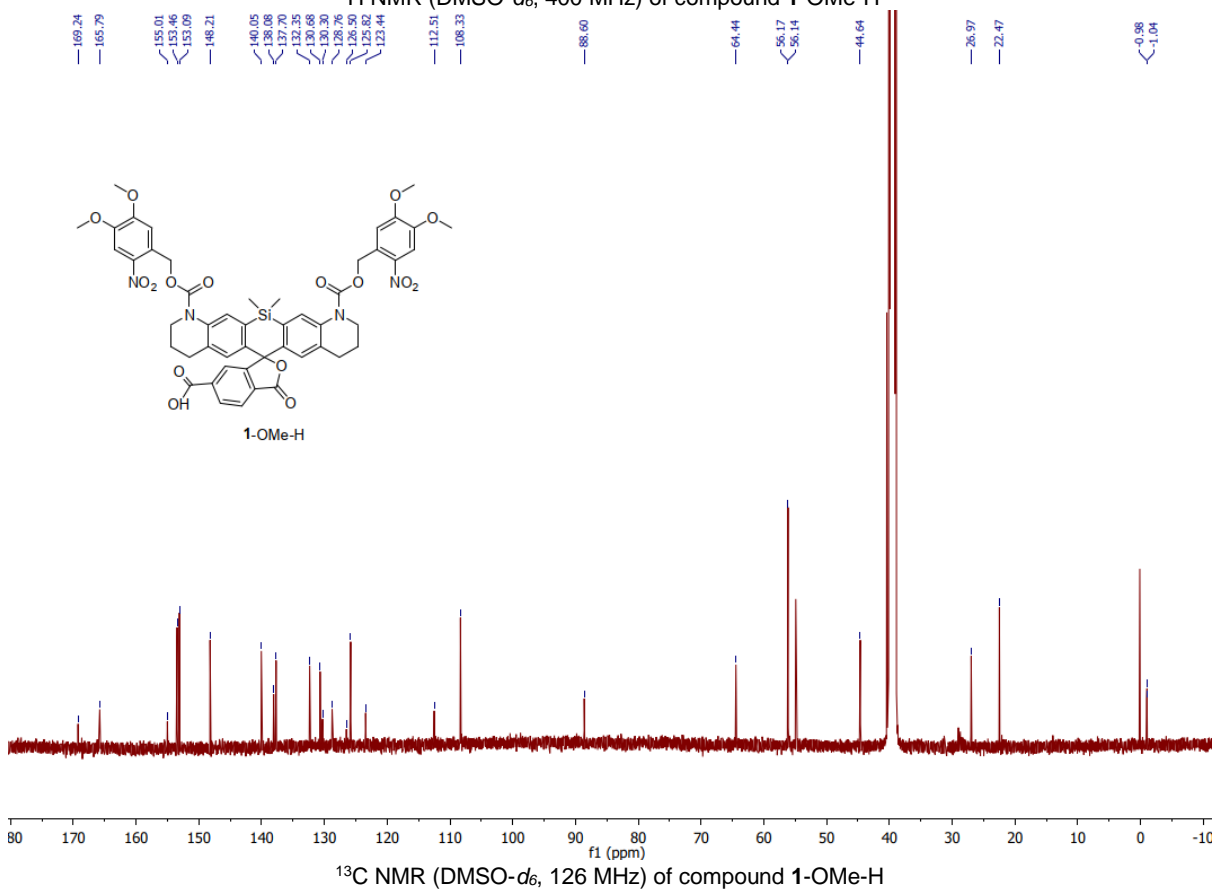
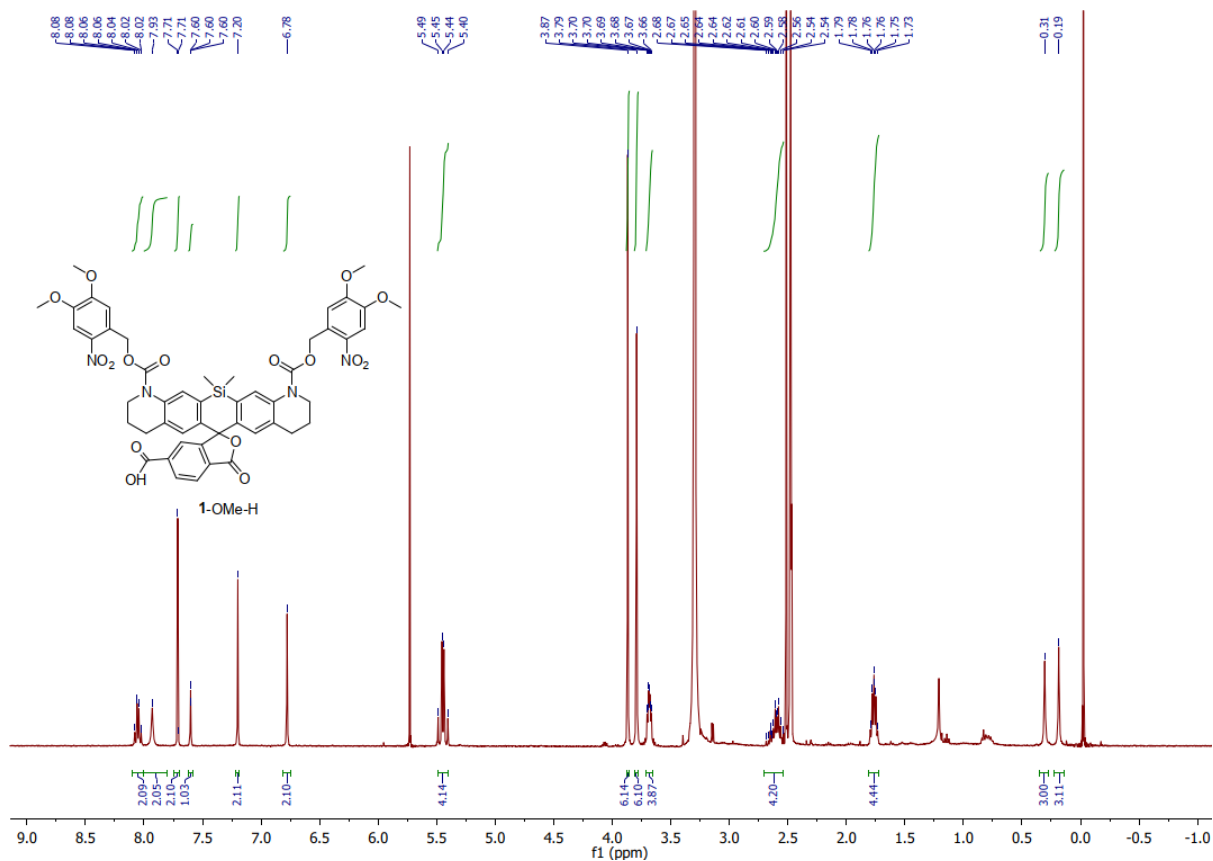


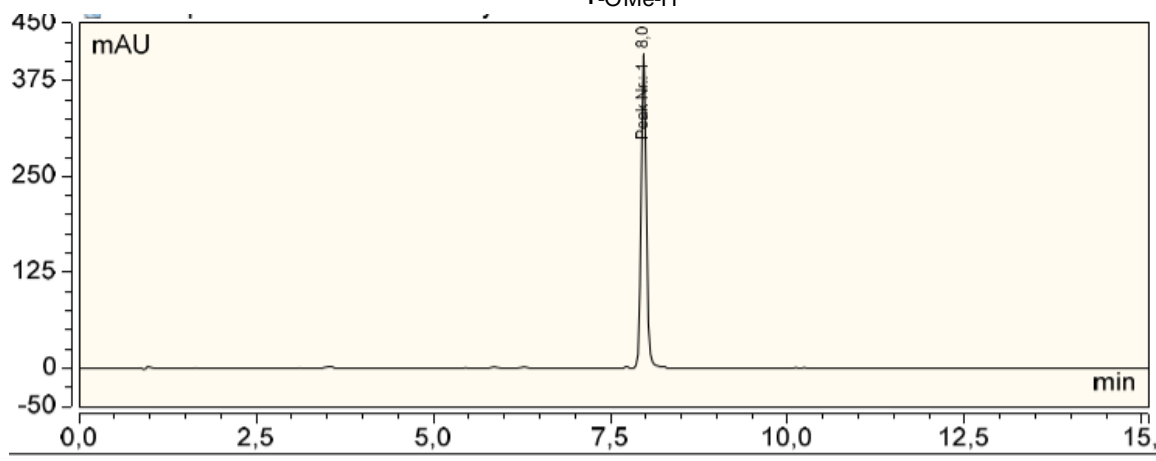
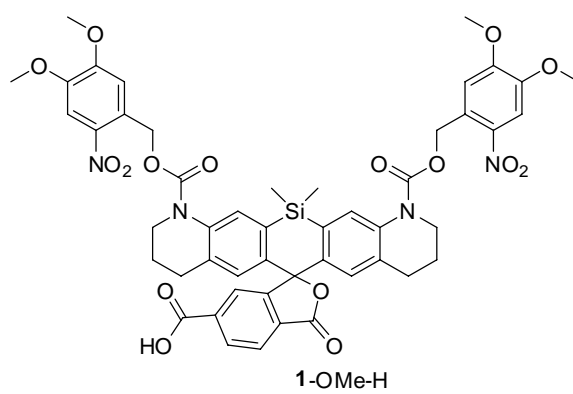
Figure S7 Confocal (A, C, E, G) and STED (B, D, F, H) images of fixed U2OS cells labeled with primary antibody against DNA (A, B, G/H: green), TOM 20 (C, D, G/H: blue) and ATP-Synthase B (E, F, G/H: red) conjugated with compound 14-H-DBCO and secondary antibodies conjugated with fluorescent dyes STAR 635P (green) and Alexa 594 (blue). Scale-bars: 5 μ m



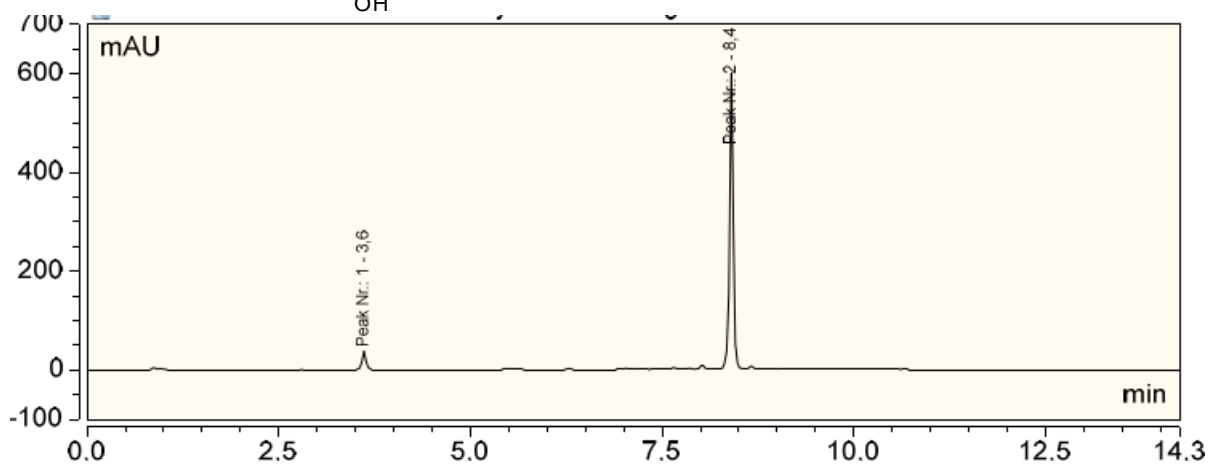
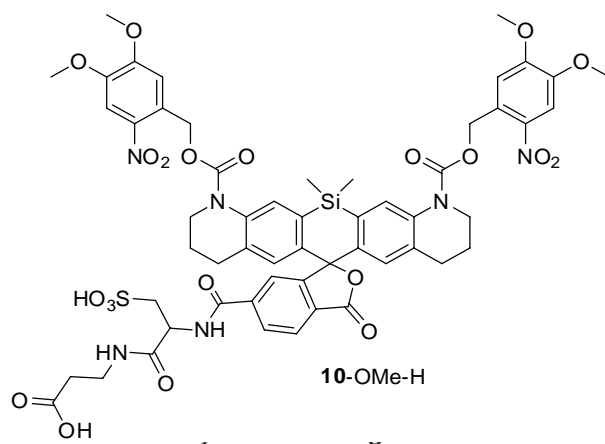




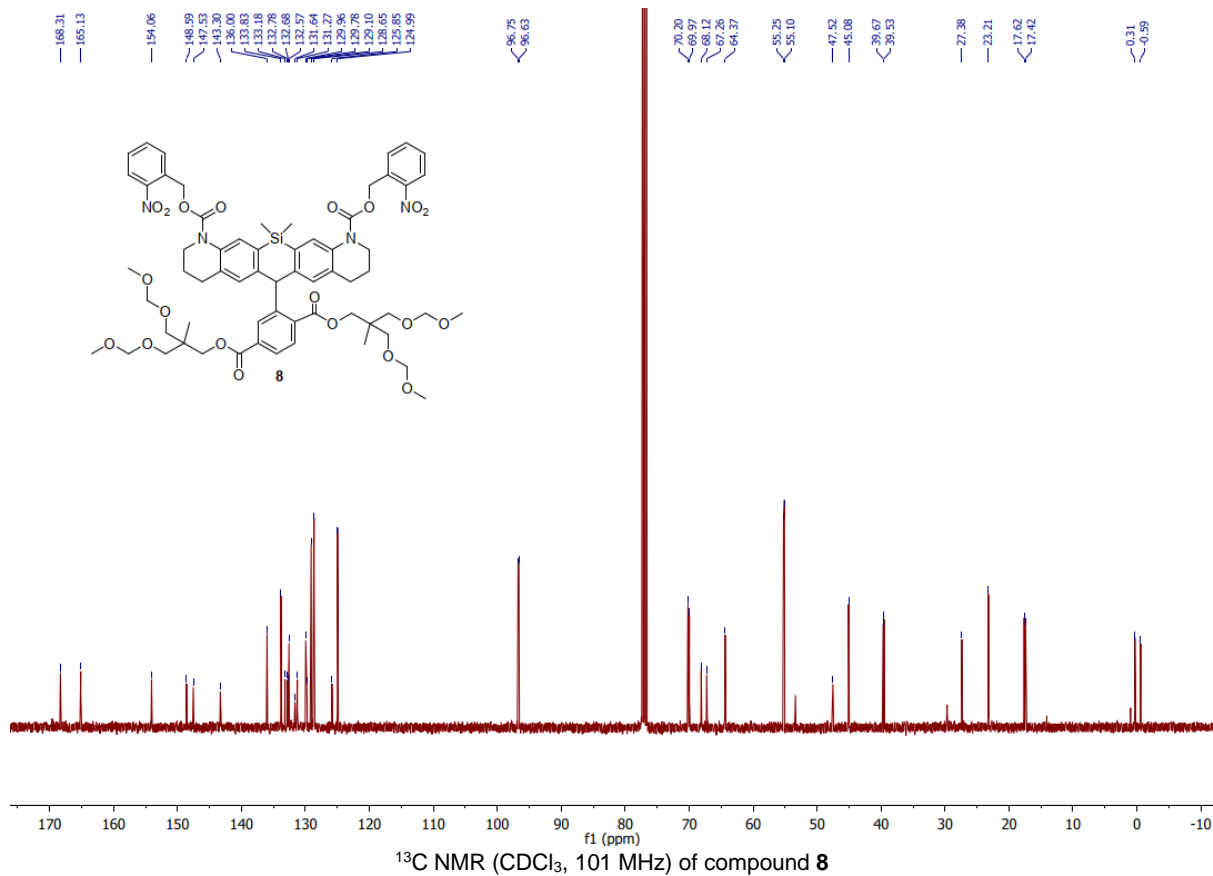
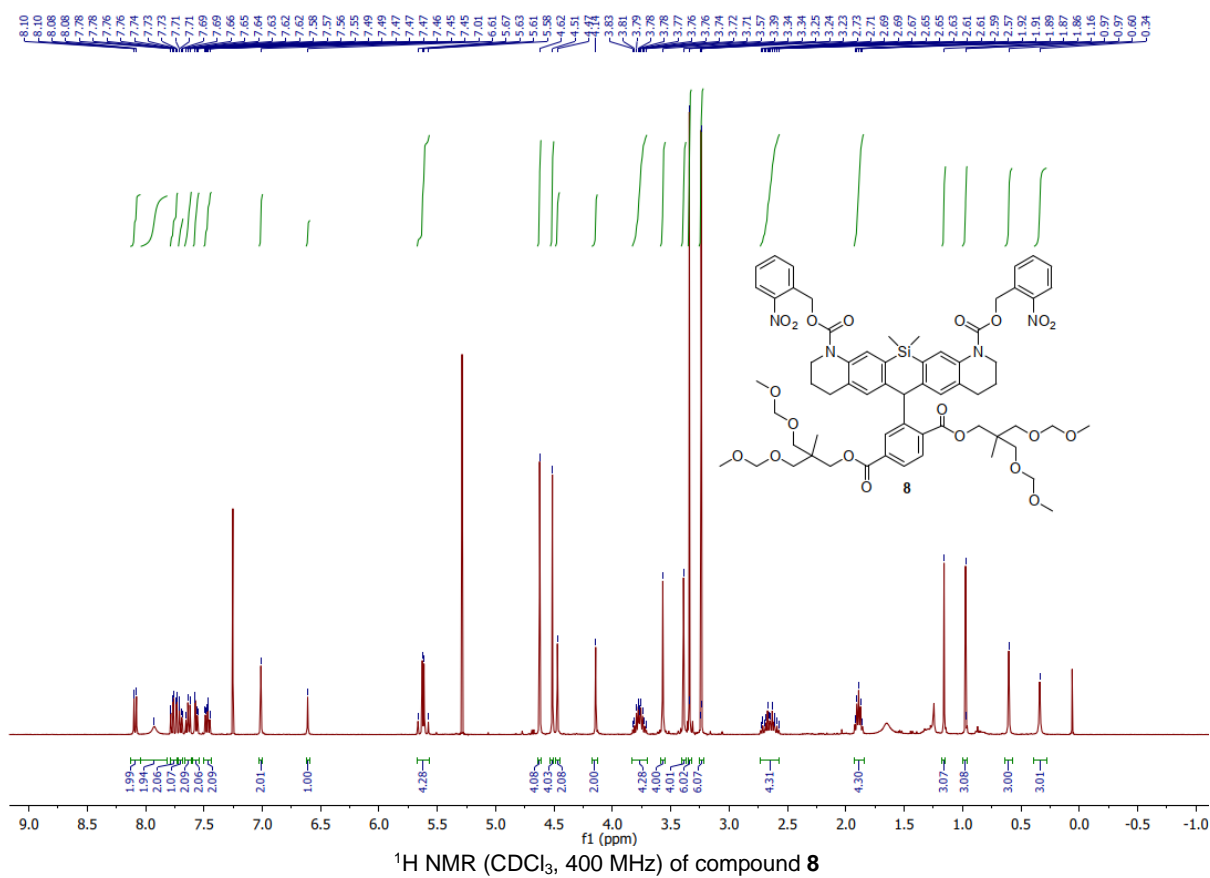


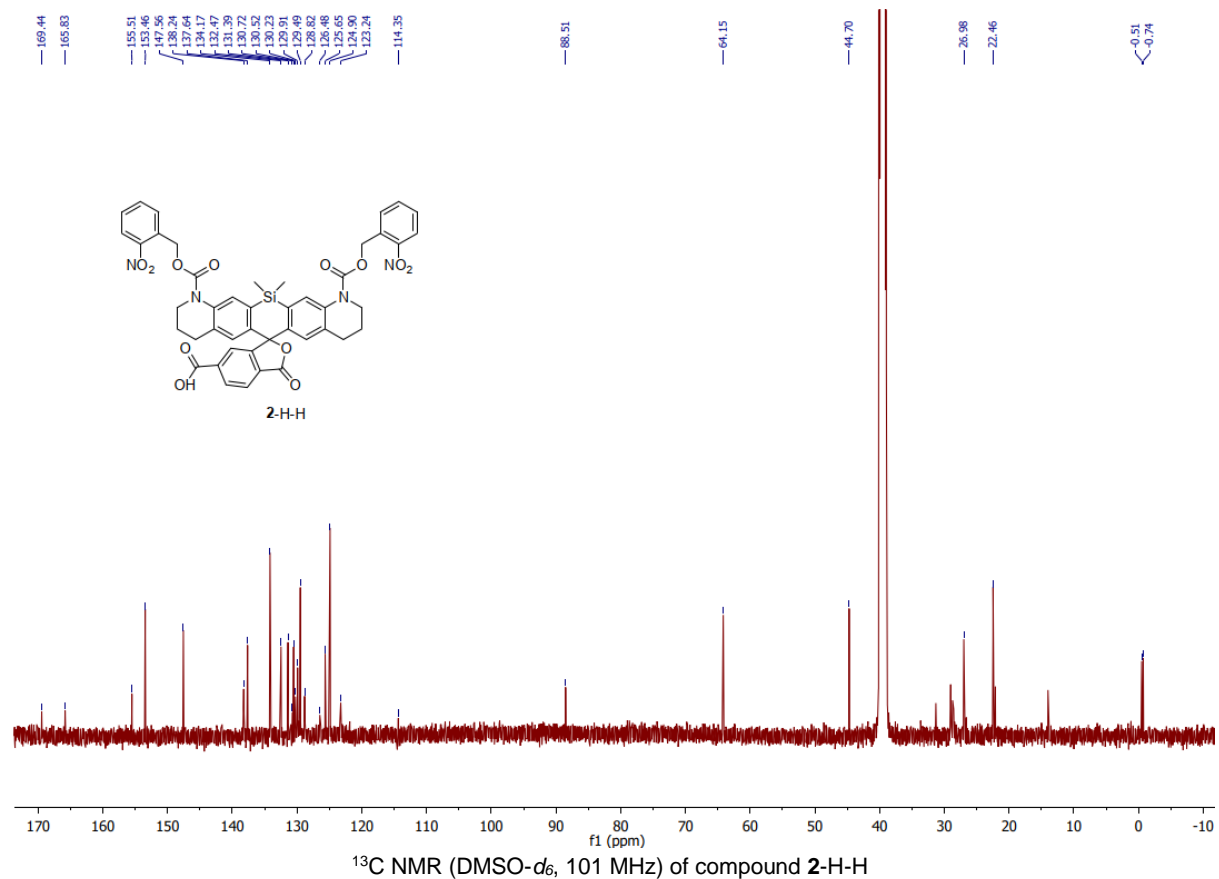
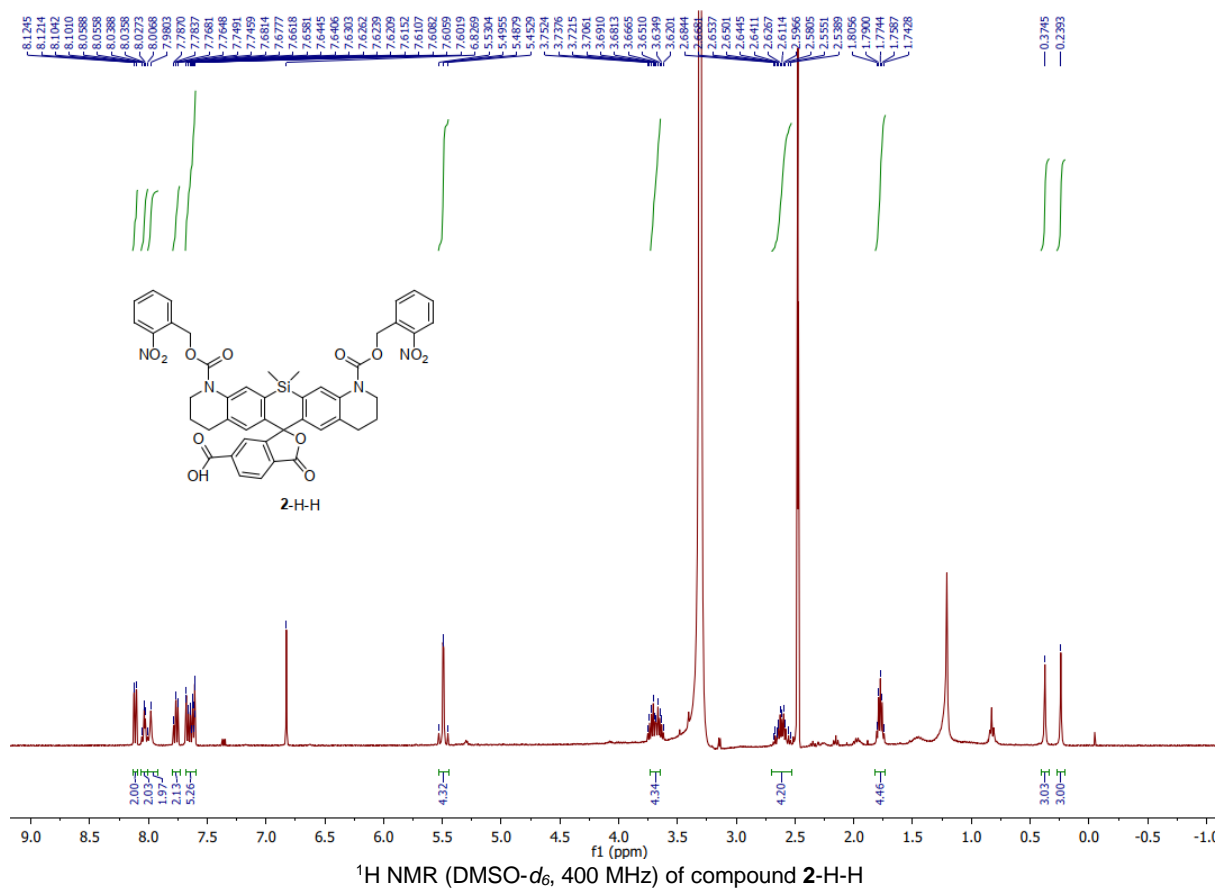


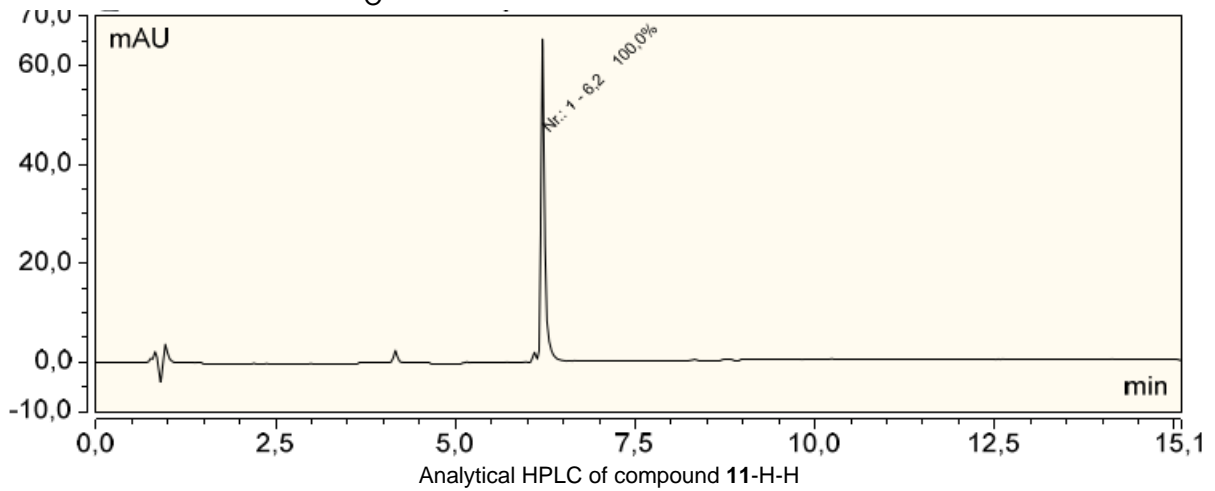
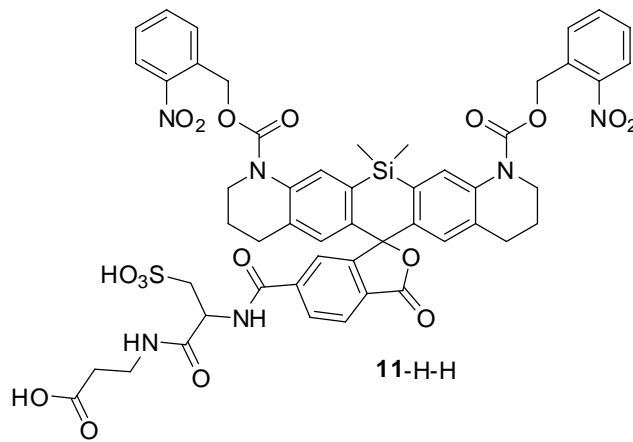
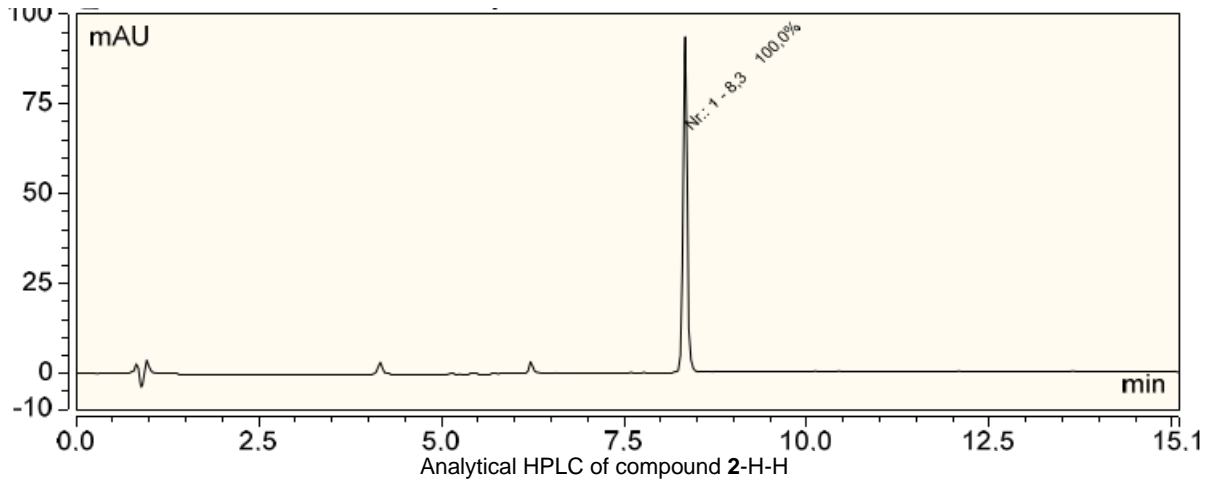
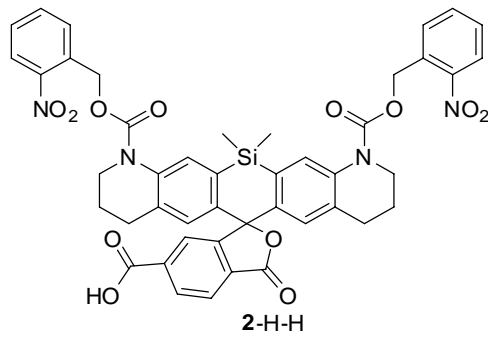
Analytical HPLC of compound 1-OMe-H

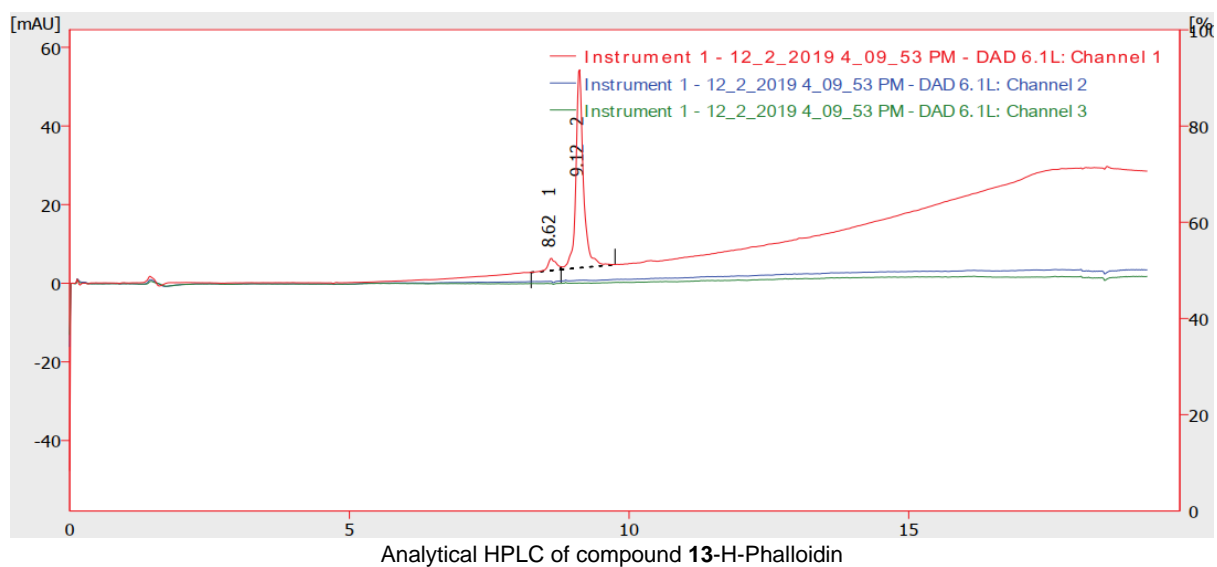
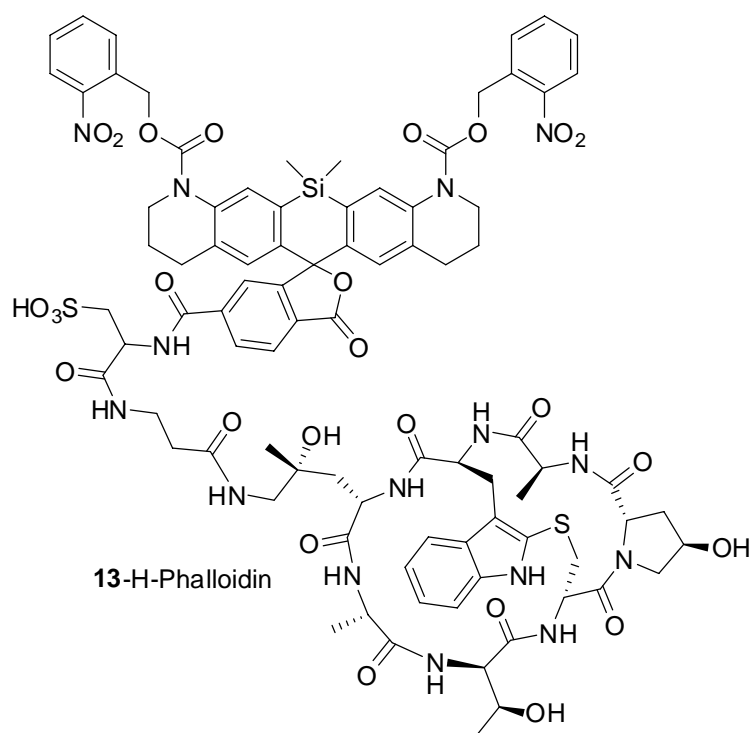


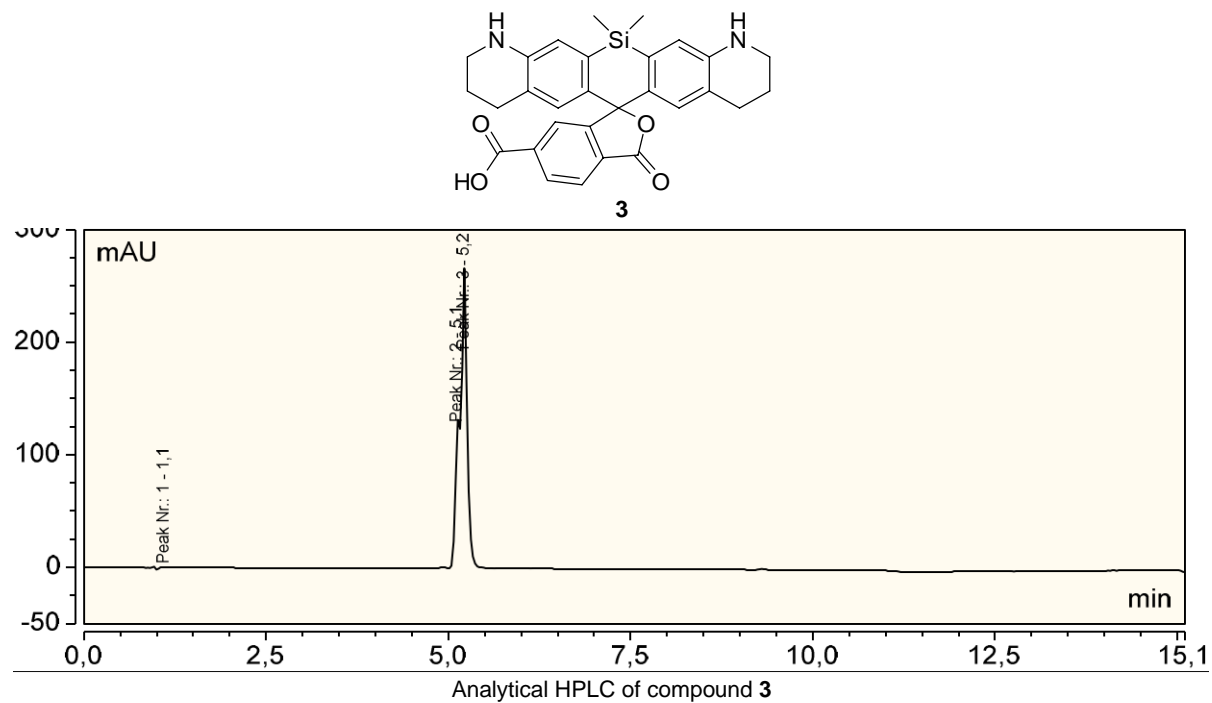
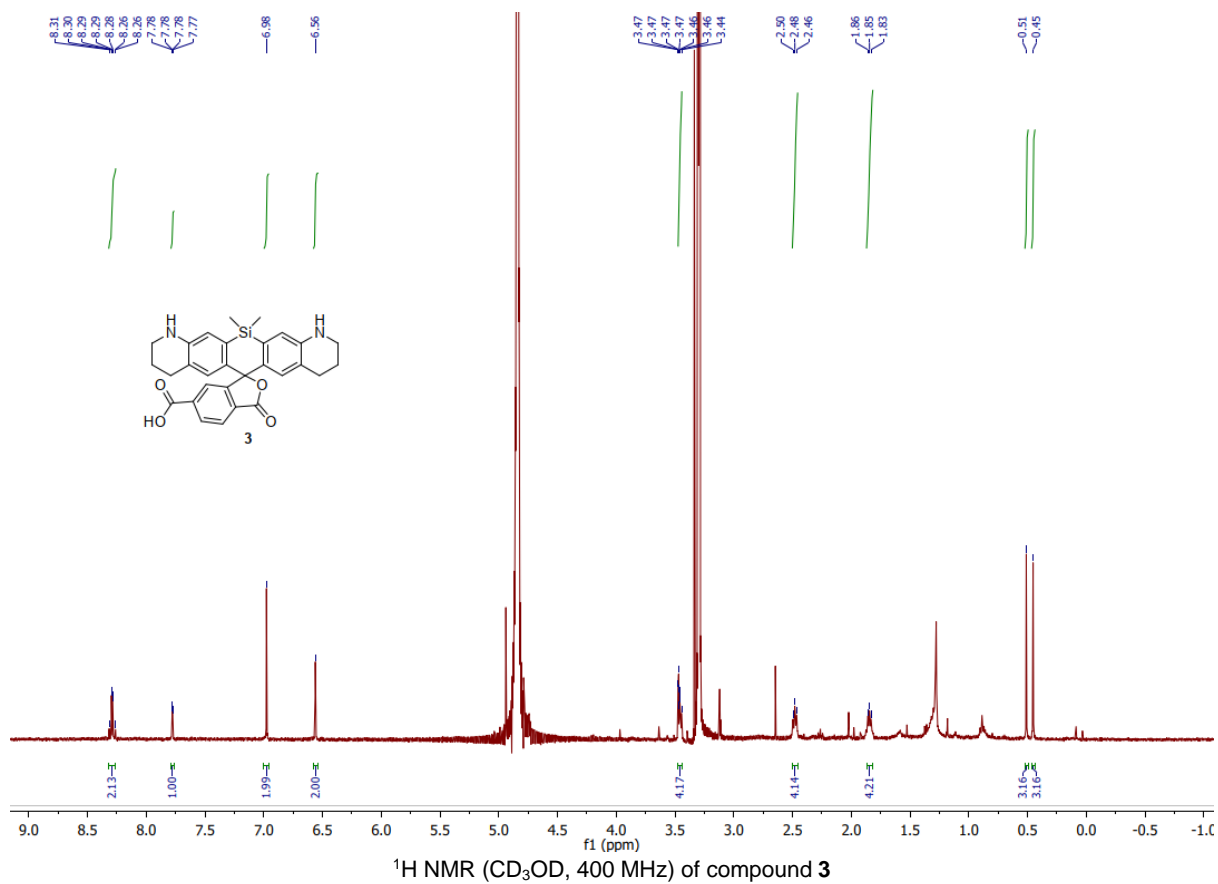
Analytical HPLC of compound 10-OMe-H











References

- [1] a) A. N. Butkevich, M. L. Bossi, G. Lukinavičius, S. W. Hell, *J. Am. Chem. Soc.* **2018**, *141*, 981-989; b) K. Uno, M. L. Bossi, T. Konen, V. N. Belov, M. Irie, S. W. Hell, *Adv. Opt. Mater.* **2019**, *7*.
- [2] T. Pleiner, M. Bates, S. Trakhanov, C.-T. Lee, J. E. Schliep, H. Chug, M. Böhning, H. Stark, H. Urlaub, D. Görlich, *eLife* **2015**, *4*.
- [3] a) A. N. Butkevich, G. Y. Mitronova, S. C. Sidenstein, J. L. Klocke, D. Kamin, D. N. H. Meineke, E. D'Este, P.-T. Kraemer, J. G. Danzl, V. N. Belov, S. W. Hell, *Angew. Chem. Int. Ed.* **2016**, *55*, 3290-3294; b) J. B. Grimm, T. A. Brown, A. N. Tkachuk, L. D. Lavis, *ACS Cent. I Sci.* **2017**, *3*, 975-985.
- [4] J. B. Grimm, T. Klein, B. G. Kopek, G. Shtengel, H. F. Hess, M. Sauer, L. D. Lavis, *Angew. Chem. Int. Ed.* **2016**, *55*, 1723-1727.
- [5] a) R. G. Dyer, K. D. Turnbull, *J. Org. Chem.* **1999**, *64*, 7988-7995; b) G. E. Negri, T. J. Deming, *ACS Macro Lett.* **2016**, *5*, 1253-1256.
- [6] B. Roubinet, M. Bischoff, S. Nizamov, S. Yan, C. Geisler, S. Stoldt, G. Y. Mitronova, V. N. Belov, M. L. Bossi, S. W. Hell, *J. Org. Chem.* **2018**, *83*, 6466-6476.
- [7] A. M. Brouwer, *Pure Appl. Chem.* **2011**, *83*, 2213-2228.

6.3. Manuscript III: MINSTED

Supplementary information

MINSTED fluorescence localization and nanoscopy

In the format provided by the authors and unedited

Supplementary information

Supplementary text

MINSTED localization method

Image scans were performed until the total number of detected photons of the current and previous columns and rows exceeded a threshold n_{ON} of typically 5-10. When the threshold was exceeded, the image scan was interrupted and the detections at the last image positions were used for an initial estimation \vec{r}_0 of the fluorophore position \vec{r}_fl by a weighted average. A circular scan was started, whose initial centre position $\vec{C}_0 = \vec{r}_0$ and whose radius $R_0 \approx d_0/2$ was approximately half the PSF diameter as illustrated in Fig. 1b. During the localization, the centre converged towards the fluorophore position. Thus, the fluorophore was exposed to a moderate STED intensity because it was kept within a distance d from the doughnut position \vec{S} most of the time, typically at about the scan radius R (Fig. 1c). Upon detection of photon i at the doughnut position \vec{S}_i , the centre, scan radius and E-PSF diameter were updated immediately. The centre was moved towards \vec{S}_i by a fraction α and the scan radius and E-PSF diameter were scaled by $\gamma < 1$. The scanning continued around the new centre $\vec{C}_i = (1 - \alpha)\vec{C}_{i-1} + \alpha\vec{S}_i$ with radius $R_i = \gamma R_{i-1}$ and $d_i = \gamma d_{i-1}$ until the next photon was detected and the update repeated. The scan radius and the E-PSF diameter were decreased only until reaching their preset lower limits, whereas the centre position was updated throughout. The localization was terminated if less than a minimum of n_{OFF} photons were detected within a time interval τ_{OFF} .

The real-time FPGA control logic was kept simple and lean. All localization traces consisting of centre positions, doughnut positions, detected photons and detection times were transferred to the computer for storage and further evaluation using MATLAB and custom analysis tools. The fluorophore position after N photon detections was estimated by the last centre position for $N \leq N_c$, where N_c is the number of detections to reach the smallest scan radius and sharpest E-PSF. For $N > N_c$ the fluorophore position was estimated by the average centre positions during the remaining photon detections.

$$\hat{\vec{r}}(N) = \begin{cases} \vec{C}_N & \forall N \leq N_c \\ \frac{1}{N - N_c + 1} \sum_{i=N_c}^N \vec{C}_i & \forall N > N_c \end{cases} \quad (S1)$$

MINSTED localization uncertainty

Due to the continuous update of the centre position, the localization uncertainty – this means the Cramer-Rao bound (CRB) – could not be easily obtained analytically for the interesting case of many photon detections. Instead, we repeatedly simulated the localization of a fluorophore and estimated the localization uncertainty by the root mean square (RMS) localization error versus the number of detected photons N .

Given the estimates $\hat{\vec{r}}_j(N) = (\hat{x}_j(N), \hat{y}_j(N))$ of the fluorophore position after N detections for $j = 1 \dots K$ runs of the simulation, the localization uncertainty along x and y was estimated by the root mean square errors along the coordinate axes:

$$\sigma_{\text{loc}}^2(N) = \frac{1}{K} \left(\sum_{j=1}^K (\hat{x}_j(N) - x_{\text{fl}})^2 + \sum_{j=1}^K (\hat{y}_j(N) - y_{\text{fl}})^2 \right)^{1/2} \quad (\text{S2})$$

Simulated localizations that ended prematurely after $i < N$ detections (too few detections for too long terminate the localization) or whose positions were off by more than five times the median error of the simulations were flagged as failures for the remaining detections. Equation (S2) was evaluated for the successful localizations only. Fig. 2a–c, Fig. 3c,d illustrate localization uncertainties with simplified fast calculations, whereas Suppl. Fig. S1 and Suppl. Fig. S2 illustrate results based on complete simulations including the detection times and the termination of the fluorophore’s active state.

For the experimental localizations, the true fluorophore position and thus the accuracy is unknown. Based on simulated localizations, we found that the estimation of the localization precision similar to camera-based localizations is unreliable due to the history of the centre trace, which introduces a varying degree of correlation among the centre positions. Instead, we estimated the precision of an individual localization by sub-sampling. Therefore, we split the centre trace in groups of different sizes M , estimated the fluorophore position for each of these groups, and extrapolated the precision from the groups to the entire localization.

Given $N \gg N_c$ detected photons, we calculated for consecutive groups of $M = \lceil 10^{\{1.5, 1.6, 1.7, \dots\}} \rceil \leq (N - N_c + 1)/5$ detections the standard deviations $\sigma_M(M)$ of the groups’ mean centre positions. We then estimated the precision of the localization by extrapolating the relation

$$\sigma_M(M) \approx \frac{\hat{\sigma}_1}{\sqrt{M}} + \hat{\sigma}_\infty \quad (\text{S3})$$

to $M = N - N_c + 1$. Here, $\hat{\sigma}_1 > 0$ is approximately the standard deviation among uncorrelated centre positions and $\hat{\sigma}_\infty \geq 0$ is an empirical offset, both obtained by least-squares decomposition of $\sigma_M(M)$.

$$\hat{\sigma} \approx \frac{\hat{\sigma}_1}{\sqrt{N - N_c + 1}} + \hat{\sigma}_\infty \quad (\text{S4})$$

Suppl. Fig. S3 compares the localization uncertainty obtained from numerous simulated localizations with the estimated precision extracted from the individual localizations. The extracted precision provides a reasonable and rather conservative estimate of the true uncertainty, but at least 200 detected photons are required for this extrapolation.

Simulated localization

The fluorophore was placed at $\vec{r}_{\text{fl}} = (x_{\text{fl}}, y_{\text{fl}})$ and the localization started with a centre position \vec{C}_0 that was normally distributed in the (x, y) plane around this position with a standard deviation 90 nm. Hence, the initial centre distribution approximated the profile of the confocal fluorophore image used for searching the fluorophores.

The time-gated pulsed STED E-PSF was approximated by a 2D Gaussian as defined by the quadratic increase in STED intensity near the minimum, the exponential depletion of the excited state and the detection PSF. A peak detection rate ε and a background detection rate β were assumed; that is a peak signal-to-background ratio $\text{SBR} = \varepsilon/\beta$. The average detection rate $\bar{n}_i(t)$ at doughnut position $\vec{S}_i(t)$ was therefore

$$\bar{n}_i(t) = \varepsilon \exp\left(-4 \ln(2) \frac{|\vec{S}_i(t) - \vec{r}_{fl}|^2}{d_{i-1}^2}\right) + \beta. \quad (\text{S5})$$

The scan trajectory leading to the i^{th} detection was determined by the centre position \vec{C}_{i-1} and the radius R_{i-1} after the previous detection.

$$\vec{S}_i(t) = \vec{C}_{i-1} + R_{i-1} \begin{pmatrix} \cos(-\omega t) \\ \sin(-\omega t) \end{pmatrix} \quad (\text{S6})$$

For each photon detection $i = 1 \dots N$ an exponentially distributed number m_i with average value $\bar{m}_i = 1$ was drawn. The detection time t_i was then determined by integrating the signal $\bar{n}_i(t > t_{i-1})$ along the scan trajectory $\vec{S}_i(t)$ until its cumulative value reached m_i .

$$m_i = \int_{t_{i-1}}^{t_i} \bar{n}_i(t) dt \quad (\text{S7})$$

Upon each detection, the E-PSF was sharpened until reaching the minimal value d_{min} found for the maximal STED beam power. The scan radius was reduced equally until reaching its minimum R_{min} . Suppl. Fig. S4 illustrates that the doughnut position $\vec{S}_i(t)$ stays from the fluorophore at a narrow distance distribution centred on the scan radius during the entire localization. Therefore, the fluorophore is exposed only to a moderate STED intensity, which lowers photobleaching by the doughnut as compared to conventional raster-scanned STED imaging.

Camera-based localization uncertainty

The theoretical localization precision for single-molecule localizations by analysing camera images is given by Rieger and Stallinga²² as

$$\sigma_{cam}^2 \approx \frac{\sigma_{PSF}^2 + p^2/12}{S} \left(1 + 4\tau + \sqrt{\frac{2\tau}{1 + 4\tau}}\right) \text{ with } \tau = \frac{2\pi b}{p^2 S} \left(\sigma_{PSF}^2 + \frac{p^2}{12}\right), \quad (\text{S8})$$

where S is the total number of detected signal photons; p is the pixel size; b is the average background per pixel without dark counts; σ_{PSF} is the standard deviation of the image PSF approximated by a Gaussian spot; and σ_{cam} is the localization uncertainty.

We estimated the camera-based localization uncertainty for a pixel size of 100 nm and a diffraction-limited PSF at 670 nm wavelength. Fitting the simulated PSF with a 2D Gaussian profile yielded $\sigma_{PSF} = 116$ nm, whereas measuring the FWHM led to $\sigma_{PSF} = 118$ nm. Hence, we used $\sigma_{PSF} = 117$ nm. For the total image background B we considered 25 pixels: $B = 25b$. The total signal S is given by the peak signal s and the width of the 2D Gaussian distribution: $S = 2\pi s \sigma_{PSF}^2/p^2$. Hence, S was defined by the signal fraction of the detected photons $N = S + B$:

$$S = \frac{SN}{S + B} = \frac{N}{1 + \frac{25p^2}{2\pi\sigma_{PSF}^2} \frac{b}{s}} = \frac{N}{1 + \frac{2.91}{SBR}} \quad (\text{S9})$$

With the chosen imaging parameters, equation (S8) evaluates to

$$\sigma_{\text{cam}} \approx 121 \text{ nm} \sqrt{\frac{1}{N} \left(1 + \frac{2.91}{\text{SBR}}\right) \left(1 + \frac{4.24}{\text{SBR}} + \sqrt{\frac{2.12}{\text{SBR} + 4.24}}\right)}. \quad (\text{S10})$$

The localization accuracy is further affected by any differences in pixel responses, which is particularly critical when seeking an uncertainty of 10 nm or less with (scientific) CMOS camera images.

Comparison of MINSTED and camera-based localization

Suppl. Fig. S1 illustrates the simulated localization uncertainty for different peak SBRs and the following settings: scan radius $R = d/2$ from 103 nm initially down to 13 nm; a centre update step $\alpha = 15\%$ of the scan radius; a reduction factor $\gamma = 0.97$; $\omega = 2\pi \times 125$ kHz circling frequency; and $\varepsilon = 30$ kcps peak emission rate, corresponding to about 15–20 kcps average detection rate including background. The localizations were terminated after 10000 photon detections, or earlier when less than $n_{\text{OFF}} = 10$ to 15 photons were detected in a $\tau_{\text{OFF}} = 3$ ms interval. For each setting, we simulated 500 localizations. Less than 3% of the localizations terminated early. If the estimated fluorophore position $\hat{r}_{\text{fl}}(i)$ was further off than 5 times the median error of all simulated localizations, we deemed the localization as failure and excluded it for the remaining $i \dots N$ photon detections. A fraction of up to $1/\text{SBR}$ localizations failed during the homing-in. An uncertainty of 1 nm along the x and y directions was obtained with 300 to 800 photon detections.

Suppl. Fig. S1 also shows the camera-based localization uncertainty without background and for the lowest peak SBR used in the simulations. Dotted lines extend these estimates for low photon numbers that are usually discarded. After a transitory phase, the scanning-based localization massively benefits from the zooming-in with an ever sharper E-PSF. Localization uncertainties of 3 nm or less can be achieved by camera-based localizations but require 30 to 50 times the number of detected photons than MINSTED.

If the fluorophore supports a higher exposure to STED light during the localization, a larger scan radius with respect to the PSF diameter further squeezes the required photon detections. Suppl. Fig. S2 shows that MINSTED can reach 1 nm precision with as few as 200 detected photons, which is about 50 times more photon-efficient than camera-based localizations and on par with iterative MINFLUX⁸.

Comparison of MINSTED and MINFLUX

A detailed comparison with MINFLUX based on the achievable resolution is hampered by the numerous assumptions necessary for the different imaging parameters (e.g. fluorophore density, background, response of the background to STED). For a coarse comparison at large N , the localization precision of MINSTED can be approximated with a localization by two Gaussian beams placed at R distance on both sides of the molecule. Using this approximation, Suppl. Table T1 compares the major contributions to the performance of both methods.

Suppl. Table T1 | Estimated performance of MINFLUX and MINSTED.

	MINFLUX	MINSTED
Fluorophore requirements	High contrast between off and on state	High contrast between off and on state <i>under STED conditions</i>
Resolution 1D (ref. 8)	$\sigma = \frac{L}{4\sqrt{N}}$	$\sigma \approx \frac{\alpha d^2}{R\sqrt{N}} \quad (\alpha < 1)$ Static Gaussian approximation: $\sigma = \frac{d^2}{4R \ln 2 \sqrt{N}}$
Decreasing L/d with neighboring molecule	 Undesired molecule is excited stronger than desired one	 Undesired molecule is suppressed by STED
Imperfect doughnut zero	Additional counts are background counts → SBR decreases	Signal decreases → SBR decreases
Excitable background	Smaller L → stronger excitation of the background and weaker excitation of molecule → SBR decreases	Smaller d → same excitation of background and molecule → SBR constant
STED-sensitive background	-	Smaller d → background suppressed by stronger STED → SBR increases
STED-induced background (not observed)	-	Smaller d → more background by stronger STED → SBR decreases

Animations

Suppl. Video V1 illustrates the evolutions of the centre-to-fluorophore distance distributions during the detection of 100 photons for update steps $\alpha = 10\%$, 15% , 20% and 25% of the scan radius and for peak SBR of 50, 20, 10, 5 and 2. The diameter of the solid circle and the radius of the dashed circle equal the E-PSF diameter d , which is twice the scan radius R . Each run starts with a uniform centre-to-fluorophore distance distribution in the dashed circle. If the centre-to-fluorophore distance leaves this region, the fluorophore is considered “lost” because the centre would rarely re-approach the fluorophore in practice. Fluorophores get lost mostly during the first few detections when a step in the wrong direction can be fatal. Once the distribution converges, losses occur only if the background is too high and/or the step too large. Towards the end of each run, the standard deviation σ_c of the converged distribution is shown in units of the scan radius.

Suppl. Video V2 animates the localization of a fluorophore. Yellow to red dots mark the most recent centre coordinates and the circular line illustrates the recent doughnut positions. Photon detections are illustrated by a flash with the shape of the E-PSF at the doughnut position of the detection event. The scan trajectory is updated immediately upon the detection of a photon. Weighted histograms of the centre positions are shown above and to the right of the image. After homing in on the

fluorophore, these histograms converge towards normal distributions, whose centres indicate the fluorophore position and whose standard deviations equal the values shown in Suppl. Video V1. The animation is sped up about ten-fold by removing full scan circles without detection event.

MINSTED microscope

The core of the implemented MINSTED microscope is outlined in Suppl. Fig. S7. The microscope incorporates a laser beam-scanning path and descanned confocal detection using two galvo scanners to address a field of $100\ \mu\text{m} \times 100\ \mu\text{m}$ in the sample. A cw laser with 633 nm wavelength provides the excitation light and a single-photon avalanche diode (APD) detects the fluorescence light emitted from the sample. A 355 nm cw laser beam illuminates a central region of about $4\ \mu\text{m}$ diameter to activate the fluorophores. These two laser beams are s-polarized on the main dichroic mirror DM_2 that was customized to transmit the p-polarized laser beams from the second excitation path with pulsed 635 nm excitation light and 775 nm STED light. The STED beam passes through a vortex plate VP to create the lateral STED doughnut. A purposefully tilted notch filter N cleans up its polarization and an achromatic quarter-wave retardation plate ($\lambda/4$) sets up the required circular polarization. The second excitation path features two electro-optical deflectors (EODs) to address rapidly a field of $2.6\ \mu\text{m} \times 2.6\ \mu\text{m}$ without any mechanical movement. The control electronics and the driver of the EODs provide a bandwidth of 150 kHz, which is used to scan the beam in circles around the estimated position of the fluorophore at 125 kHz frequency.

A two-axis stick-and-slip piezo stage moves the sample laterally over large distances, such that the region of interest can be centred to the EODs' image field. The sample position is actively stabilized by a three-axis piezo stage with sub-nanometre precision. The focus feedback signal is obtained by tracking the position of the reflected beam on the z-lock camera CAM_z (out-of-plane excursion in Suppl. Fig. S7). The lateral position feedback signal is obtained by tracking the images of fiducial markers on the x-y-lock camera CAM_{xy} . The fiducial markers are imaged in a field of about $50\ \mu\text{m} \times 70\ \mu\text{m}$ off-axis to avoid interference with the imaged field of the sample. The tracker field is limited by the field stop F. Both focus locks are polarization filtered to suppress stray light and reflections as much as possible. For the x-y-lock, a pupil filter P is used to block the direct reflection at the coverslip-sample interface. Infrared filters IR block the excitation and STED light below 850 nm wavelength.

The z-lock uses an 8-bit CMOS camera imaging the lateral position of the reflected beam at 800 to 1500 frames per second (fps) depending on the extent of the selected region of interest. 16 consecutive camera images are binned and then processed to extract the beam centre. The deviation of the beam centre with respect to the target position is integrated and scaled to obtain the control signal. Including mechanical inertia, the closed-loop control bandwidth was 15 to 30 Hz.

The x-y-lock uses a 16-bit sCMOS camera imaging fiducials with 150 to 200 fps depending on the extent of the region of interest. The fiducial positions are estimated by least squares fitting of their images to a two-dimensional Gaussian profile with constant background. The deviation of the lateral positions of trustworthy fiducials with respect to their initial positions is integrated and scaled to obtain the control signal. The closed-loop control bandwidth was about 80 Hz. Fiducials are manually selected as trustworthy if neither their positions nor their intensities fluctuated noticeably.

For clarity, the polarization, spatial and spectral cleaning of the laser beams and their power modulations are not shown. In particular, the APD, the lasers at 355 and 775 nm wavelength and the super-luminescent LED at 980 nm wavelength are pig-tailed and/or fibre-coupled to the system. The excitation lasers at 633 and 635 nm wavelengths are fed through pinholes to clean-up the beam profiles. All laser beams are linearly polarized by Glan-Thompson polarizers (Bernhard Halle) and

spectrally cleaned by excitation filters (Chroma Technology and Semrock). All light sources can be blocked by shutters and their beam powers can be modulated internally or externally.

Main components

355nm	Zouk 0355-05-01-0010-500 (10 mW cw), Cobolt, Solna, Sweden; beam power modulated by an acousto-optic modulator MQ110-A3-UV with driver MODxx, AA optoelectronic, Orsay, France; fed through polarization-maintaining single-mode fibre PMC-360Si-2,3-NA012-3-APC-500P, Schäfter+Kirchhoff, Hamburg, Germany.
633nm	HeNe laser 25-LHP-073-230 (< 25 mW cw), Melles Griot, Rochester, NY, USA.
635nm	Pulsed diode laser LDH-P-C 635b (< 80 MHz, < 100 ps, < 1 mW) with driver PDL 800-B, PicoQuant, Berlin, Germany.
775nm	Pulsed fibre laser ELP-5-755-DG (20 MHz, 1.2 ns, < 5 W), IPG Photonics, Oxford, MA, USA; beam power modulated by an electro-optic modulator LM0202 5W VIS, Linos Photonics, Göttingen, Germany; with custom driver 400 V, 75 mA, 600 kHz, MPI for Biophysical Chemistry, Göttingen, Germany; fed through polarization-maintaining single-mode fibre PM780-HP-FC/APC, Thorlabs, Newton, NJ, USA.
980nm	Super-luminescent LED SLD-1000-100-PM-25, Innolume, Dortmund, Germany; with driver LDR1000E, Laser 2000, Wessling, Germany.
APD	Single-photon counting module SPCM-AQR-13-FC, PerkinElmer, Wiesbaden, Germany.
CAM _{xy}	USB3 sCMOS camera pco.panda 4.2 (2048×2048 pixels 6.5×6.5 μm ² , 16 bits, 100 fps), PCO, Kelheim, Germany.
CAM _z	USB3 CMOS camera acA1300-200um (1280×1024 pixels 4.8×4.8 μm ² , 8/10 bits, 203 fps), Basler, Ahrensburg, Germany.
EOD	Electro-optic deflectors 311A (AD*P, Ø2 mm, 200 mm long, 7 μrad/V, 180 pF, ±500 V), Conoptics, Danbury, CT, USA; high-voltage drivers PZD700A-1-H-SHV-CE (±700 V, 200 mA, 150 kHz), Trek, Lockport, NY, USA.
FPGA	PCIe board 7852R with drivers and software LabVIEW 2017, National Instruments, Austin, TX, USA.
Galvo _{x,y}	Galvo-mirrors 6 mm × 10 mm, galvo 6215H, servo drivers 671, Cambridge Technology, Bedford, MA, USA.
Objective	Magnification 100×/1.4 NA oil-immersion, Leica Mikrosysteme, Wetzlar, Germany.
Stages	Three-axis piezo stage P-733.3DD with controller E-725.3CDA on two-axis piezo stage M-686.D64 with controller C-867.262, Physik Instrumente, Karlsruhe, Germany.

Filters

F	Adjustable rectangular field stop
P	Custom pupil filter Ø6.5 mm with central obscuration Ø1.4 mm on 2 mm thick window.
PH	Pinhole Ø300 μm
VP	Vortex plate VL-209-M-Y-A, Holo-Or, Ness Ziona, Israel.
DM ₁	Dichroic mirror Z660DCXR, Chroma Technology, Bellows Falls, VT, USA.
DM ₂	Custom dichroic mirror HR350-730nm HT450-475nm/p+630-640nm/p at 45° incidence, LaserOptik GmbH, Garbsen, Germany.
DM ₃	Back-polished mirror BB01-E02P, Thorlabs, Newton, NJ, USA.
DM ₄	Dichroic mirror Z355RDC, Chroma Technology, Bellows Falls, VT, USA.
DM ₅	Notch filter StopLine NF01-633-25, Semrock, Rochester, NY, USA.
E	Emission filters ET750-SP-2P8 and ET680/80m, Chroma Technology, Bellows Falls, VT, USA.
IR	Infrared filter RG 850 (2 mm thick), Schott, Mainz, Germany.
N	Notch filter StopLine NF03-808E-25, Semrock, Rochester, NY, USA.

Lenses

L ₁	Achromatic doublet 200 mm, 322328000, Linos Photonics, Göttingen, Germany.
L ₂	Achromatic doublet 40 mm, AC254-040-B, Thorlabs, Newton, NJ, USA.
L _{3,8,10,14}	Achromatic doublet 300 mm, 322273322, Linos Photonics, Göttingen, Germany.
L _{4,5,6}	Achromatic doublets 100 mm, 49-333, Edmund Optics, Mainz, Germany.
L ₇	Achromatic doublet 60 mm, 49-329, Edmund Optics, Mainz, Germany.
L ₉	Asphere 30 mm, 355 nm V-coating, 33-012, Edmund Optics, Mainz, Germany.
L _{11,12,13}	Hasting triplets 40 mm, THR254-040-A, Thorlabs, Newton, NJ, USA.
L _{15,19}	Achromatic doublet 160 mm, 322270322, Linos Photonics, Göttingen, Germany.
L ₁₆	Achromatic doublet 16 mm, 322207000, Linos Photonics, Göttingen, Germany.
L ₁₇	Fibre collimator 11 mm, 60FC-0-A11-02, Schäfter+Kirchhoff, Hamburg, Germany.
L ₁₈	Achromatic doublet 40 mm, 322337000, Linos Photonics, Göttingen, Germany.
L ₂₀	Achromatic doublet 100 mm, AC254-100-B, Thorlabs, Newton, NJ, USA.
L ₂₁	Achromatic doublet 400 mm, 322275322, Linos Photonics, Göttingen, Germany.
L ₂₂	Achromatic doublet 200 mm, 322353000, Linos Photonics, Göttingen, Germany.

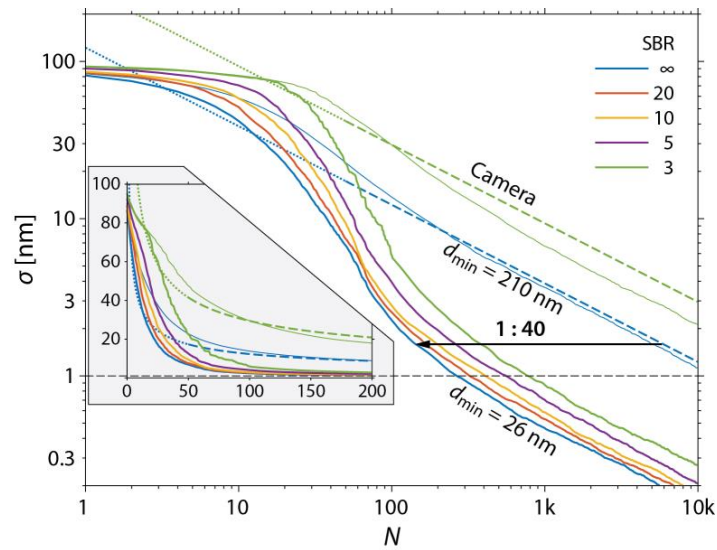
Polarization optics

GT	Glan-Thompson polarizing prisms PGT 1.08, Bernhard Halle, Berlin, Germany.
PBS	Polarizing beam splitter cubes PTW 2.20, Bernhard Halle, Berlin, Germany.
$\lambda/4$	Achromatic quarter-wave retarder plate RAC 4.4.10, Bernhard Halle, Berlin, Germany.
$\lambda/2$	Achromatic half-wave retarder plates RAC 4.2.10, Bernhard Halle, Berlin, Germany.

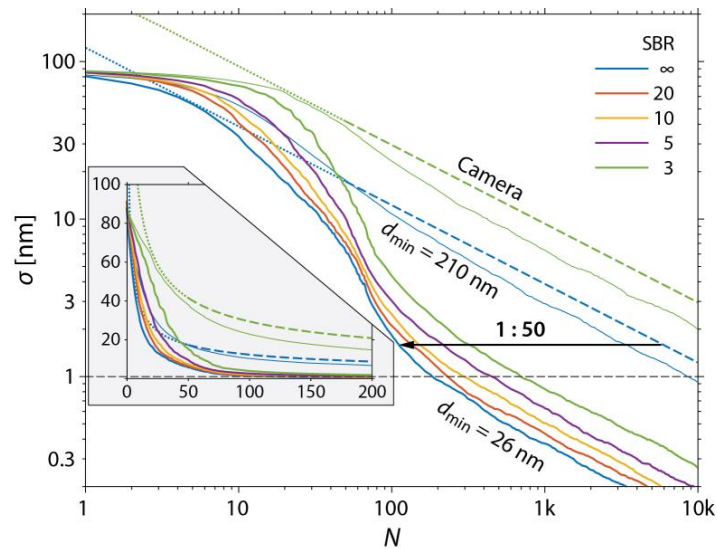
Supplementary references

22. Rieger, B. & Stallinga S. The Lateral and Axial Localization Uncertainty in Super-Resolution Light Microscopy. *ChemPhysChem* **15**, 664–670 (2014).

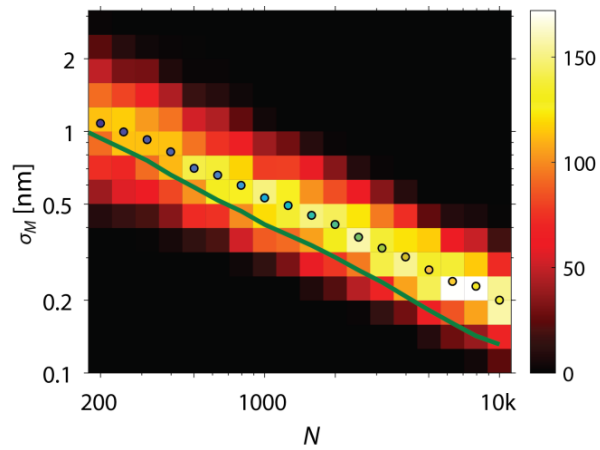
Supplementary figures



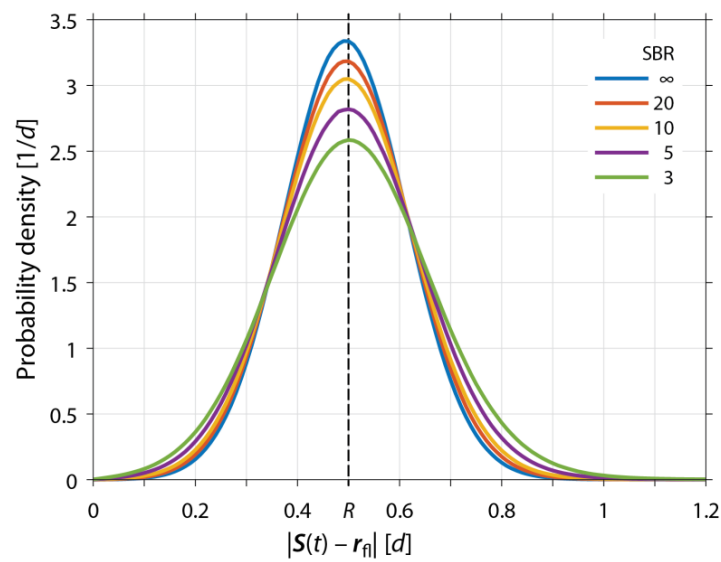
Suppl. Fig. S1 | Simulated localization uncertainty versus number of detected photons and SBR. The localizations were performed by zooming-in from $d_0 = 210$ nm PSF diameter and $R_0 = 103$ nm scan radius down to $d_{\min} = 26$ nm and $R_{\min} = 13$ nm. For $\text{SRB} = \infty$ and 3, dashed and dotted lines show the camera-based CRBs and thin lines show the uncertainties with diffraction-limited zooming-in on the fluorophore.



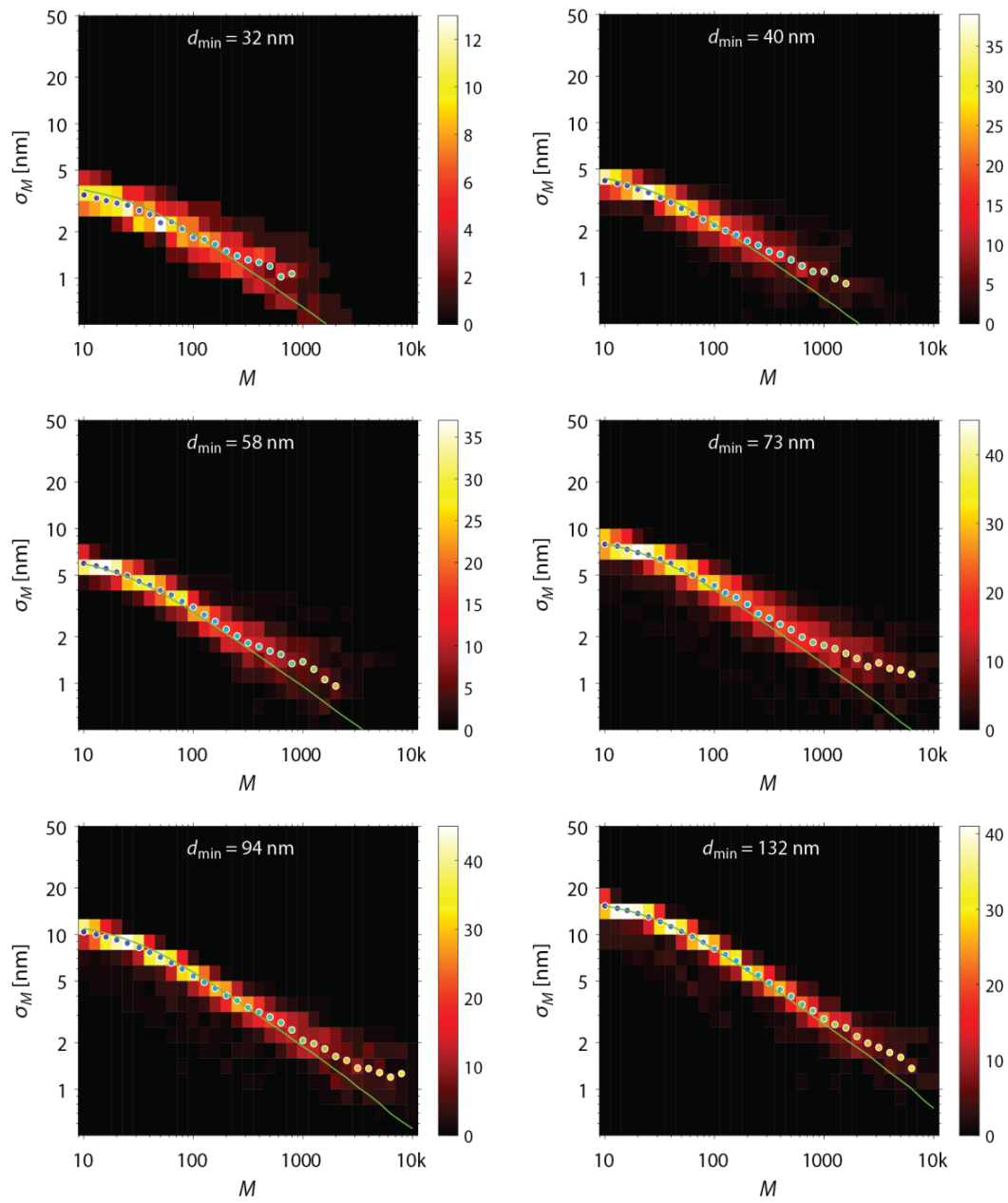
Suppl. Fig. S2 | Simulated localization uncertainty versus number of detected photons and SBR. The localizations were performed by zooming-in on the fluorophore from $d_0 = 210$ nm PSF diameter and $R_0 = 130$ nm scan radius down to $d_{\min} = 26$ nm and $R_{\min} = 17$ nm. The inset shows the results in linear scale for small photon numbers. For $\text{SRB} = \infty$ and 3, dashed and dotted lines show the camera-based CRBs and thin lines show the uncertainties with diffraction-limited zooming-in.



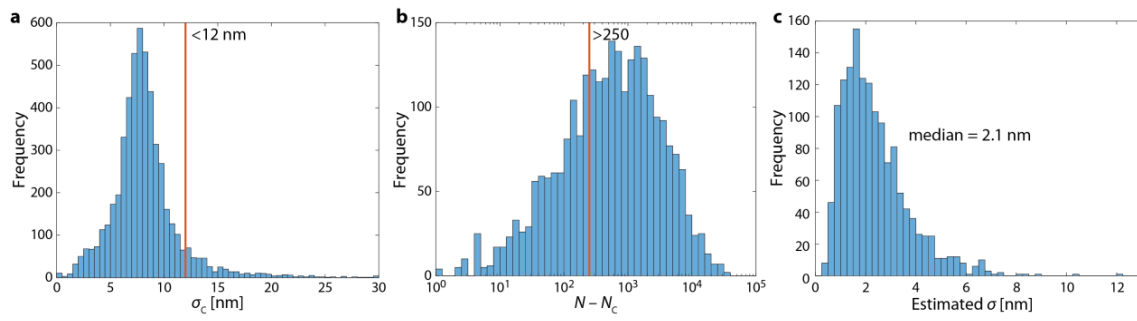
Suppl. Fig. S3 | Simulated versus estimated localization precision. The simulated localization uncertainty (solid line) was obtained by Eq. (S2) and the estimated localization precision (histogram; dots: median) by Eq. (S4).



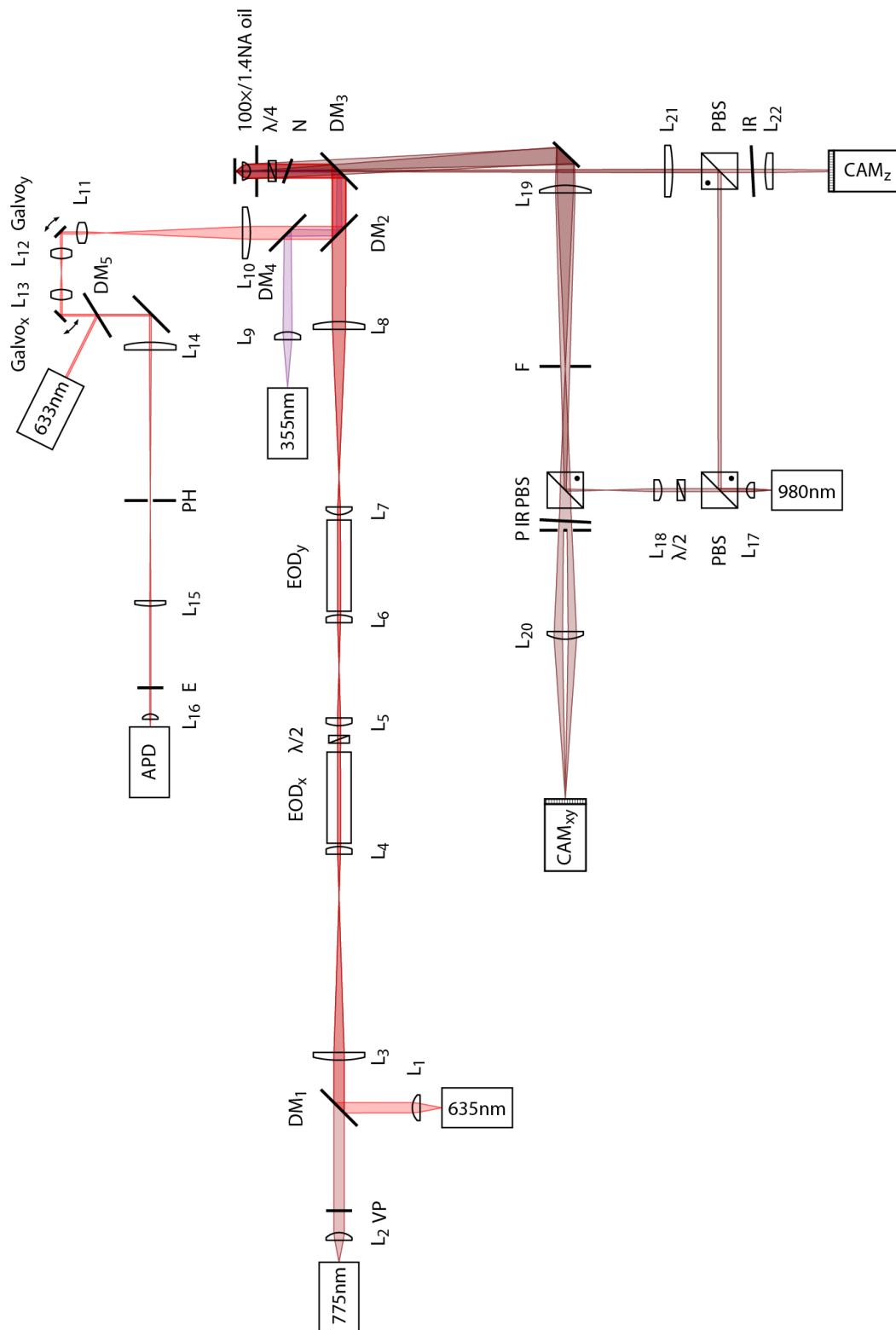
Suppl. Fig. S4 | Distribution of the doughnut-to-fluorophore distances during the simulated localizations of Suppl. Fig. S1.



Suppl. Fig. S5 | Localization precision measurements versus E-PSF diameter d_{\min} , see also Fig. 3c. Localization precision histograms of grouped localization traces of single molecules and their median localization precision (dots) compared to simulations (lines). The simulations assumed an SBR of 10 for $d_{\min} = 32, 94$ and 132 nm, an SBR of 20 for $d_{\min} = 40$ and 73 nm and infinite for $d_{\min} = 58$ nm.

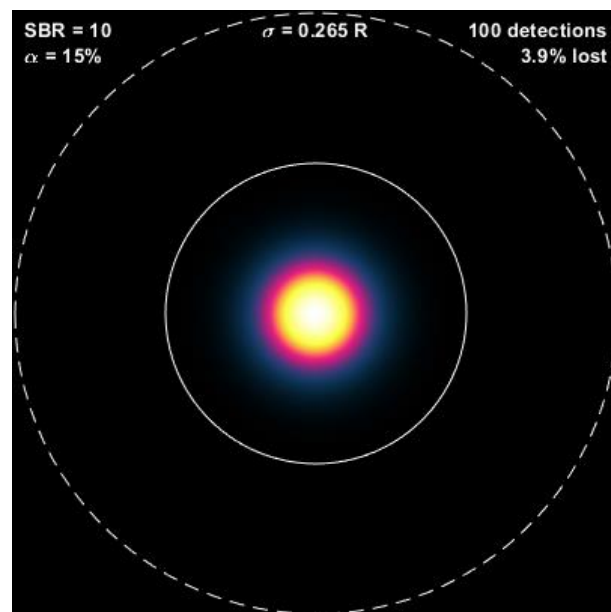


Suppl. Fig. S6 | Characteristics of the localizations measured for Fig. 4. **a**, Distribution of the standard deviation of the centre positions. **b**, Distribution of the number of detected photons used for estimating the fluorophore position. **c**, Distribution of the estimated localization precision of the rendered localizations.

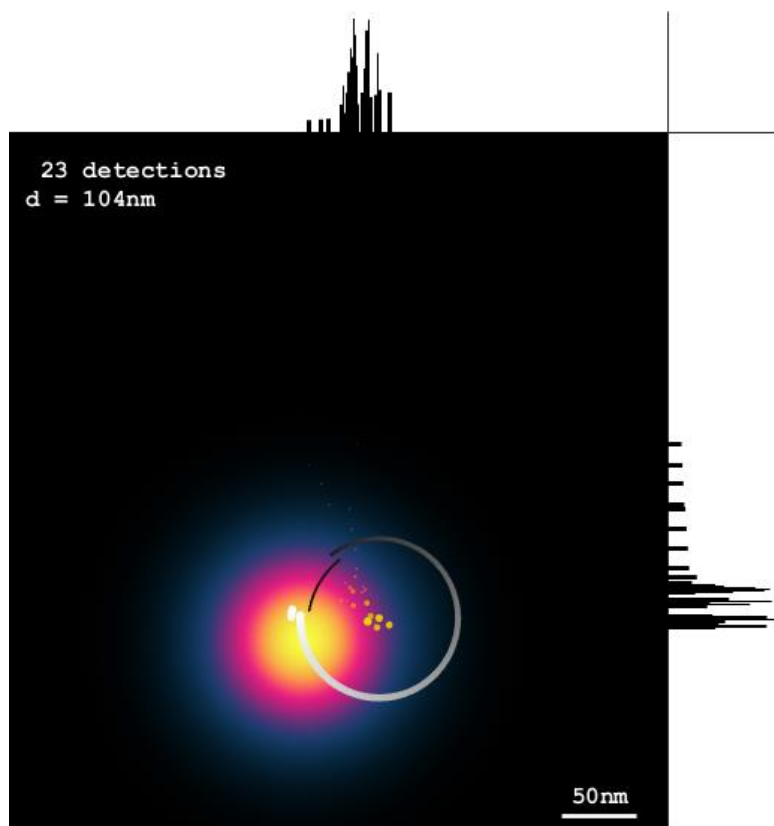


Suppl. Fig. S7 | Optical scheme of the MINSTED microscope. The lasers with 355 and 775 nm wavelength, the super-luminescent LED at 980 nm wavelength and the APD are fiber-coupled to the setup. All light sources are controlled by shutters and their powers are modulated or attenuated. The sample position is actively stabilized by feedback signals from the Z and X-Y focus locks.

Supplementary videos



Suppl. Video V1 | Distributions of the centre-to-fluorophore distances during the detection of 100 photons while circling with constant scan radius and constant E-PSF. The solid circle illustrates the scan trajectory and the E-PSF diameter.



Suppl. Video V2 | Animation of the localization of a single fluorophore with typical settings: scan radius $R = d/2$, update steps $\alpha = 15\%$ and $\gamma = 0.97$.

7. Publications

Fluorescent Photoswitchable Diarylethenes for Biolabeling and Single-Molecule Localization Microscopies with Optical Superresolution. Benoît Roubinet, Michael Weber, Heydar Shojaei, Mark Bates, Mariano L. Bossi, Vladimir N. Belov, Masahiro Irie, and Stefan W. Hell, *Journal of the American Chemical Society* 2017 139 (19), 6611-6620, DOI: 10.1021/jacs.7b00274

Photoactivatable Fluorophore for Stimulated Emission Depletion (STED) Microscopy and Bioconjugation Technique for Hydrophobic Labels. Michael Weber, Taukeer A. Khan, Lukas J. Patalag, Mariano Bossi, Marcel Leutenegger, Vladimir N. Belov, and Stefan W. Hell, *Chem. Eur. J.* **2021** 27, 421, DOI: 10.1002/chem.202004645

MINSTED fluorescence localization and nanoscopy. Michael Weber, Marcel Leutenegger, Stefan Stoldt, Stefan Jakobs, Tiberiu S. Mihalia, Alexey N. Bukevich and Stefan W. Hell, *Nat. Photonics* **2021**, DOI: 10.1038/s41566-021-00774-2

Bibliography

- [1] Sumudu A. Athukorale, Yadong Zhou, Shengli Zou, and Dongmao Zhang. Determining the liquid light scattering cross section and depolarization spectra using polarized resonance synchronous spectroscopy. *Analytical Chemistry*, 89(23):12705–12712, 2017.
- [2] J.W. Goodman. *Introduction to Fourier Optics*. W. H. Freeman, 2005.
- [3] Joseph Huff. The airyscan detector from zeiss: confocal imaging with improved signal-to-noise ratio and super-resolution. *Nature Methods*, 12(12):i–ii, 2015.
- [4] Giulia M. R. De Luca, Ronald M. P. Breedijk, Rick A. J. Brandt, Christiaan H. C. Zeelenberg, Babette E. de Jong, Wendy Timmermans, Leila Nahidi Azar, Ron A. Hoebe, Sjoerd Stallinga, and Erik M. M. Manders. Re-scan confocal microscopy: scanning twice for better resolution. *Biomedical optics express*, 4(11):2644–2656, 2013.
- [5] J. Clayden, N. Greeves, S. Warren, F. Glauner, K. Mühle, and K. von der Saal. *Organische Chemie*. Springer Berlin Heidelberg, 2017.
- [6] Benoît Roubinet, Mariano L. Bossi, Philipp Alt, Marcel Leutenegger, Heydar Shojaei, Sebastian Schnorrenberg, Shamil Nizamov, Masahiro Irie, Vladimir N. Belov, and Stefan W. Hell. Carboxylated photoswitchable diarylethenes for biolabeling and super-resolution resolt microscopy. *Angewandte Chemie International Edition*, 55(49):15429–15433, 2016.
- [7] Eric Betzig, George H. Patterson, Rachid Sougrat, O. Wolf Lindwasser, Scott Olenych, Juan S. Bonifacino, Michael W. Davidson, Jennifer Lippincott-Schwartz, and Harald F.

- Hess. Imaging intracellular fluorescent proteins at nanometer resolution. *Science*, 313(5793):1642–1645, 2006.
- [8] Michael J. Rust, Mark Bates, and Xiaowei Zhuang. Sub-diffraction-limit imaging by stochastic optical reconstruction microscopy (storm). *Nat Meth*, 3(10):793–796, 2006.
- [9] Jonas Fölling, Mariano Bossi, Hannes Bock, Rebecca Medda, Christian A. Wurm, Birka Hein, Stefan Jakobs, Christian Eggeling, and Stefan W. Hell. Fluorescence nanoscopy by ground-state depletion and single-molecule return. *Nature Methods*, 5(11):943–945, 2008.
- [10] S. W. Hell and M. Kroug. Ground-state-depletion fluorescence microscopy: A concept for breaking the diffraction resolution limit. *Applied Physics B*, 60(5):495–497, 1995.
- [11] Michael Hofmann, Christian Eggeling, Stefan Jakobs, and Stefan W. Hell. Breaking the diffraction barrier in fluorescence microscopy at low light intensities by using reversibly photoswitchable proteins. *Proceedings of the National Academy of Sciences*, 102(49):17565–17569, 2005.
- [12] Stefan W. Hell and Jan Wichmann. Breaking the diffraction resolution limit by stimulated emission: stimulated-emission-depletion fluorescence microscopy. *Optics Letters*, 19(11):780–782, 1994.
- [13] Fabian Göttfert, Tino Pleiner, Jörn Heine, Volker Westphal, Dirk Görlich, Steffen J. Sahl, and Stefan W. Hell. Strong signal increase in sted fluorescence microscopy by imaging regions of subdiffraction extent. *Proceedings of the National Academy of Sciences*, 114(9):2125–2130, 2017.
- [14] Eva Rittweger, Kyu Young Han, Scott E. Irvine, Christian Eggeling, and Stefan W. Hell. Sted microscopy reveals crystal colour centres with nanometric resolution. *Nature Photonics*, 3(3):144–147, 2009.
- [15] Francisco Balzarotti, Yvan Eilers, Klaus C. Gwosch, Arvid H. Gynnå, Volker Westphal, Fernando D. Stefani, Johan Elf, and Stefan W. Hell. Nanometer resolution imaging and

- tracking of fluorescent molecules with minimal photon fluxes. *Science*, 355(6325):606–612, 2017.
- [16] Robert Kasper, Benjamin Harke, Carsten Forthmann, Philip Tinnefeld, Stefan W. Hell, and Markus Sauer. Single-molecule sted microscopy with photostable organic fluorophores. *Small*, 6(13):1379–1384, 2010.
- [17] Vladimir N. Belov, Gyuzel Yu Mitronova, Mariano L. Bossi, Vadim P. Boyarskiy, Elke Hebisch, Claudia Geisler, Kirill Kolmakov, Christian A. Wurm, Katrin I. Willig, and Stefan W. Hell. Masked rhodamine dyes of five principal colors revealed by photolysis of a 2-diazo-1-indanone caging group: Synthesis, photophysics, and light microscopy applications. *Chemistry – A European Journal*, 20(41):13162–13173, 2014.
- [18] Tatsuhiko Nagasaka, Tomohiro Kunishi, Hikaru Sotome, Masafumi Koga, Masakazu Morimoto, Masahiro Irie, and Hiroshi Miyasaka. Multiphoton-gated cycloreversion reaction of a fluorescent diarylethene derivative as revealed by transient absorption spectroscopy. *Physical Chemistry Chemical Physics*, 20(30):19776–19783, 2018.